A novel approach of selective near-IR dye-sensitized solar cells as colorless and transparent photovoltaic : aesthetic evaluation and performance optimization

Waad Naim

To cite this version:

Waad Naim. A novel approach of selective near-IR dye-sensitized solar cells as colorless and transparent photovoltaic : aesthetic evaluation and performance optimization. Material chemistry. Université de Picardie Jules Verne, 2022. English. ⟨NNT : 2022AMIE0042⟩. ⟨tel-04080329⟩

HAL Id: tel-04080329
https://theses.hal.science/tel-04080329v1

Submitted on 24 Apr 2023

Thèse de Doctorat

Mention : Chimie
Spécialité : Chimie des matériaux

présentée à ***l'Ecole Doctorale en Sciences Technologie et Santé (ED 585)***

de l’Université de Picardie Jules Verne

par

Waad NAIM

pour obtenir le grade de Docteur de l’Université de Picardie Jules Verne

A novel approach of selective near-IR dye-sensitized solar cells as colorless and transparent photovoltaics: aesthetic evaluation and performance optimization

Soutenue le 24 janvier 2022, après avis des rapporteurs, devant le jury d’examen :

M. Michel SLIWA, Directeur de Recherche, CNRS, Université de Lille	**Président/ Examinateur**
M. Richard LUNT, Professeur, Michigan State University	**Rapporteur**
M^{me} Elizabeth GIBSON, Professeur, University of Newcastle	**Rapporteur**
M^{me} Claudia BAROLO, Professeur, Université de Turin	**Examinateur**
M. Mathieu MORCRETTE, Ingénieur de Recherche, CNRS, UPJV	**Examinateur**
M. Fabrice ODOBEL, Directeur de Recherche, CNRS, Université de Nantes	**Invité**
M. Frédéric SAUVAGE, Directeur de Recherche, CNRS, UPJV	**Directeur de thèse**

Acknowledgement

I would first like to thank my thesis advisor Dr. Frédéric SAUVAGE who gave me the opportunity to be part of his research group. He has made available his support in many ways and steered me in the right direction whenever he thought I needed it.

I would also like to acknowledge Dr. Mathieu MORCRETTE. The door to his office was always open whenever I ran into a trouble spot, while he supported me with his enthusiasm and patience.

The realization of this thesis would not have been possible without the VISION-NIR family. Many thanks to Dr. Fabrice ODOBEL, Dr. Yann PELLEGRIN, and Thibaut BARON from CEISAM, university of Nantes, Prof. Stefan HAACKE, and Ilias NIKOLINAKOS from IPCMS, University of Strasbourg, for the collaboration and fruitful discussions. I was honored to be part of this collaborative research work. Also, I would like to acknowledge our partners from LCMCP, university of Sorbonne, Prof. Sophie CASSAIGNON, Dr. Capucine SASSOYE, and Dr. Tsou His Camille CHAN CHANG.

Special thanks to my colleague (and best friend), Fionnuala GRIFONI. Without her, this research work wouldn’t be complete. I would also like to give special thanks to Dr. Iva DZEBA and Dr. Thomas ALNASSER, who greatly contributed to this research.

I would like to extend my gratitude to the G+lyte family. Special thanks to Sylvain CEURSTEMENT and Dr. Vijay CHALLURI for all the help, support, and shared knowledge during the last three years.

I am grateful to all the members of LRCS for making this journey much better. Special thanks to Anne CHARBONNIER, Nathalie SAULNIER, and Daphné BOURSIER for their continuous help with all the administration work. Also, big thanks to Christine SURCIN for always being there for us in the lab, ensuring we are all secure.

I owe my deepest gratitude to my family, my support… Each achievement is dedicated to them.

الإهداء...لأبي وأمي دومًا. أنتما الحياة.

فقد الأحبة غربة... لكن ذكراهم وطن.

جدي الغالي... لروحك السلام.

Contents

Abbreviations

A.M.1.5G: air mass 1.5 global

ACN: acetonitrile

ARC: anti-reflecting coating

AVT: average visible transmittance

B1: interhalogen electrolyte (bromide/iodide)

BAPV: building-attached photovoltaics

BIPV: building-integrated photovoltaics

CB: conduction band

CCT: correlated color temperature

CDCA: chenodeoxycholic acid

CIE: international commission of lightning

CMF: color matching functions

CRI: color rendering index

CV: cyclic voltammetry

DADS: decay-associated difference spectra

DFT: density functional theory

DPP: diketopyrrolopyrrole

DSSC: dye sensitized solar cells

D-π-A dyes: donor-π-acceptor dyes

ECo: cobalt-based electrolyte

EI: iodine-based electrolyte

EQE: external quantum efficiency

ESA: excited state absorption

ESI: sulfur/iodine binary electrolyte

FF: fill factor

FTO: fluorine-doped tin oxide

GSB: ground-state bleach

HOMO: highest occupied molecular orbitals

IMVS/PS : intensity modulated photovoltage/photocurrent spectroscopy

IPCE: incident photon-to-electron conversion efficiency

ITO: indium-doped tin oxide

J_{sc}: short-circuit current density

LSC: luminescent solar cells

LUE: light utilization efficiency

LUMO: lowest unoccupied molecular orbitals

NIR: near infrared

OD: optical density

OPV: organic photovoltaics

PCE: power conversion efficiency

PL: photoluminescence

PPcy: pyrrolopyrrole cyanine

PSC: perovskite solar cells

PV: photovoltaics

QDSC: quantum dot solar cells

SE: stimulated emission

SPD: spectral power distribution

SQ: Shockley-Queisser

SSA: steady-state absorption

SSE: steady-state emission

STPV: semi-transparent photovoltaics

TAS: transient absorption spectroscopy

TCSPC: time-correlated single-photon counting

TD-DFT: time-dependent density functional theory

TMAS: tetramethylammonium sulfide

TPA: triphenylamine

TPV: transparent photovoltaics

UV: ultra violet

V_{oc}: open-circuit photovoltage

General introduction

General introduction

From the crisis onset of climate change, the research community extensively contributed to raising the alarm to decision-makers and helping to provide possible directions to lower the carbon footprint of human activities. However, global energy consumption keeps growing with the same trend of the demography and the demanded technological access. Since the 1880s, human and industrial activity sectors have relied on fossil fuel (such as coal, oil, and gas) as an energy source, which is non-sustainable and led eventually to one of the biggest challenges of our era: global warming.

The demand for rapid, faster-paced, and more disruptive energy developments achieving complete decarbonization of energy production has never been more vital. A transition towards higher shares of renewable energy (RE) will simplify achieving universal access to clean and affordable energy. For instance, the European energy roadmap 2030 aims to reduce 40% of the greenhouse gas emissions, increase the share of renewable energy to 32% of consumption, and achieve 32.5% energy efficiency compared to 1990 levels. This transition has already started with renewables providing more than 27% of the global electricity generation by the end of 2019,[1] including about 11% generated by new renewable energy technologies, mainly wind turbines and solar photovoltaics (PV). Driven by cost reductions, renewable electricity is increasingly cost-competitive with conventional thermal power plants. In some regions, RE cost is lower than running costs of existing fossil and nuclear power plants,[2] and solar PV has emerged as the least-cost source of electricity production in the history of humankind.[3]

The building sector accounts for ca. 34% of the energy demand according to the 2021 World Energy Issue Monitor (Figure 1.a). These buildings are also responsible for more than 30% of the greenhouse gas emissions, creating an immense challenge for governments worldwide to prompt critical requirements on energy-efficient buildings. Energy-efficient buildings, net-zero energy buildings (nZEBs), or green buildings, are an outcome of a design philosophy focusing on increasing resource use efficiency while reducing the environmental impact in the whole buildings' lifecycle. In other words, they are described as highly energy-efficient buildings in which renewable energies provide residual electricity demand. Reaching the COP21 Paris agreement in keeping temperature increase below 1.5°C, several countries have already introduced essential requirements towards zero energy buildings. To address this problem and reduce CO_2 emissions, the International Energy Agency suggests a 30% reduction in buildings' energy use by 2050.[4]

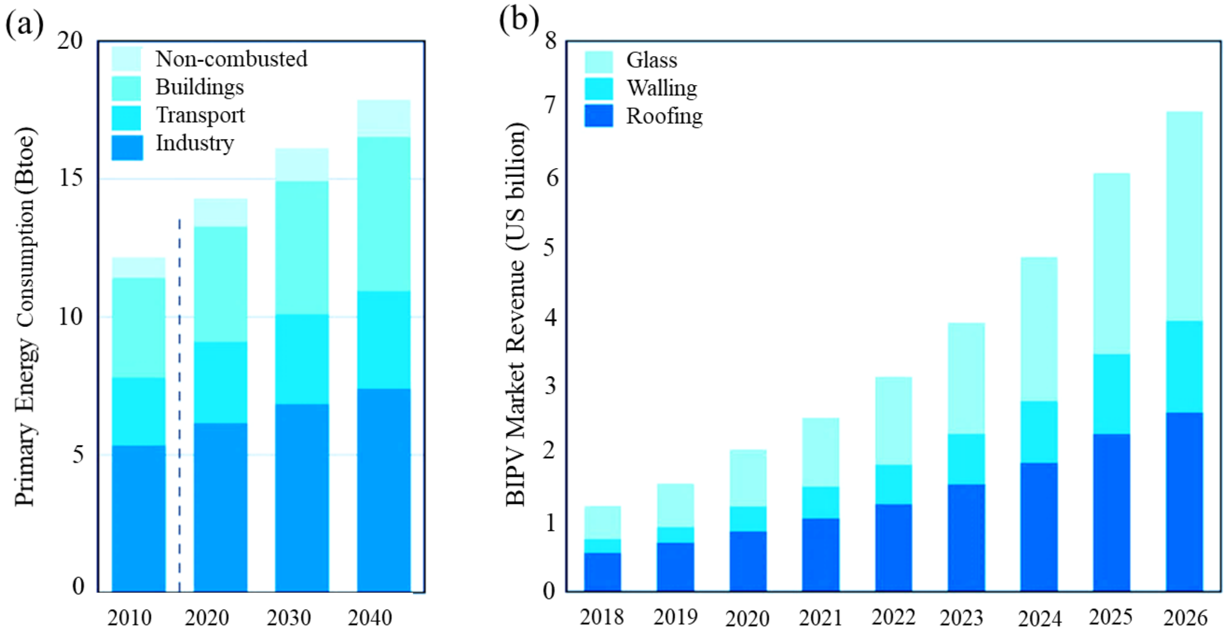

*Figure 1. Statistical proof that pressure on energy saving and CO_2 emission reduction in the building sector will drive the BIPV market. (**a**) Worldwide primary energy consumption by different end-use sectors. Data extracted from BP Energy Outlook.*[5] *(**b**) Worldwide BIPV commercial market revenue 2018–2026, predicted by n-tech Research, 2017*[6].

Photovoltaics (PVs) are deemed one of the most important building-adapted renewable energy technologies, for their feasibility to be deployed on building façades, windows, and roofs, providing us with cleaner electricity. The last decade has witnessed a drastic drop in solar costs, alongside a tremendous growth in the PV market, leading to more building applied/attached PV modules (BAPV).[7] This current situation imposes two main limitations: the accessible area in cities is restricted to rooftops and only some façades, and from an architectural point of view, these BAPV provide poor aesthetics. This scheme was the original impetus for building integrated PVs (BIPVs) to appear as a more desirable solution (Figure 1.b). In contrast to BAPV, reports argue that PV materials can become a true raw building material, like wood, concrete, or glass, if their integration is considered from the early design stages.[8,9] Following this, BIPV can represent both an aesthetically attractive option for new construction or renovation projects and an option adapted to the specificities of urban contexts, characterized by strict limitations on construction. A wide range of BIPV electric generation capacity is reported in the literature, ranging from a few MWhr/yr to more than 100 MWhr/yr, with efficiency values ranging from 5% to 18%.[10]

In the past, PV technologies, as many other renewable energy systems, have often been thought of as performance-driven rather than driven by styling and social acceptance. However, different surveys from the last decade have raised attention on visual aspects. In 2018, a survey of 500 Swiss homeowners showed that 85% of them were considering installing PV, willing to pay a premium of 22% for a roof with architecturally integrated panels compared to a rack-mounted PV installation.[11] Another survey of 138 Californian solar panel installers found that the aesthetics of solar panels was mentioned by 40% of installers as a key factor when selecting a panel to recommend to homeowners.[12] Moreover, aesthetics was found to be a limiting factor to the adoption of solar power in the UK back in 2006,[13] while 17% of respondents of a US survey reported that they were not interested in installing solar panels because they found these panels not aesthetically attractive.[14] This suggested a new trend towards valuing the aesthetic properties of the PV panels rather than on a simple return of investment metric.

Theoretically, BIPV can produce electricity at an attractive cost once considered for energy-generating function and as construction materials, such as roof tiles or façade claddings. This is of particular interest in the context of decarbonizing energy production, especially in densely built areas where traditional ground-mounted PV systems cannot be easily used. As numbers have always influenced science and business, several recent analyses estimated that the BIPV market could grow by nearly 20% compound annual growth rate (CAGR) in the next decade, reaching over US$2.7 billion.[15] The global cumulative installed power of BIPV was 2218.2 MW in 2011 and 4426.1 MW in 2015, holding an average growth rate of ca. 18.3%, with Europe being the largest production region for a market share of ~34 %, while North America contributes to ca. 23% of the production share.[16] As such, this was paid off by real-life applications, where we can see best-practice BIPV examples including the Heron Tower, London, UK (Figure 2.a), the Water and Life Museums and Campus, California, USA (Figure 2.b), the Graz tower in Austria (Figure 2.c), the Xicui Entertainment Complex, Beijing, China (Figure 2.d), the Bordeaux Botanical Gardens, Jourda, France (Figure 2.e), the Konstanz Customer Center, Konstanz, Germany (Figure 2.f) or the dye solar cell façade at SwissTech convention center, Lausanne, Switzerland (Figure 2.g).

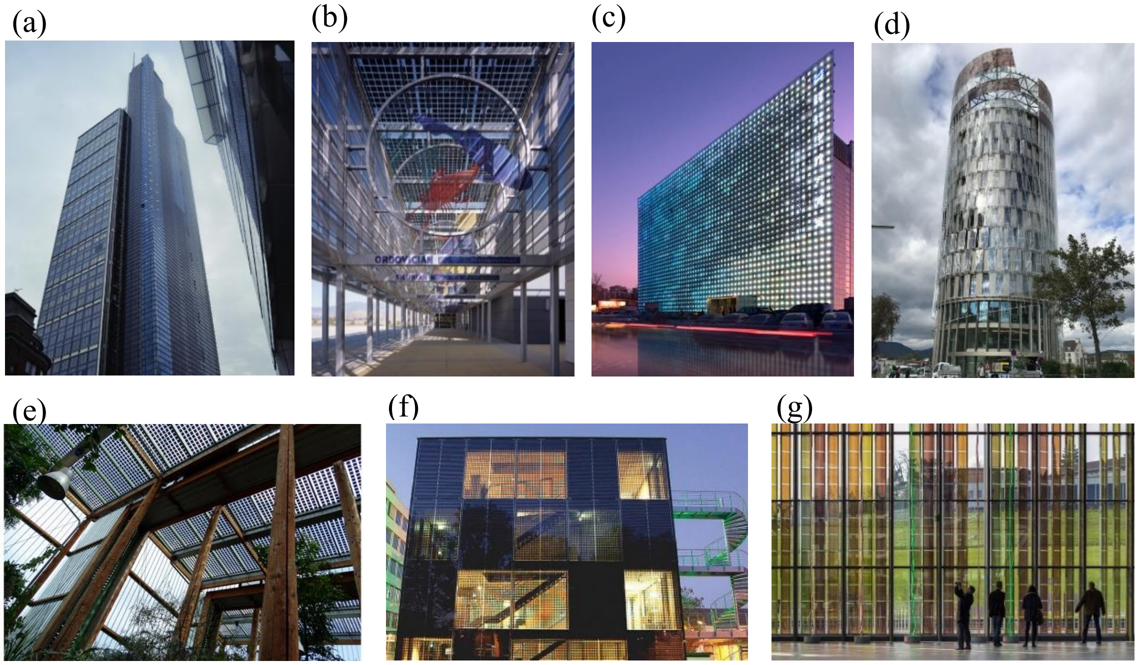

*Figure 2. Best-practice BIPV examples. (**a**) the Heron Tower, London, UK, (**b**) the Water and Life Museums and Campus, California, USA, (**c**)the Graz tower in Austria (**d**) the Xicui Entertainment Complex, Beijing, China, (**e**) the Bordeaux Botanical Gardens, Jourda, France, (**f**) the Konstanz Customer Center, Konstanz, Germany, and (**g**) the dye solar cell façade at SwissTech convention center, Lausanne, Switzerland.*

From the first sketches to the final design stage, a better awareness of the possibilities offered by solar panels needs to be shared among the many stakeholders involved. The BIPV value chain includes manufacturers, suppliers, building owners, tenants, property managers, financing bodies, architects, and installers. Each has different priorities, technical constraints, and competencies, so there is a need for creating new collaboration networks between these diverse stakeholders to bridge the gaps. As costs go down with volume and manufacturing automation, the final PV integration expenditures should also decrease. Notably, the branding and sale of PV façades should present PV as a multifunctional building element rather than a semiconductor product,[17] for which only performance matters. For instance, the efficiency losses of colored or white modules become irrelevant when selling a building element: in addition to being the building skin, the PV module can produce between 70–140 kWh/m^2 per year, which is still a significant amount. Hence, broadening the BIPV market does not only require cost decreases but better marketing and communication of its multiple benefits. The BIPV market is segmented between rooftops, skylights, and façade projects.[18,19] Façades can allow similar electricity production in summer and winter in high-latitude countries or sizable production in a dense environment. BIPV elements can find a high-end segment market entrance in substituting expensive ventilated façades (made, for example, out of glass, stones, or marmor), where the cost per square meter of the customized BIPV elements can be in the range of those of the material to be substituted (typically 200 to 400 €/m^2).[20] In the long run, with increased volume and considering that standard silicon modules are at 60–90 €/m^2, the cost of BIPV elements could drop below those of many façade materials and even come close to high-quality-roofing tiles that are about 50 €/m^2. Customization of color and sizing should not increase the costs by more than 20–100 €/m^2, depending on the techniques applied, the size of the elements, and, of course, on the level of manufacturing automation. Notably, the rooftop market is easier to address, as the visual impact of dummies (non-active modules) is not as critical as it would be for façades.

Transparency, colors, and visual comfort, these terms associated with windows industries, façades, and glass for buildings, have stimulated the work on PV materials that can possess these characteristics while providing efficient solar harvesting and energy conversion. During the last decade, the tremendous growth of attempts to harness solar energy also shed light on the fact that there are still plenty of opportunities for new solar power applications before we can generate enough solar energy to meet our current demand. For instance, see-through solar technologies with the partial light transmission have triggered new possibilities of integration that cannot be explored by conventional Si-based modules, such as Automotive-Integrated (AI)-PV, electronic displays, autonomously powered electronic-glazing, etc. Out of the three solar cells generations, the third-generation technologies evolved on both physical and chemical concepts. They emerged as very credible technologies to cut down the cost of solar by using low-cost printing processes with abundant and non-toxic materials. They also benefit from the known organic chemistry richness to design new efficient materials and nanostructures to optimize light absorption, carrier separation, and their transport towards collection. This third-generation PV gathers organic photovoltaics (OPV), dye sensitized solar cells (DSSCs), quantum dots solar cells (QDSC), and perovskite solar cells (PSC).

Although it may appear that DSSC is not the best performing among the emerging technologies (Figure 3), they remain the most mature in terms of stability and from an industrial processing point of view, with an evaluated energy payback time of ca. 3 months.[21] Moreover, DSSCs have numerous advantages in non-standard conditions. For instance, they are characterized by the possibility of semi-transparency and bifacial conversion.[22,23] This technology offers unique features such as a high sensitiveness to diffuse light or low power conditions, which pave the way for indoor applications to generate power for IoTs. The power conversion efficiency (PCE) is almost independent of operating temperature and light intensities. Last, the DSSC exhibits broad coloration opportunities depending on the type of chromophore used, which is interesting for BIPV applications.

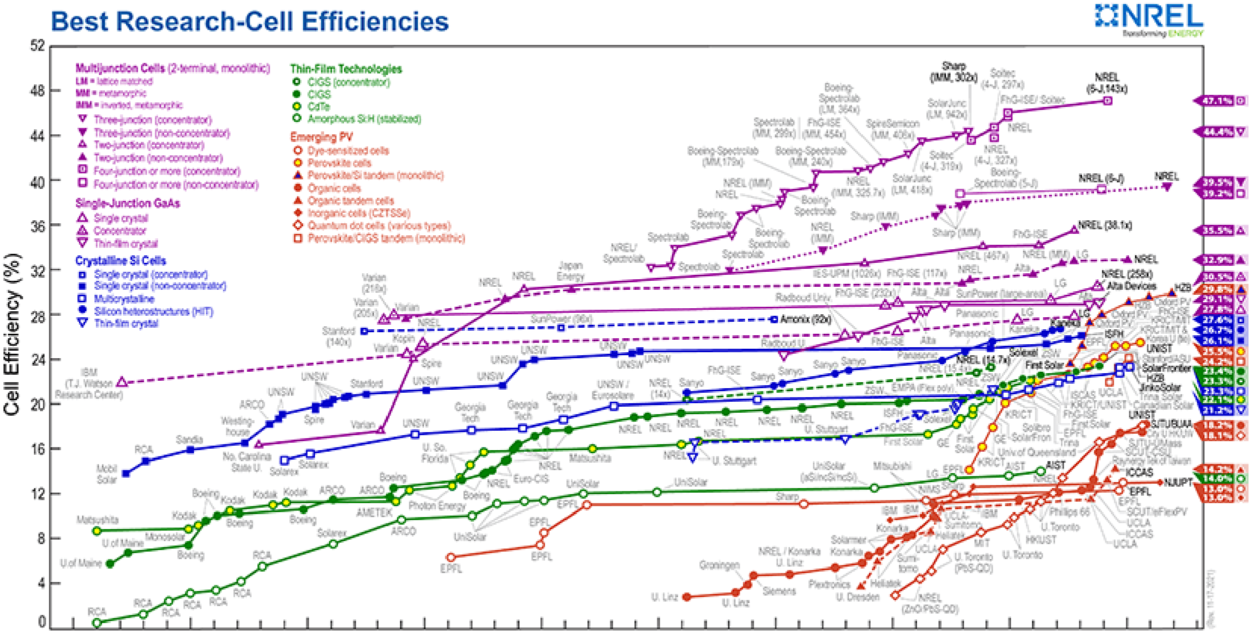

Figure 3. Evolution of the certified record power conversion efficiency for each existing technology since 1976. (Source: National Renewable Energy Laboratory -http://www.nrel.gov/pv/; accessed on September 2021).

This thesis aims to develop and optimize a selective near-infrared (NIR) DSSC with final motivation to create a fully colorless, transparent, and efficient PV. Following the general introduction discussed above, the thesis starts with a chapter about the state-of-art of different transparent photovoltaic (TPV) technologies. After highlighting the main achievements in the TPV domain, a brief yet exhaustive description of NIR-DSSC is presented. In this context, the principle of DSSC is discussed, followed by an overview of the semitransparent DSSCs in the literature. Particular attention is paid to the efforts carried out on molecular engineering to extend light capture of the dyes towards the NIR region.

Chapter 2 is dedicated to the aesthetics evaluation of PV systems. Starting from understanding the visual system and how we perceive colors, the different colorimetry parameters and metrics defined by the international commission of lightning (CIE) are introduced and discussed. This chapter provides guidelines followed in my thesis work regarding the aesthetics evaluation of the developed NIR-DSSC. Moreover, we propose standardizing the criteria followed when referring to the color evaluation of PV by presenting a simple yet precise method.

Chapter 3 presents our first attempt towards selective-NIR light-harvesting in DSSC, followed by optimizing the cyanine dye coded **VG20-C$_x$**. Different approaches targeting the dye structure, the sensitizing conditions, and the electrolyte composition are followed and presented in detail. The performances and limitations are discussed based on intensity-modulated photovoltage/photocurrent spectroscopy (IMVS/PS), dark charge extraction experiments, time-correlated single-photon counting (TCSPC), and ultrafast pump-probe absorption and fluorescence spectroscopy.

Based on the results achieved with the cyanine dye **VG20-C$_x$**, and upon identifying the limiting processes, chapter 4 presents our approach towards higher PCE by developing a new series of dyes from the pyrrolopyrrole cyanine (PPcy) family. Following the presentation and the computational studies of these dyes, their integration for the first time in DSSC is presented. Once again, the IMVS/PS, dark charge extraction experiments, TCSPC, and ultra-fast pump-probe absorption and fluorescence spectroscopy were combined to provide robust insights on the device performances.

In the last chapter, the aesthetics optimization of the best performing dye from the PPcy family is discussed, covering the different parameters contributing to the visual aspect of the DSSC, such as photoanode's thickness, electrolyte composition, and sensitizing conditions. Finally, we present our most recent results in achieving high PCE with NIR harvesting by DSSC technology while rendering the devices transparent and color-neutral. This research work led to the development of NIR-DSSC with PCE > 4% and AVT > 75%, which credibly places this technology as one of the best TPV systems.

Chapter 1

Chapter 1. The emergence of transparent photovoltaics (TPV): a state of the art

In general, PV modules were always designed to absorb as much visible light as possible for the sake of producing a maximum of energy. Consequently, the resulting panels are opaque, mainly black or dark blue. To enhance their adoption in the BIPV domain, these panels had to produce a colored outlook at least, thus reflecting a part of the visible light spectrum, inevitably causing a reduction in the power conversion efficiency (PCE). In addition to the more desirable colors, transparency is a major key factor for the BIPV to be acceptable by industries and end-users. In the recent past, BIPVs were still hindered from large-scale implementations due to the struggling of the standard PV modules in meeting the architectural materials' transparency level and aesthetics standards. The emergence of semi-transparent and transparent photovoltaics (STPVs and TPVs), which consider both light absorption and transmission, had shown great potential by combining both visible transparency and solar power conversion.[24] Similar to the conventional ones, STPVs and TPVs' photovoltaic performances are still evaluated based on the power conversion efficiencies under standard illumination conditions (A.M.1.5G).

Nonetheless, the transparency must be evaluated according to an acceptable standardized metric. In general, the window industry relies on the average visible transmittance (AVT) as a truthful value to evaluate the optical transparency of glazing and thus compare different products within the same metric.[25] As such, AVT was adopted by the PV industries as an aesthetic parameter. It is defined as the weight of the integration of the transmission spectrum of the PV module against the photopic response of the human eye and the solar photon flux.

$$\boldsymbol{AVT = \frac{\int T(\lambda)V(\lambda)S(\lambda)d(\lambda)}{\int V(\lambda)S(\lambda)d(\lambda)}}$$

Where λ is the wavelength, $T(\lambda)$ is the transmission of the tested device, $V(\lambda)$ is the photopic response, and $S(\lambda)$ is the solar photon flux (AM1.5G). AVT calculation and other aesthetics parameters evaluation, namely the chromaticity coordinates, color rendering index, correlated color temperature, color purity, and dominant wavelength of the PV modules, will be explained in-depth in Chapter 2.

To discuss different STPV and TPV technologies, it is salient to group them into two variants according to the approach for light-harvesting, i.e., wavelength-selective or non-wavelength-selective (Figure 4).[24] Not all PV technologies can afford selective conversion of specific wavelength regions. Indeed, the established crystalline semiconductors for which the formed band structure entails unselective photon absorption for all energies greater than the bandgap value. On the other hand, molecular-based PV devices are in stark contrast with the latter since light absorption involves discrete electronic transitions.

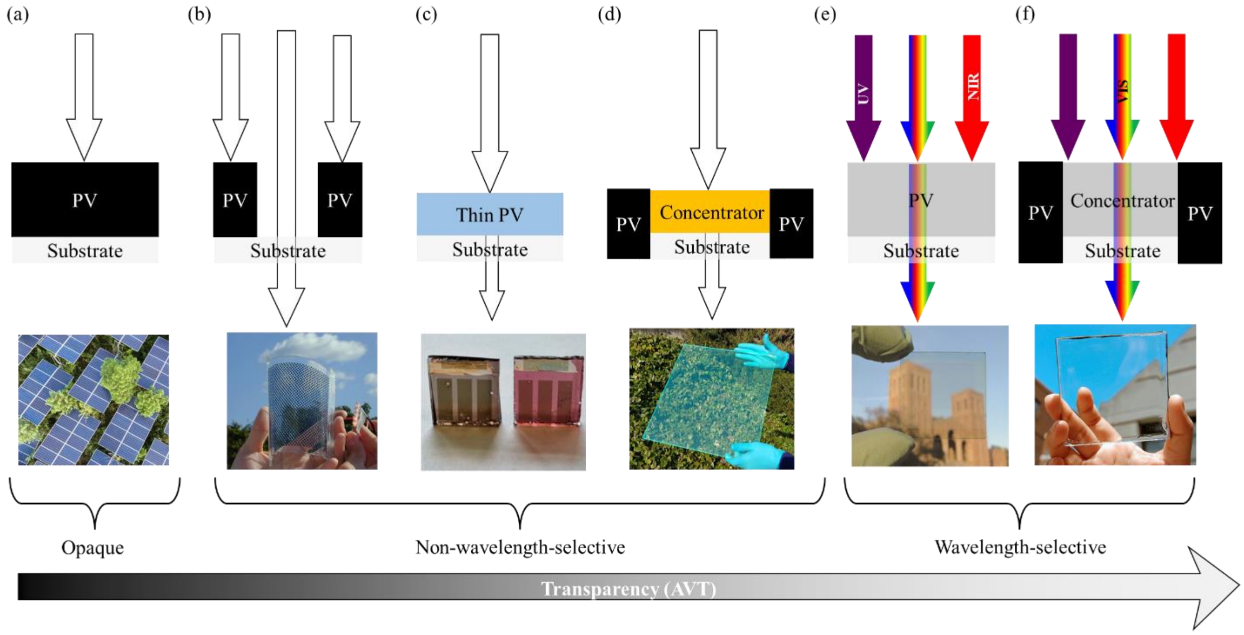

Figure 4. PV systems with various degrees of transmission (adapted from reference).[24] *(**a**) Diagram of a conventional opaque PV (full spectrum sunlight represented by white arrows) and an example of a resulting PV module. **(b)** Diagram of spatially segmented PV and an example of a final module from ref.*[26] ***(c)** Diagram of a non-wavelength-selective, thin-film PV and an example perovskite-based module*[27] *(narrow white arrow represents partial transmission). (**d**) Diagram of a non-wavelength-selective solar concentrator and a photo of colored LSC.*[28] *(**e**) Diagram of a wavelength-selective TPV and an OPV example cell.*[29] *(**f**) Diagram of a wavelength-selective LSC and a wavelength-selective LSC module. Wavelength-selective TPV technologies preferentially harvest UV (violet arrows) and NIR (red arrows) light while permitting the transmission of visible light (rainbow-colored arrows)*

1.1. Non-wavelength-selective TPV

As their name implies, the non-wavelength-selective TPVs exhibit a broad absorption of the solar spectrum, including the visible range. To achieve transparency, the first attempts were based on spatial segmentation of the traditional opaque PVs, which is dispersing the opaque solar cells across a transparent substrate.[27,30,31] Another approach is based on the thinning of the absorbing layer to increase the transparency of the device.[32–34] On average, these technologies feature PCE values between 0.1%[34] to 14%[35] and AVT values up to 50%.[34] They exhibit an intense color, which can be an advantage for some applications, but also a limitation for others.

Despite their remarkable PCE values, solar cells based on III–V technologies are not highly recommended for BIPVs. Due to the high production cost, GaAs is restricted to particular markets that demand high efficiency while the price is lowly considered, such as space technologies.[36] Emerging technologies enabling low-cost and large-scale production of GaAs might make a change. However, the toxicity of As and the scarcity of Ga still hinder it from wide application in civil uses. A similar situation exists for InP, GaInP, and multijunction solar cells stacked with III-V group materials. Consequently, in the foreseeable future, it is hard to witness large-scale implementations of these technologies for the BIPV field.

As Si PV technology dominates the market owing to high PCEs and its large-scale industrialization, which substantially cut the cost per energy, early practices of TPV appeared on Si-based solar cells. Conventional crystalline Si (c-Si) wafers, with thicknesses in the range of 150–200 µm, which are primarily used in commercial technology, are unable to transmit wavelengths in both the visible and NIR portion (340–1100 nm).[37] Even though thinning of c-Si was considered an approach to increase the transparency, the absorption of long-wavelength light ($\lambda > 600$ nm) becomes extremely limited in thin films.[38] As such, their transmitted light usually appears to be dark brown to reddish light brown, which means that their potential application to solar cells is very limited (Figure 5.a).[39] Recently, the commercial developments of tandem amorphous/microcrystalline silicon (a-Si/µc-Si) thin-film modules have been studied for see-through or colored BIPV modules (Figure 5.b).[39] This proof of concept was yet limited to low transmission values of the final panels (20%). Differently, "Silver cells," which are thin, single-crystal silicon solar cells, can show higher transparency due to the module architecture based on spatial segmentation of many individual solar cells. The work of Franklin et al. in 2007 presents a preview of how spatial segmentation of opaque solar cells will appear (Figure 5.c).[40] A high value of >75% AVT was evaluated from the work of Biancardo and co-workers for non-wavelength-selective microspherical semi-transparent solar cells based on Si wafers (Figure 5. d).[26] This high AVT is for a device of 1.17% PCE yet bearing a low aesthetic appearance. An alternative approach was recently demonstrated to construct transparent color-neutral c-Si substrate by placing microhole-shaped light transmission windows utilizing a 200-µm-thick c-Si wafer, achieving 12.2% PCE with a transmittance value of 20% (Figure 5.e).[41] For such technology, a photolithography process and a deep reactive ion etching process were used to fabricate the microhole arrays on c-Si wafers, which brings new obstacles such as cost and larger-scale compatibility with the existing production line.

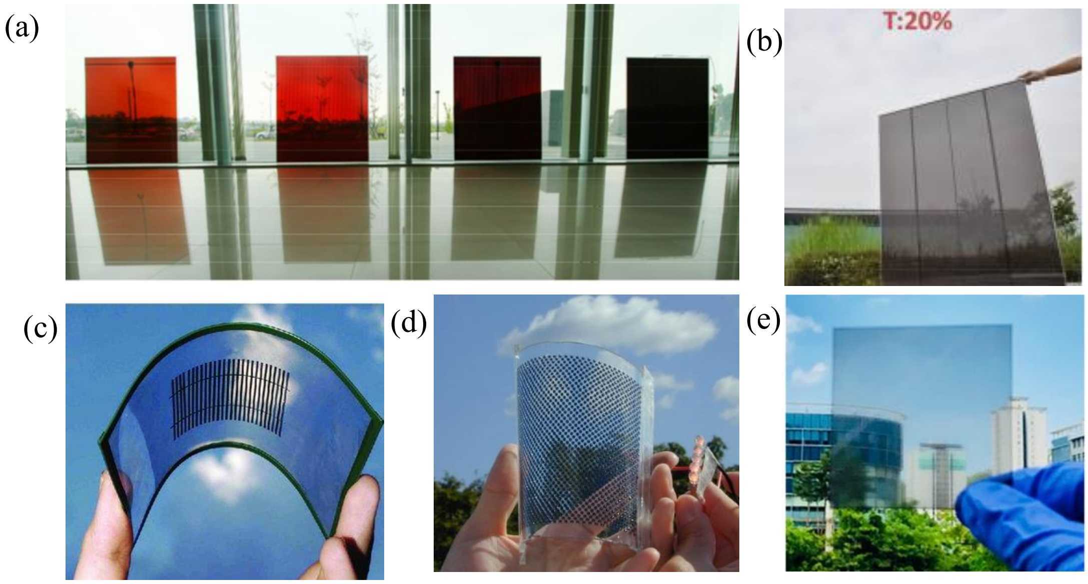

*Figure 5. (**a**) See-through BIPV modules with different light transparency based on different thicknesses of a-Si/μc-Si thin films. (**b**) Light-through a-Si/μc-Si thin-films BIPV modules with 20 % transparency.*[39] *(**c**) A flexible solar cell module based on spatially segmented silver cells.*[40] *(**d**) Sphelar® module based on spherical silicon solar cells.*[26] *(**e**) A transparent substrate of a 200-μm-thick c-Si wafer, fabricated with hole-shaped light transmission windows.*[41]

Accordingly, as perovskite PVs recorded a certified PCE of 25.5%, which is a value close to crystalline silicon technology,[42] there have been attempts to fabricate segmented perovskite STPVs.[27,31,43] Despite their high potentials, inferior electrical properties of patterned perovskite films to conventional un-patterned ones made it difficult to reach a PCE of over 20%.[44,45,46] The loss in performance is mainly attributed to the low compatibility of the patterning processes with perovskite materials. It resulted in lower-quality films, inferior interface quality between the electron transport layer and the perovskite layer, and non-uniformity between patterned microcells.[43,46–49]

Colored semi-transparent perovskite solar cells with a PCE of around 6.5% were reported by Eperon et al. back in 2014, with an AVT < 25% (Figure 4. c).[27] This was achieved by creating microstructured arrays of perovskite, called islands, on a length-scale small enough to appear continuous to the eye yet large enough to enable unattenuated transmission of light between the islands. The best result in terms of PCE is 10.3%, with an AVT of 38%, showing the potentiality of this technology for STPV applications (Figure 6.a).[50] This was achieved by fabricating patterned perovskite films based on a microsphere lithography SiO_2 honeycomb scaffold template, which was derived by a combination of air-water interface self-assembly and O_2 plasma etching. However, perovskite-based technology still faces many impeding issues before large-scale deployment, particularly the stability and toxicity originating from soluble lead and DMF/DMSO solvents for processing.

It is noteworthy to mention that stemming from research on lead halide perovskite solar cells, PbI_2 (a common perovskite precursor) was found to function as a photovoltaic material.[51] Recently, Lunt et al. showed that the lead halide TPVs are presented to achieve a PCE over 1.0% after device optimization while the AVT exceeds 70% (Figure 6.b).[52]

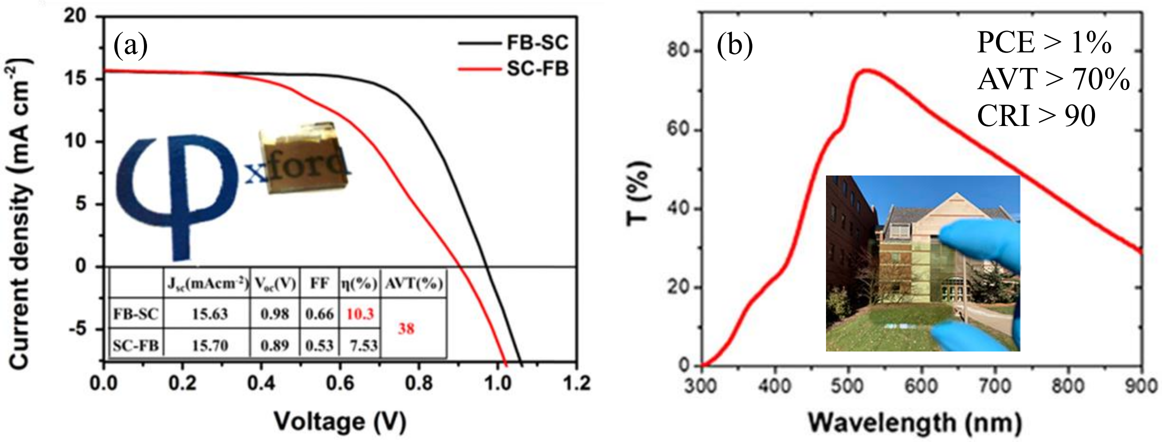

*Figure 6. TPV devices based on (**a**) semitransparent perovskite solar cell reprinted from reference [50], and (**b**) lead-halide solar cells reprinted from reference [52].*

To sum up, the literature reports two pathways to achieve non-wavelength-selective TPV: either by spatial segmentation of the opaque solar cells or by thinning the visible-light absorbing materials to achieve a higher transparency level. However, The Shockley-Queisser limit in broadband absorbing architectures varies sharply with AVT due to the inherent trade-off between performance and transmission, where PCE approaches zero as AVT approaches 100%. This will be highlighted next while discussing the wavelength-selective TPV technologies.

1.2. Wavelength-selective TPV

Regardless of all the development in the non-wavelength-selective PV technologies, the trade-off between the PCE and AVT is one first limitation of this approach, and secondly, the optical characteristics of the absorbing materials result in a colored device. As color-neutral appearance brings new opportunities for PV integration, wavelength-selective PV has appeared to be a game-changing material. In principle, to build a wavelength-selective TPV achieving both high transparency and color neutrality, the TPV device should transmit solely and totally the incident visible. By contrast, the ultra-violet (UV) ($\lambda < 390$ nm) and the near-infrared (NIR) part of the light ($\lambda > 720$ nm), which are both outside the human eye sensitiveness, are required to be quantitatively absorbed by the photoactive material to generate electricity. In order to absorb the UV light selectively and transmit all the visible light above this wavelength, the semiconductor requires a bandgap higher than 3.1 eV. As such, these high-bandgap materials are limited to a Shockley-Queisser limit of ca.6%, imposing significant restrictions on future performances. However, the NIR part of the solar spectrum can be harvested by means of molecular devices, as will be discussed in the following.

The theoretical limit of PCE for a single junction wavelength-selective TPV technology, combining UV-selective and NIR-selective absorption, with an average visible transmittance (AVT) of 100% is 20.5%. This value is lower than the 33.2% Shockley-Queisser (SQ) limit for an opaque single-junction cell of 1.34 eV bandgap. This value has been determined based on the work of Lunt et al. by applying the ideal EQE curves to the Shockley-Queisser limit model.[53] In practice, only 10.8% can be expected after considering all optical losses from the selective conversion of both UV and NIR regions. As presented in Figure 7.a, an increase in AVT will inevitably cause a reduction of the PCE for all optical excitonic gaps. Considering, for example, the bandgap value of crystalline silicon technology (1.12 eV), a wavelength-selective TPV shows evident advantages in the PCE limit against a spatially segmented one, mainly when a high AVT is essential (AVT > 60 %) (Figure 7.b). As aforementioned, wavelength-selective TPV requires molecular-based devices. Organic PV (OPV), luminescent solar cells (LSC), quantum dots solar cells (QDSC), and dye-sensitized solar cells (DSSC) are the main technologies for which the individual molecular electronic structure rules the photon absorption capability, making them suitable technologies for wavelength-selective TPV purposes.

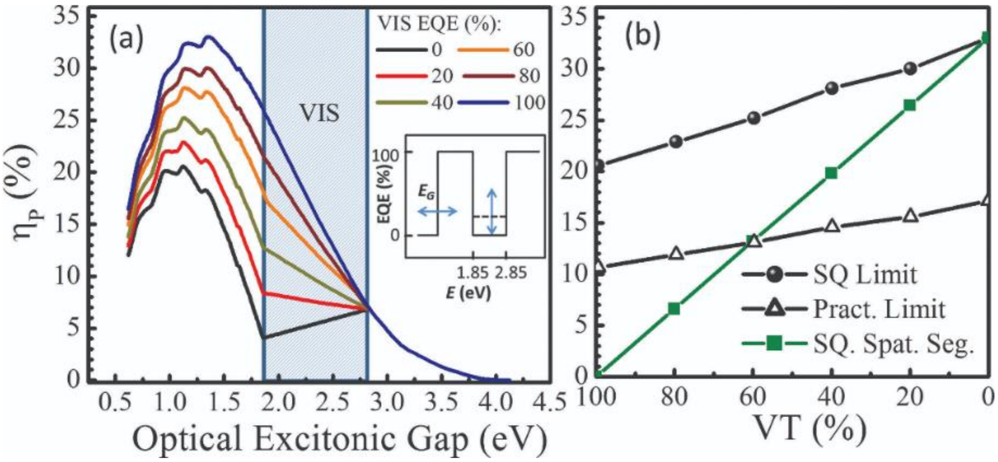

*Figure 7. (**a**) Calculated thermodynamic limiting efficiencies for single-junction photovoltaic cell as a function of the optical excitonic gap for transparent and semi-transparent architectures with varied EQE contribution from the visible part of the spectrum. (**b**) Maximum single-junction efficiencies as a function of the total level of visible transparency in the Shockley-Queisser thermodynamic (closed circles), practical (open triangles), and SQ spatially segmented visibly opaque (closed squares) junction limits. Reprinted from reference [53].*

When AVT value is greater than 60%, wavelength-selective technologies are appealing to be developed. However, it calls for new developments in terms of materials and device design to reduce all parasitic losses of incident visible light. As discussed, the common solid-state semiconductors cannot meet the requirements as their continuous energy levels lead to continuous photon absorption above the bandgap value. For UV-selective light-harvesting, we find in literature practices on using some metal oxide semiconductors, such as NiO and ZnO.[34,54] Even though promising AVT values were achieved (> 70%), low photocurrents were obtained with this approach, resulting in low PCE (< 0.5%). Once again, the emergence of perovskite has provided study material for TPV due to its excellent bandgap tunability. By substituting iodide with smaller halides ($I^- > Br^- > Cl^-$), the absorption onset of perovskites is gradually blue-shifted with a potentiality to end up with UV-selective, transparent solar cells. The first demonstration of perovskite-based TPV devices was reported by Liu et al. in 2018, with either $MAPbCl_3$ (E_g = 3.04 eV) or $MAPbCl_{2.4}Br_{0.6}$ (E_g = 2.83 eV) compositions.[55] $MAPbCl_{2.4}Br_{0.6}$ -based devices were better performing, even though the champion PCE remains low (0.52%). The main outcome is the aesthetics, as the authors reached an AVT of 73% (Figure 8). As this prototype only has an EQE of 20–30% and a FF of 45%, a future PCE value approaching 4% is in prospect when an EQE above 90% and a V_{oc} of 2.0 V can be achieved.

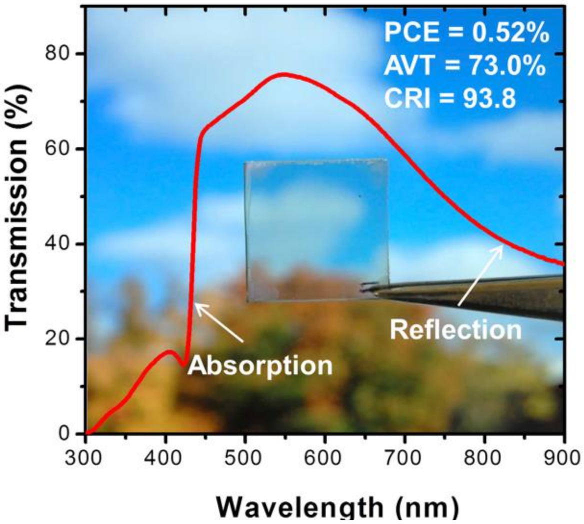

Figure 8. transparent perovskite solar cell with $MAPbCl_{2.4}Br_{0.6}$ composition. reprinted from reference [55].

According to the energy distribution of the AM 1.5G solar spectrum, 51% of the solar energy lies within the infrared (IR) region (Figure 9).[56] As a result, the theoretical PCE of a selective-IR-wavelength absorption PV can be as high as the device with only visible absorption, or even better. Organic solar cells based on polymer or small-molecule organic materials gave an obvious solution for NIR selective absorption due to the nature of relatively discrete molecular orbitals revealed in a non-continuous absorption. And so on, what was deemed a defect limiting light absorption in these PV devices has turned out to be irreplaceable for developing high-performance TPVs.[57] In 2011, Lunt et al. pioneered the field of NIR-selective OPV by their work on a planar heterojunction structure, consisting of C_{60} as the acceptor and chloroaluminium phthalocyanine (ClAlPc) as the donor, with an absorption peak at 740 nm. With a device of 1.7% PCE and 56% AVT, Lunt's group opened a new door for high-performance-TPV based on OPV technology. By utilizing PBDTT-

DPP as a donor and PCBM as an acceptor to form a bulk heterojunction blend as the photoactive layer (sandwiched between two transparent electrodes: top: AgNW-based composite and bottom: ITO), the work of Chen et al. realized a device of 4.01% PCE along with a 64.4% AVT.[29] The design presented in this work has been a typical design in that stage, with a film consisting of a low-bandgap polymer donor and fullerene acceptor being sandwiched by transparent electrodes.[58–64] The non-fullerene small molecules acceptors emerged not so long after, paving the way to further improved performances for OPV cells and organic TPV based on NIR-response donors and acceptors. Following this strategy, scientists have developed devices since 2017 possessing a PCE of 7-10% with an AVT of 30-50%, proving the enhancement in performance. Recently, Liu et al. demonstrated a remarkable device with a narrow-bandgap acceptor (FOIC) and PTB7-Th as the donor, with a maximum absorption peak at 820 nm, achieving 8.32% PCE and AVT values >50%.[65] However, most of the used organic materials still uniformly absorb in the visible range revealing a recognizable color, which necessitates the addition of dielectric layers to modify the spectral transmittance and thus enabling a real sense of color-neutral TPV.[66]

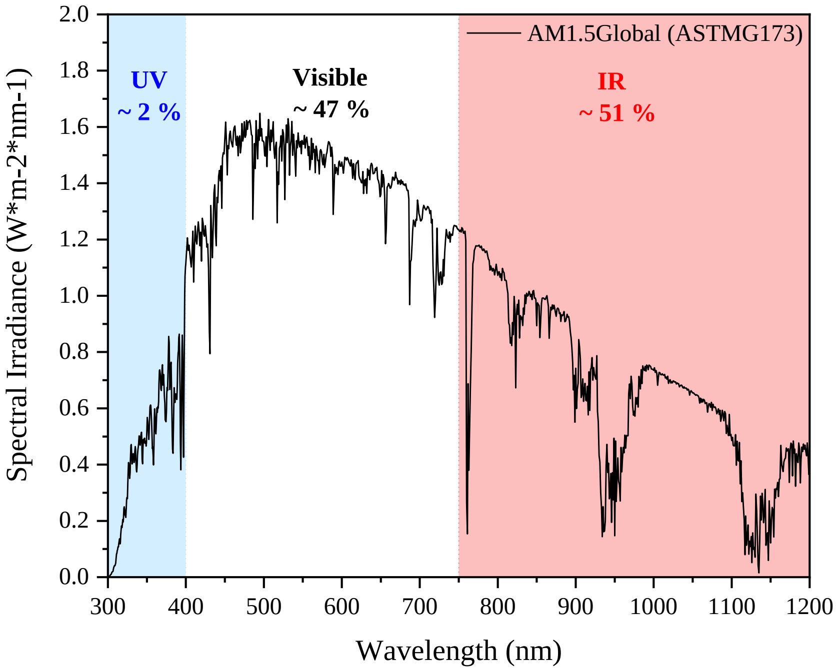

Figure 9. Evolution of the solar irradiance as a function of wavelength under A.M.1.5G conditions.

Discussing different TPV technologies, we highlight the Luminescent Solar Concentrators (LSCs) that work by decoupling the light-harvesting component and the active solar cells. In other words, a LSC typically consists of a polymeric or a glass waveguide with solar cells attached to its edges. The waveguide is embedded with molecular chromophores that harvest the incident light and re-emit photons by fluorescence at a longer wavelength.[67] These photons are guided through total internal reflection until reaching the edge-mounted solar cells, such as GaAs, Si, and DSSC. As such, areas of solar cells are reduced in LSC systems, and an excellent level of transparency can be reached because there are no electrodes exposed to incident light. The color and transparency of LSCs can be adjusted to a great extent by regulating the type and concentration of chromophores. Three types of families have been reported in the literature. The first, reported by Luo et al., consists of Yb^{3+} doped perovskite nanocrystals absorbing in the UV region while exhibiting photoluminescence (PL) in the NIR range, thus having sufficiently high Stokes shift.[68] This approach is limited by the low solar irradiance in UV. Another strategy consisted in inserting a NIR absorber which also emits deeper NIR photons. As such, a spectral overlap between the absorption and the PL spectra needs to be avoided in order to limit photon-recycling phenomena within the absorbing layer. This approach was discussed by Zhao et al. in 2014, using fluorescent organic cyanine salt that selectively harvests NIR photons, yielding a very high AVT value of 86% and a color-neutral appearance.[69] Recently, Lunt et al. reported a PCE of 1.12% after device optimization of the CO_i8DFIC-LSCs, with an AVT exceeding 75%.[70]

Nevertheless, photon recycling events still exist in these materials, therefore hindering to some extent higher performances to be obtained. Recently, Yang et al. reported a new strategy by introducing a dual-band selective-harvesting LSC composed of two distinct waveguides: UV-selective phosphorescent hexanuclear nanoclusters, which are coated on the top waveguide, and a fluorescent organic small molecule to harvest NIR photons selectively on the bottom.[70] With such a dual-band structure, a PCE of over 3% is achieved with an active area of ca. 25 cm² and an AVT of over 75%, setting an outstanding example for developing transparent LSCs with high performance.

1.3. Dye sensitized solar cells: semi-transparency and ensuing advantages

A dye sensitized solar cell (DSSC) is a molecular cell that relies on electrochemical processes, composed of two electrodes, namely the photoanode and the counter-electrode, separated by an electrolyte containing a redox mediator (Figure 10).[71] The core of such a device is the dye, anchored onto the anatase TiO_2 nanocrystals, which rules the device performance in terms of light-harvesting and the final aesthetics depending on the absorption fingerprint of the latter. Based on the dye structure and the possibility of fine molecular tuning, different levels of transparency and color can be given. Consequently, the DSSCs have been deemed an interesting technology to achieve efficient energy conversion and required visual comfort by being wavelength-selective. The record PCE reported in the literature is 14.2% by associating a D-π-A porphyrin dye with cobalt (+III/+II) polypyridil complex.[72]

The operating principle of a DSSC and the main processes at different time scales are reported in Figure 10. As the light is absorbed by the dye, electrons get promoted from the ground state to the excited state (process **1**). This is followed by electron injection from the dye excited-state into the conduction band of TiO_2 in the fs-ps timescale (process **2**). The injected electrons are transported between the TiO_2 nanoparticles (ms timescale) and diffuse towards the transparent conducting oxide (process **3**), where they travel to the counter electrode through an external load. At the counter electrode/electrolyte interface, the oxidized species of the redox couple get reduced, and thus the dye regeneration takes place due to hole capture by the reductive redox species in μs timescale (process **4**). Finally, the diffusion of the redox mediator to/from the counter electrode with electron transfer at this latter occurs in a ms-s timescale, thus closing the loop of the electrochemical cell. However, competitive processes are also governing the device's performance. For some dyes, the electron injection can enter in competition with the deactivation processes of the excited states, ruling dye injection efficiency. The dye regeneration can also compete with a back electron transfer reaction (i.e., geminate recombination presented as process **5**), ruling the dye regeneration efficiency. Last, the electron transport competes with a non-geminate recombination path, i.e., electron transfer from TiO_2 to the oxidant form of the redox mediator (process **6**). The successful production of current, therefore high IPCE, relies not only on efficient light-harvesting efficiency but also on a quantitative yield of electron injection, dye regeneration, and charge collection efficiency. Each unfavorable deactivation path requires to be at least 10^3 times slower than the favorable pathway to reach 99.9 % yield.

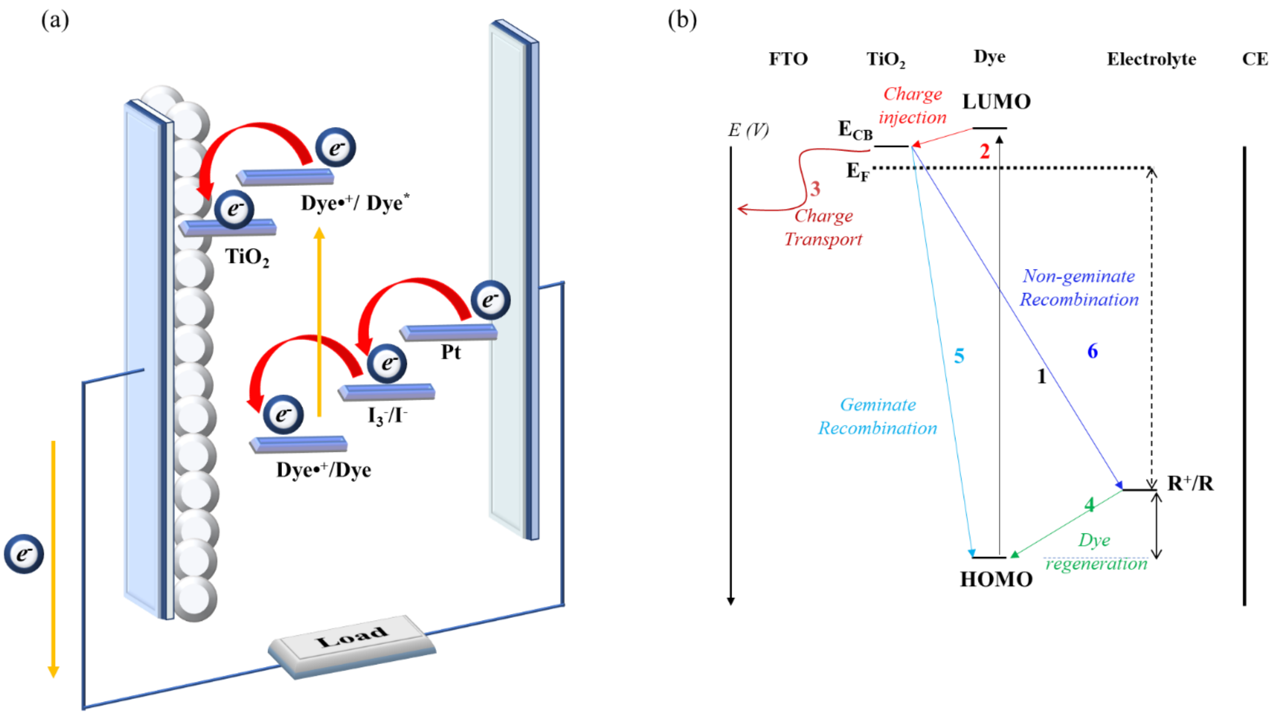

*Figure 10. (**a**) Schematic representation of a DSSC and (**b**) the different charge transfer processes taking place under load and illumination: Dye photo-excitation (**1**), electron injection (**2**), electron transport (**3**), dye regeneration (**4**), geminate electron recombination (**5**), and non-geminate electron recombination (**6**).*

Han et al. were the first to report in 2014 a green-colored see-through DSSC with a PCE of 3.66% and a peak maximum transmittance value of 60% at 560 nm (Figure 11.a).[73] This green semi-transparent technology is based on the co-sensitization between two efficient dyes absorbing in the visible range, one short D–π–A dye (**Y1**) for blue-light conversion (λ = 400 nm) and a central-modified squaraine dye (**HSQ5**) absorbing in the red region (λ = 700 nm) leaving an absorption valley in the green. A photochromic semi-transparent DSSC was also proposed by Demadrille et al., who reported an AVT value of 59% in the dark without photovoltaic activity. The AVT value decreases to 27% under illumination, affording the possibility of converting sunlight with a PCE maximum of 3.7% (Figure 11.b).[74] Semi-transparent DSSC based on a visible absorbing dye **N719** was also proposed by Mallick et al., who reported a maximum AVT of 44% depending on the photo-anode thickness with an efficiency of 2.4%.[75,76] Recently, a dual-band luminescent solar converter-coupled with a dye-sensitized solar cell was reported by Moon and co-workers (Figure 11.c). They achieved so far the most efficient semi-transparent DSSC, with a 7.8% PCE and 43 % AVT.[77]

Whereas a significant amount of research has been carried out to optimize the device performances of lab cells (< 1cm^2), research on large area DSSC modules is merely ∼1% of that on DSSC. [78] A few years ago, Demadrille et al. reported an orange-reddish benzothiadiazole-containing dye, namely **RK1** (PCE_{max}= 10.2% for a 0.16 cm^2 active area), which was one of the first purely organic photosensitizers to be implemented in a large semitransparent DSSC module and suitable for BIPV, with a power output of 10.5 W/m^2 for an active area of 1400 cm^2 (Figure 11.d). [79] Recently, they reported mini-modules fabricated by Solaronix based on the Ru-based dye **N719** and a benzothiadiazole-based dye **YKP-88** (Figure 11.e).[80] The **YKP-88** mini-module (23 cm^2) shows an aesthetic burgundy red tint with an AVT of 26% (measured between 380 nm and 740 nm). This prototype showed a current, I_{sc} of 58.1 mA, a V_{oc} of 3.63 V, and a FF of 58.26%, leading to a power output of 122.9 mW when measured under 1 Sun. This corresponds to a surface power density of 53.4 W/m^2. These performances are higher than those obtained for the reference **N719** mini-module that exhibited a current, I_{sc}, of 51.8 mA, a V_{oc} of 3.52 V, and a FF of 48.5%, leading to a power output of 88.5 mW.

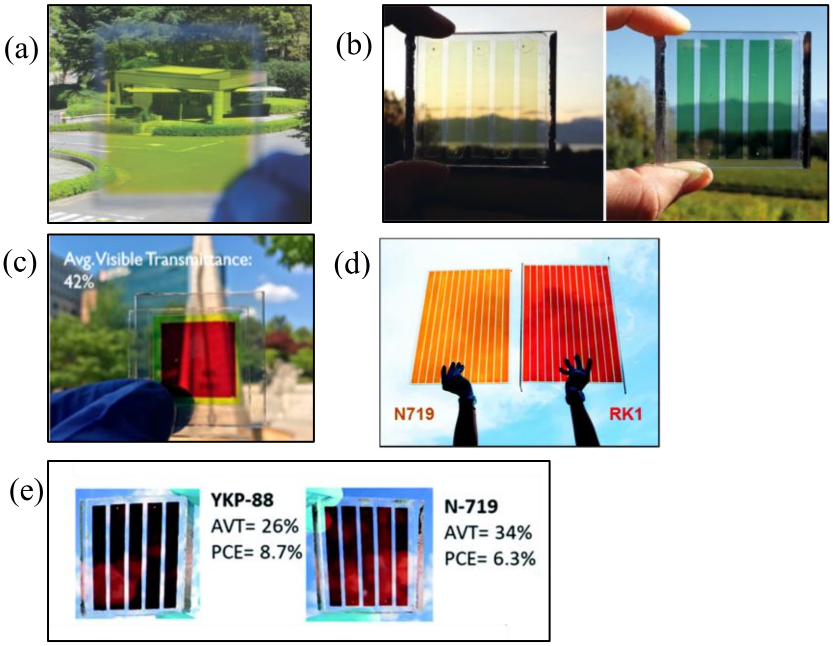

*Figure 11. Semi-transparent DSSC cells and modules. (**a**) **Y1/HSQ5** cocktail cell, reprinted from reference [73] , (**b**) evolution of color of semitransparent **NPI**-based module when exposed to natural light, reprinted from reference[74], (**c**) dual LSC/DSSC device based on **D205** dye, reprinted from reference [77], (**d**) large area DSSC panels fabricated by Solaronix, reprinted from reference [79], and (**e**) mini-modules fabricated with **YKP-88** and **N719** dyes, reprinted from reference [81].*

1.4. Towards selective light-harvesting: NIR-dyes for fully colorless and transparent DSSC

The peculiarity of being highly transparent can meet with color-neutrality by consolidating the capability of NIR or UV-selective light harvesting with a fully colorless electrolyte. During the past 30 years of research, an extensive library of dyes has been developed to improve either the overall performance of DSSC or to fill in the rainbow coloration possibility. A conventional photosensitizer requirement is to reach panchromatic absorption, covering the whole visible to the NIR region. Scrutinizing the UV part was trickier as the FTO, TiO_2, and the conventional electrolytes absorb in the UV region, limiting the expectations from harvesting this wavelength range in DSSCs. A common approach toward panchromatic absorption is dye engineering to broaden its spectral response. A well-known example for Ru complexes is the **N749** dye, also known as "Black Dye."[82] Introducing a terpyridyl ligand in replacement to the bipyridyl counterpart (**N3** dye) resulted in an extended response of 100 nm to the red. A further red-shifted metal-to-ligand charge-transfer (MLCT) transition has also been obtained in **N1044** dye bearing a quaterpyridine ligand, leading to an IPCE spectrum reaching 33% at 800 nm and extending till 910 nm.[83]

Nevertheless, the low molar extinction coefficient in the NIR region of this class of dyes led to the investigation of other sensitizers based on different transition metal or metal-free organic dyes and the use of NIR dyes as co-sensitizers.[84] However, involving MLCT transition in this class of dyes renders the selective absorption of the NIR region not possible. The design of a sensitizer fulfilling this requirement should stem from singlet-to-singlet transitions with narrowed exciton gap energy. Consequently, electron injection and dye regeneration kinetics will be affected, representing one crucial challenge in optimizing such dyes and their interplay with the selective contacts. To assure an effective electron injection, it is typically well-verified that the LUMO level should be located at least 0.2 eV above the conduction band edge of TiO_2 (E_{CB} = -0.45 V vs. NHE). This will place the LUMO level of the sensitizers at ca. -0.75 V vs. NHE, and thus, its HOMO level in the range of +0.75 V vs. NHE for a sensitizer with an optical energy gap in a range of 1.5 eV (ca. 820 nm). Specific dye designs are also required when replacing conventional redox mediators with a metal-based redox couple to afford successful dye regeneration. One approach consists of adding the bulky triarylamine building block with four alkyl chains known as "The Hagfeldt donor."[85]

A variety of dyes have been synthesized for DSSC to reach NIR conversion.[86] Nevertheless, to reach selective NIR-light harvesting, the dye requires no absorption in the whole spectral region covered by the Human eyes. The different classes of dyes possessing energetic levels that can ensure an efficient injection while having an energy gap sufficiently narrow to absorb selectively the NIR region are limited. Mainly phthalocyanines, porphyrins, and polymethine structures are of interest.[87–91] Phthalocyanine (Pc) dyes, known for their high molar extinction coefficient and thermal/chemical stability, can exhibit an absorption maxima in the NIR region with PCE values ranging between 1 and 6.5%.[92–98] Nonetheless, Pc molecules with their planar macrocycle rich of π-electrons tend to form strong aggregates in solution and when anchored onto TiO_2, thus limiting their performances. Overcoming the aggregation problem, porphyrin dyes (Por) are advantageous over the Pc family. These dyes achieved a PCE record of 13 % with **SM315** dye. This latter exhibits a broad absorption spectrum with the longest wavelength maximum at 668 nm.[99] However, even upon structural engineering to extend the absorption towards the red part, Por dyes are still considered as visible light absorbers, and thus the NIR-selective absorption is still to be demonstrated through molecular engineering. DSSC based on phthalocyanine or porphyrin dyes may not be colorless due to absorption residuals in the visible range with a high molar extinction coefficient. However, their high thermal and chemical stability makes them suitable for application in building integration. Furthermore, many efforts have already been made in dye engineering, paving the way for new opportunities, particularly in the case of porphyrin dyes.

Polymethine dyes are highly conjugated molecules and a family well-known for their NIR absorption, a high molar extinction coefficient, and easily tuneable properties through central core or lateral units' modification.[100,101] They have been first explored as sensitizers for silver halide photography, associated with other large bandgap semiconductor materials, and as probes for biological applications.[102,103] By varying the length of the polymethine chain and the lateral units, it is possible to shift the $S_0 \rightarrow S_1$ transition from the visible towards the NIR region. However, a critical drawback in this class of dyes is also the self-aggregation, mainly when anchored onto the semiconductor surface.[104] Aggregates are very detrimental for the device performance and can even cause an onset of new absorption bands, which can overlap with the human eyes photopic response, therefore conferring device coloration. Aggregation can be mitigated by a co-sensitization approach, adding a de-aggregating agent such as the chenodeoxycholic acid (CDCA) or by introducing bulky lateral units or long alkyl chains.[105] Herein, both squaraine and cyanine dyes that belong to the polymethine dyes family are reviewed, presenting the first promising candidates for NIR-selective conversion in DSSC.

1.4.1. Squaraine dyes

Squaraine dyes have been widely investigated for DSSC applications because of their peculiar molecular structure.[106,107] The core is composed of a four-membered aromatic ring derived from squaric acid. Depending on the lateral units, they can be either asymmetric, which were at the core of all first squaraines developed so far to induce charge directionality in the excited states, such as in the most-known **SQ01** by Nazeeruddin et al.[108], or symmetric, which brings ease to the synthesis while maintaining the same optoelectronic properties as demonstrated by Viscardi and coworkers.[109] After inserting a -C_8 alkyl chain as an N-alkyl substituent, the longer alkyl chain led to the reduction of the molecular dye aggregation at the surface of TiO_2, achieving a PCE of 4.5% (J_{sc} = 10.5 mA/cm², V_{oc} = 603 mV, ff = 0.71). However, this type of dye is not enough red-shifted to become a real candidate for transparency owing to its absorption maximum at 636 nm.

Adding an aromatic ring in the indolenine unit induced a bathochromic shift of 25 nm for **SQ02** other than improving photovoltage and photocurrent with an overall 5.4% PCE (J_{sc} = 11.3 mA/cm², V_{oc} = 667 mV, FF = 0.72).[110] The IPCE spectra of **SQ01** and **SQ02** are reported in Figure 12. Geiger et al. synthesized a squaraine dimer **BSQ01** with strong and sharp absorption at 730 nm and a very high molar extinction coefficient (ε = 389000 $M^{-1}cm^{-1}$), presenting an effective approach for red-shifting the squaraine absorbance.[111] However, the performances of this type of dye were rather limited (PCE = 1.3% J_{sc} = 3.11 mA/cm², V_{oc} = 545 mV, FF = 0.76). Following this concept, Maeda et al. proposed the LSQ series that reached 2.3% PCE for **LSQa** dye (J_{sc} = 9.05 mA/cm², V_{oc} = 0.46 V, FF = 0.54) and strong absorption between 770 - 800 nm, however with tails in the visible range.[112] The structures of the reported dyes are summarized in Figure 12.

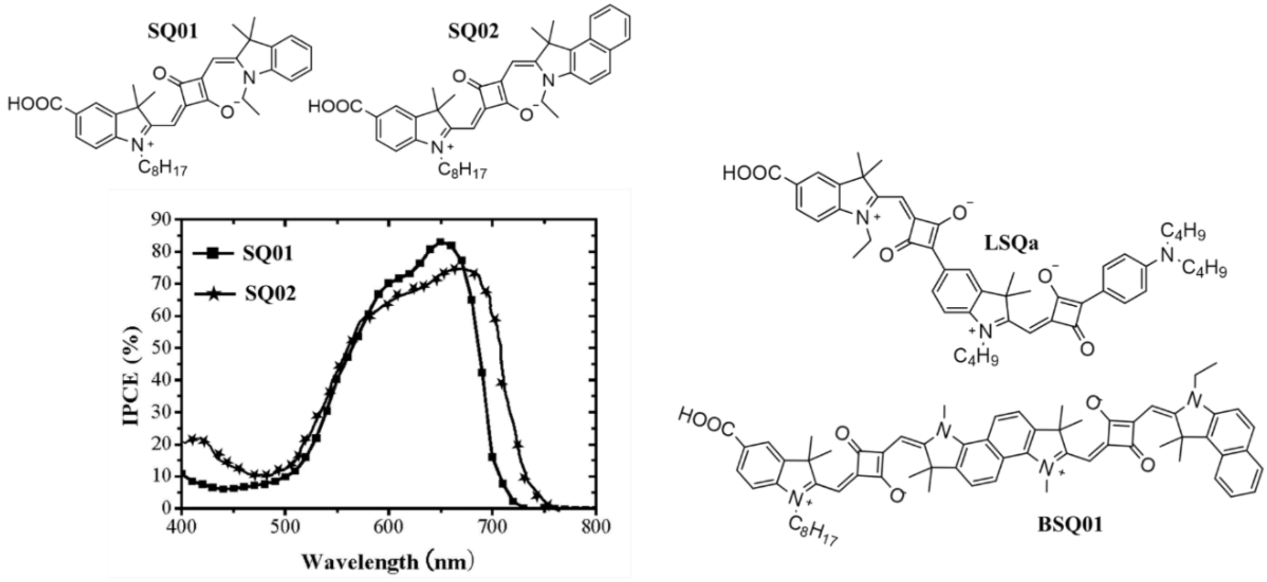

*Figure 12. Chemical structure of the squaraine dyes **SQ01**, **SQ02**, **LSQa**, and **BSQ01** and the IPCE spectra of **SQ01** and **SQ02** dyes.*[113]

Magistris et al. developed **VG5** dye, where the introduction of a benz[*c*,*d*]indolenine unit affords reaching 36% IPCE at 800 nm with a tail of conversion up to 900 nm.[114] However, also in this case, although the optoelectronic properties of the dye are highly promising, it reveals in devices a low PCE value of 1.1% only (J_{sc} = 7.3 mA/cm², V_{oc} = 350 mV, FF = 0.43). One particularity of this dye lies in the position of the anchoring group, which is not located on the benzoindolenine unit but on the other indolium ring. A remarkable accomplishment was achieved by Han et al. with hemisquaraine **HSQ5**,[73] reaching a maximum PCE of 2.3% when associated with a very thick opaque photoanode structure (J_{sc} = 5.47 mA/cm², V_{oc} = 603 mV, FF = 0.70). The absorption spectra and the structure of both **VG5** and **HSQ5** are reported in Figure 13.

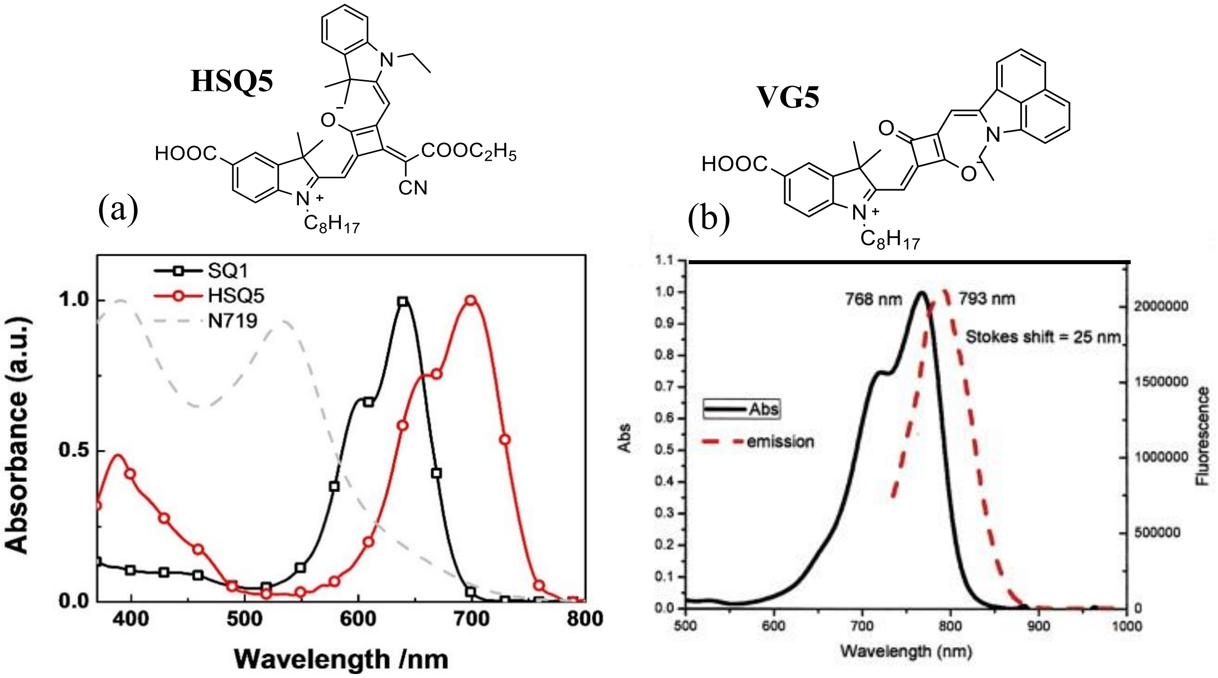

*Figure 13. (**a**) Chemical structure of **HSQ5** squaraine dye and its absorption spectrum (compared to **SQ1**-squaraine and **N719**-Ru dyes). (**b**) Chemical structure of **VG5** squaraine dye and its absorbance and emission spectra*

As aforementioned, developing asymmetric squaraine dyes was questioned upon the development of the symmetrical **VG1** dye showing similar performances to **SQ01** counterpart (PCE = 4.6%, J_{sc} = 9.4 mA/cm^2, V_{oc} = 629 mV, FF = 0.77).[109] **VG1**'s IPCE spectrum is red-shifted by 15 nm, and it generates more photocurrent due to the locked structure in the *cis* conformation, as also proved by Maeda and Han, who inserted a dicyanovinilene unit as an electron-withdrawing group on the squaric core (**SQM-1a)** (PCE = 4.6% J_{sc} = 9.4 mA/cm^2, V_{oc} = 629 mV, FF = 0.77).[115] Viscardi et al. developed **VG10** dye with a maximum absorbance at 673 nm, incorporating for the first time two carboxylic acid directly conjugated on the benzoindolenine ring instead of on the N-alkyl substituent. It delivers a PCE of 6.2% (J_{sc} = 13.6 mA/cm^2, V_{oc} = 641 mV, FF = 0.70).[116] Han et al. demonstrated the advantages of positioning two carboxylic anchoring groups in terms of stability to suppress dye desorption (**HSQ4** reaches a PCE = 5.6% J_{sc} = 15.6 mA/cm^2, V_{oc} = 558 mV, FF = 0.65) in association with a low-volatile electrolyte based on MPN.[117] Adding an electron-withdrawing group on the core unit induces a bathochromic shift of the maximum absorption of about 50 nm and the occurrence of a second absorption band at higher energies, leading to a 30 % enhancement in PCE.[91] Galliano et al. designed a series of squaraine dyes obtaining a photoconversion onset that reaches 51% maximum IPCE at 740 nm with a tail of conversion up to 800 nm for the **VG12-C8** dye bearing a cyano-ester group on the squaraine central core and two benzoindolenine units.[118] Nonetheless, these dyes still absorb in the visible region, implying that further developments are needed to achieve a dye that selectively absorbs the NIR portion. The dyes' structures and absorption spectra are shown in Figure 14.

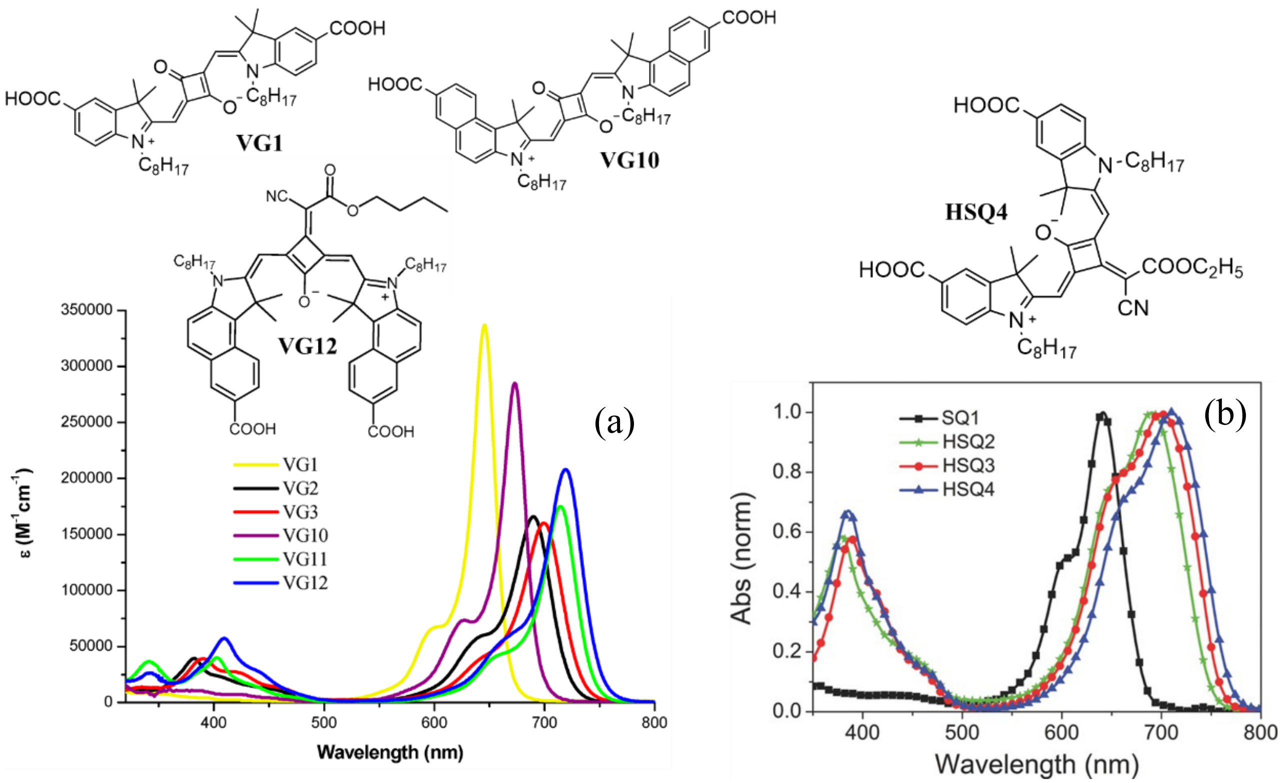

*Figure 14. (**a**) Chemical structure of the squaraine dyes **VG1**, **VG10**, and **VG12** with their corresponding absorption spectra and (**b**) **HSQ4** dye with its absorption spectrum compared to other squaraine dyes.*

1.4.2. Cyanine dyes

Cyanine dyes belong to the polymethine family. This class of dyes possesses several key characteristics for their application in NIR-DSSCs. One important is their tunability. Indeed, a slight modification within the chemical structure has the ability to shift the absorption maximum, for instance, with the introduction of the vinylene moiety (-CH=CH-). The first cyanine dye integrated into DSSC was limited to the conversion of visible light. Despite this, it also led to low PCE values inferior to 1%.[119] Soon after, different studies were taking advantage of these dyes to absorb in the NIR region with final motivation to maximize light harvesting in DSSC either by co-sensitization[120,121] or to explore selective NIR-DSSC.[122]

Sayama et al. synthesized a series of cyanine dyes, for which the absorption maximum was red-shifted from 443 nm, 555 nm, to 660 nm by increasing the number of vinylene units from 0 to 2, with the latter achieving the best performance with a PCE of 2.5% and an IPCE maximum of 50 % up to 600 nm.[123] One of the most efficient NIR dye is the cyanine **NK-6037** reported by Arakawa et al. in 2009, achieving a PCE of 2.3% (J_{sc} = 8.85 mA/cm², V_{oc} = 450 mV, FF = 0.58).[122] The introduction of the benzo-condensed heteroaromatic unit in the polymethine chain leads to an absorption of over 800 nm. When associated with an unusually thick photo-anode (i.e.,> 25µm), they reported an IPCE of over 50 % at 840 nm with a tail extending up to *ca.* 950 nm. Later Matsui and co-workers proposed another cyanine dye coded **KFH-3** (λ = 787 nm and ε = 263000 $M^{-1}cm^{-1}$) associated with ZnO photo-anode.[124] The authors achieved an overall 1.2 % PCE (J_{sc} = 3.34 mA/cm², V_{oc} = 490 mV, FF = 0.76) for a 7 µm thick ZnO electrode and an IPCE maximum of 33 % at *ca.* 790 nm.

A comparison between symmetrical and unsymmetrical cyanine dyes was investigated by Nüesch et al.[125] They showed that the symmetrical cyanine offers a red-shifted absorption and the highest molar extinction coefficients, similarly to squaraines. The dye **Hepta4** is designed as a polymethine core rigidified by a cyclohexene moiety and one anchoring carboxylic group terminating the benzoindolenine (Figure 15). The dye reached an absorption maximum at 758 nm (ε = 82500 $M^{-1}cm^{-1}$) and a PCE of 1.2 % (J_{sc} = 3.22 mA/cm², V_{oc} = 480 mV, FF = 0.78) with a transmittance of 40-55% in the visible range. A transparent pale-green DSSC was achieved based on this cyanine dye (Figure 15), thus highlighting the relevance of developing such dyes for TPV. First explanations on the systematically low PCE values for cyanine dyes were reported in 2015 by Ziolek et al. using ultrafast pump-probe transient absorption spectroscopy (ref). The authors proved that one main limitation is the strong tendency for dye aggregation. For this, they investigated **MK-245** dye, which the structure is closely related to **NK-6037**, however without being as efficient (PCE = 0.46%, J_{sc} = 2.51 mA/cm², V_{oc} = 375 mV, FF = 0.49).[126]

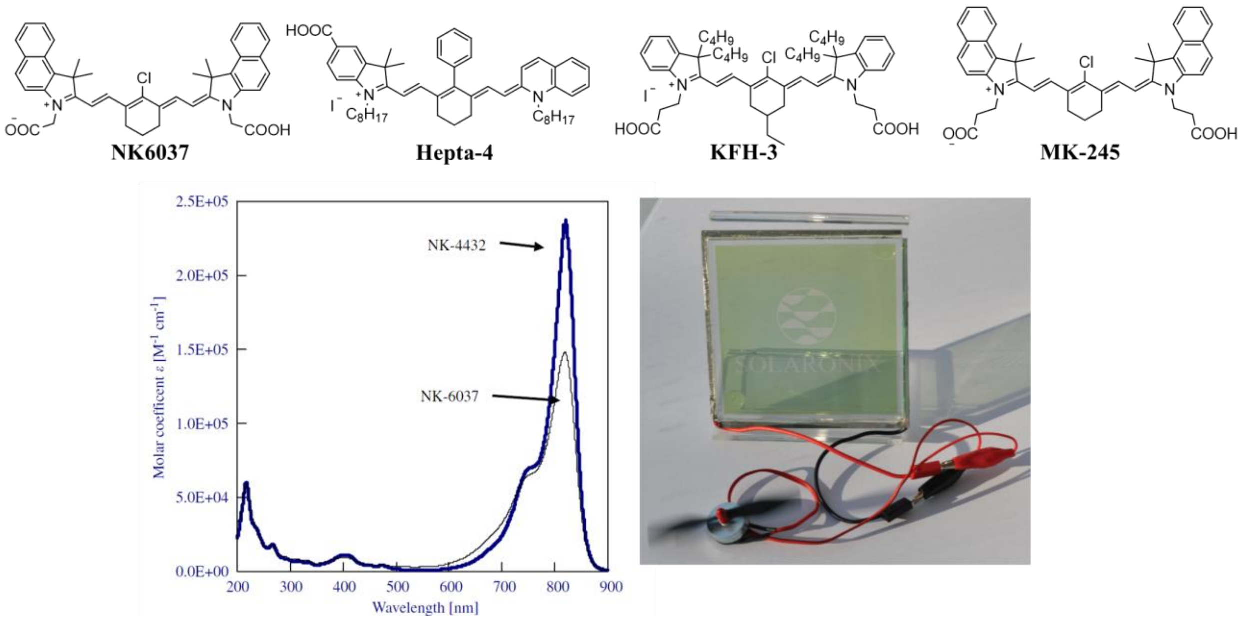

*Figure 15. Chemical structures of the cyanine dyes **NK6073**, **Hepta-4**, **KFH-3**, and **MK-245**. The absorption spectrum of **NK-6037** dye (to the left) is shown in black representing sharp absorption in the NIR region with minimal residuals in the visible part. To the right is a Solaronix-big area- DSSC based on **Hepta-4** dye.*

1.5. Conclusions

The scope of this chapter was to provide a general but in-depth description of the state-of-the-art of the different transparent photovoltaic (TPV) technologies. These technologies can be either wavelength-selective or non-wavelength selective. We reviewed the best achievements in both groups and highlighted the importance of wavelength-selective light conversion, namely the UV and NIR-light, to achieve fully transparent and colorless PV. The inherent trade-off between PCE and AVT for non-wavelength-selective technologies can be avoided by moving to NIR/UV-selective light conversion, where a theoretical PCE of 20.5% can be achieved with an AVT of 100%.

Not all PV technologies can afford selective conversion of the UV/NIR regions to reach high transparency. Indeed, the band structure of established crystalline or amorphous inorganic semiconducting PV technologies entails unselective photons absorption above the bandgap energy. Molecular-based devices such as OPV, LSC, and DSSC are needed by taking advantage of the charge separation from discrete orbital levels. As such, DSSC technology affords to harvest the NIR light of the solar spectrum selectively. The visual rendering of DSSC technology is particularly advantageous since both coloration and transparency levels can be adjusted. In the context of TPV in the literature, we reviewed different studies on semitransparent DSSC.

Moreover, a particular attention has been given to dye engineering towards NIR light harvesting. Different classes of dyes have been developed and investigated so far for dye-sensitized solar cells. The approach of dye engineering has afforded to develop DSSC devices with a variety of colors and with a good level of performance. However, with the aim to develop a selective NIR-DSSC, the choice of sensitizers becomes limited to a very few families. In the current state of the art, the most interesting family remains the polymethine dyes from an optical point of view. The most interesting for this application is clearly the cyanine dyes because of their absorption spectrum's tunability, the high molar extinction coefficient, and the sharp and strong absorption in the NIR region.

Chapter 2

Chapter 2. Colorimetry for photovoltaics: A route to assimilate how to report a solar panel’s color

The concept of color is one of the most fundamental building blocks on which we humans interpret the world surrounding us. It is a pervasive part of our visual experience. For that, colorimetry, or the science of color, which is closely associated with human vision, has attracted a great deal of interest that spans many centuries. Understanding how we perceive colors necessitates understanding the human eye's sensitivity, after which we will be able to quantify the color characteristics (Figure 16). In this chapter, colorimetry for photovoltaics is explained in detail. Definitions, equations, and metrics to evaluate colors of opaque and semi-transparent solar cells are given. Requirements to achieve fully colorless and transparent photovoltaics are highlighted.

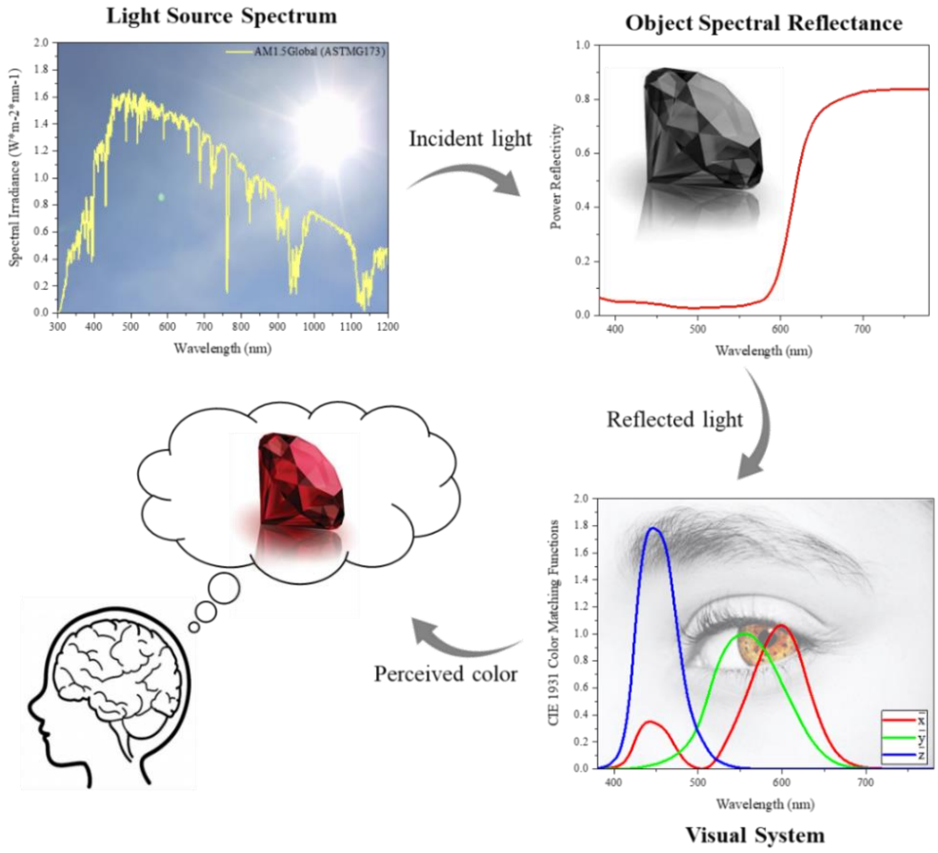

Figure 16. Schematic representation of the human eye perception of the color of a red object

2.1. Human eye sensitivity: How do we perceive colors?

The inside of the human eyeball is clad by the retina, which is the light-sensitive part. It is composed of rod cells and cone cells (Figure 17.a). The number of rod cells is higher than the cone ones. Rods are more sensitive to light over the entire visible spectrum, providing us with twilight vision. Since the 18th century, the human visual system has been defined to possess a trichromatic color vision based on the three primary colors: red, blue, and green. The physiological evidence for the trichromatic theory was later given, as proved by color-matching experiments.[127] As such, three types of cone cells are at the basis of the eye's sensitivity, namely the red, green, and blue cones. Depending on the luminance level of the light, the vision is mediated by either cone or rod cells, leading to three different vision regimes (Figure 17.b). The scotopic vision regime relates to human vision at low ambient light levels, such as at night. In this case, the rods mediate the vision for luminance lower than 5.10^{-2} cd/m^2. Even though the rods have higher sensitivity than the cones, the sense of color is essentially lost within the scotopic vision regime. At higher luminance levels, greater than 6 cd.m^2 like during full daylight, our cones mediate the vision. This is the photopic regime. Between the scotopic and photopic regimes, we have the intermediate mesopic vision, where both cone and rod cells are active.

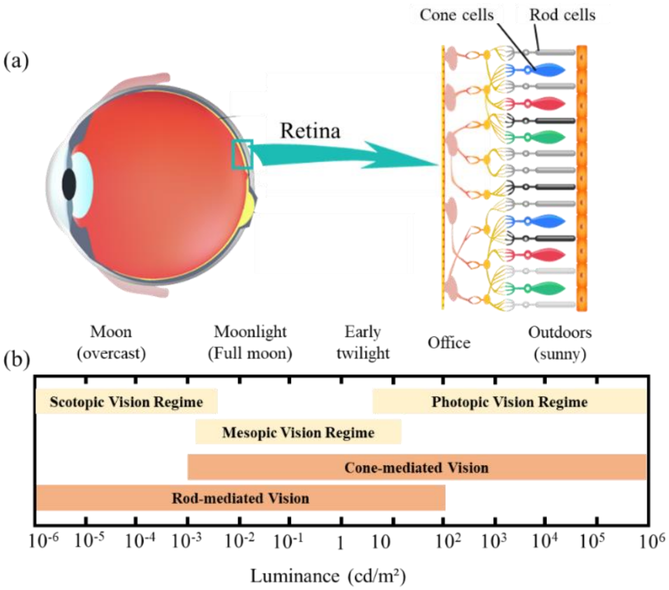

*Figure 17. (**a**) Cross-section schematic of a human eye and schematic view of the retina including rod and cone cells, and (**b**) Approximate ranges of vision and receptor regimes.*

The physical properties of light are usually characterized by radiometric units such as radiant flux, radiant intensity, irradiance, etc.… However, these units are irrelevant considering the light perception. For instance, infrared radiation causes no luminous sensation in our eyes. Therefore, photometric units are needed to characterize the light and color perception by the human eye. For example, defining the light intensity of an optical source as perceived by the human eye gives us the photometric quantity of luminous intensity, i.e., the ratio of the luminous intensity emitted divided by the projected surface area gives us the luminance. This is the unit used to classify the different vision regimes. The conversion between radiometric and photometric units is provided by the luminous efficiency function or eye sensitivity function: the photopic response, $V(\lambda)$.[128] Initially defined by the Commission Internationale de l'Eclairage (CIE) in 1931, the photopic response function $V(\lambda)$ evolved to obviate any underestimation of the response of human eyes in the blue and violet spectral region (<460 nm). The CIE 1978 $V(\lambda)$ function, which can be considered the most accurate description of the eye sensitivity in the photopic vision regime, is shown in Figure 18.

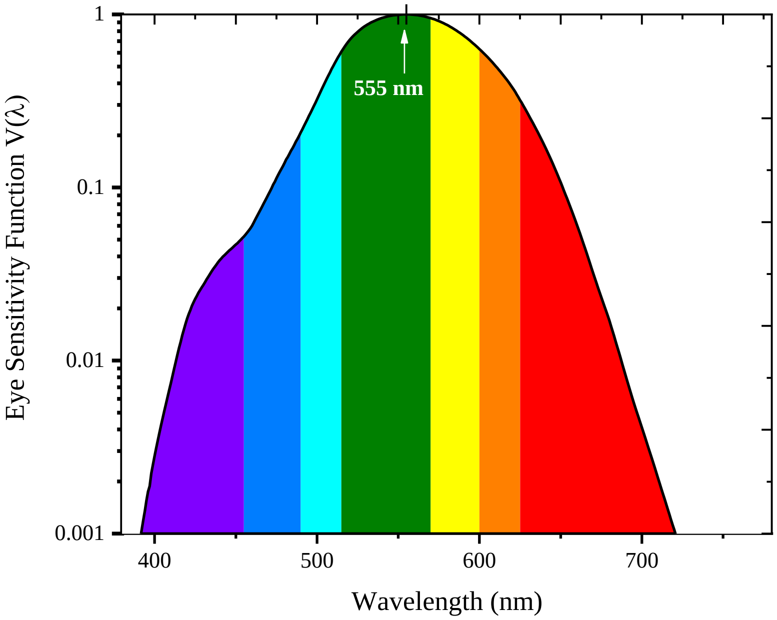

Figure 18. Eye sensitivity function V(λ) extracted from CIE 1978 data. V(λ) is equal to unity at 555 nm.

The photopic eye sensitivity function $V(\lambda)$ has maximum sensitivity in the green spectral range at 555 nm; i.e., $V_{(555\,\mathrm{nm})} = 1$. For wavelengths ranging from 390 to 720 nm, the eye sensitivity function $V(\lambda)$ is greater than 10^{-3}. Even though the human eye may be sensitive to light with wavelengths

< 390 nm and > 720 nm, the sensitivity at these wavelengths is extremely low. Therefore, we can define the visible light in the wavelength range 390 nm ≤ λ ≤ 720 nm. However, for accuracy and to prevent color perception underestimation, 380 nm ≤ λ ≤ 780 nm range is considered in all calculations.

Starting from this point, whenever referring to the transparency of solar cells, Average Visible Transmittance (AVT) is a recommended and generally accepted approach by the window industry.[129] AVT is defined as the weight of the integration of the transmission spectrum of a given solar cell $T(\lambda)$ against the photopic response of the human eye $V(\lambda)$ and the solar photon flux under A.M. 1.5G conditions $S(\lambda)$ (Eq. 1):

$$\boldsymbol{AVT = \frac{\int T(\lambda)V(\lambda)S(\lambda)d(\lambda)}{\int V(\lambda)S(\lambda)d(\lambda)}} \qquad Eq.(1)$$

The AVT in residential windows can range from 15% for highly tinted glass up to 78% for common double-glazing clear glass. In general, glass with an AVT value above 60% looks clear, and any value below 50% begins to look dark, colored, and/or reflective.[130] Achieving highly transparent PV requires then a minimum AVT value of 60%. However, being transparent does not mean being colorless. Therefore, to develop color-neutral PV, other metrics should be taken into consideration.

2.2. Colorimetry for photovoltaics

2.2.1. How to define a color: Useful terminology and definitions

As solar panels marked their sixth decade in commercial applications, aesthetics became a more crucial criterion, and the PV market demand was more than just efficiencies. For instance, transparency, color, and color-neutrality were introduced in the field. Such new perceptions of PV panels create a new value for building integration, agri-photovoltaic, urban street equipment, Internet of Things (IoT), or smart panels. Each of these applications necessitates standards of aesthetic appearance in terms of transparency and colors. To accurately report an object's color, a few terms and their definition are to be discussed. This section covers our view on most of the salient points of the topic in relation to the thesis work on selective NIR-dye sensitized solar cells.

The perception related to the wavelengths of the visible light was often described through sets of primary colors, such as the red, green, and blue system (RGB), and the sets of combinations of these primary colors. This set of colors, defined as the ***gamut***, is usually projected into a ***color space***, where colors are represented mathematically in a specific organization. In different color spaces, color is usually measured by the following four attributes (Figure 19):

(1) Hue: it is the sensation according to which an area appears to be similar to one, or proportions of two, of the perceived colors red, yellow, green, and blue.[131] The hue angle is thus expressed as between 0 and 360° (hue circle). The hue error (ΔH) is used to indicate color difference, but the color brightness/lightness is ignored in this value. As discussed later, the hue can be expressed by the dominant wavelength.

(2) Brightness: it is the human sensation by which an area exhibits more or less light; as such, ***lightness*** is defined as the sensation of an area’s brightness relative to a reference white color. Brightness (used for light) and lightness (used for objects) are key parameters in defining a color. It can also be described as the intensity of a color (***value***), on a scale of 0 to 100%, with zero being completely black and 100 being the brightest and revealing the most color.

(3) Saturation: as the human eye differentiates different levels of a color hue, the saturation of color indicates this differentiation relative to the brightness. It describes the amount of gray in a particular color from 0 to 100%. Reducing this component to zero introduces more gray and thus produces a faded effect.

(4) Chroma: Chromaticness, colorfulness, of an area judged as a proportion of the brightness of a similarly illuminated area that appears white or highly transmitting. It is similar to the concept of saturation but not quite the same.

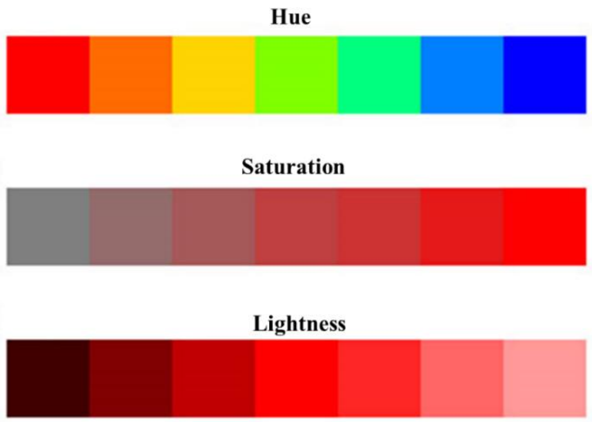

Figure 19. The three main dimensions of an object's color, hue, saturation, and lightness are expressed in three panels. In each panel, one dimension is changing linearly while the other two remain constant.

In the history of colorimetry, different color spaces were used. For example, the *RGB* color space represents colors as a numeric array whose elements specify the intensity of the red, green, and blue color channels. As the hue (*H*), saturation (*S*), and value (*V*) are used to define color, the *HSV* color space is also used in computer vision and image analysis for the segmentation process. However, the international commission of illumination, Commission Internationale de l'Eclairage (CIE), which is considered the authority on the science of light and color, standardizes the measurements of color in their CIE color spaces by means of color matching functions and chromaticity diagram. The CIE most used color spaces discussed below are: the CIE 1931 *x,y* chromaticity diagram, the CIE 1976 *u',v'* uniform chromaticity diagram (that leads to CIELUV space), and the CIE *L**, *a*,b** (CIELAB) color space.

2.2.2. Color Rendering Index

More closely to the desired application of colorimetry in the PV field, we highlight the color rendering index (CRI), introduced by the CIE as a metric to describe quantitatively how accurately the color of a given object is rendered either from a light source or through a transparent medium with respect to an "ideal" illumination source. In our case, it is a transparent medium that is considered for see-through TPV devices. The CRI value is calculated as an average score on eight different test color samples within an evolution of functions. Color rendering gained its tangible importance with the introduction of commercial fluorescent lamps in the twentieth century.[132] For comparison, white fluorescent tubes have a CRI value of around 60, standard LED lights score around 80, and only incandescent lamps score 100, which are, effectively, almost blackbody radiators.[128] Depending on the application, the appropriate CRI value is selected; for example, while highway lighting CRI value is usually below 70, a minimum of 80 is required for an office work environment. The selection of the appropriate CRI range for semi-transparent and transparent solar cells in BIPV is stringent as the CRI value defines the spectral transmissive quality of windows and thus encompasses the receiver's visual comfort.[75] In architectural daylight concepts, values above 90 are considered excellent, while CRI < 80 provides an attenuated perception of the colors (Figure 20)[133] This evaluation is of a critical role for TPV to be considered in BIPV applications such as solar windows, as the CRI value will determine how the outside is scene through the PV glazing.

CRI > 90 **CRI < 80**

Figure 20. Illustrative representation of the effect of the windows' CRI value on the color perception.

2.2.3. Color Matching Functions (CMFs) and Tristimulus Values

There are two fundamental methods of producing color stimuli: additive and subtractive color mixing. Basic colorimetry is based on additive color mixing, resulting in color matching experiments. As the cone sensitivity functions are not usually used directly in color calculations, the color matching functions (CMFs) were introduced (Figure 21), namely $\bar{x}(\lambda)$, $\bar{y}(\lambda)$ and $\bar{z}(\lambda)$, as the numerical description of the chromatic response of the observer (defined by the CIE 2° standard observer; dimensionless). These three CMFs reflect the fact that human color possesses trichromacy; that is, just these three variables can describe the color of any perceived light.

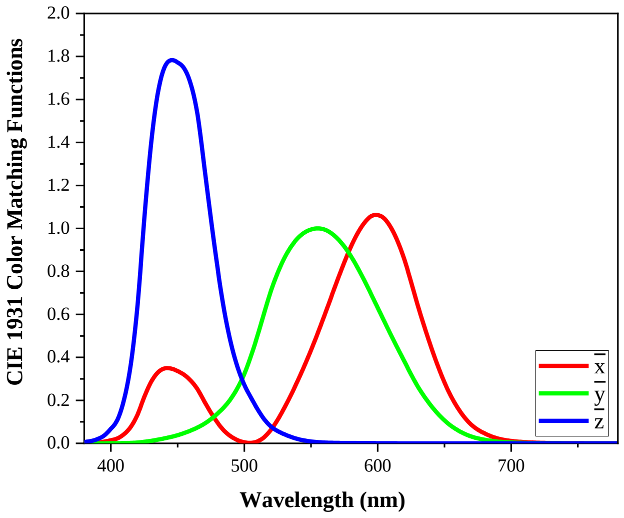

Figure 21. CIE 1931 $\bar{x}$, $\bar{y}$ and $\bar{z}$ color matching functions (CMFs). The $\bar{y}$ is identical to the eye sensitivity function V(λ).

The most basic quantities in colorimetry are the tristimulus values (*X*, *Y*, *Z*), as they define the three-color perception values of the human vision. CIE introduced them in 1931 as a more practical replacement of the well-known (red, green, blue) system.[134] Therefore, the CMFs can be thought of as the spectral sensitivity curves of three linear light detectors yielding the CIE tristimulus values, *X*, *Y*, and *Z*.

X, *Y*, and *Z* tristimulus values give the stimulation (i.e., power) of each of the three primary colors (red, green, and blue) needed to match the color of a given spectral-power density (SPD) *P(λ)*. The latter can be determined for the PV "test sample," which is the photovoltaic cell in our case. Because of the distinct similarity of the three retinal-cone-sensitivity functions on the one hand and the color-matching functions on the other hand (both groups of functions have three peaks), each tristimulus value represents the approximate degree of stimulation that each type of retinal cone experiences when illuminated by a light source (illuminant) with spectrum *P(λ)*. For instance, the tristimulus values for a semi-transparent or transparent solar cell are given as follows:

$$X_t = \sum_{380}^{780} P(\lambda)\tau(\lambda)\bar{x}(\lambda)\,\Delta(\lambda) \qquad \textit{Eq.(2)}$$

$$Y_t = \sum_{380}^{780} P(\lambda)\tau(\lambda)\bar{y}(\lambda)\,\Delta(\lambda) \qquad \textit{Eq.(3)}$$

$$Z_t = \sum_{380}^{780} P(\lambda)\tau(\lambda)\bar{z}(\lambda)\,\Delta(\lambda) \qquad \textit{Eq.(4)}$$

Where $\tau(\lambda)$ is the spectral transmittance of the PV device measured using a UV-Vis spectrophotometer. Note that the green color-matching function, $\bar{y}(\lambda)$, is chosen to be identical to the photopic eye response, $V(\lambda)$. The product of the relative SPD of the illuminant $P(\lambda)$ by the test-sample spectral transmittance $\tau(\lambda)$ or reflectance $\rho(\lambda)$ (in case of opaque solar cells as discussed later in section 2.2.7) is defined as the color stimulus function. We emphasize here the importance of the $\Delta(\lambda)$ value, which is the step of the optical transmittance measurements of the solar cell. In some studies, it has been reported a $\Delta(\lambda)$ of 10 nm.[76,135] In our study and all the calculations that will be presented, a $\Delta(\lambda)$ of 1 nm is considered to avoid any overestimation of both the AVT and the CRI evaluation.

In addition to the PV cell test sample and the reference illumination source (A.M.1.5G in this case), ***test-color samples*** are instrumental in determining the CRI of an object. In the interest of international standardization, a specific set of 14 test-color samples has been agreed upon for the purpose of determining the CRI. These 14 test-color samples are a subset of a larger collection of the Munsell test-color samples.

As aforementioned, the CRI is an average for a set of eight test-color samples shown in Figure 22. These test-color samples are defined by their spectral reflectivity $\beta_i(\lambda)$ and are used in deriving the 1931 CIE tristimulus values of light transmitted by the TPV and reflected by each of the 8 test colors:

$$X_t = \sum_{380}^{780} P(\lambda)\tau(\lambda)\beta i\,(\lambda)\,\bar{x}(\lambda)\,\Delta(\lambda) \qquad Eq.(5)$$

$$Y_t = \sum_{380}^{780} P(\lambda)\tau(\lambda)\beta i\,(\lambda)\bar{y}(\lambda)\,\Delta(\lambda) \qquad Eq.(6)$$

$$Z_t = \sum_{380}^{780} P(\lambda)\tau(\lambda)\beta i\,(\lambda)\bar{z}(\lambda)\,\Delta(\lambda) \qquad Eq.(7)$$

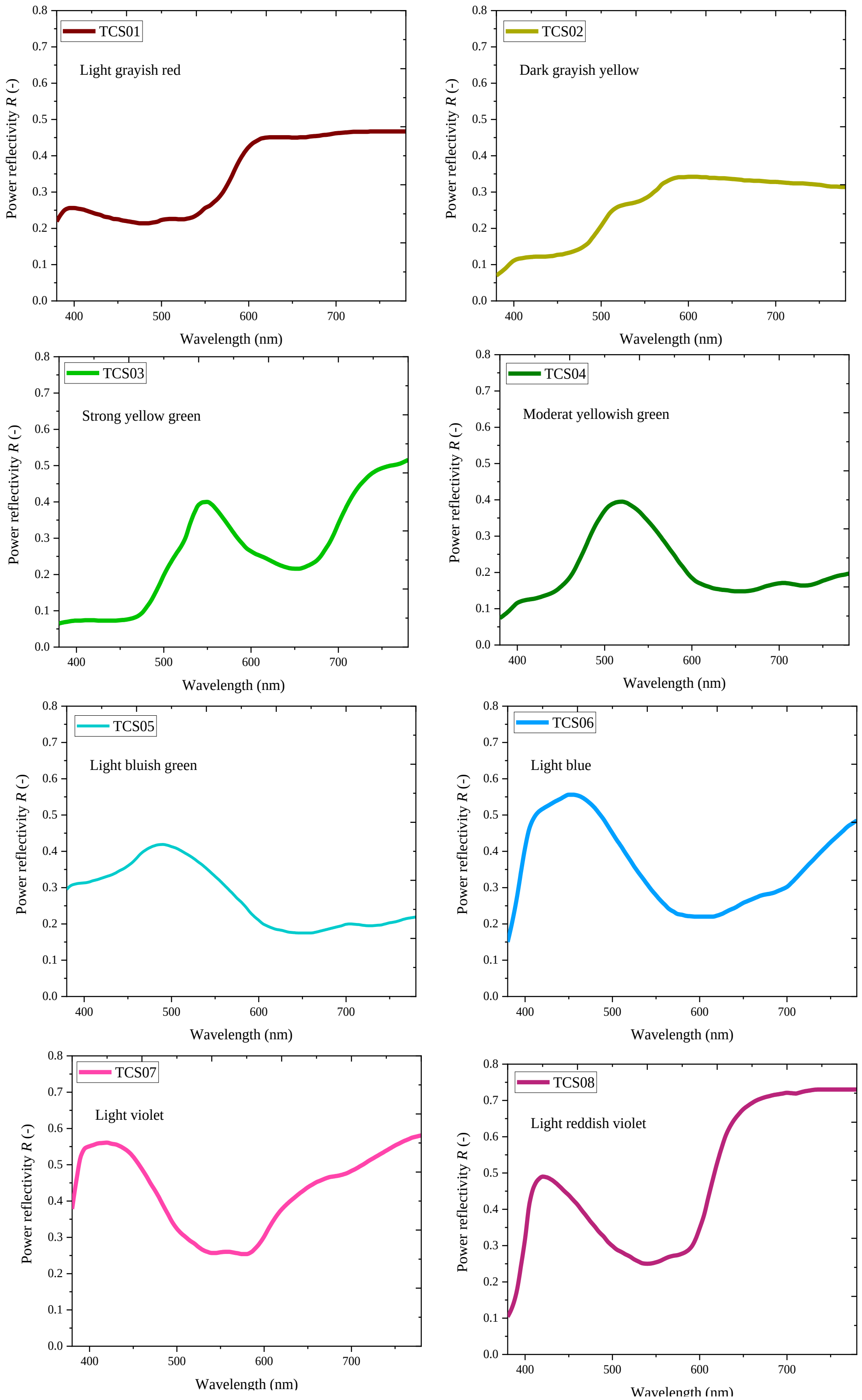

Figure 22. Power reflectivity of CIE test color samples (TCS) used to calculate the general color rendering index (data after CIE, 1995)

2.2.4. Chromaticity coordinates: the CIE 1931 Chromaticity diagram

Inspection of Eqs. (2-7) suggests that the unit of the tristimulus values is "watt." However, the tristimulus values are usually given as dimensionless quantities. The prefactor "watt $^{-1}$" in front of the integral can be included to make the tristimulus values dimensionless. If only ratios of tristimulus values are employed, as below, the prefactors and units cancel and thus become irrelevant. The Y tristimulus value represents the evaluation of the luminance of the color; this provides a basis for a correlation with a perceptual attribute of brightness.[131] As the Y value correlates approximately with brightness, the X and Z values do not correlate with any perceptual attribute. Important color attributes are related to the relative magnitudes of the tristimulus values; these relative magnitudes are known as the chromaticity coordinates and are computed as follows:

$$x = \frac{X}{X+Y+Z} \qquad \textit{Eq.(8)}$$

$$y = \frac{Y}{X+Y+Z} \qquad \textit{Eq.(9)}$$

$$z = \frac{Z}{X+Y+Z} \qquad \textit{Eq.(10)}$$

However, only *x* and *y* of these coordinates are needed to describe the color and are represented in a two-dimensional map, the 1931 CIE chromaticity diagram (Figure 23).[134]

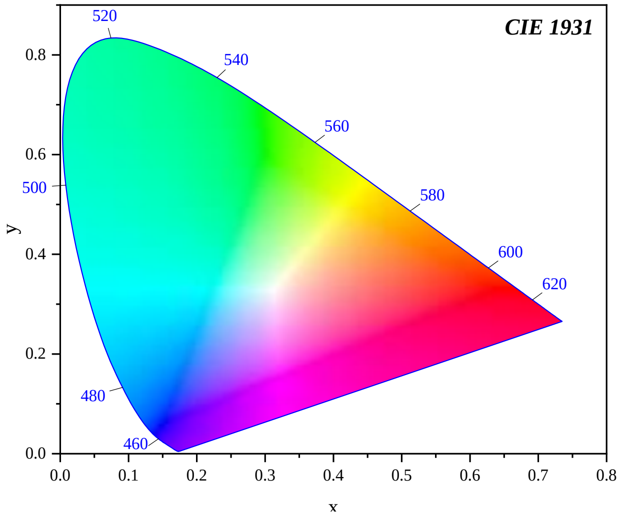

Figure 23. CIE 1931 (x,y) chromaticity diagram. Monochromatic colors are located on the perimeter, and the white color is located in the center of the diagram.

2.2.5. Uniform chromaticity coordinates: CIELAB and CIELUV color spaces

David MacAdam showed in 1943 that the chromaticity difference, which corresponds to a just noticeable color change, is not homogenous in different areas of the x,y chromaticity diagram.[136] These areas are known as the MacAdam ellipses. However, in the chromaticity diagram, it is very desirable for the color difference to be proportional to the geometric difference.[128] This has motivated the CIE to introduce the uniform (u,v) chromaticity coordinates in 1960 and (u',v') in 1976, which form the uniform chromaticity diagram as represented in Figure 24.[137] The new uniform chromaticity coordinates are calculated from the tristimulus values according to:

$$u = \frac{4X}{X+15Y+3Z} \qquad \textit{Eq.(11)}$$

$$v = \frac{6X}{X+15Y+3Z} \qquad \textit{Eq.(12)}$$

$$u' = \frac{4X}{X+15Y+3Z} \qquad \textit{Eq.(13)}$$

$$v' = \frac{9X}{X+15Y+3Z} \qquad \textit{Eq.(14)}$$

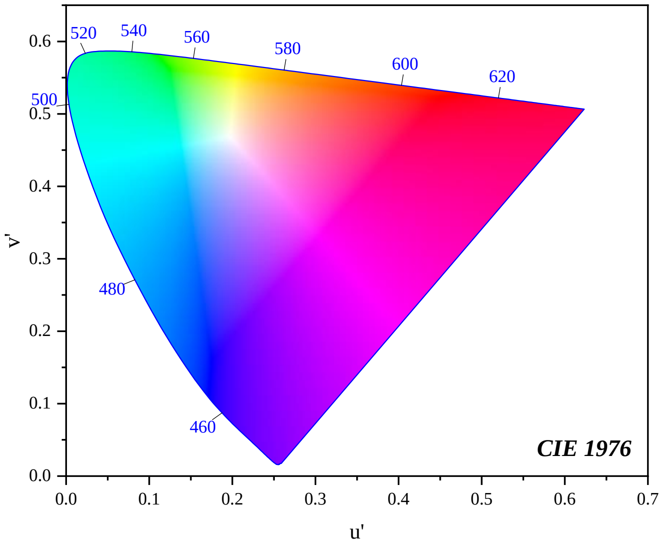

Figure 24. CIE 1976 (u',v') uniform chromaticity diagram calculated using the CIE 1931 2° standard observer

The CIE made a major advance in 1976 with the introduction of the CIELAB system of color specification. In this new system, the non-linear conversion of the *XYZ* values provides a partial solution to both color appearance and color difference problematics. The transformation from tristimulus values to *L*a*b** coordinates is given by the following equations:

$$L^* = 116\,(Y/Y_n)^{1/3} - 16 \qquad \text{Eq.(15)}$$

$$a^* = 500[(X/X_n)^{1/3} - (Y/Y_n)^{1/3}] \qquad \text{Eq.(16)}$$

$$b^* = 200[(Y/Y_n)^{1/3} - (Z/Z_n)^{1/3}] \qquad \text{Eq.(17)}$$

Where X_n, Y_n, and Z_n are the tristimulus values of a specified white achromatic stimulus. CIELAB provides a three-dimensional color space where the *a*-b** axes form one plane to which the *L ** axis is orthogonal (Figure 25).

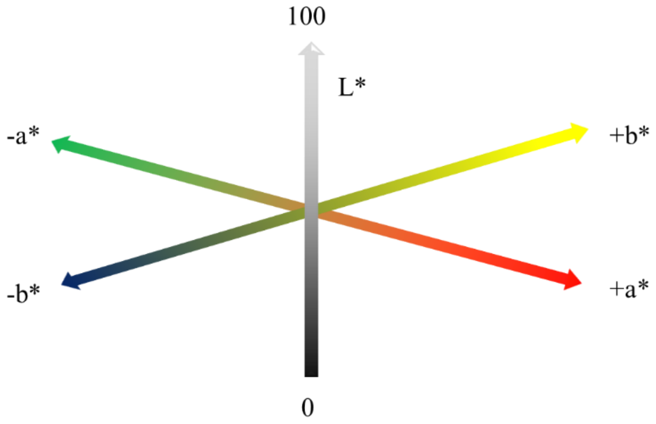

Figure 25. A schematic representation of the CIELAB color space.

The CIELAB transform was intended to be used for surface colors and includes several interesting features. First, the inclusion of the difference signals crudely models the processes that are believed to occur in the human visual system. Thus, whereas the retina initially captures responses derived from the cone spectral sensitivities, these retinal responses are combined at an early stage of visual processing to provide first a luminance signal and secondly two opponent signals that can be described as being yellow-blue and red-green. Similarly, CIELAB represents color stimuli as an achromatic signal (*L**) and two chromatic channels representing yellow-blue (*b**) and red-green (*a**). The normalization by the specified white achieves a color space that makes better predictions of color appearance than the tristimulus space from which it is derived. Thus, whereas a perfectly white surface's x and y chromaticity vary with the illuminant, the CIELAB coordinates remain constant at $L^* = 100$, and $a^* = b^* = 0$. CIELAB also allows the representation of a color stimulus by dimensions of lightness, chroma, and hue. It is reasonable to describe CIELAB as a color appearance space. In contrast, this label is not appropriate for a tristimulus space, which is strictly for color specifications. Lastly, the non-linear transform of tristimulus values in the CIELAB equations allows the Euclidean distance between two points in the new space to predict better the visual color difference. Consequently, the color difference metric known as ΔE^*_{ab} has been used effectively to quantify the color difference in a wide range of industries, such as projectors and digital displays. Costumers approach products with ΔE^*_{ab} closer to zero where the observed image has a non-perceptible color difference than the original scene. It is computed by the following formula:

$$\Delta E^*_{ab} = [(\Delta L^*)^2 + (\Delta a^*)^2 + (\Delta b^*)^2]^{1/2} \qquad Eq.(18)$$

where ΔL^*, for example, denotes the difference in L^* between the tested sample and the reference.

Although CIELAB is more perceptually uniform than XYZ space, it is still a long way from being completely uniform. Industrial practitioners of color science would appreciate applying a single tolerance on the value of ΔE^*_{ab} that defines the perceptibility or acceptability boundaries throughout color space; however, this is not yet possible.

The color appearance of each test color sample under the test sample is not identical with the color appearance under a reference illuminant. However, chromatic adaptation is the well-known ability of humans to adapt to certain illumination environments without substantial loss of color perception. For this reason, a procedure developed by CIE (1995) considers the adaptive color shift that follows from the human ability of chromatic adaptation and accounts for the adaptive color shift.[138] In this case, the (u,v) coordinates are transformed into new (c,d) coordinates using the equations below:

$$c_n = \frac{4 - u_n - 10v_n}{v_n} \qquad Eq.(19)$$

$$d_n = \frac{1.708v_n + 0.404 - 1.481u_n}{v_n} \qquad Eq.(20)$$

Where n= *t* for the test sample, *t,i* for the test sample with the contribution of test color samples reflectivity, and *r* for the reference illuminant.

The trichromatic coordinates correction after distortion by chromatic adaptation is provided by the adaptive color-shifted chromaticity coordinates (u^*, v^*) as follows:

$$u^*_{t,i} = \frac{10.872 + 0.404\frac{c_r}{c_t}c_{t,i} - 4\frac{d_r}{d_t}d_{t,i}}{16.518 + 1.481\frac{c_r}{c_t}c_{t,i} - \frac{d_r}{d_t}d_{t,i}} \qquad Eq.(21)$$

$$v^*_{t,i} = \frac{5.520}{16.518 + 1.481\frac{c_r}{c_t}c_{t,i} - \frac{d_r}{d_t}d_{t,i}} \qquad Eq.(22)$$

where $u^*_t = u_r$ and $v^*_t = v_r$.

As the brightness (for light source) and lightness (for an object) are factors that define the color perceived, the CIE introduced the lightness/brightness coordinate W^*, and thus the resulting colorimetric data are transformed into the 1964 CIE uniform color space chromaticity coordinates as follows:

$$W^*{}_{t,i} = 25\left(\frac{100Y_{t,i}}{Y_t}\right)^{\frac{1}{3}} - 17 \qquad Eq.(23)$$

$$U^*_{t,i} = 13W^*_{t,i}\left(u'_{t,i} - 0.1978\right) \qquad Eq.(24)$$

$$V^*_{t,i} = 13W^*_{t,i}\left(v'_{t,i} - 0.3122\right) \qquad Eq.(25)$$

However, in 1976 the CIE introduced the $L^*u^*v^*$ or the CIELUV color space, where L^* was used instead of W^*. L^* function in the CIELUV space is the same as that of the CIELAB space.

2.2.6. Resultant color change (ΔE_i)

Since the color stimulus can be represented as a point in a color space, the color difference (ΔE_i) between two stimuli is calculated as the Euclidean distance between these two points. The change in chromaticity coordinates of the transmitted light from the reference source attributes to the color shift of the illumination source. When the latter is combined with the adaptive color shift, we quantify the resultant color shift by evaluating the color difference ΔE_i (CIE 1964 uniform color space):[139]

$$\Delta E_i = \sqrt{(U^*_{t,i} - U^*_{r,i})^2 + (V^*_{t,i} - V^*_{r,i})^2 + (W^*_{t,i} - W^*_{r,i})^2} \qquad Eq.(26)$$

For the final step in calculating CRI, the special color rendering index R_i for each test color sample is calculated:

$$Ri = 100 - 4.6\Delta Ei \qquad Eq.(27)$$

And then, the arithmetical mean of the basic eight special color indices is computed:

$$CRI = \frac{1}{8} \sum_{i=1}^{8} Ri \qquad Eq.(28)$$

The color rendering index is a number less than or equal to 100. It is neither a percentage nor a fraction. Looking at Eq(27), we find the scaling factor 4.6 that was chosen such that CRI is 51 for a specified CIE Illuminant (warm white fluorescent lamp), and the reference illuminant has a score of 100. One important thing to bear in mind is that the difference from 100 is the value that matters. In other words, a CRI of 60 means that there is four times the average color shift than in the case of 90 CRI value. For PV systems developed for solar windows application, a CRI > 90 is targeted to achieve a similar visual aspect as the conventional double-glazing windows.

2.2.7. Color evaluation for opaque solar cells:

One of the objectives of my thesis work is to highlight the importance of aesthetics in the adoption procedure of PV systems in different applications. As such, applying aesthetic evaluation on opaque solar cells is briefly discussed herein. The goal is to emphasize that we can step forward towards energy-efficient buildings once both opaque and transparent PV systems are integrated. The theoretical power conversion efficiency limits of ideal colored opaque photovoltaics have been evaluated to be > 29%. This corresponds to a relative performance loss of less than 14% compared to an ideal black solar cell. As color can improve the visual aesthetics of PV, modifications on opaque solar cells with anti-reflective coatings,[140] Bragg reflectors[141], or luminescent materials[142] have been elaborated to either reflect or emit a targeted color. For opaque colored solar cells, the spectral reflectance $\rho(\lambda)$ of the device is considered as a substituent of the spectral transmittance. Hence, the relative luminosity of the device is, in this case, the average visible reflectance (AVR), which is an equivalent property to the average visible transmittance (AVT) used in the context of semi-transparent/transparent solar cells.[143]

As the final color of these opaque solar cells can be fully controlled in accordance with the customer's wish, the tristimulus values of the targeted color are known, and thus, the relative error between the target color and the color produced (C_{error}) is determined by:

$$C_{\text{error}} = \frac{|\Delta X| + |\Delta Y| + |\Delta Z|}{X + Y + Z} \qquad \text{Eq.(29)}$$

where ΔX, ΔY, and ΔZ are the differences between the produced and the target XYZ coordinates.

2.2.8. CIE standard illuminants

As it is not possible to measure a color directly, it is always based on a comparison.[131] Moreover, the colors may appear differently depending on the type of illumination. Therefore, for the sake of comparison, a reference system is necessary. Indeed, in Eqs (2-4), it is established that an incident light irradiation is needed to describe the colorimetric characteristics of a reflecting or transmitting material. In this case, the relative SPD ($P(\lambda)$) is part of the relative color stimulus function. The radiation $P(\lambda)$ is modified by the reflectance or transmittance of the material. Thus, to be able to reproduce the colorimetric measurements, the SPD of the irradiating source has to be reproduced too. With this aim, the CIE has standardized a few SPDs and recommends their use for the colorimetric characterization of materials whenever possible. Only the relative SPD is needed for calculations, and such theoretical sources are called "illuminants."

For light sources, it is useful to refer to the temperature of the blackbody (expressed in Kelvin), for which the radiation most closely resembles that of the light source. As shown in Figure 26, it is represented the color temperature of a black body, graphed as a line through the CIE x,y chromaticity diagram. This line is known as the Planckian Locus. It is the path (locus) that the color of an incandescent black body would take in a particular chromaticity space as the black body temperature changes. A deep red is obtained at low temperatures, orange, yellowish-white, white, and bluish-white at very high temperatures such as >6000 K.

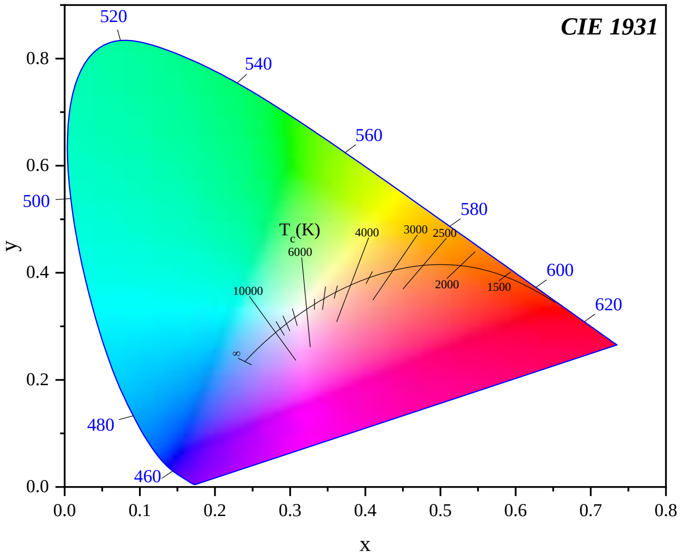

Figure 26. CIE 1931 chromaticity space projecting black body (Planckian) locus (black line).

When the color of our reference white illuminant does not fall on the Planckian locus, the correlated color temperature (CCT) in Kelvin is used. As the spectrum of transmitted daylight changes passing through a transparent colored or colorless medium, the perceived color and brightness of the illuminated PV cell differ. Here, the usage of the CCT metric can be helpful to simplify the communication of the color: a low CCT reveals a yellowish or reddish-white while a high CCT appears bluish-white (Figure 27).

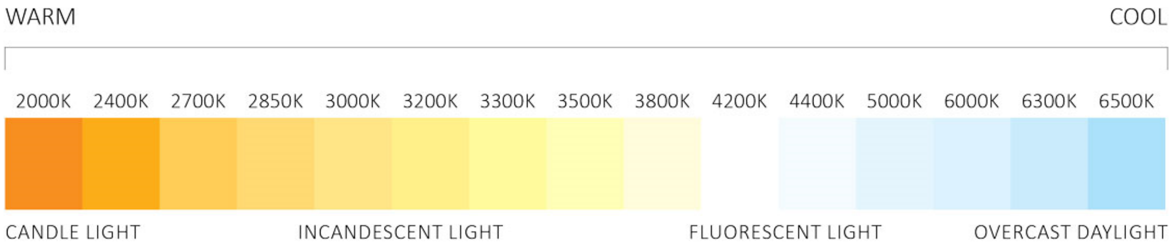

Figure 27. Correlated color temperature scale. At lower temperatures, the light is considered warm and reveals a reddish-white, while at higher temperatures, it is attributed as cool light with a bluish appearance.

The CCT value is calculated from McCamy's equation reported below (Eq 30).[76]

$$CCT= 449n^3 + 3525n^2 + 6823.3n + 5520.33 \qquad Eq.(30)$$

Where $\mathbf{n} = \frac{(\boldsymbol{x}-\mathbf{0.3320})}{(\mathbf{0.1858}-\boldsymbol{y})}$; x and y are the chromaticity coordinates in the CIE 1931 color space.

For PV aesthetic evaluation, we will use the value of CCT of the transmitted light through our transparent devices. This can help define if the white light transmitted is falling in the visual comfort regime and if the light is more bluish- or reddish-white.

If we consider daylight as an illuminant reference for solar cells used in BIPV application, its irradiance varies substantially depending on the geographic position, time, and weather. However, the CIE accepted a recommendation by Judd and co-workers [144] to describe phases of daylight.[145] These authors found that the chromaticities of different phases of daylight fall on a curve more or less parallel to the Planckian locus on the chromaticity diagram. As such, the CIE standardized two main illuminants: A and D_{65}. The CIE draft standard stated: "CIE standard illuminant A is intended to represent a typical domestic tungsten-filament lighting. Its relative spectral power distribution is that of a Planckian radiator at a temperature of approximately 2856 K. CIE standard illuminant A should be used in all applications of colorimetry involving the use of incandescent lighting, unless there are specific reasons for using a different illuminant." [146] The tristimulus values and chromaticity coordinates of CIE standard illuminant A are:

X = 109.85; Y = 100.00; Z = 35.58; x = 0.44758; y = 0.40745

For the human visual system, the natural illumination is daylight. For that, the CIE stated: "CIE standard illuminant D_{65} is intended to represent average daylight and has a correlated color temperature of approximately 6500 K. CIE standard illuminant D_{65} should be used in all colorimetric calculations requiring representative daylight, unless there are specific reasons for using a different illuminant. Variations in the relative spectral power distribution of daylight are known to occur, particularly in the ultraviolet spectral region, as a function of season, time of day, and geographic location. However, CIE standard illuminant D_{65} should be used pending the availability of additional information on these variations." [146] The tristimulus values and chromaticity coordinates of CIE standard illuminant D_{65} are:

X = 95.04; Y = 100.00; Z = 108.88; x = 0.31272; y = 0.32903

2.2.9. Relationship between color and chromaticity

Having a complete description of chromaticity allows us to revisit the definition of the color of a PV device by the CIE. For the aim of color evaluation, we always refer to the chromaticity coordinates of the tested PV cell compared to the chromaticity coordinates of the A.M.1.5G reference, known as the white point. The fundamental definition of a white point in a color space is an achromatic reference stimulus producing the perception of white. For color evaluation of light sources, the white point is usually set at $x= y= 1/3$, known as the equal-energy point, whereas it is usually set at the illuminant point for object colors, and thus for the case of PV systems. In my work, when positioning the calculated chromaticity coordinates of our transparent DSSC, it is desirable to be as close as possible to the coordinates of the white point in order to report color neutrality. The D_{65} illuminant is the dominant standard to represent daylight, and its coordinates are considered for the white point. However, for PV applications, it seems evident that as the A.M 1.5G is the standard spectrum used in photovoltaics evaluation, its chromaticity coordinates can be considered the white point for this system. Here, it is needed to emphasize that the way the CRI calculations and color functions are defined makes the energy flux for AM 1.5G utilized (and not the photon flux) given how human vision works. The $(x,y,)$ coordinates of AM 1.5G is (0.3322, 0.3439) with a CCT value of 5513 K. Nonetheless, it is still valid to use the D_{65} standard illuminant as a reference for color evaluation for PV systems, especially considering BIPV application as it will provide the color perception of the PV window from outside observers. However, to evaluate the colors of PV in different lighting conditions, like for indoor application, different standard illuminants should be taken into account, and thus, a different white point needs to be considered.

The importance of the white point is not only limited to the positioning of the ideal white color under a specific illumination, as its chromaticity coordinates are used for the calculation of other important metrics such as the dominant wavelength and the color purity. Thus, instead of using chromaticity coordinates, the dominant wavelength can be combined with the color purity to define the color. Since the dominant wavelength expresses hue and the color purity expresses saturation, this specification method is helpful to describe the appearance of a color stimulus.

The dominant wavelength is defined by the wavelength located in the perimeter of the chromaticity diagram that is the closest to the device's color. It relates the final coloration of the PV device to a monochromatic color. The dominant wavelength is an equivalent metric to the hue. It is determined by drawing a straight line from the equal-energy point ($x_{ee}= y_{ee}= 1/3$) to the chromaticity coordinates of the test sample and then by extending this straight line to the perimeter of the chromaticity diagram.[147]

Color purity (P_c), sometimes also called color saturation, is the distance in the chromaticity diagram between the chromaticity coordinates of the test sample and the coordinates of the equal-energy point divided by the distance between the equal-energy point and the dominant wavelength point.

$$\textbf{Color purity } (P_c)= \frac{\sqrt{(x-x_{ee})^2+(y-y_{ee})^2}}{\sqrt{(x_d-x_{ee})^2+(y_d-y_{ee})^2}} \qquad Eq.(31)$$

Where (x_d, y_d), (x_{ee}, y_{ee}) and (x, y) are the chromaticity coordinates of the dominant wavelength, equal-energy point, and the tested sample, respectively. If P_c is nearly unity, the point is near the spectrum locus (the purple boundary) and will tend to represent a highly saturated color. If P_c is near zero, the point is near the reference white and will tend to represent a very pale color.[131]

For a more precise evaluation, and as the x,y diagram is non-uniform in its color distribution, the CIE 1976 uniform diagram provides other measures to correlate more uniformly with hue and saturation. These measures are the hue angle (h_{uv}) and u,v saturation (s_{uv}), as given by the following equations:

$$\text{CIE 1976 } u,v \text{ hue-angle, } h_{uv} : h_{uv} = \arctan[(v'-v'_r)/ (u'-u'_r)] \qquad Eq.(32)$$

$$\text{CIE 1976 } u,v \text{ saturation, } s_{uv} : s_{uv} = 13[(u'-u'_r)^2+ (v'-v'_r)^2]^{1/2} \qquad Eq.(33)$$

The definition of a chromaticity diagram requires that any mixture of two colors falls on the straight line joining those two colors. In this system, and as L*, a*, and b* are calculated based on ratios of tristimulus values incorporated as cube-roots (reported in Eq.15-17), there can be no chromaticity diagram associated with the CIELAB space, and therefore no correlate of saturation can be given.[131] Thus, the hue-angle h_{ab} and chroma C_{ab} has to be evaluated using these two equations:

CIE 1976 a^*,b^* hue-angle, h_{ab} : $h_{ab} = arctan(b^*/a^*)$ *Eq.(34)*

CIE 1976 a^*,b^* Chroma, C^*_{ab} : $C^*_{ab} = (a^{*2}+b^{*2})^{1/2}$ *Eq.(35)*

2.3. Conclusions

Even though the science of color is significantly more complex than the description given in this chapter, the aim of the latter is to assess how the color of a solar panel can be expressed. By defining the targeted integration of the transparent solar panel, its aesthetic can be defined. Therefore, transparency, as expressed by the AVT, reflectivity as expressed by the AVR, and color as described by the CRI, CCT, and chromaticity coordinates can be evaluated and compared across the different TPV technologies.

For a good level of transparency, a TPV device should achieve at least an AVT value of 60%. However, the description of TPV aesthetic is not only restricted to the AVT quantification, but it also needs to reach CRI values superior to 90, a threshold value to reach color neutrality.

Out of all the earlier evaluations, based on this chapter and following our experience in TPV, we recommend a standardization in the approach to quantify the level of transparency and color of TPV devices. As for the device performance or accelerating stability test protocols, adopting standard aesthetic metrics are crucial to afford comparative description of the different TPV technologies. In this thesis work, the CIE 1931 color space, where x,y coordinates are reported, the dominant wavelength to define the hue, the color purity to express saturation, the CCT, and the CRI are used in addition to AVT to describe the aesthetic level of the selective NIR-DSSC.

Chapter 3

Chapter 3. Symmetrical VG20 cyanine dye: From a proof of concept to an efficient and transparent NIR-DSSC

In the first chapter, we break down the transparent photovoltaic into different technologies. We categorized such TPV systems into two families, i.e., the wavelength and the non-wavelength-selective technologies. We stressed the relevance of dye sensitized solar cells as a potential wavelength-selective technology based on a molecular absorbing layer with promising power conversion efficiencies and aesthetics. For the core assessment of this latter, chapter 2 gives in-depth details on the aesthetic evaluation for TPV, along with the requirements to reach high transparency and color neutrality. The work presented in this chapter considers the human eye photopic response to optimize a selective near-infrared (NIR) sensitizer based on a polymethine cyanine structure, coded **VG20-C$_x$**.

In the first section, we will briefly describe the synthetic procedure yielding to **VG20-C$_x$**, with x being 2, 8, or 16 carbons constituting the lateral alkyl chain. Then, a detailed spectroscopic characterization of this dye in solution and computational characterization is given, followed by a photodynamic study using time-correlated single-photon counting (TCSPC) and fs-transient absorption spectroscopy (fs-TAS).

The second section focuses on device optimization to reach the highest level of performance for this type of dyes. The self-assembled monolayer (SAM) optimization on the surface of TiO_2, the influence of electrolyte composition, and the effect of different sensitization conditions are discussed based on UV-visible absorption spectroscopy and intensity-modulated photocurrent/photovoltage spectroscopy (IMPS/IMVS). The levels of transparency and coloration of **VG20**-based NIR-DSSC are evaluated. Finally, this chapter ends with a discussion on the limiting factors governing the device performance, on the basis of ultrafast spectroscopies, in particular using picosecond or femtosecond pump-optical probe transient absorption spectroscopy.

3.1. Synthesis and characterization in solution of VG20-C_x dyes

Based on existing literature about NIR dyes covered in chapter 1, our first attempt relies on the synthesis of a series of symmetrical heptamethine dyes, coded **VG20-C_x**, with x value varying from 2 to 16 carbons on the alkyl chain (Scheme 1). The **VG20-C_x** series of dyes were developed in collaboration between LRCS and prof. Claudia Barolo at the University of Torino within the frame of the Ph.D. thesis of Vittoria Novelli (2014-2017).

In this dye, the *trans* configuration of the polymethine bridge is stabilized by a classical cyclohexene moiety, substituted by a chloride atom. The two 1*H*-benzo[*e*]indole end units, differently positioned from the closely-related dye reported by Arakawa et al., are decorated with a carboxylic acid anchoring group in position 7.[122] The central chloride atom has an electron-withdrawing property, which contributes to pulling electrons from the polymethine chain, causing the dye's absorbance to shift in the NIR region. Besides facilitating synthesis up-scalability, the rationale behind the synthesis of symmetrical dye, in which the anchoring groups are directly conjugated on the lateral heteroaromatic groups, is also to further red-shift the absorption maxima as previously demonstrated on symmetrical squaraines.[116,118,148] This molecular design, inspired by Arakawa's work, affords a better overlap between the Lowest Unoccupied Molecular Orbital (LUMO) of the dye and the conduction band (CB) of TiO_2 to favor charge injection.

The synthetic procedure to obtain the symmetrical heptamethine cyanine dyes **VG20-C_x** is reported in Scheme 1. The synthesis and purification were carried out in collaboration with Prof. Claudia Barolo (Torino University). Briefly, it involves the condensation of the quaternary heterocyclic salts (**2**), bearing an activated methyl group, with the Vilsmeier-Haack reagent (**3**). The 1,1,2-trimethyl-1H-benzo[*e*]indole-7-carboxylic acid (**1**) was readily obtained exploiting the Fischer indole synthesis, as previously described for symmetrical squaraine dyes.[116] The subsequent quaternization of the benzoindolenine ring, performed under microwave conditions,[149] led to increasing the methyl group acidity, which enabled the cyanine bridge formation (Step 1 in Scheme 1). All the symmetrical cyanine dyes were synthesized in a one-step reaction under microwave (MW) heating by reacting two equivalent of quaternary heterocyclic salts **2** with the Vilsmeier−Haack reagent **3** in the presence of potassium acetate and ethanol. The brownish solid in the reaction mixture was filtered and washed with diethyl ether. Unreacted potassium acetate crystals were then removed by dichloromethane (DCM). Finally, recrystallization in acetonitrile was performed, and once all the precipitate was dissolved, a few drops of acetic acid were added to protonate the carboxylic moieties completely.

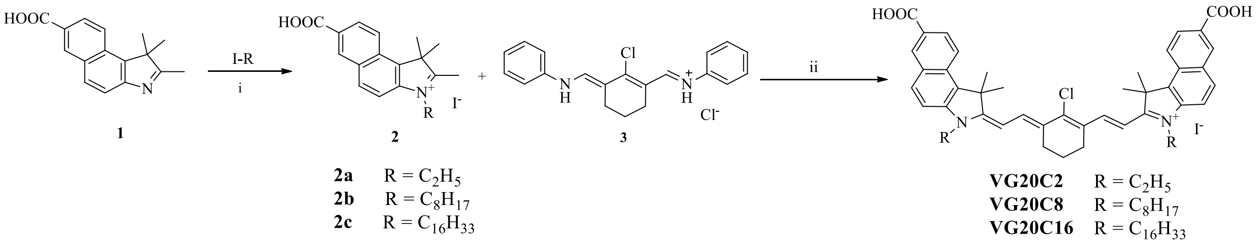

Scheme 1. Synthesis procedure of the VG20-C_x cyanine dyes. The experimental conditions: (i) anhydrous acetonitrile, iodoalkane, MW, 40 min, 155°C; (ii) potassium acetate, absolute ethanol, MW, 10 min, 120°C.

3.1.1. Optical and electrochemical properties of VG20-C_{16} in solution

VG20-C_x dye in solution exhibits a sharp and intense absorption band in the NIR region, with a maximum at λ_{max} = 834 nm (ε = 154000 $L.mol^{-1}.cm^{-1}$) corresponding to the S_0-S_1 electronic transition of VG20-C_{16} (Figure 28). The narrow absorption band is a characteristic of symmetrical cyanine dyes as the difference in the carbon-carbon equilibrium bond lengths are small.[150] The UV-vis absorption spectra of **VG20-C_x** with different alkyl chain lengths show a very similar fingerprint, thus indicating that the alkyl chain has no effect on the dye's electronic structure. The shoulder at 765 nm is principally related to vibronic states in the molecule, as suggested by the TD-DFT calculations presented below. However, as it is also discussed in the following, this shoulder can also be influenced by the presence of H-aggregates in the self-assembled monolayer. Higher energies singlet transitions (S_0–S_n) lead to a residual broad and weak absorbance in the blue region at ca. 410 nm. Such absorption characteristic makes this dye well-suited for light transparency purposes by bringing the dye's absorbance very precisely outside the human's eye photopic response (Figure 28). The fluorescence of **VG20-C_{16}** exhibits a sharp emission band at λ_{max} = 850 nm leading to a narrow Stokes shift of 225 cm^{-1}. The vertical excitation energy is $E_{0\text{-}0}$ = 1.47 eV, a value remarkably close to the optical bandgap (E_g = 1.49 eV). This means that the dye in solution undergoes negligible structural rearrangements in the excited states, thus limiting intra-molecular energy losses through rearrangement. It has a high photoluminescence quantum yield (PLQY) of 47 %, which makes this class of cyanine dyes attractive as a NIR fluorescent label.[103,151]

As previously discussed in chapter 1, cyanine dyes tend to form molecular aggregation. To avoid the formation of such harmful aggregates in solution, chenodeoxycholic acid (CDCA) is introduced in different ratios into the dye solution. At the same time, we also kept the dye solution highly diluted (0.1 mmol/L) to avoid aggregation. Systematical increase of CDCA concentration into **VG20-C$_{16}$**–based dye solution has no influence neither on the shoulder amplitude nor on the width of the absorption band (Figure 28.b). This indicates evidence that H-type aggregates are unlikely to form in DMSO/ethanol solvent mixture (1/9 ratio, *v/v*) at a dye concentration of 0.1 mmol/L.

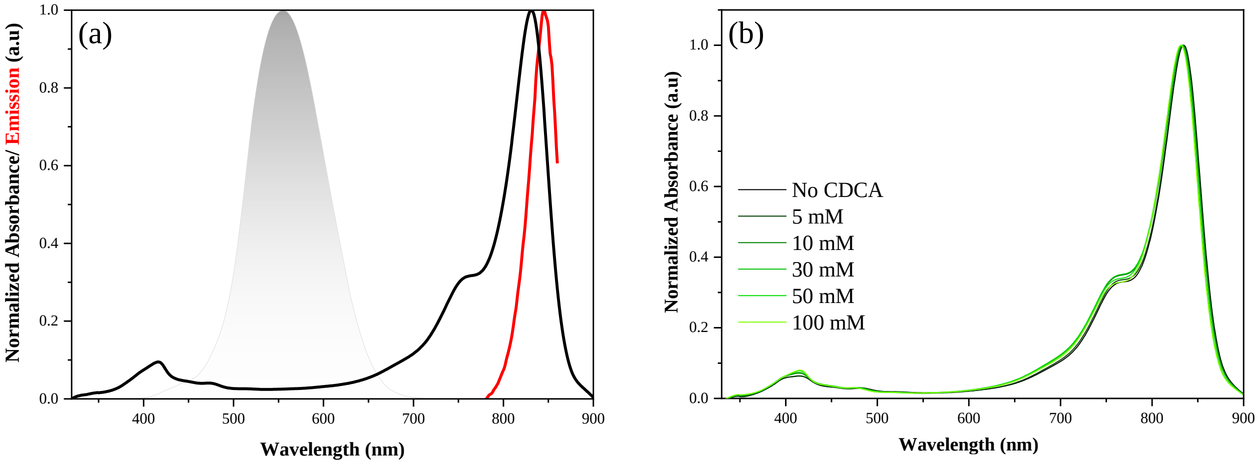

*Figure 28. (**a**) Normalized UV-visible absorption spectrum of **VG20-C$_{16}$** in solution (black curve) and steady-state photoluminescence (red curve) in 1/9 (v/v) DMSO/ethanol solvent mixture (dye concentration 0.1 mmol/L, CDCA concentration 50 mmol/L). (**b**) Normalized absorption spectra of **VG20-C$_{16}$** dye solution including different concentration of CDCA.*

When **VG20-C$_{16}$** dye is dissolved in a solvent of different polarity, a solvatochromic effect is observed (Figure 29). A blue shift is observed in a high polar solvent such as acetonitrile (ACN), and inversely a red-shift is experienced in a lower polar solvent such as dichloromethane (DCM). This indicates that the polar ground state of the solute is stabilized by a polar solvent. In addition, one can also observe that the solvent modifies the relative height of the shoulder. This can be attributed to the dipole-to-cyanine transition induced by solvent polarity.[152,153]

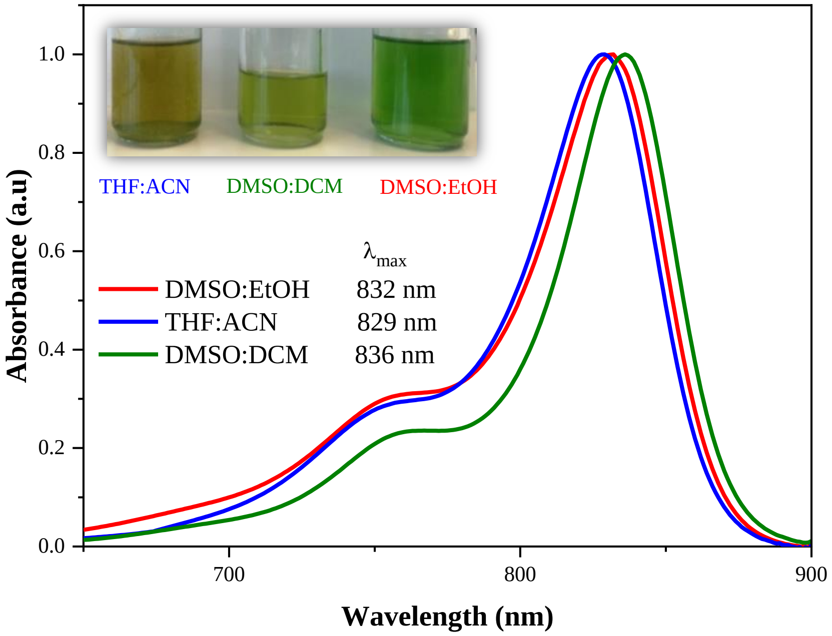

Figure 29. Solvatochromic effect observed in ***VG20-C*** $_{16}$ *in different solvents. The inset picture shows the visual aspect of the dye solution depending on the solvent.*

Upon a preliminary optimization step, a mixture of DMSO/ethanol with a 1/9 ratio by volume was chosen as a dipping solution. This choice of the solvent mixture has an influence on the device stability and power conversion efficiency, as it will be presented later in the chapter.

The HOMO and LUMO energy positions were determined by cyclic voltammetry (Figure 30). The two quasi-reversible peaks at +0.24 V (vs. Fc^+/Fc) and +0.57 V (vs. Fc^+/Fc) are attributed to the HOMO and HOMO+1 energy levels. The LUMO level is situated at -1.06 V (vs. Fc^+/Fc). These values lead to the HOMO and HOMO+1 at +0.87 V and +1.20 V (vs. NHE), respectively. The LUMO level at −0.43 V (vs. NHE), considering the Fc^+/Fc redox potential at +0.63 V vs. NHE.[154] The dye regeneration is thus thermodynamically favorable in association with I_3^-/I^- redox couple (+0.35 V vs. NHE) and by extension to most of the redox mediators developed so far for conventional DSSCs.[155,156] However, we can postulate more difficulties for the electron injection step into the conduction band of TiO_2 ($E_{CB} \approx -0.45$ V vs. NHE)[157] owing to a clear lack of a sufficient energetic driving force.

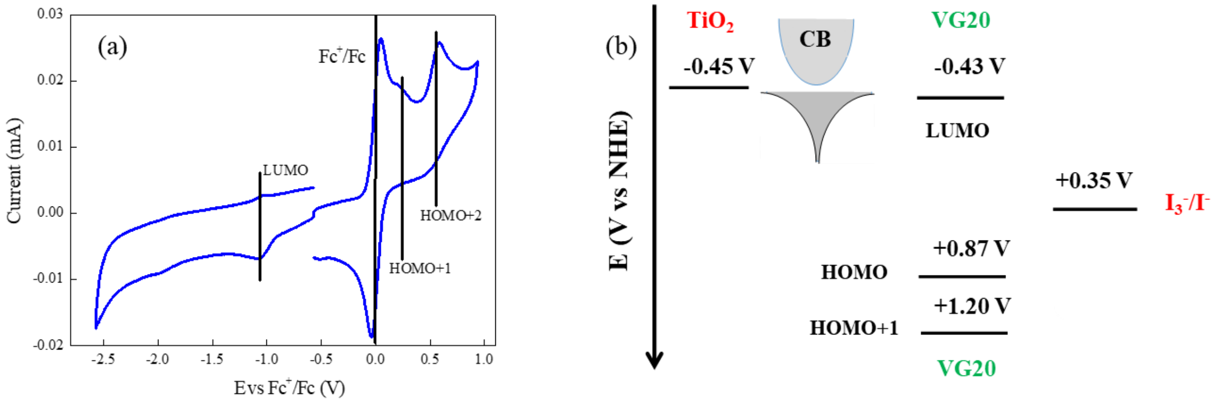

*Figure 30. (**a**) First scan of the cyclic voltammogram recorded for **VG20-C$_8$** in the presence of ferrocene as an internal reference. (**b**) Energetic diagram placing the HOMO and LUMO energy levels of **VG20-C$_8$** with respect to the conduction band level in TiO$_2$ and the redox potential of I$_3^-$/I$^-$ redox couple.*

3.1.2. Computational analysis of VG20-C$_x$ dye by TD-DFT

This part of the work has been carried out in collaboration with Prof. Raffaele Borrelli at the University of Torino (IT). Theoretical-computational analyses have been performed employing TD-DFT calculations. Structural energy calculations point out that this cyanine dye should co-exist in two stable conformational isomers (*cis*- and *trans*-) given by the double bonds of the polymethine chain (Figure 31). The *trans*-conformation is 1.3 kcal.mol^{-1} higher in energy than the *cis*-isomer. Hence, the latter conformer represents around 90% of the entire population in solution at room temperature. The allowed electronic transitions have been computed in vacuum for the *cis*-form using the second-order algebraic-diagrammatic-construction ADC (2) level of theory. It shows a strong absorption at 832 nm corresponding to the first excited singlet state $S_0 \rightarrow S_1$ in agreement with the experimental data.

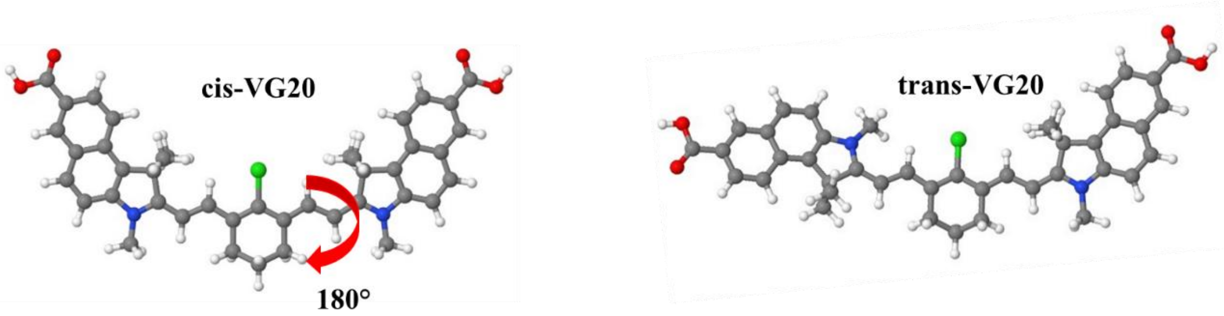

*Figure 31. The two lowest energy isomers (cis- and trans-) of **VG20** at room temperature.*

The S_1 singlet state is assigned to a π-π* HOMO to LUMO transition. The calculated molecular frontier orbitals involve almost exclusively the polymethine chain (Figure 32). The theoretical analysis does not show any additional electronic transition at around 750 nm, in agreement with the above assignment of a vibronic-induced transition. Computational details and further spectral assignments are provided in Table 1.

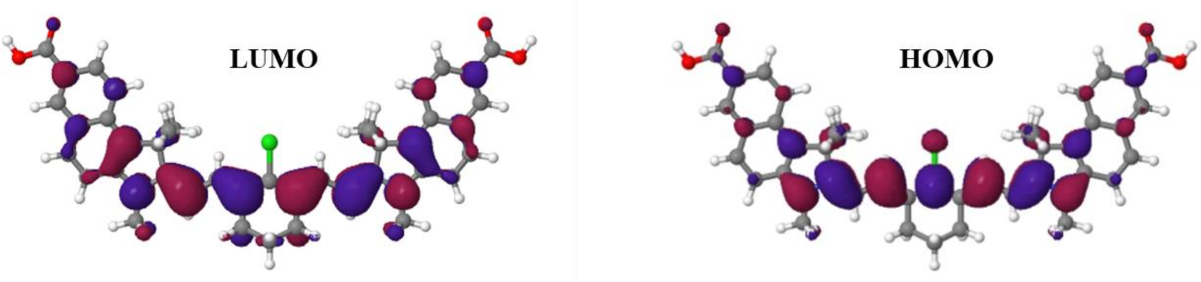

*Figure 32. Distribution of the molecular frontier orbitals of **VG20** dye based on ADC (2) calculations.*

*Table 1. Computed vertical excitation energy, transition type, and oscillator strength of **VG20** dye in vacuum. All calculations have been performed using the TURBOMOLE software package. The geometry of the ground state of the dye has been optimized at MP2 level with the def2-TZVP basis set. The vertical excitation energy has been computed with the ADC(2) method using the same basis set.*

	Abs. wavelength (nm)	**Electronic states**	**Oscillator strength**
I	832	HOMO-LUMO (94%)	1.55
II	458	HOMO1-LUMO (84%)	0.06
III	386	HOMO2-LUMO (90%)	0.12

3.1.3. Photodynamic characterization of VG20-C_x in DMSO/ethanol solvent mixture

The photodynamic study of **VG20-C_x** in solution has been carried out combining picosecond Time-Correlated Single Photon Counting (TCSPC) (Figure 33) and femtosecond time-resolved Transient Absorption Spectroscopy (TAS) (Figure 34) to assess the kinetics of both the radiative and the non-radiative deactivation processes.

The photoluminescence (PL) decay of the dye in DMSO/Ethanol solvent mixture shows two sub-nanosecond components: τ_1 = 391 ps (f_1 = 93 %) and τ_2 = 925 ps (f_2 = 7 %). These two lifetimes are attributed to the coexistence between the *cis*- and *trans*- configuration. The fraction of the two components is in good agreement with the population ratio deduced by TD-DFT calculations. Such values of lifetime are significantly faster than the benchmark ruthenium or organic dyes used in conventional DSSCs, which lie between 2 to 100 ns.[148,158–160] This short-life of the excited states is due to the highly bounded Frenkel excitons in the cyanine backbone leading to a comparatively poorer electron/hole delocalization, as corroborated by the calculated molecular frontier orbitals. The alkyl-side chain length (Figure 33.a) and the CDCA content in solution (Figure 33.b) have no influence on the excited-state dynamics. This result could have been anticipated since the alkyl chain has no contribution to the dye's electronic structure. Secondly, these results highlight the absence of any experimental evidence suggesting that dye aggregation exists in DMSO/ethanol solvent mixture at this concentration.

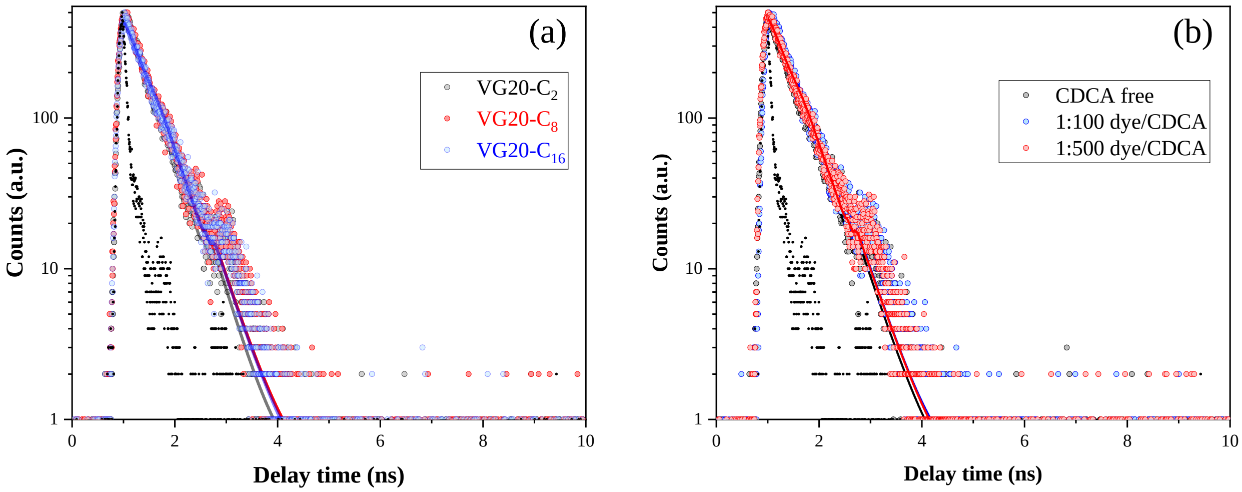

*Figure 33. Comparison of PL decay measured by TCSPC of **VG20-C$_x$** dye in DMSO/ethanol solvent mixture as a function of (**a**) the alkyl chain length, (**b**) the molar ratio of CDCA in solution.*

Interestingly, similar kinetics were measured by fs-TAS experiments. These results were obtained in collaboration with Ilias Nikolinakos (Ph.D. student) and Prof. Stefan Haacke at the University of Strasbourg (IPCMS). Upon excitation with a 50 fs-pulse at 810 nm, **VG20-C$_{16}$** exhibits pronounced excited state signatures, such as excited-state absorption (ESA) below 670 nm and beyond 1300 nm (positive signal), and stimulated emission (SE) between 850-1100 nm, partially overlapping with ground state bleach (GSB) in the 700-900 nm range (Figure 34). Kinetic traces are taken in the maximum of ESA (at 585 nm), SE and GSB (at 760, 840, and 950 nm) decay in parallel and individual wavelength fits give decay times in the range of 320 to 410 ps (Table 2). An additional rise component in the range of 1−4 ps is also observed, most likely due to intra-molecular relaxation and solvation dynamics within the DMSO/ethanol mixture.

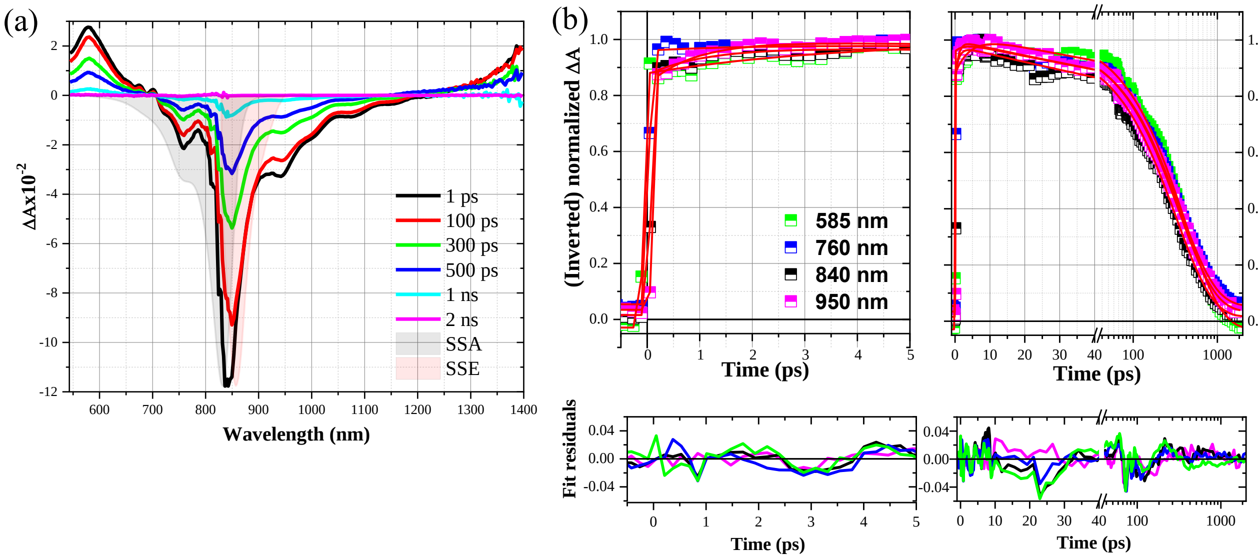

*Figure 34. (**a**) Transient absorption spectra of **VG20-C$_{16}$** dye in DMSO/ethanol (1/9) solvent mixture including 500 molar ratio of CDCA (**b**) derived TA kinetic profiles at various characteristic wavelengths: 585 nm, 760 nm, 840 nm, and 950 nm for two different time scales. The sample was pumped at 810 nm with 89 μJ/cm^2 energy pulse.*

*Table 2. Transient absorption kinetic parameters for **VG20-C$_{16}$** in DMSO/ethanol (1/9) solvent mixture obtained by femtosecond transient absorption spectroscopy*

λ (nm)	**A_1**	**τ_1 (ps)**	**A_2**	**τ_2 (ps)**
585	-15%	4.2	100%	410
760	-3%	2.6	100%	358
840	-10%	1.1	100%	323
950	-15%	0.9	100%	353

3.2. Rational optimization of the VG20-based device performance

One important starting point for device optimization is the configuration and packing of the dye molecules chemisorbed upon TiO$_2$ surface. The dye molecules can be oriented in the self-assemble monolayer (SAM) in different ways. The dye-to-dye separation can also vary in a substantial way, presumably due to steric hindrance and electronic factors.[161] The extreme case is the molecular aggregation, either prior to chemisorption or after leading to supramolecular assemblies.[162,163] In general, the optical properties of dye aggregates can be described by Kasha's molecular exciton theory.[164] This theory states that when two monomeric dyes are interacting to form a dispersive dimer, electronic coupling phenomena lead to excited-state splitting. The excitation energy of the resulting dimer depends on the arrangement of the molecular dipole moments. Side-to-side alignment of molecules, and therefore of the molecular dipoles, yields to H-type aggregates. This state is associated with a hypsochromic shifted band attributed to the H-aggregates absorption fingerprint. By contrast, the dye molecules can also pack head-to-tail leading to J-aggregates. It leads to a red-broadening or the appearance of new absorption bands in the red region. Whether a specific dye forms H- or J-aggregates strongly depends on the molecular structure of the dye, solvation, and parameters controlled by the chemisorption process. Although the cyanine molecules are notorious for forming aggregates, the abovementioned results indicate the absence of aggregation in solution when combining DMSO/ethanol (1/9 ratio *v*/*v*) solvent mixture and low dye concentration of 0.1 mmol/L is already an important step. However, literature provides us with evidence that the addition of CDCA as a deaggregating agent in the dyeing solution remains compulsory for the device performance to avoid also the molecular aggregation of the dye with the self-assembled monolayer. This is an important aspect to consider since supramolecular aggregation contributes to quench the excited states of the molecule, therefore penalizing the electron injection yield.[105,165]

One way to assess the level of aggregation in the self-assembled monolayer is to analyze the UV-visible absorption spectrum of the chemisorbed dye. Figure 35.a shows the total transmission spectra of 3 µm thick TiO_2 films sensitized with **VG20-C$_{16}$** dye as a function of CDCA molar ratio into the dye solution. From an observational point of view, increasing the CDCA amount into the dye solution leads to a decrease in the film’s coloration from green to a more color-neutral feature (Figure 35 inset picture). This is ascribed to the reduction of the dye loading, in good consistency with the diminution of the main absorption band at 850 nm. Based on the normalized absorption spectra presented in Figure 35.b, we can observe a clear evolution of the 765 nm-shoulder with respect to the main band depending on the concentration of CDCA in the dye solution. More specifically, it is observed that the contribution of the shoulder decreases with CDCA concentration. Knowing that this shoulder is not only composed of vibronic contributions, but it is also contributed by a population H-aggregation, this result raises multiple pieces of evidence that strong H-type aggregates are formed within the self-assembled monolayer. Breaking such a type of lateral aggregation is not only a key to improving the device performance, but it also constitutes an important stake for the final aesthetic.

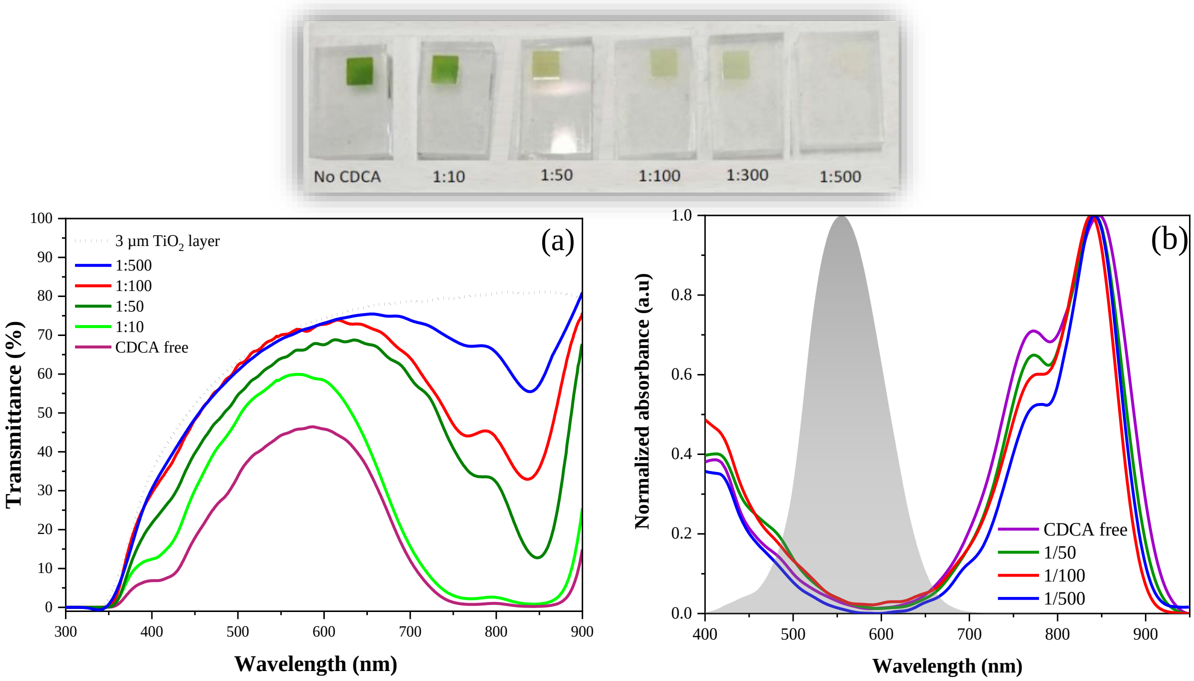

*Figure 35. (**a**) Transmittance evolution of a 3µm thick TiO$_2$ photoanode and its evolution when sensitized with **VG20-C$_{16}$** dye using a solution based on DMSO/ethanol (1/9 ratio v/v) containing a different ratio of CDCA. The measurement has been carried out in transmission mode without an integration sphere (**b**) Evolution of the normalized absorption spectra calculated from the transmittance curve. The shaded grey area represents the human's eye photopic response. A picture depicting the evolution of the photoanode's coloration for a 10 µm thick electrode is showed in inset.*

The effect of CDCA concentration, therefore of molecular aggregation, on device performance has been evaluated. The evolution of the (J-V) curve of **VG20-C$_{16}$** –based devices as a function of CDCA concentration from 10 mmol/L to 50 mmol/L is reported in Figure 36. In this experiment, the photoanode constitutes of a 6 µm mesoporous TiO$_2$ sheltered by a 5 µm scattering layer. By increasing the deaggregating agent concentration, the short-circuit current density is increasing from 8.3 mA/cm² to 12.1 mA/cm² despite the lower dye loading. The open-circuit voltage also increases from 321 mV to 347 mV, whereas the fill factor goes from 0.64 to 0.60. As a result, it is found from this simple study that the best power conversion efficiency (PCE) obtained is 2.5 % using a highly diluted dye solution (0.1 mmol/L) including 50 mmol/L of CDCA (1:500 ratio). We expect from such a high level of CDCA, that this latter is not playing the role of deaggregating agent but is also the result of its co-adsorption with the dye, thus hampering intermolecular electronic transitions.[166]

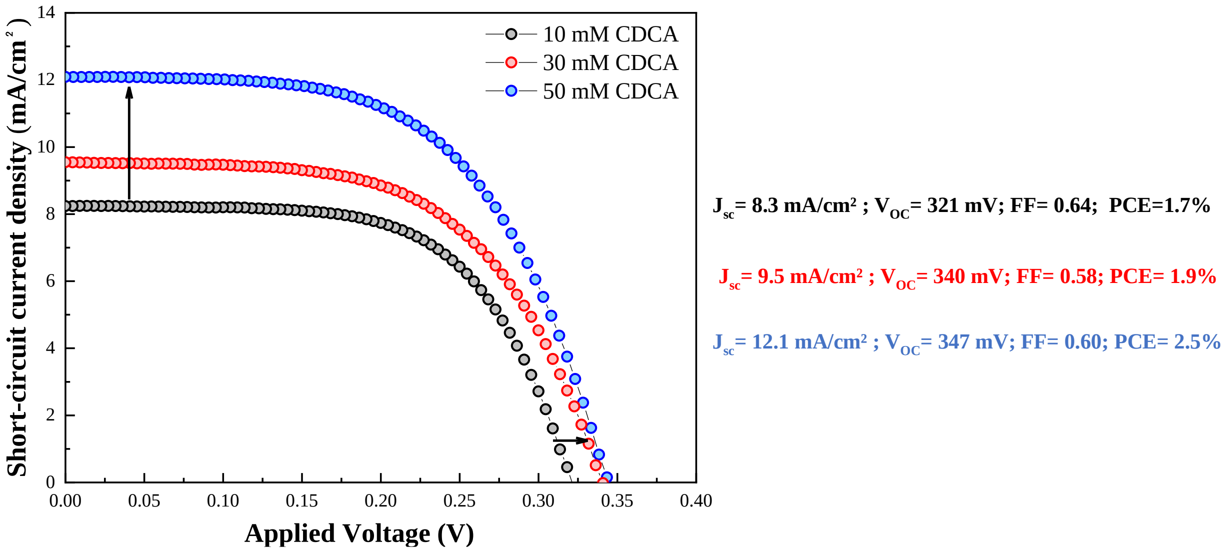

J_{sc}= 8.3 mA/cm² ; V_{OC}= 321 mV; FF= 0.64; PCE=1.7%

J_{sc}= 9.5 mA/cm² ; V_{OC}= 340 mV; FF= 0.58; PCE= 1.9%

J_{sc}= 12.1 mA/cm² ; V_{OC}= 347 mV; FF= 0.60; PCE= 2.5%

Figure 36. Evolution of (J-V) curve measured under A.M. 1.5G conditions of ***VG20-C$_{16}$*** *based DSSC as a function of CDCA concentration in the dye solution.*

To achieve this performance, the electrolyte composition needed to be carefully optimized to overcome the lack of injection driving force. One key to achieving efficient injection is to remove the Brönsted base 4-tert-butylpiridine (4-tBP) and the additive thiocyanate of guanidinium from the electrolyte composition, which are causing upshift of the TiO_2 band edges[167–170] while incorporating a sufficiently high concentration of lithium cation. This latter is known for its specific adsorption upon the TiO_2 surface. As a result, it is a potential determining cation that influences the extent of band bending on the surface of TiO_2. The flat band potential equilibrates with lithium cation in the electrolyte and quantitatively follows Nernst law, i.e., downshift in energy of 59 mV per decade of lithium concentration.[148,171,172] Therefore, the introduction of lithium cation into the electrolyte is a typical method to optimize the electron injection. This often translates into a gain of photocurrent, however frequently compensated by a loss of photovoltage due to the Fermi level downshift.

In my work, I studied the effect of Li^+ concentration on the device performance using LiTFSI salt. Four different concentrations between 0.1 to 1 mol/L were investigated (Figure 37). The results presented in Figure 37 and Table 3, show that in the case of VG20-C$_{16}$ dye, a concentration of 0.1 mol/L of Li^+ in the electrolyte is required to reach a short-circuit current density (J_{sc}) of 5.5

mA/cm^2. Increasing LiTFSI concentration to 0.25, 0.5, and 1 mol/L leads to an increase in the J_{sc} to 8.4, 9.6, and 12.1 mA/cm², respectively. This enhancement is at the expense of the cell photovoltage, which decreases by a value close to the 59 mV once the LiTFSI concentration is increased from 0.1 to 1 mol/L. This drop is thermodynamically expected from the Nernst equation (from 395 mV to 347 mV). Nevertheless, the noticeable increase in the current is much more significant than the loss of photovoltage (-14%), resulting in the PCE increase from 1.6 to 2.5%.

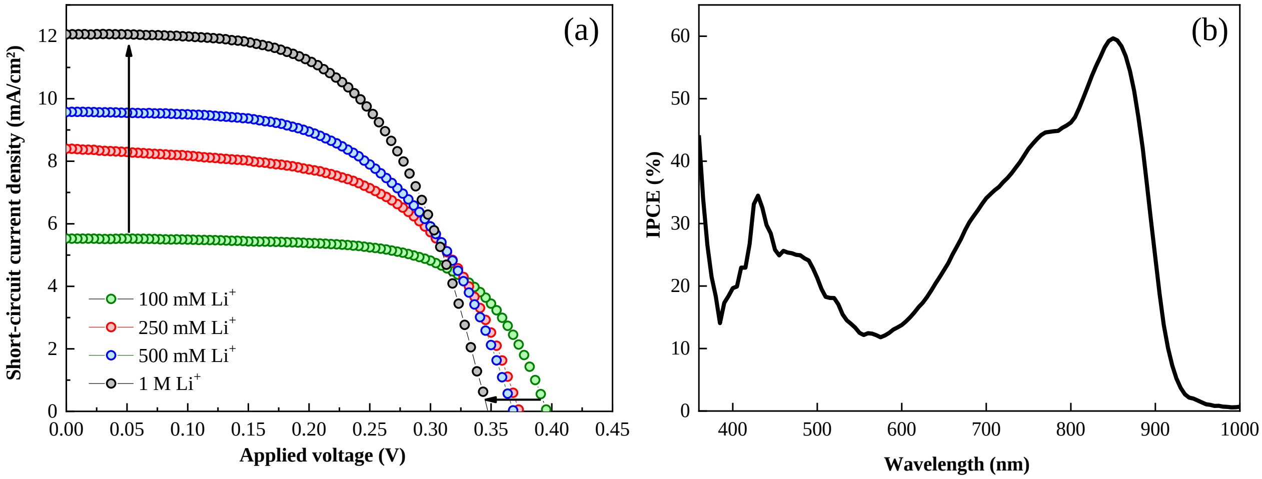

*Figure 37. (**a**) Evolution of the (J-V) curve recorded under A.M.1.5G conditions of **VG20-C16** based DSSC as a function of Li$^+$ concentration in the electrolyte. (**b**) IPCE spectrum of **VG20-C16** based-DSSC with triiodide/iodide-based electrolyte including 1 M of LiTFSI.*

*Table 3. Cell characteristics depending on the lithium concentration in the electrolyte for **VG20-C16**-based DSSC (electrolyte composition is 1 mol/L DMII, 0.03 mol/L I$_2$, and different concentrations of LiTFSI in acetonitrile/valeronitrile solvent mixture (85/15 v/v).*

[Li$^+$]	V_{oc} (mV)	J_{sc} (mA/cm^2)	Fill factor	PCE (%)
0.1 mol/L	395	5.5	0.66	1.6
0.25 mol/L	375	8.4	0.58	1.9
0.5 mol/L	368	9.6	0.56	2.2
1.0 mol/L	347	12.1	0.58	2.5

The IPCE spectrum of **VG20-C16**-based DSSC with the optimized conditions (50 mmol/L of CDCA in dye solution and 1 mol/L of LiTFSI in the electrolyte) presented in Figure 37.b shows a maximum of 60 % at 850 nm. The integration of the IPCE leads to a J_{sc} value of 11.6 mA/cm^2, thus is good consistency with the recorded value measured with the sun simulator. Although the

S_0-S_n transitions are only weakly absorbing, they contribute to a broad conversion between 20 to 30 % of the action spectrum, thus suggesting that the conversion of high energy photons is herein an efficient process.

Another approach to hamper lateral aggregations lies in the introduction of longer lateral alkyl chains in the dye design.[173]. Whereas the proof of concept described in the preliminary work was achieved using a C_8 chain, we herein investigated different lengths, namely C_2, C_8, and C_{16}. This modification does not influence the energy positions of both HOMO and LUMO frontier orbitals, as it is also suggested by the DFT calculations. This inactive part of the dye, with respect to its electronic properties, has a striking influence on the device performance, i.e., 1.5 % PCE is obtained for **VG20-C$_2$**, 1.9 % PCE for **VG20-C$_8$**, and 2.5 % PCE for **VG20-C$_{16}$** (Figure 38.a and Table 4). This improvement stems mainly from the photocurrent produced, increasing from 7.1 mA/cm^2 to 12.0 mA/cm^2 and secondly enhancing the cell photovoltage from 328 mV to 343 mV.

To grasp more insights on the origin of this improvement, Intensity Modulated Photovoltage / Photocurrent Spectroscopy (IMVS/PS) analyses were carried out as small perturbation techniques in order to assess the non-geminate recombination and electron transport dynamics (Figure 38.b-d). Whereas C_8 and C_{16} behave very comparably in terms of electron lifetime and transport time, reducing the number of carbon to C_2 leads to a shortening of electron lifetime by ca. one order of magnitude and the transport time to a lesser extent. The charge collection efficiency (η_{cc}), expressed as the time ratio between the electron lifetime and the sum of electron lifetime and transport time is enhanced by extending the length of the alkyl chain from η_{cc} = 70% for C_2 to η_{cc} = 80% for C_8 and C_{16}. These results suggest, in agreement with previous literature, that longer alkyl chain length helps to repel tri-iodide species from TiO_2 surface, therefore to prolong the electron lifetime. Additional charge extraction experiments in dark conditions provide an indication that shallow traps energy is affected by the alkyl chain length without modifying their distribution (Figure 38.d). This result highlights that the interfacial dipole moment of the dye to the TiO_2 surface is modified as a result of a different arrangement of the dye packing in the self-assembled monolayer. The gain of 15 mV photovoltage is thus the result of the combination between the one order of magnitude longer electron lifetime (+ 59 mV expected) and 40 mV energy downshift of the traps.

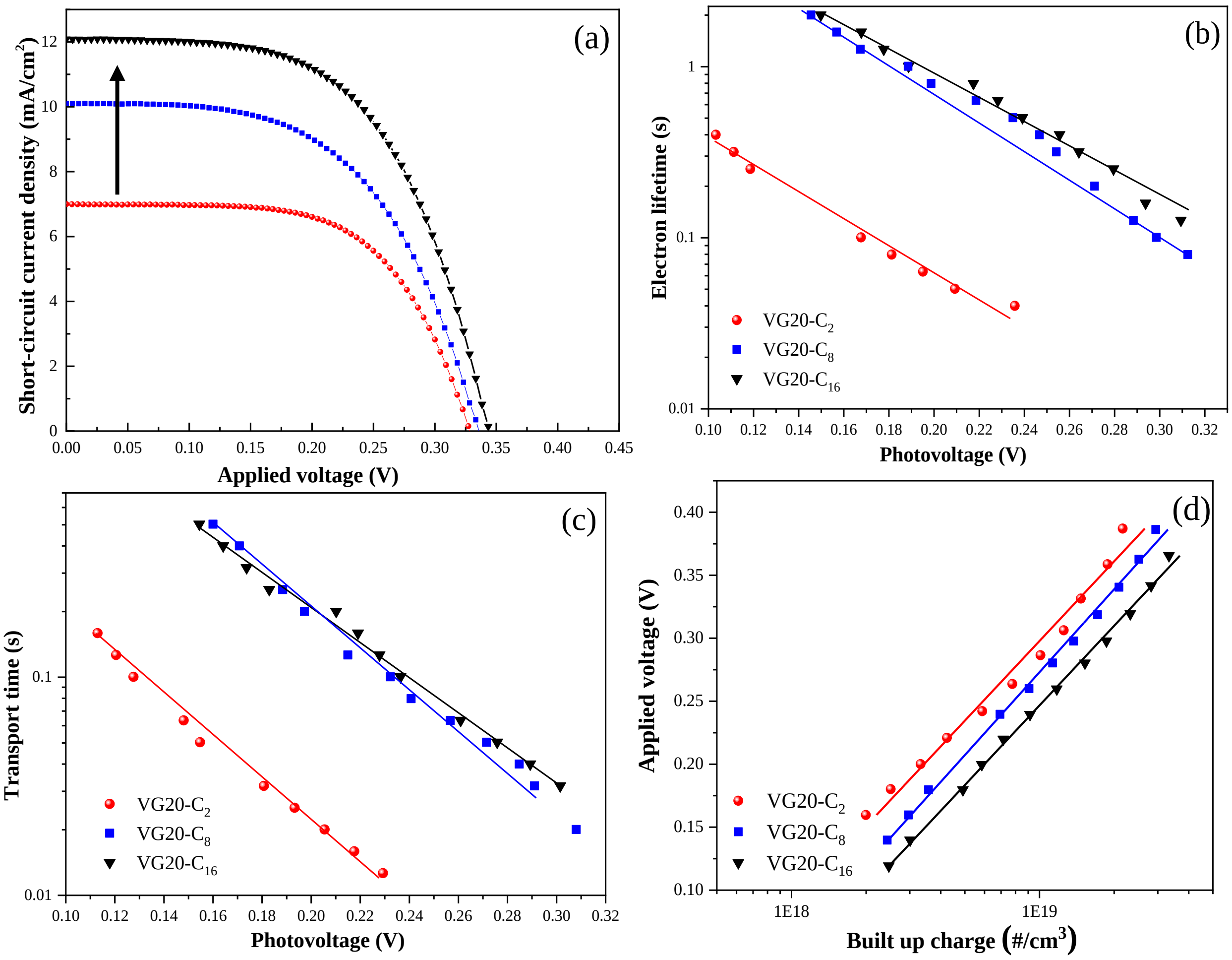

*Figure 38. (**a**) Evolution of the (J-V) curve under A.M. 1.5G conditions of **VG20-C$_x$** –based DSSC as a function of the alkyl chain length (**b**)evolution of the electron lifetime by IMVS, (**c**) evolution of transport time deduced by IMPS spectroscopy, and (**d**) dark charge extraction measurements.*

*Table 4. Cell characteristics depending on the alkyl chain length of **VG20-C$_x$** based DSSC.*

Alkyl Chain	**V_{oc} (mV)**	**J_{sc} (mA/cm^2)**	**Fill factor**	**PCE (%)**
C_2H_5	328	7.1	0.62	1.5
C_8H_{17}	336	10.1	0.55	1.9
$C_{16}H_{33}$	343	12.0	0.58	2.5

In addition to the CDCA and the alkyl chain length parameters, the sensitization temperature can modify the dye packing, as it has been previously demonstrated on ruthenium-based complexes.[174] Three different temperatures have been herein investigated: room temperature

(RT), 4°C, and -20°C. To compensate for the slower dye chemisorption, the sensitization time has been prolonged from 14 hours to 7 days at -20°C to maintain similar dye loading on the photo-anode (Figure 39.a). Without dramatically losing the cell photocurrent, lower temperature increases the open-circuit voltage from 343 mV at RT to 402 and 422 mV at 4°C and -20°C, respectively (Figure 39.b). A PCE maximum of 3.1 % can be reached after sensitizing the electrodes at -20°C (Table 5).

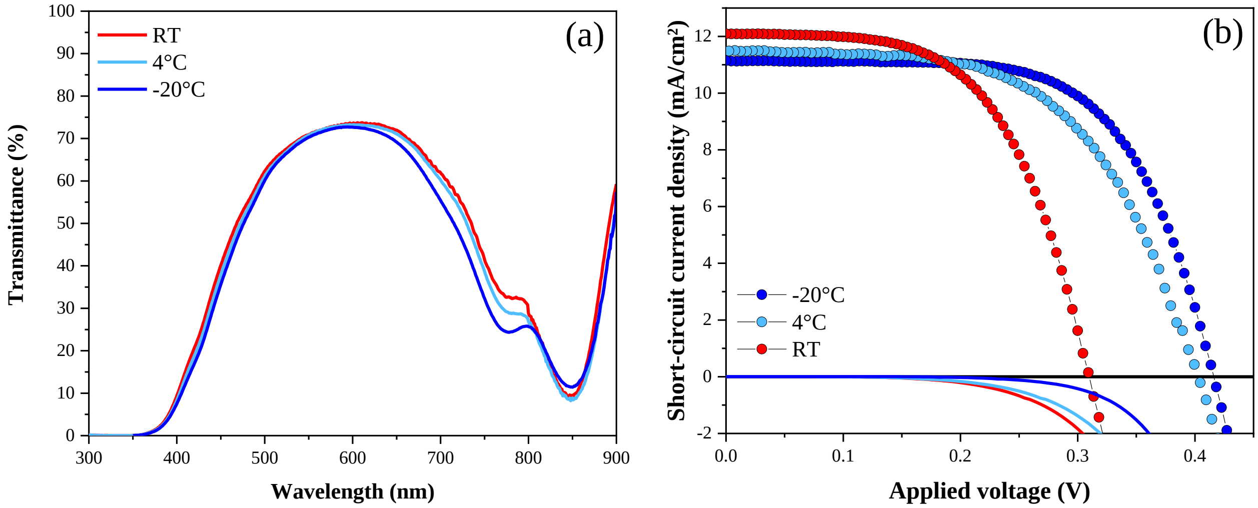

*Figure 39. (**a**) Evolution of UV-visible transmittance spectrum of **VG20-C$_{16}$** -photoanode sensitized at different temperatures (RT in red, 4°C in light blue, and -20°C in dark blue). (b) Evolution of the (J-V) curve under A.M. 1.5G conditions or under darkness of **VG20-C$_{16}$**-based DSSC as a function of the sensitization temperature.*

*Table 5. Cell characteristics depending on the sensitization temperature **VG20-C$_{16}$**-based DSSC.*

Temperature	V_{oc} (mV)	J_{sc} (mA/cm^2)	Fill factor	PCE (%)
RT	343	12.0	0.58	2.5
4°C	402	11.5	0.58	2.6
-20°C	422	11.2	0.65	3.1

IMVS experiments show that the sensitization temperature of -20°C reduces the non-geminate recombination compared to sensitization at RT or 4°C, thus explaining the higher photovoltage in the cell (Figure 40.a). Nevertheless, in the latter condition, it is also found that the transport time towards collection is longer (Figure 40.b). These evolutions stress that the two parameters are compensated and lead to a similar charge collection efficiency of ca. 80 %. Interestingly, the charge extraction experiments shown in Figure 40.c suggest also in the case of this cyanine dye that the temperature of sensitization influences the dye arrangement on the surface of TiO_2 in light of the observed substantial movement of the shallow traps and even a redistribution in these states when decreasing the temperature. As a result, an 80 mV increase in V_{oc} is observed, leading to the PCE of 3.1 %, thanks to reducing non-geminate recombination and energy downshift of the traps.

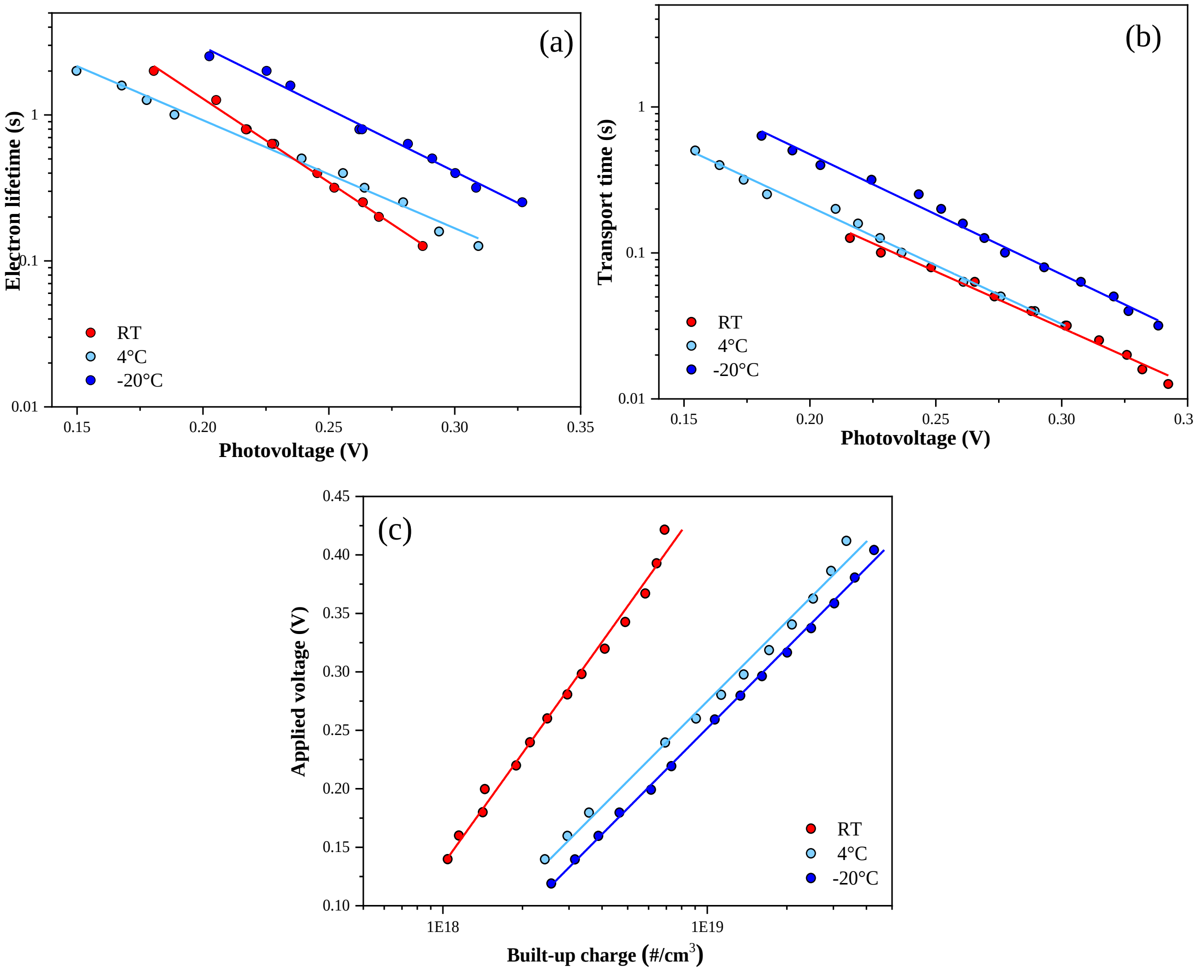

*Figure 40. Effect on the sensitization temperature on (**a**) electron lifetime, (**b**) transport time, and (**c**) distribution of shallow states deduced from IMVS/IMPS and charge extraction techniques, respectively, for **VG20-C_{16}**-based DSSC.*

To our best knowledge, the stability of polymethine-based sensitizers in DSSCs has never been demonstrated so far in the literature. This is one important drawback of this family of dyes. Besides the solvatochromic effect, alternative dyeing solvents were explored for both performance and stability purposes. Table 6 summarizes the photovoltaic parameters obtained depending on three different solvent mixtures previously presented, namely DMSO/ethanol, DMSO/DCM, and THF/ACN. THF/ACN leads to a drastic drop in short-circuit current density, from 12.1 to 7.5 mA/cm², together with a slight decrease in the open-circuit voltage from 347 mV to 333 mV. It results in a decrease in PCE from 2.5 % for DMSO/ethanol solvent mixture to a PCE of 1.6%. DMSO/ACN also leads to a drop in short-circuit current density to 8.3 mA/cm². However, this solvent affords to increase the cell photovoltage slightly by 40 mV to reach 387 mV under A.M.1.5G condition. The fill factor is increased to 0.64 compared to 0.58 for DMSO/ethanol. As for other parameters, the solvent used for sensitization plays an important role in the device's performance. This is the result of possible solvent-induced molecular aggregation and its possible effect on the dye geometry composing the self-assembled monolayer. We compared the two best solvents in terms of shelf-life stability. More surprisingly, we found that the device stability is much affected (Figure 41). Indeed, although initially less performing, the DMSO/DCM solvent mixture affords to improve the shelf-life stability of the devices substantially, reaching a PCE retention of over 92 % for 480 hours aging. For comparison, under the same conditions, the PCE of the devices based on DMSO/Ethanol dropped by 80 % after 480 hours as a result of an important loss of short-circuit current density.

Table 6. Cell characteristics depending on the sensitization solvent mixture for ***VG20-C$_{16}$****-based DSSC*

Solvent mixture (1/9)	**J_{sc} (mA/cm^2)**	**V_{oc} (mV)**	**Fill factor**	**PCE (%)**
DMSO/ethanol	12.1	347	0.58	2.5
DMSO/DCM	8.3	387	0.64	2.1
THF/ACN	7.5	333	0.63	1.6

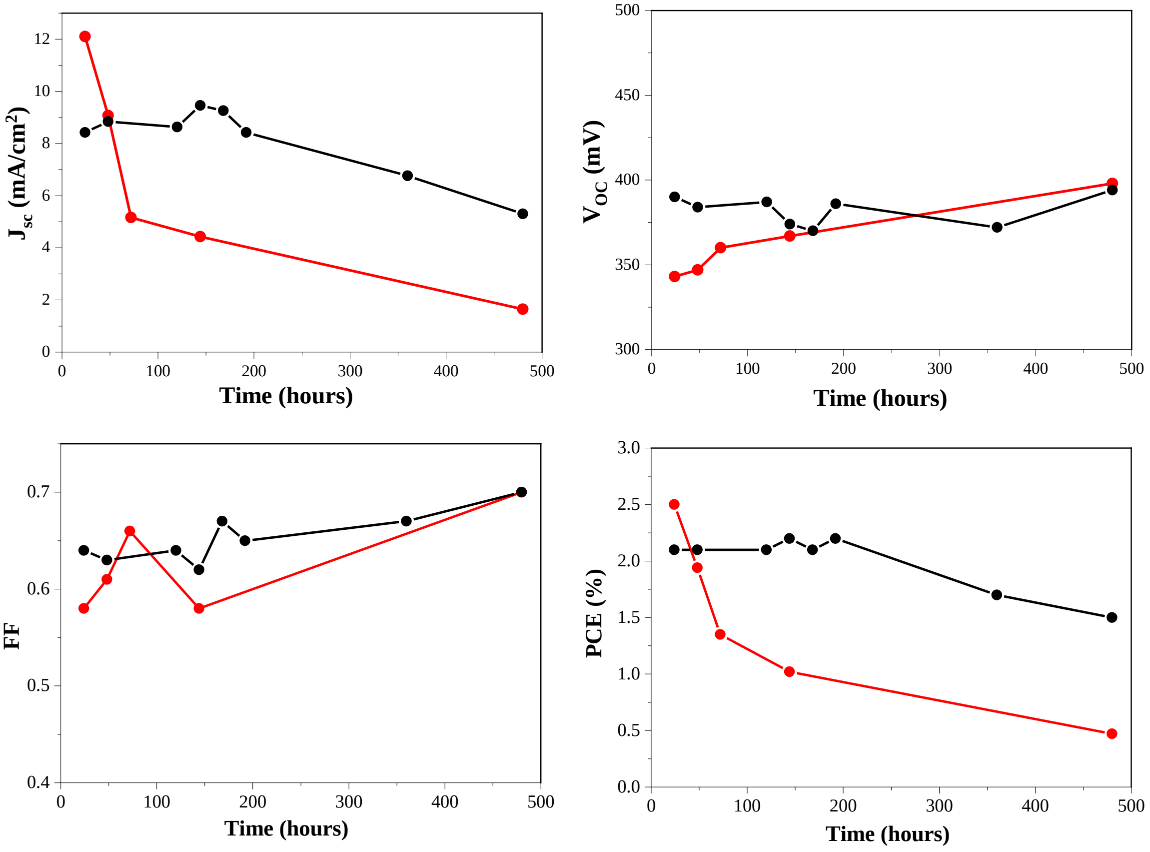

Figure 41. Evolution of the device characteristics upon shelf-life aging for ***VG20-C$_{16}$*** *DSSC (room-temperature sensitization) either using DMSO/ethanol (in red) or DMSO/DCM (in black).*

3.3. Aesthetic evaluation of VG20-C$_{16}$-based DSSC with triiodide/iodide electrolyte.

We have scrutinized different parameters to decipher the main limitations of the final transparency to optimize the visible light transmittance and the color rendering properties; in particular sensitization conditions, photo-anode thickness, electrolyte composition, and anti-reflective coatings. One critical aspect for a final good aesthetic is to avoid molecular H-aggregation. It gives rise to a broadening of the main S$_0$-S$_1$ transition and its shoulder to the visible range, thus strengthening the electrode coloration and reducing the AVT value.

As aforementioned, the molecular H-aggregation affects the device transparency and coloration noticeably. We quantified the effect of supramolecular aggregation on aesthetics, i.e., AVT and coloration (Figure 42). For this set of experiments, the NIR-DSSC devices were composed of an electrode thickness of 2 µm and including an inert electrolyte at this stage (i.e., no redox couple). Without CDCA in the dye solution, the transmission curve shows a minimum of 2.5 % at 848 nm leading to an average visible transmittance of 61 %.

However, introducing and increasing the concentration of CDCA in solution affects noticeably the final device's aesthetic. The total AVT is reaching 64 % and 71 % upon adding 10 mmol/l and 50 mmol/L of CDCA, respectively. The observed increase of transmittance at the dye absorption maximum is the result of two factors: the dye loading decreases due to the competitive process of CDCA chemisorption on the surface of the TiO_2 nanocrystals and the decrease of aggregated dye population. Unfortunately, direct evaluation of the dye loading on the electrode by the common desorption method was, in our case, not feasible due to the dye decomposition in alkaline media. In addition to transparency, the dye aggregation also influences the device tint (Figure 42.b). Indeed, the calculated CIE 1931 *x,y* coordinates show a noticeable shift toward the white point corresponding to the center of the chromaticity diagram upon increasing the CDCA concentration. As a result, the CRI value is increasing from 90 to 96. These essential first results, summarized in Table 7, stress the importance of mitigating the H-type aggregation of dyes in order to achieve high AVT value and more neutral coloration. Moreover, we determined the dominant wavelength for the 50 mmol/L CDCA condition to be 571 nm with a color saturation of 16%.

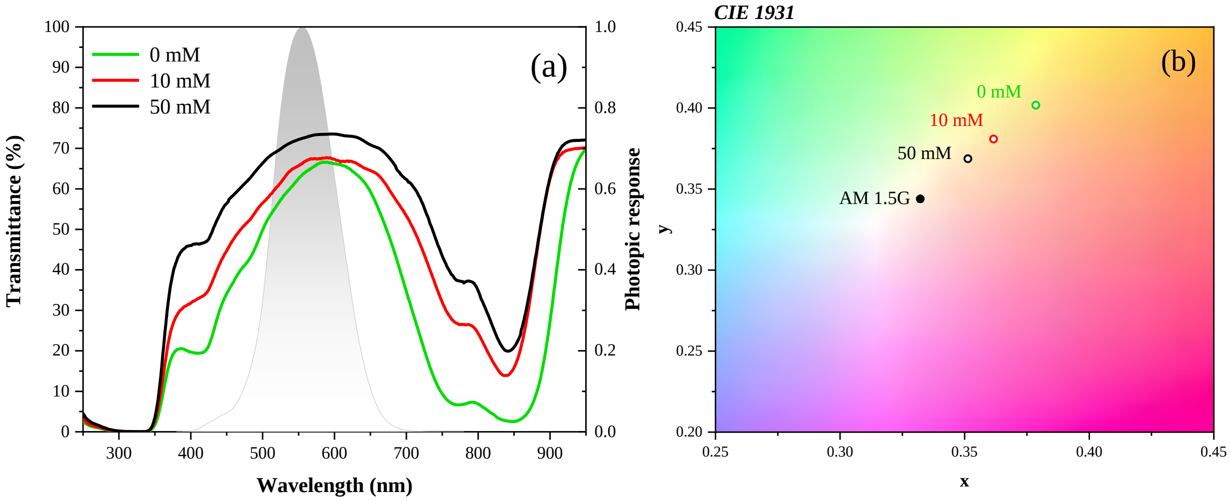

Figure 42. Optical assessment of NIR-DSSC devices based on a 2 µm thick TiO_2 photo-anode sensitized ***with VG20-C_{16}*** *dye in a solution containing different CDCA concentration. The electrolyte is based on inert acetonitrile. (**a**) Evolution of the device transmittance (the shaded grey area represents the human eyes photopic response), (**b**) evolution of x,y coordinates in CIE 1931 color space diagram.*

Table 7. Different aesthetic metrics evaluation of the NIR-DSSC based on ***VG20-C$_{16}$*** *with different CDCA concentration in a complete devices including only inert electrolyte based on pure acetonitrile solvent.*

[CDCA] (mM)	AVT (%)	CRI	CCT (K)	x,y CIE 1931
0	61	90.3	4213.6	x = 0.3786 y = 0.4018
10	64	93.8	4567.0	x = 0.3616 y = 0.3809
50	71	95.8	4842.2	x = 0.3513 y = 0.3687

Figure 43 shows the total transmittance spectrum of full NIR-DSSC device with **VG20-C$_{16}$** dye, including the optimized composition based on I_3^-/I^- redox mediator and optimized CDCA concentration (50 mmol/L). It is compared to the transmittance of a reference cell, including a non-sensitized TiO_2 film and the optimized electrolyte to decipher the dye effect on aesthetic. The AVT of this reference device reaches a maximum value of 74 %. This value is reported without subtraction of glass reflections; this latter accounts for 9.5 to 11 % depending on the incident wavelength.[175] Taking advantage of the **VG20-C$_{16}$** design, we achieved to match remarkably the higher cell transmittance region to the maximum of the human eye's photopic response, thus leading to an entirely transparent DSSC device. The transmission maximum is even slightly better in the presence of dye, which may suggest a better matching of the refractive index in contact with the electrolyte. The electrolyte contribution in the total absorbance is in the UV and the blue region ($\lambda < 500$ nm) due to tri-iodide. This region corresponds to an area in which the human cones are much less sensitive. We can observe that the dye aggregation slightly overlaps with the red part tail of the photopic response. Compared to the reference cell (AVT = 74 %), the sensitization of the photoanode decreases the AVT value to 70 % as a result of the supramolecular self-aggregation of the dyes. Comparing our full device, including the full electrolyte (AVT = 70%), to the one discussed above incorporating only acetonitrile solvent (AVT = 71%), we conclude that the introduction of I_3^-/I^- redox mediator doesn't highly affect the AVT value, but however leads to the yellow coloration as revealed by the picture in Figure 43.

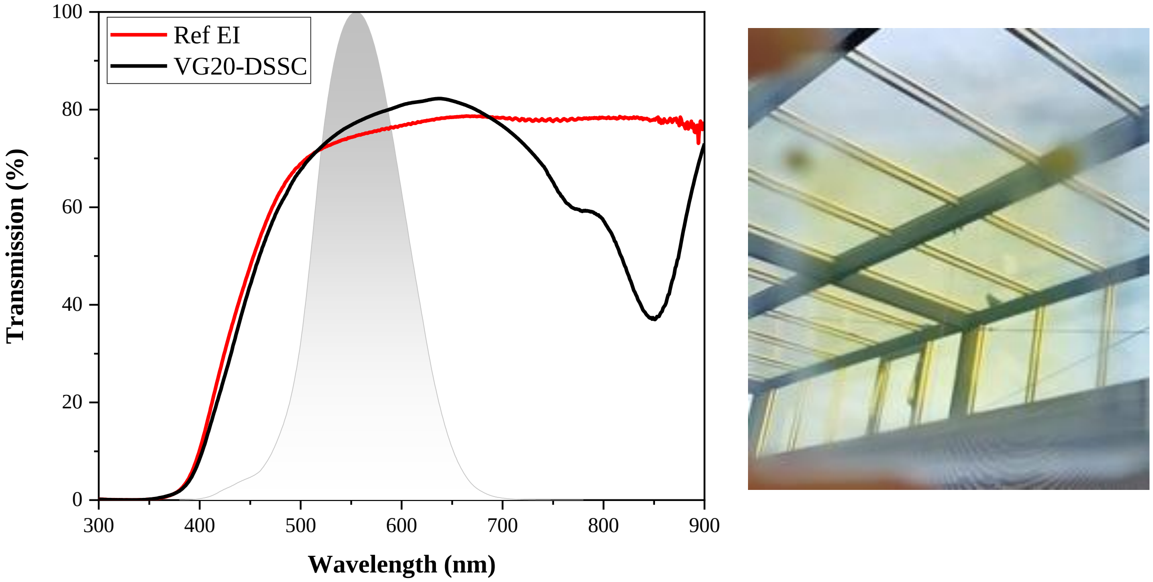

*Figure 43. Comparison of total cell transmittance measured using an integration sphere between a reference cell (Ref EI) without dye and with the optimized electrolyte composition (red curve) and **VG20-C$_{16}$** based NIR-DSSC (black curve). The photo-anode thickness for each cell is 2.0 µm. A picture depicting the aspect of the resulting NIR-DSSC is also provided.*

In order to minimize the light reflection at the glass/air interfaces, we optimized a procedure to deposit an anti-reflecting coating (ARC) based on a thin layer of SiO_2 nanoparticles by spin-coating on the surface of the two external sides of the devices. This part of the optimization work has been carried out by Dr. Thomas Alnasser, a post-doctoral fellow in the group. The interest in SiO_2 stems from its refractive index of ca. 1.45 in the visible range, thus better matching with air than glass (n_{glass} = 1.52). After optimization of the size of SiO_2 nanoparticles and the deposition parameters, the introduction of these ARC layers contributed to significantly enhancing the AVT values to 78 % for the reference EI cell and to 76 % for the full NIR-DSSC devices based on **VG20-C$_{16}$** dye. For comparison with the state-of-the-art, this AVT value lies well beyond the values reported so far in semi-transparent DSSCs.[73–75]

For a quantitative color perception, we calculated the CIE 1931 *x,y* chromaticity coordinates, CRI, CCT, the dominant wavelength, and the color purity of this NIR-DSSC device. For the reference cell, we obtained a CRI value of 94.3, with x = 0.3646, y = 0.3877, and CCT value of 4514.0 K. The sensitization of the TiO_2 photo-anode with **VG20-C$_{16}$** has only a minor influence on these aesthetic parameters, i.e., a CRI value of 93.4, with x = 0.3743, y = 0.3970, and CCT value of 4297.5 K. (Figure 44 and Table 8). Both dominant wavelength and color purity are intuitive quantities and can be considered an alternative to the numerical *x*,*y* coordinates.[147] The dominant wavelength for the reference cell is 573 nm and for **VG20**-DSSC is 572 nm representing an orange-yellowish color (Figure 44). This is dominated by the color of the electrolyte, and it is in good agreement with the visual aspect of the device, as shown in Figure 43. We calculated a color purity (color saturation) value of 0.26 (26%) for the reference cell, whereas this value increases to 0.31 (31%) for the **VG20-C$_{16}$** based NIR-DSSC. This slight increase in color saturation (+5%) and the 200 K difference in CCT are caused by the additional light absorption by the dye molecules. Nonetheless, it is hardly noticeable by our eyes. These results confirm that the introduction of the dye does not lead to significant changes in the final aesthetics parameters, and thus the electrolyte is the color determining factor in this case. Moreover, compared with the **VG20-C$_{16}$**-DSSC with acetonitrile instead of the full electrolyte, the color saturation is doubled (from 16% to 31%), emphasizing the role of the electrolyte in the final coloration of our NIR-DSSC.

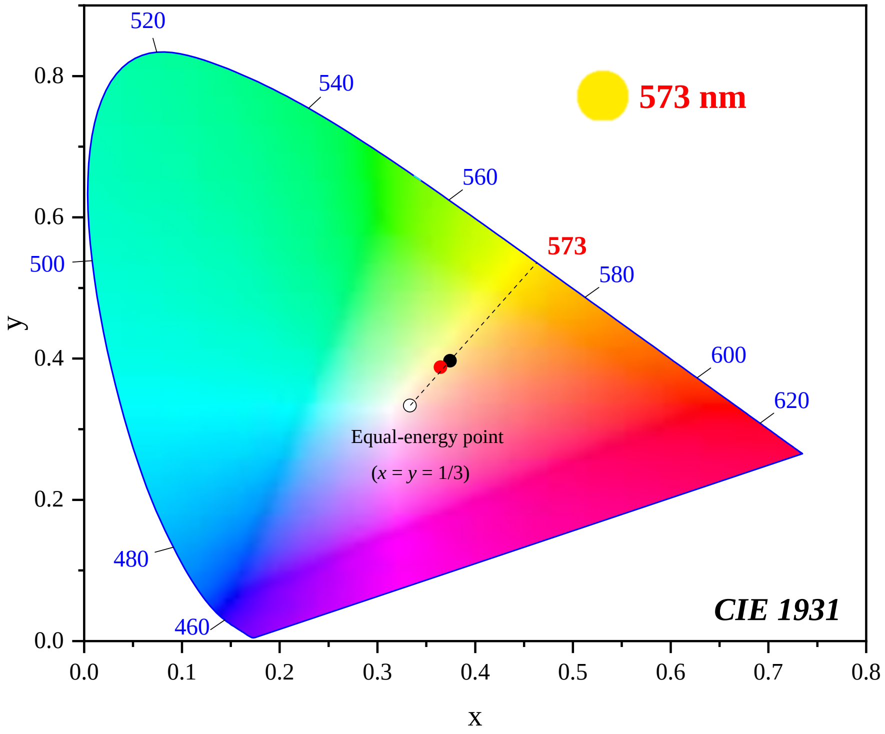

*Figure 44. CIE 1931 x,y coordinates calculated for the reference device (red point) and the complete NIR-DSSC based on **VG20-C$_{16}$** dye (black point). The dashed line in black represents the extension of the straight line joining the equal-energy point (white point) and the points referring to our NIR-DSSC to the perimeter of the chromaticity diagram to determine the dominant wavelength (573 nm).*

*Table 8. Aesthetic metrics evaluation for the reference cell (no sensitizer) and **VG20-C16** based NIR-DSSC.*

	TiO_2 thickness (µm)	AVT (%)	AVT with ARC (%)	CRI	CCT (K)	x,y CIE 1931
VG20-DSSC	2	70	76	93.6	4297.5	x = 0.3743 y = 0.3970
Ref EI	2	74	78	94.3	4515.0	x = 0.3646 y = 0.3877

3.4. Dye regeneration and electron injection kinetics

To better understand the processes limiting the performances of **VG20-C16** –based NIR-DSSC, dye regeneration and electron injection kinetics have been studied using either picosecond pump or femtosecond pump – optical probe transient absorption spectroscopy. The picosecond study has been performed at LRCS and in part collaboration with Dr. Iva Dzeba (post-doctoral fellow at LRCS). The femtosecond study has been carried out in collaboration with Ilias Nikolinakos (Ph.D. student) and Prof. Stefan Haacke from IPCMS laboratory in Strasbourg, within the frame of the ANR VISION-NIR project.

Figure 45 depicts the dye regeneration kinetic evolution depending on the electrolyte composition, i.e., either for I_3^-/I^- redox mediator (Figure 45.a) or for a redox couple-free inert electrolyte including 1 mol/L of LiTFSI (Figure 45.b). **VG20-C16** radical cation absorbs in the visible range in agreement with the literature.[176] It shows up a broad transient absorption between ca. 500 nm and 720 nm, for which the kinetic clearly differs if the electrolyte is composed or not of a redox mediator (note the time scale difference in the Streak images).

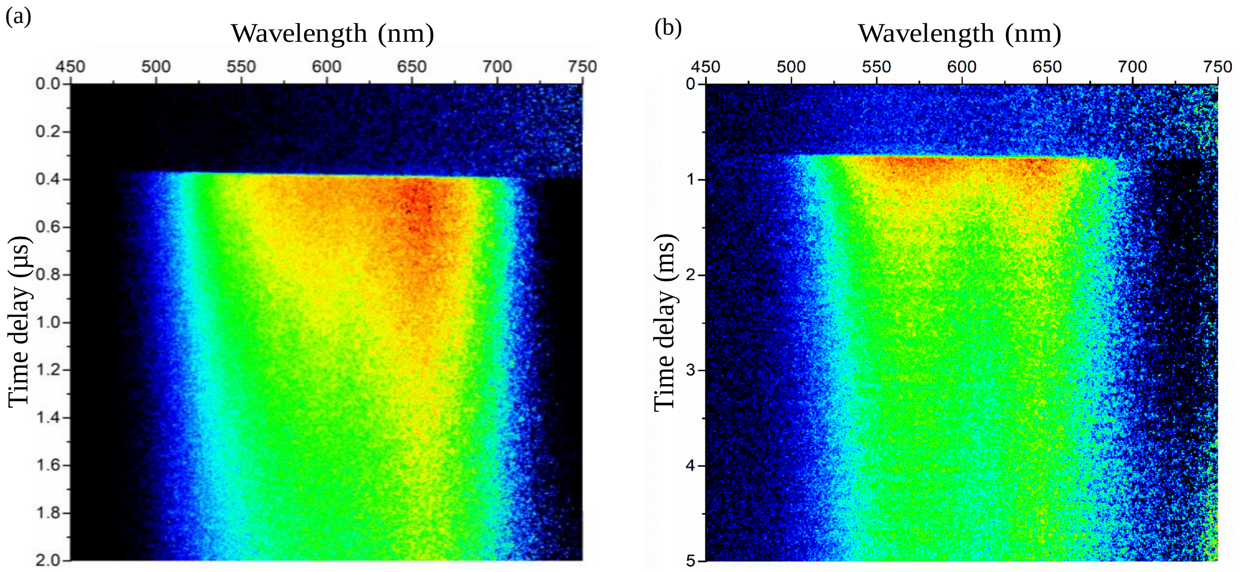

Figure 45. Time-resolved transient absorption spectrum recorded on a streak camera of the ***VG20-C$_{16}$*** *based DSSC for (**a**) I_3^-/I^- redox couple in the electrolyte (**b**) no redox couple (inert electrolyte). The devices were pumped at 830 nm with $E_{830\ nm} \approx 0.18\ mJ/cm^2$.*

The corresponding transient decay is attributed to the depopulation of the dye radical cation after a 30 ps pump pulse at 830 nm (Figure 46). The exponential decay systematically requires two components to account for a fast and slower process in the dye regeneration. For I_3^-/I^- redox couple, dye regeneration takes places within $\tau_1 = 1.5$ µs (± 0.09 µs) and $\tau_2 = 19.4$ µs (± 1.3 µs). These values are in the same order of magnitude as those reported in the literature for conventional ruthenium and D-π-A dyes.[148,177–179] A long-lived radical dye cation is experienced in contact with an inert electrolyte, i.e., free of redox couple to block the dye regeneration and measure the geminate recombination process (electron capture by the oxidized dye) (Figure 46.b). The halftime of the geminate recombination takes place within 0.94 ms (± 0.02 ms). It does not totally decay even beyond the upper limit of the 5 ms sweep time of our Streak camera. Based on these results, we can conclude that dye regeneration yield is close to being quantitative and does not constitute a limiting step of the IPCE, i.e., $\Phi_{reg} > 98\ \%$ in I_3^-/I^-. This is in good agreement with the cyclic voltamperometry experiment, which showed a driving force of ca. 500 mV for the dye regeneration.

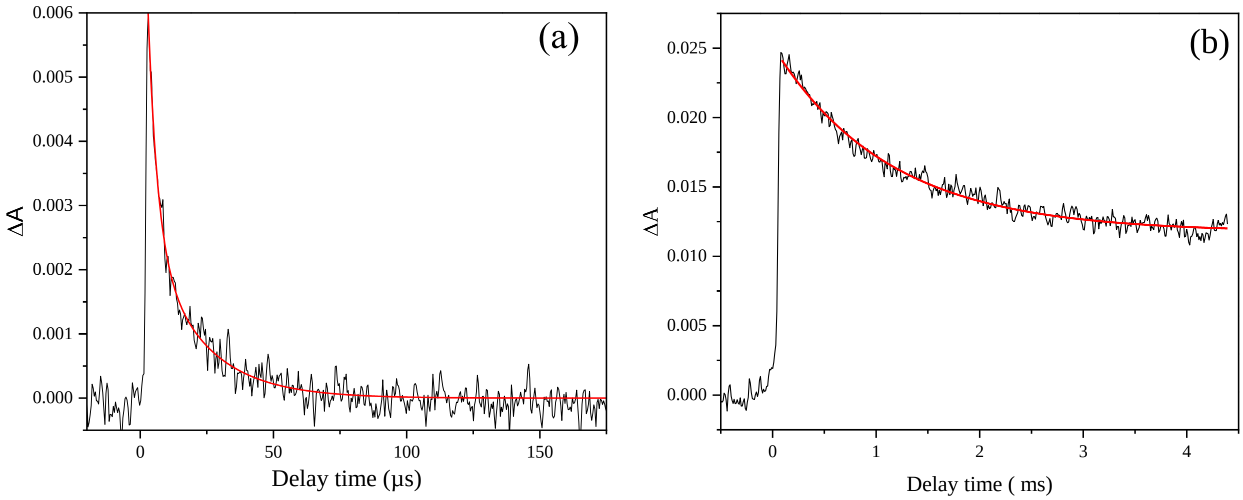

Figure 46. Transient absorption kinetic of ***VG20-C$_{16}$*** *based DSSC probed at 650 nm: (****a****) in the presence of I_3^-/I^- redox couple and (****b****) with an inert redox-free electrolyte.*

The femtosecond dynamics of the excited state of **VG20-C$_{16}$** have also been investigated in order to monitor the charge injection dynamic. Figure 47 shows the differential absorption spectra obtained in an average-representing data set characteristic for TiO_2 and non-injecting ZrO_2 devices. The transient absorption kinetics are presented for selected wavelengths representative of the steady-state absorption (SSA) and steady-state emission (SSE) contribution (Figure 48). These spectra are characterized by a prominent excited state absorption (ESA) peaking at 580 nm, which, unlike for the data obtained in solution, decays rapidly within 25 ps leaving behind a broad, red-shifted absorption with a maximum at 660 nm and a long tail spanning the visible part of the spectrum (cf. 100 ps delay). Such a residual long-lived signature is assigned to the absorption of the **VG20-C$_{16}$** radical cation (VG20$^{\bullet+}$) in good agreement with the transient spectra measured with Streak camera in our picosecond TAS setup (Figure 45-46).

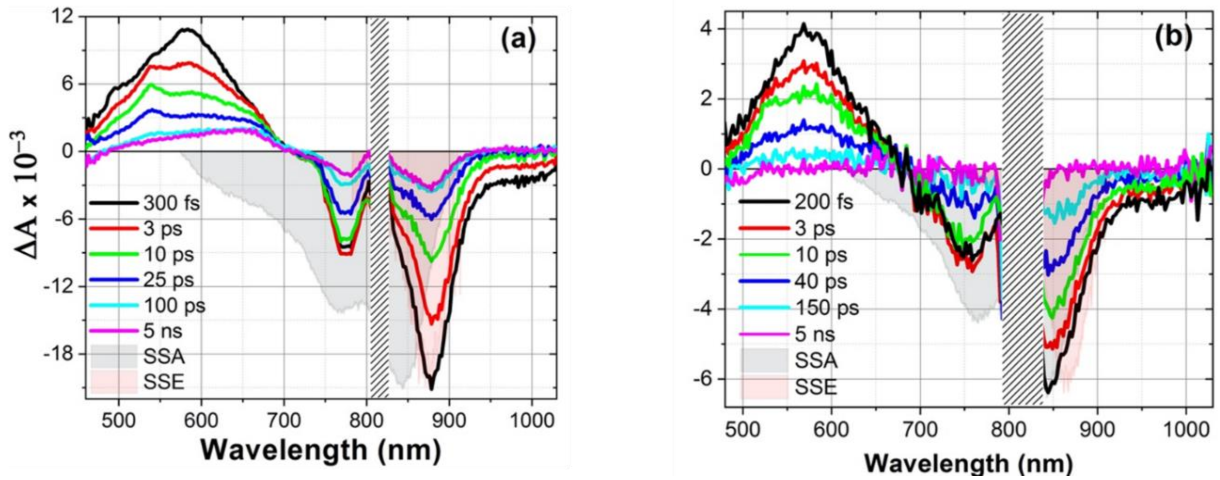

Figure 47. Transient spectra of ***VG20-C_{16}*** *–based DSSC with the dye anchored on (****a****) injecting TiO_2 nanocrystals (****b****) non-injecting ZrO_2 nanocrystals. The devices were pumped at 800 nm with an energy of 90 µJ/cm^2.*

In the NIR part, the stimulated emission (SE) is observed in the 850-1030 nm range, which decays within 25 ps. The GSB signal, between 730 and 900 nm, shows a double peak structure, akin to the steady-state absorption spectra due to monomers and aggregates. According to the ground-state absorption spectra (SSA) of **VG20-C_{16}** in solution and on TiO_2, one infers that the high-energy band at 780 nm is dominated by aggregates, while the low-energy band is a combination of GSB bleach of monomers and aggregates and SE from monomers. The 880 nm band has decayed by half its amplitude within 10 ps and reaches a stable level of ≈ 20% of the initial value by 100 ps. While the fast decay is due to SE decay and partial ground state recovery, the long-time asymptote is due to the radical dye cation.

The 780 nm band shows different kinetics. A slight rise of this aggregate-dominated band is observed until 2 ps (Figure 48), which is a clear signature of excitation of aggregates due to energy transfer (ET) from monomers. In addition, a sharp absorption feature develops at λ ≈ 535 nm on a 2-ps time scale. Since it is not observed in monomers, it is attributed to the ESA of aggregates, rising according to the monomer-aggregate energy transfer process.

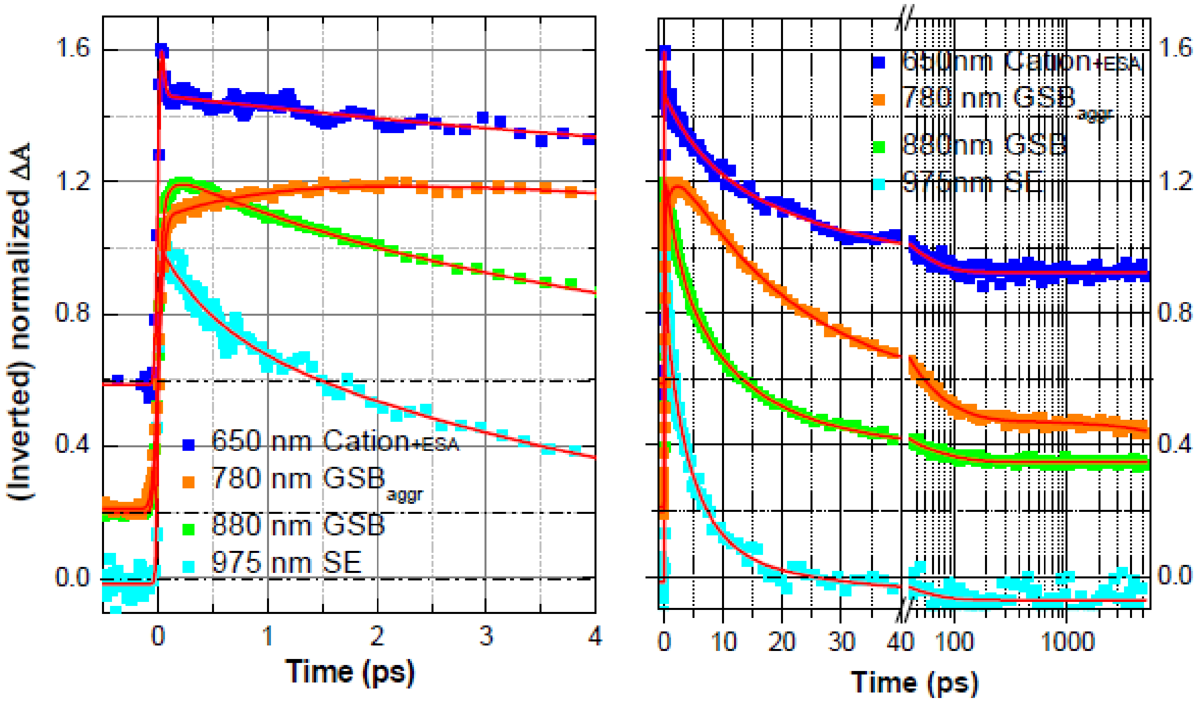

Figure 48. Normalized TA kinetic traces of ***VG20-C16****–based devices using injecting TiO_2 nanocrystals detected at various wavelengths and in two different time windows. 650 nm: ESA and cation absorption maximum, 780 nm: high-energy GSB portion dominated by aggregates, 880 nm: maximum of GSB and SE, 975 nm: SE, and absorption of free electrons in TiO_2 (> 50 ps). Traces are vertically shifted by 0.2 units for clarity; dash-dotted lines indicate the zero-signal level. The slow rise in the 780 nm trace is due to monomer-to-aggregate energy transfer, occurring dominantly on a ≈0.4 ps time scale. The fast SE decay (975nm) and the slow ESA decay (650 nm) do not match because, in the latter, the rise of dye cation absorption retards the signal decay.*

If all molecules, monomers and aggregates, became photo-oxidized, and since the cation absorption is negligible in the region of dominant GSB (800-900 nm), the negative ΔA signal should not decay with time, contrary to what is herein observed, meaning that the carrier injection yield (Φ_{inj}) is well below 100%. Hence, the ratio GSB(t=0.2ps) / GSB(t=5 ns) provides an estimate of Φ_{inj}. However, part of ΔA is due to SE, thus making the determination of the pure GSB component difficult. Nevertheless, analyzing the ΔA(t=0)/ΔA(t=5 ns) ratio at different wavelengths (780-850 nm) provides an upper limit of $\Phi_{inj} \approx$ 30-35%. Although lower, this value is relatively consistent with the IPCE at 810 nm (≈ 40-45%) (Figure 37.b). The discrepancy is explained first by the TAS experimental conditions, which are different from the IPCE and (J-V) experiments in terms of excitation power (i.e., nonlinear response of DSSCs between cell photocurrent and incident light power) and the absence of a scattering layer in the device made for TAS measurements.

We have also studied the excited state dynamics in non-injecting ZrO_2-based devices, which serve as a reference to identify excited-state processes, e.g., energy transfer which may be in kinetic competition with the electron injection in TiO_2 devices with an equivalent degree of aggregation. The differential spectra for ZrO_2-based devices show clear differences compared with TiO_2 (Figure 49.b). Indeed, the radical cation signature is absent, and the GSB fully recovers (zero signal) by ca. 1 ns. The SE (> 900 nm) decays slower than TiO_2 devices since a weak signature can still be observed at a delay of 150 ps. The monomer-to-aggregate energy transfer (ET) is also observed for ZrO_2, as a small increase of the bleach band at 760 nm. Plots of kinetic traces and detailed multi-exponential fits are gathered in Figure 49.

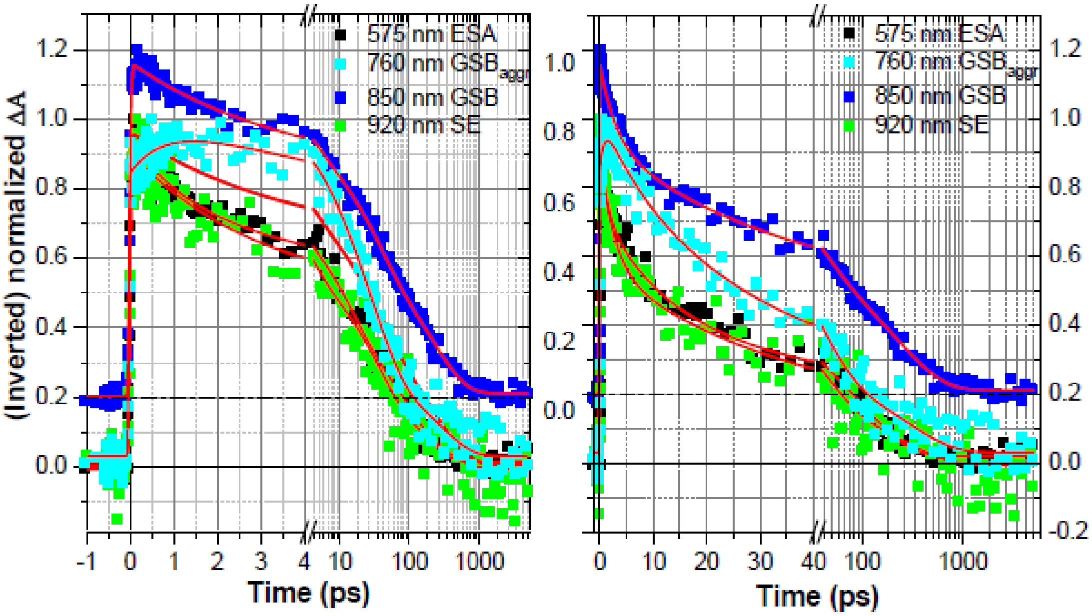

*Figure 49. TA kinetic profiles of **VG20-C$_{16}$**-based DSSC on ZrO_2, probed at various wavelengths: 575 nm, 760 nm, 880 nm, and 975 nm, in two different time windows. The devices were pumped at 800 nm with 90 $\mu J/cm^2$ pulse energy.*

In order to highlight the carrier injection processes and their kinetics, Figure 50 shows kinetic traces obtained by averaging seven TiO_2-based and three ZrO_2-based devices. Selected wavelengths represent the monomer ESA (A), dye radical cation absorption (B), the low-energy GSB band (C), and SE (D). The prominent long-time signal for TiO_2 is due to the **VG20-C$_{16}$** radical cation absorption (580 and 650 nm) and incomplete GSB recovery (880 nm). Note a small positive absorption in the SE trace of TiO_2 ($\lambda \approx 975$ nm), most likely due to absorption by free carriers in TiO_2 or to a near-IR tail of the radical cation absorption.

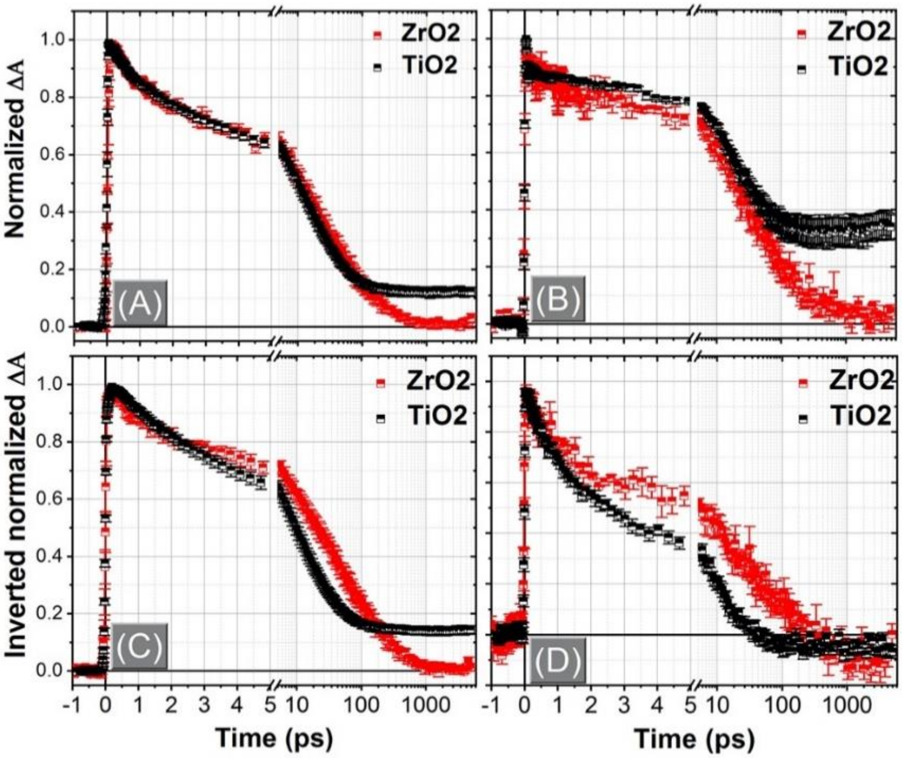

*Figure 50. Comparison of normalized transient absorption kinetic profiles for **VG20-C$_{16}$**-based DSSC using either ZrO$_2$ nanocrystals or TiO$_2$ nanocrystals at **(a)** 570 nm (ZrO$_2$) and 585 nm (TiO$_2$), **(b)** 640 nm (ZrO$_2$) and 650 nm (TiO$_2$), **(c)** 860 nm (ZrO$_2$) and 880 nm (TiO$_2$) and **(d)** 960 nm (ZrO$_2$) and 975 nm (TiO$_2$). All DSSC devices were pumped at 800 nm with 90 µJ/cm^2. The kinetics are averaged over 7 samples for TiO$_2$ and 3 samples for ZrO$_2$. Error bars indicate the standard statistical error.*

The data suggest two distinct reaction pathways for **VG20-C$_{16}$** on TiO$_2$ and ZrO$_2$, as summarized in Scheme 2 starting from photo-excited monomers (VG20*) and aggregates (Agg*).

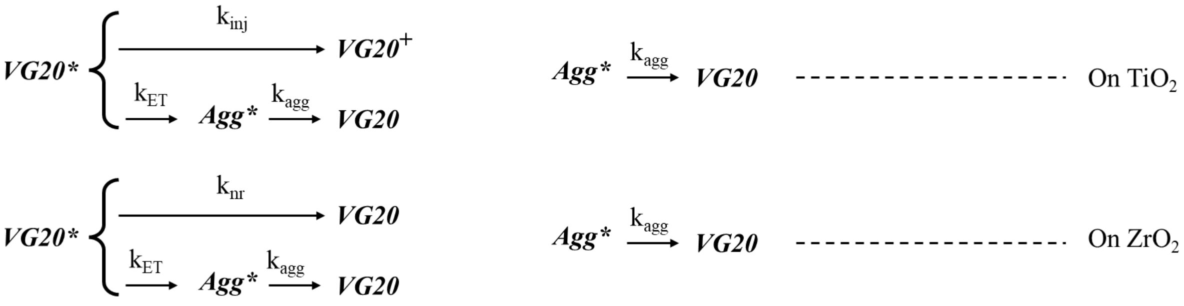

Scheme 2. Excited-state reaction schemes: On TiO$_2$, VG20 can form the VG20$^+$ cation due to electron injection or decay into excited state aggregates (Agg*) due to energy transfer. Photo-excited aggregates return to the ground state (VG20) due to self-quenching. On ZrO$_2$, VG20* undergoes ET, but also dominantly non-radiative recombination to VG20. Rates as indicated; their relation to the observed lifetimes will be explained below.*

As summarized in Table 9, characteristic lifetimes for **VG20-C$_{16}$** on TiO_2 are in the 0.5-1, 4-8, and 20-40 ps range, in addition to a fixed 100 ns time accounting for the non-decaying signals at long delays. In order to identify the most relevant characteristic lifetimes and processes, a global fit approach was carried out, i.e., the wavelength-dependent decay times are approximated by four wavelength-independent values. For TiO_2 (Figure 51.a), the global decay constants are obtained: 0.4 ps, 4.3 ps, 25 ps, and 100 ns, this latter being fixed for the fit. Special features in the decay-associated difference spectra (DADS) allow identifying the main excited state processes, i.e., monomer-to-aggregate energy transfer, carrier injection/radical cation formation, and their respective lifetimes. For the former, and as discussed above, the rise of the 770 nm GSB band and the 530 nm aggregate-ESA peak are the fingerprint reflected in the DADS with dominating positive and negative signals, respectively. Hence, the energy transfer with rate k_{ET} is operative during the sub-picosecond (0.4 ps) and the ≈ 4 ps phases. Charge injection/radical cation formation is best identified as a rise of the absorption at the radical cation peak wavelength (660-670 nm) and monomer excited state decay, i.e., the decay of SE (> 950 nm). The DADS of Figure 51.b shows that charge injection, rate k_{inj}, occurs concomitantly with the energy transfer, dominantly during the ≈ 4 ps timescale, and to a lesser extent at shorter times (0.4 ps DADS). The 25 ps DADS is characterized by SE and ESA decay both for monomers and aggregates (band at 530 nm), but these decay amplitudes hide possible weaker signatures of radical cation formation since the 25-ps DADS at 660 nm is purely positive (i.e., ESA decay).

The same global analysis on ZrO_2 is reported in Figure 51.b. It reveals four-time constants: 1.7 ps, 22 ps, and 200 ps in addition to a long-lived contribution which is almost vanishing in 100 ns, used for consistency with fits of the TiO_2 data, its amplitude being in the noise level. The fastest 1.7 ps component (black line) displays a DADS very similar to TiO_2, with all the features consistent with monomer-to-aggregate energy transfer (k_{ET}). The ca. 24 ps component (red curve) displays signatures of both monomer and aggregate excited state decay: monomer SE > 850 nm, monomer and aggregate ESA decay (450-680 nm), with the weak sharp feature at 530 nm already identified for TiO_2 as due to aggregate ESA (k_{agg}). Note that the fast sub-10 ps component observed for electron injection (negative DADS at 660-680 nm) is absent as expected. Remarkably, the longer ≈ 200 ps component (blue curve) is due to a second slower monomer excited state decay (k_{nr}) since it displays very similar SE, ESA and GSB recovery, though with a shorter lifetime than VG20-C_{16} in solution (Figure 33-34).

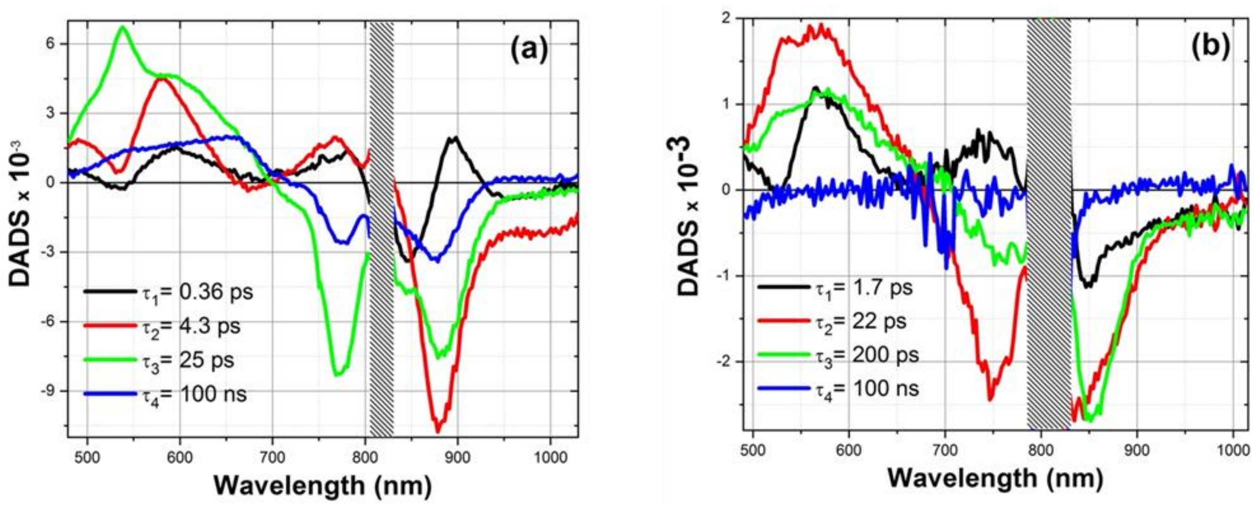

Figure 51. Wavelength-dependent amplitude of ***VG20-C_{16}****-based devices including (****a****) injecting TiO_2 nanocrystals (****b****) non-injecting ZrO_2 nanocrystals.*

Table 9. Transient absorption kinetic parameters for ***VG20-C_{16}*** *and TiO_2 DSSCs obtained by femtosecond transient absorption studies.*

	A_1	**τ_1(ps)**	**A_2**	**τ_2(ps)**	**A_3**	**τ_3(ps)**	**A_4**	**τ_4(ns)**
540 nm ESA aggr/mono	Small rise	1.0	69%	17.7	16%	70	15%	100
585nm ESA/cation	10%	1.1	43%	8.3	41%	33.6	5%	100
650nm ESA/cation	Small rise	1.1	33%	12.8	21%	41.6	45%	100
780nm H-GSB	Clear rise	1.2	70%	24.9	6%	213	24%	100
880nm GSB/SE	Rise	0.07	25%	3.7	50%	21.0	13%	100
975nm SE	20%	0.4-1	20%	4.0	59%	21.6	15%	100

Table 10. Transient absorption kinetic parameters for ***VG20-C₁₆*** *and ZrO_2 DSSCs obtained by femtosecond transient absorption studies.*

	A_1	**τ_1(ps)**	**A_2**	**τ_2(ps)**	**A_3**	**τ_3(ps)**	**A_4**	**τ_4(ps)**
575nm ESA	14%	0.8	21%	4.2	31%	21	35%	133
760nm H-GSB	-18%	0.8	15%	7.5	61%	31	22%	300
850nm GSB	6%	1.2	21%	4.4	36%	37	36%	272
920nm SE	23%	2.0	12%	5.2	47%	38	19%	297

In summary, the comparison of **VG20-C₁₆** on TiO_2 and ZrO_2 allows to identify the kinetic signature of the electron injection within dominantly 4 ps most probably from monomers (k_{inj}), competing with monomer-to-aggregate energy transfer (k_{ET}) identified already on a 0.4 ps time scale, but also on the slower 4 ps lifetime (Table 11). This kinetic competition limits the electron injection efficiency from the monomer to ca. 30 %. Injection from the monomers and aggregates may also take place on the 25 ps time scale since prominent excited state decay is observed, but a clear radical cation formation signature is missing, possibly due to compensating ESA decay/radical cation formation. Based on these important results, we can clearly confirm that aggregate formation and the related energy transfer from monomer to the aggregates limit the injection efficiency and performance of this type of NIR-DSSC using polymethine cyanine dyes.

Table 11. Average lifetimes characterizing the main photophysical processes for ***VG20-C₁₆*** *on TiO_2 and ZrO_2 DSSCs obtained from femtosecond TAS studies.*

VG20-C_{16} DSSC	**τ_1 (ps)**	**τ_2 (ps)**	**τ_3 (ps)**	**τ_4 (ns)**
TiO_2 + 50mM CDCA	0.4	4.3	25	100
ZrO_2 + 50mM CDCA	1.7	22	200	100

3.5. Conclusions

In this work, a family of NIR-selective polymethine cyanine dyes coded **VG20-C$_x$** was developed. The main attribute of **VG20-C$_x$** is its strong and sharp S_0-S_1 transition in the near-infrared region (λ = 832 nm) and a minimized S_0-S_n contribution in the far blue where the human retina is poorly sensitive. By bringing the NIR-selective dye-sensitized solar cell transmittance in the maximum region of the photopic response, we herein demonstrated a never reached level of aesthetic performances for DSSC technology with an AVT value of 76 %, a CRI value of 93.4, and CCT of 4297.5 K when associated with I_3^-/I^--based electrolyte. The dominant wavelength was determined to be 573 nm, associated with a yellowish-orange coloration and a color saturation of 31%. In the same conditions but removing the contribution of the I_3^-/I^--based electrolyte, the color saturation calculated is 16%, highlighting the importance of the electrolyte in determining the final coloration of our NIR-DSSC. Moreover, the formation of aggregation was determined to be a limitation for both performances and aesthetics.

After carefully optimizing the dye structure and device components, we demonstrated a PCE as high as 3.1 % under A.M.1.5G conditions. As a result of the absorber bandgap narrowing, we revealed that the electron injection process falls in direct kinetic competition with non-productive monomer-to-aggregate energy transfer, thus limiting the device performance when associated with this type of polymethine cyanine dyes.[126,180] Nevertheless, in this chapter, we presented NIR-DSSC from a first proof-of-concept to an efficient device with a high level of transparency. Based on this first work with cyanine dyes, we direct the next steps developing NIR-DSSC towards achieving higher power conversion efficiencies by avoiding the harmful aggregation formation. Moreover, we estimated AVT values greater than 80 % by developing more transparent redox mediators and by abating molecular aggregation in the SAM.

Chapter 4

Chapter 4. A new approach for efficient NIR light conversion with symmetrical pyrrolopyrrole cyanine dyes

Pyrrolopyrrole cyanine (PPcy) dyes are derivatives prepared from the synthetic pigment diketopyrrolopyrrole (DPP), with the latter exhibiting many attractive properties, such as high resistance to heat and light.[181] Moreover, the easy structural modifications of DPP by chemical means, along with their remarkable electro-optical properties, pave the way for applications in the field of organic electronics, such as organic field-effect transistors (OFET),[182] light-emitting diodes (LED),[183] and organic photovoltaics (OPV). [184,185]

A relatively few examples of PPcys synthesis are described in the literature. Their uses mainly concern biological applications such as imaging,[186] photoacoustics,[187], and pH indicators.[188] In photovoltaic devices, PPcy has been integrated as an electron donor molecule in OPV systems. **PPcy1** and **PPcy2** shown in Figure 52 were combined with the fullerene acceptor C_{60}, reaching 0.38% and 0.53 % power conversion efficiencies, respectively.[189] Although these PCEs are relatively modest, this study comprises the first application of PPcys for photovoltaic applications.

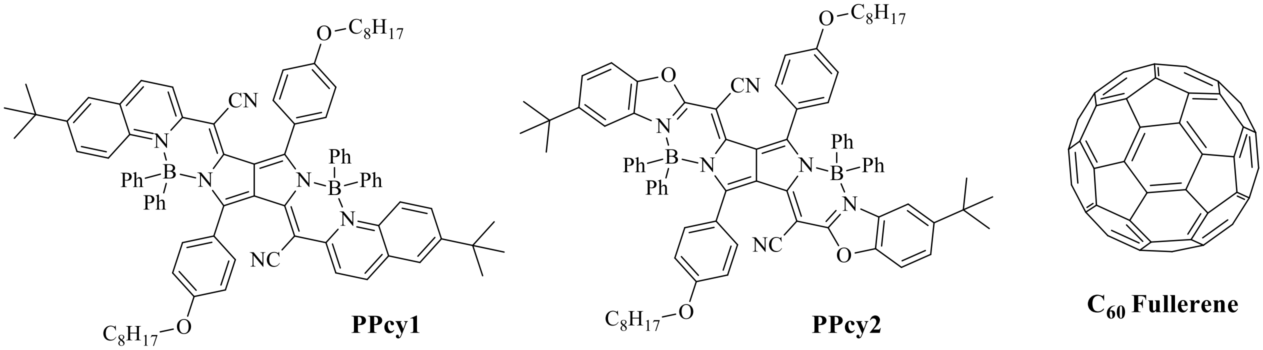

PPcy1

PPcy2

C_{60} Fullerene

Figure 52. Structures of pyrrolopyrrole cyanines used as electron donors in combination with C_{60} fullerene in OPV systems.

Photosensitizers possessing the DPP skeleton have been developed for n and p-type DSSCs achieving good power conversion efficiencies.[190–195] Zumbusch et al. showed that PPcys dyes exhibit a fine and very intense absorption band ($\varepsilon > 150000$ $M^{-1}.cm^{-1}$) between 750 and 900 nm. They also have excellent stability under irradiation and are characterized by remarkable photoluminescence quantum yields, ranging between 0.4 and 0.6, with emission lifetimes of several nanoseconds.[196] These properties make PPcy dyes a promising family for NIR light conversion in DSSC.

In this chapter, we present a new series of dyes from the PPcy family and their integration into DSSC devices. The motivation behind synthesizing this new series of dyes for NIR light conversion is discussed based on computational, electrochemical, and optical characterization. Detailed optimization of the photovoltaic performances is given, comparing the different structures and their roles in achieving the best performances. Finally, ultrafast spectroscopy measurements using fluorescence up-conversion and transient absorption spectroscopy techniques are applied to compare the most promising PPcy dye to the cyanine dye **VG20-C_{16}.**

In the previous chapter, we revealed that for **VG20-C_{16}** dye, the electron injection is in kinetic competition with a non-productive monomer-to-aggregate energy transfer, limiting the device performance. As such, minimizing aggregation was the first obstacle to tackle by dye engineering. With this aim, we selected the pyrrolopyrrole cyanine (PPcy) family targeting two main goals: adding bulky side groups instead of the linear ones as in **VG20** dye, which will result in less aggregation, and providing a better-pushed electron distribution towards the anchoring groups to render better injection rate.

4.1. Computational study of PPcy dyes

The general structure of PPcy dyes is presented in Figure 53, highlighting the different possible chemical modifications that can be applied to improve the dye for the targeted applications. For instance, the work of Fisher et al. showed that the nature of the aromatic ring **1** generates a modification in the spectroscopic properties and that it is possible to substitute the boron on position **3** with fluorine or phenyl.[196] The introduction of phenyl units leads to a bathochromic shift in wavelength and an increase in the molar extinction coefficient.[197] This shift is mainly related to the electron-donor nature of the phenyl group compared to the fluorine atoms, which are highly electron acceptors. The nature of the hindered units at position **2** placed on the pyrrolopyrrole cyanine core also plays an essential role in providing sufficient solubility of the PPcy molecules. Moreover, substituting an electro-deficient group, such as pyridine, by an electron-rich unit such as benzothiazole at position **1** results in a bathochromic shift of the absorption band.

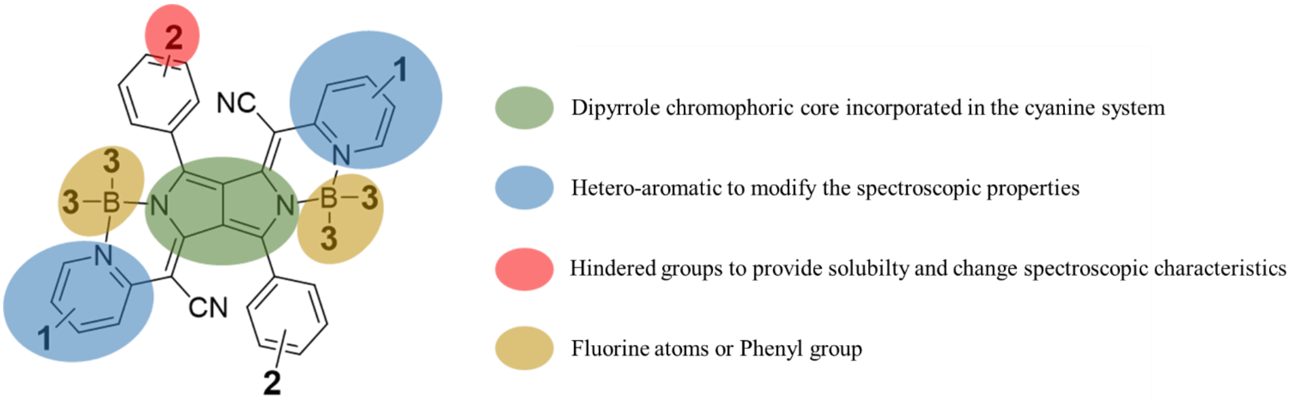

Figure 53. The general structure of pyrrolopyrrole cyanine dyes (PPcy) showing the diversity of possible chemical modifications.

Preliminary molecular targets were studied by the density functional theory (DFT) for the properties of the ground state and the time-dependent density theory (TD-DFT) for the properties of the excited state. The complete study is reported in the annex. Based on this study, our collaborators in the ANR “VISION-NIR” selected the most promising molecules to synthesize. This work is part of the Ph.D. study of Thibaut Baron, under the supervision of Dr. F. Odobel and Dr. Y. Pellegrin, University of Nantes. Prof. D. Jacquemin carried out the computational work.

The computational study on different PPcy structures provides us with important guidelines. The electron spin densities of the HOMO orbitals were found to mainly populate the pyrrolopyrrole cyanine core and slightly the level of the boron vicinity. For the LUMO levels, the electronic densities are also mainly located in the cyanine backbone with a higher density on the nitrogen atom of the pyridine ring. A short-range delocalization of electron densities is highlighted towards the end units of the molecule, even when a π-conjugated linker is introduced. In order to favor the electron injection process when chemisorbed upon TiO_2 surface, the anchoring group is placed directly on the pyridine ring without incorporating a π-conjugated linker. An enrichment of electron density is observed for the LUMO orbitals when the anchoring group is positioned in para of the nitrogen atom.

Following these computational results, two PPcy sensitizers, coded **TB144** and **TB207**, were synthesized and studied. The structures of these novel dyes are presented in Figure 54. These two symmetrical dyes have the carboxylic acid functions positioned in the para position of the nitrogen atom and differ in the nature of the groups on the boron atom, with fluorine for **TB144** and phenyls for **TB207**. The calculations predict that both **TB144** and **TB207** dyes have a sufficiently negative HOMO to be regenerated by I_3^-/I^- (E = +0.35 V vs. NHE) and a LUMO slightly higher than the energy level of the TiO_2 conduction band (CB_{TiO2} = -0.45 V vs. NHE).

As observed from Figure 54, the spin densities on the LUMO orbitals appear to be sufficiently intense on the carboxylic acid functions ensuring an effective charge injection process. The HOMO is localized on the core of the dye, whereas the LUMO is slightly more extended, showing contributions going up to the carboxylic anchoring groups. The DFT calculations suggest that the HOMO level of **TB207** located at E = -6.32 eV vs. vac., is upshifted by 0.29 eV compared to **TB144** (E_{HOMO} = -6.61 eV vs. vac.) as a result of the replacement of the fluorine atoms (**TB144**) by the phenyl groups (**TB207**). The LUMO level is also upshifted by 0.20 eV for **TB207** (E_{LUMO} = -2.87 eV). Consequently, it is calculated that the absorption maximum is 633 nm for **TB144,** and the latter is red-shited to 671 nm for **TB207** dye (Table 12).

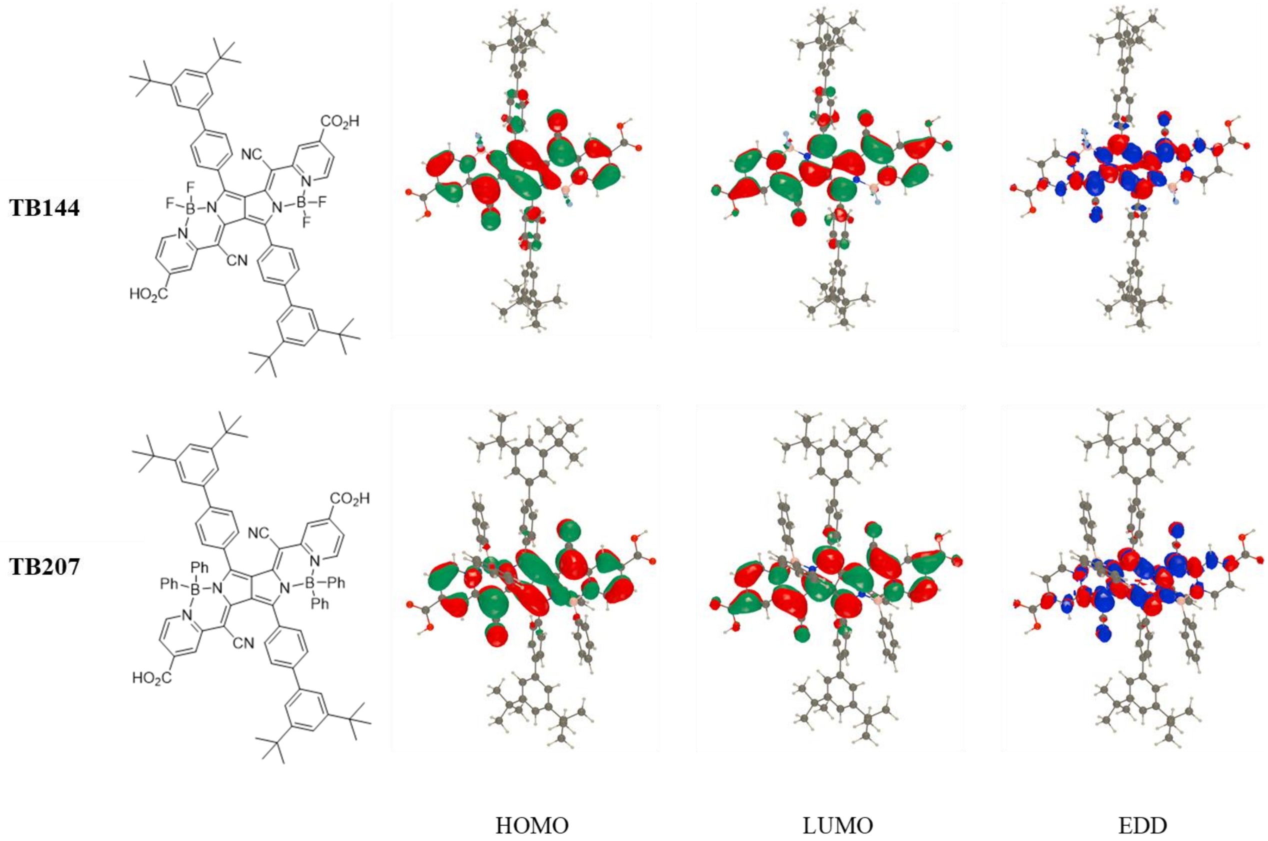

*Figure 54. From left to right: Structure, HOMO frontier orbitals, LUMO frontier orbitals, and electron density difference (EDD) (S_0-S_1) representation for **TB144** (top) and **TB207** (bottom) dyes. On the EDD, the blue and red regions represent regions of decrease and increase of electronic density upon excitation, respectively.*

*Table 12. Maximum absorption wavelength, nature of the electronic transition, and the HOMO and LUMO levels calculated for the PPcy dyes **TB144** and **TB207** by DFT and TD-DFT computational analyses.*

	Transition	**λ_{max} (nm)**	**HOMO (eV)**	**LUMO (eV)**
TB144	HOMO → LUMO	633	-6.61	-3.07
TB207	HOMO → LUMO	671	-6.32	-2.87

Although DFT calculations are very precise in predicting absorption shift, it is less precise in predicting absolute values. Comparing the calculated optical properties of the PPcy dyes **TB144** and **TB207** to our reference NIR dye **VG20-C$_{16}$** and considering the human photopic response, it seemed that a further shift in the NIR may be needed. It has been reported that the substitution of the phenyl groups on the PPcy ring with thienyl units affords a bathochromic shift of absorption.[198] As such, two symmetrical thienyl-PPcy dyes were studied, coded **TB179** and **TB202**. **TB179** and **TB202** are analogous to **TB144** and **TB207**, respectively. The molecular modification lies only in the replacement of the phenyl unit on the PPcy ring by a thienyl group.

Similar to **TB144** and **TB207**, the computational analysis of the thienyl-PPcy dyes shows that the electronic density is concentrated on the PPcy core for both HOMO and LUMO levels, with also a short-range delocalization of the excitons (Figure 55). From these results, the introduction of the thienyl unit into the PPcy ring does not noticeably affect the electronic density and distribution within the molecule. However, the introduction of the thienyl unit stabilizes the energetic of the LUMO level, which may hinder the electron injection process. The calculations predict a bathochromic shift of 20-30 nm for **TB179** and **TB202**. These results are gathered in Table 13.

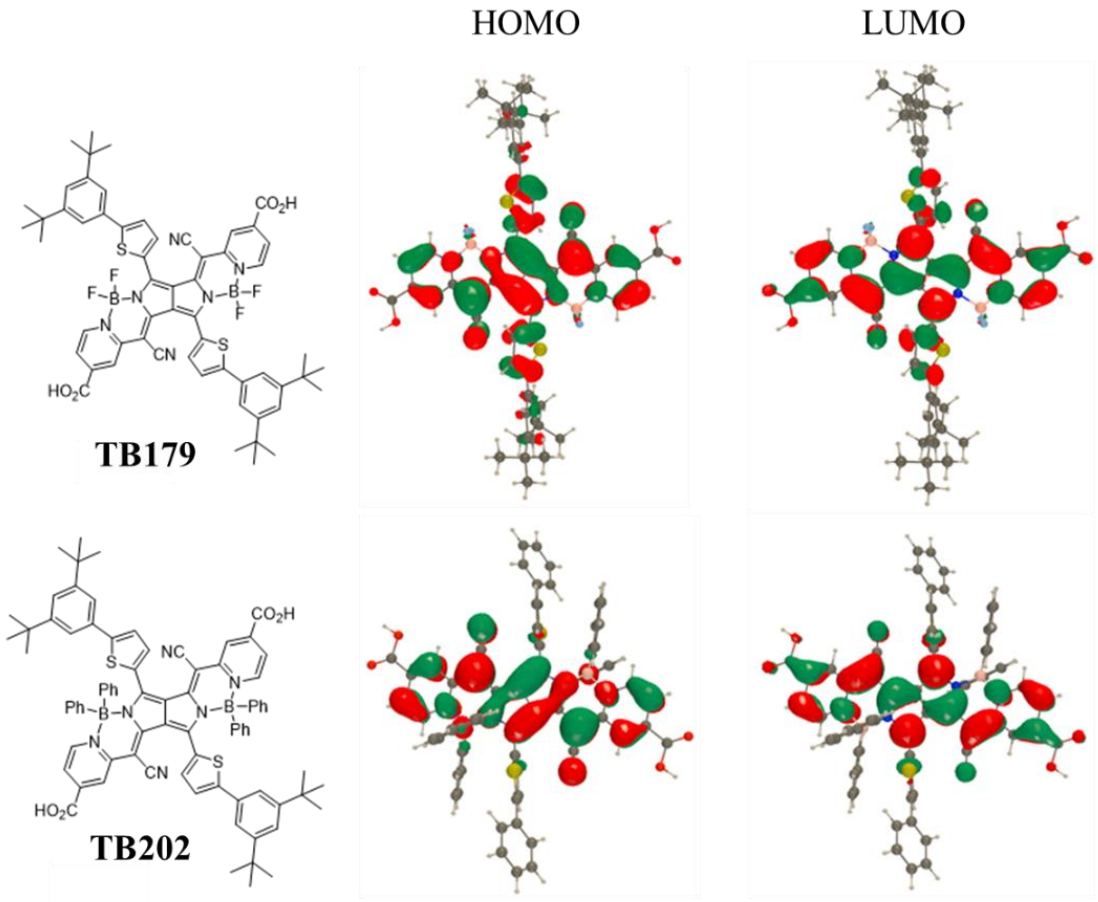

Figure 55. Dye structure and repartition of electronic density in the HOMO and LUMO frontier orbitals for the thienyl-PPcy dyes ***TB179*** *and* ***TB202****.*

Table 13. The maximum absorption wavelength, the transition state, and the HOMO and LUMO levels calculated for the thienyl PPcy dyes ***TB179*** *and* ***TB202*** *by DFT and TD-DFT computational analyses.*

	Transition	λ_{max} (nm)	HOMO (eV)	LUMO (eV)
TB179	HOMO → LUMO	665	-6,61	-3,19
TB202	HOMO → LUMO	690	-6,45	-3,04

4.2. Synthesis and electrochemical properties of PPcy and thienyl-PPcy dyes

The synthesis procedures of **TB144** and **TB207** dyes are summarized in Scheme 3. From a synthetic point of view, **TB207** dye can be easily produced from an intermediate resulting from the synthesis of **TB144**. The pyrrole and pyridine units of the intermediate after step **I** were complexed by boron using either BF_3-OEt_2 (step **II**) or $B(Ph)_2Cl$ (step **III**) before saponification of the ester groups in mild basic conditions to lead to the desired dyes **TB144** and **TB207**.

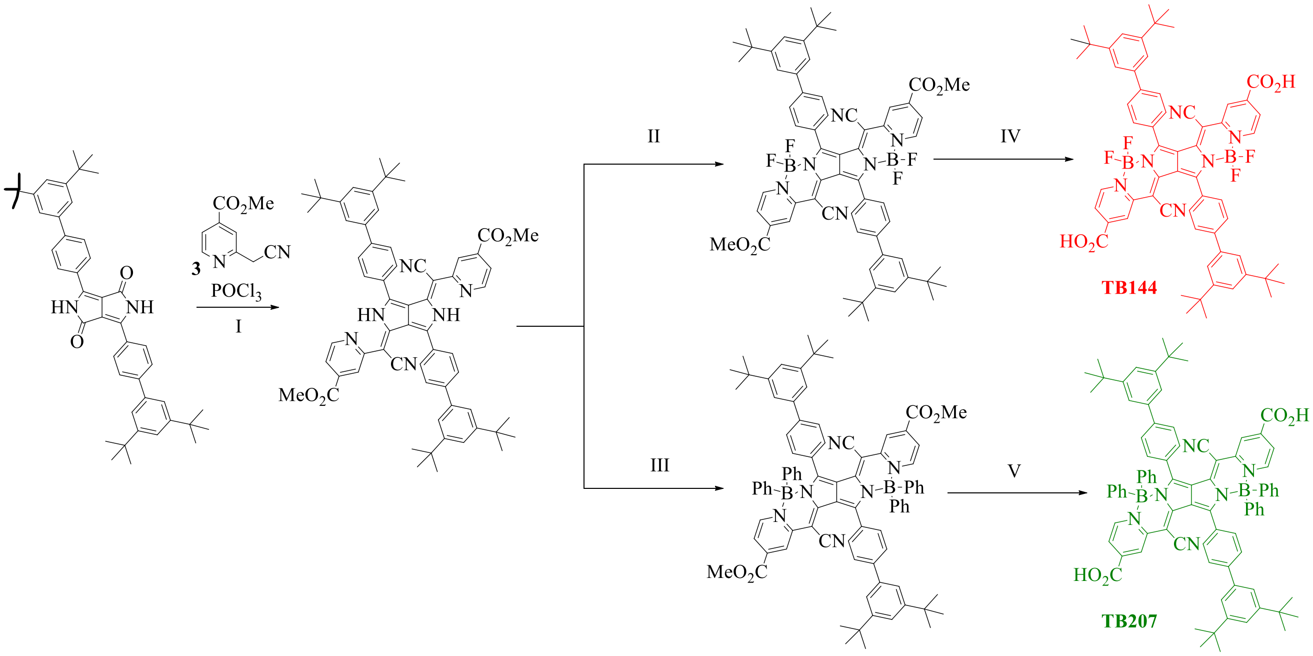

Scheme 3. Synthetic procedure of the PPcy dyes ***TB144*** *and* ***TB207*** *I) $POCl_3$, 3, Toluene, 130°C, 2 h, 68%; II) BF_3-OEt_2, DIPEA, CH_2Cl_2, 45°C, 30min, 100%; III) LiOH, THF/H_2O, RT, 2h, 72%; IV) $B(Ph)_2Cl$, DIPEA, CH_2Cl_2, 45°C, 30min, 41%; V) LiOH, THF/H_2O, RT, 2h, 81%.*

To synthesize **TB179** and **TB202**, the complexation of molecule **A** shown in Scheme 4 with boron trifluoride etherate is carried out. The hydrolysis of the products obtained under two different conditions (indicated in the scheme) yields to the formation of **TB179** and **TB202** dyes.

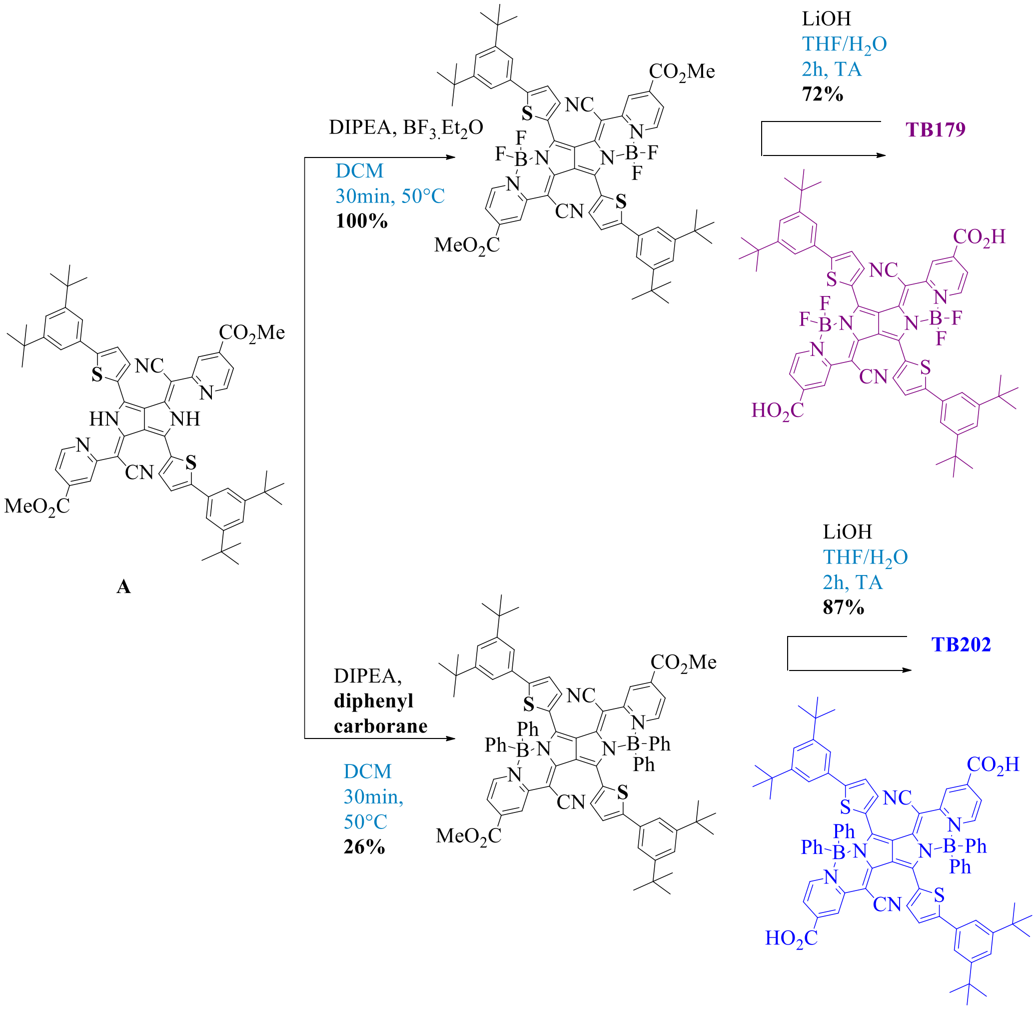

*Scheme 4. Starting from molecule A: synthesis of the thienyl- PPcy dyes **TB179** and **TB202**.*

The redox potentials of the PPcy and thienyl-PPcy dyes were determined by cyclic voltammetry (CV) and reported in Figure 56. For this experiment, platinum was used as the working electrode, a stainless-steel wire as the counter electrode, and the reference electrode was a saturated calomel electrode (SCE). Tetrabutylammonium hexafluorophosphate (0.1 mol/L) solution was used as a supporting electrolyte in dimethylformamide.

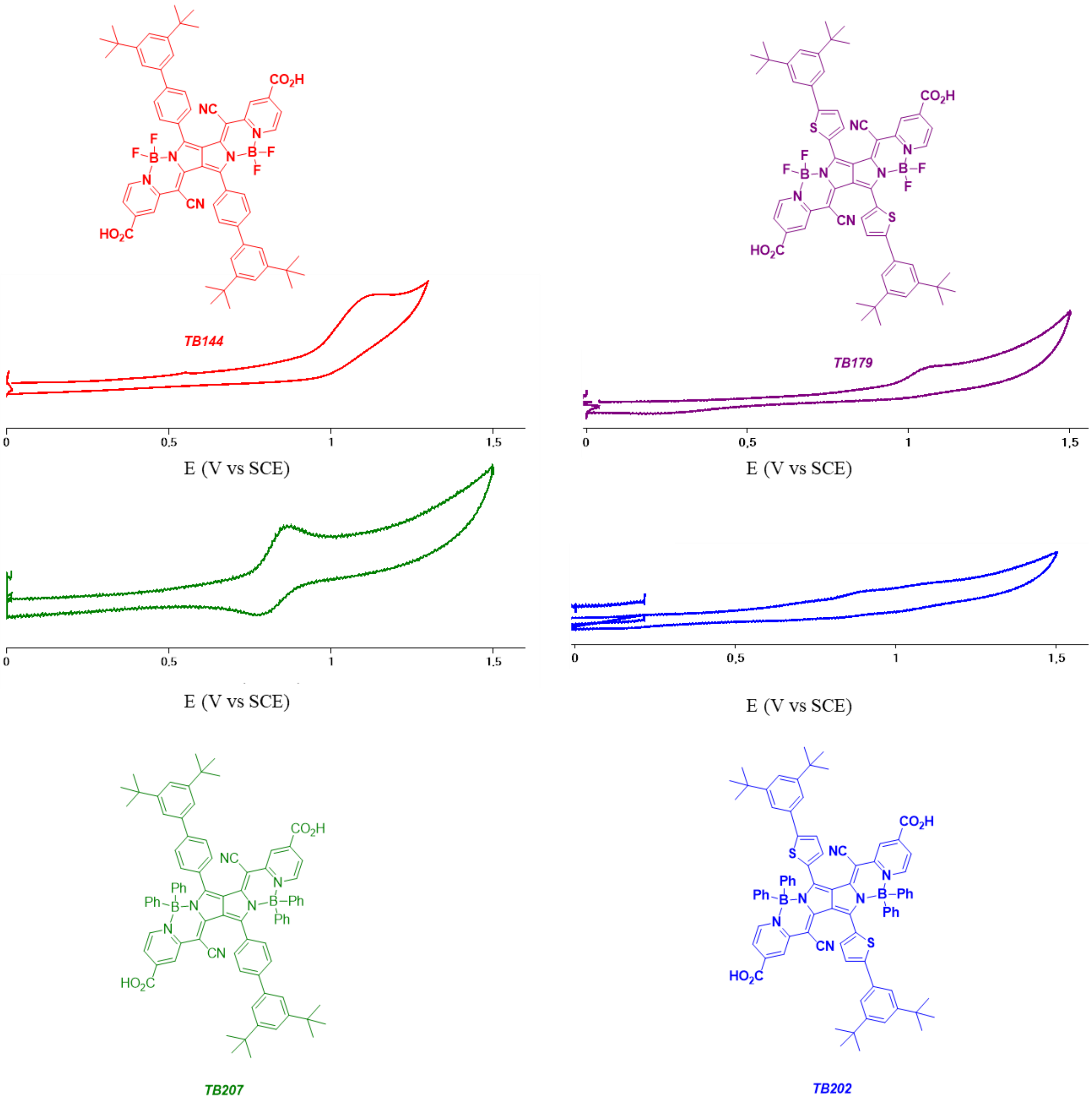

Figure 56. Cyclic Voltamperogram of ***TB114*** *(red),* ***TB179*** *(purple),* ***TB207*** *(green) and* ***TB202*** *(blue) recorded in DMF solution with TBAPF$_6$ supporting salt (0.1 mol/L) and at a scan rate of 100 mV/s. The potentials are referenced to SCE.*

TB207 exhibits reversible one-electron oxidation at 0.63 V vs. SCE, corresponding to the formation of the radical cation located on the pyrrolopyrrole cyanine unit. The oxidation potential of **TB144** is anodically shifted compared to that of **TB207**, confirming the electron-withdrawing character of fluorine on boron also in good agreement with the DFT calculations. The thienyl-PPcy **TB179** exhibits irreversible oxidation at 1.10 V vs. SCE. The substitution of fluorine atoms by phenyls decreases the oxidation potential as **TB202** reversibly oxidizes at 0.84 V vs. SCE.

Therefore, we can conclude experimentally that the complexation of boron by fluorine or phenyl units mainly modifies the oxidation strength of the dyes. Moreover, modifications are observed on the electrochemical properties when thienyls substitute the PPcy core compared to phenyls. As a result, the oxidation potential in the excited state (S^+/S^*) of thienyl-PPcy dyes is less negative. **TB207** oxidizes at -0.80 V vs. SCE in the excited state against -0.72 V vs. SCE for **TB202**. As such, thienyl-PPcy dyes are weaker electron donor in the excited state than classical PPcys, and **TB207** is the most promising for efficient injection. The energy level of both the HOMO and LUMO determined experimentally are summarized in Table 14 and Scheme 5.

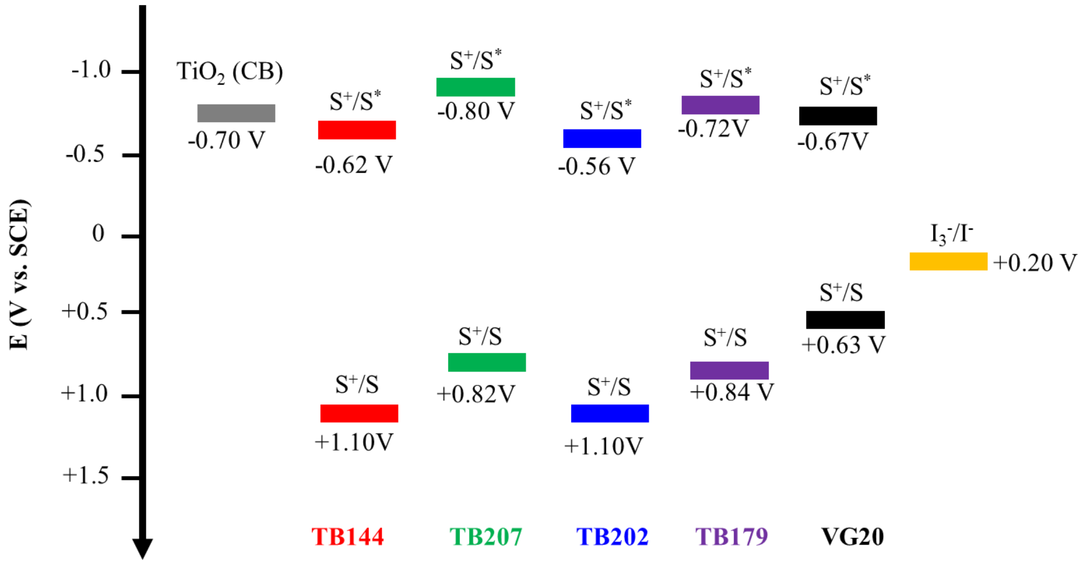

*Scheme 5. Energetic diagram placing the HOMO and LUMO energy levels of PPcy dyes compared to **VG20** with respect to the conduction band level in TiO$_2$ and the redox potential of I_3^-/I^- redox couple. HOMO and LUMO were calculated such as : HOMO = - (E_{ox} - E_{Fe} + 4,8) and LUMO = HOMO + E_{00} (E_{00} is the optical band gap).*

Table 14. Redox potential of the HOMO and LUMO levels determined by cyclic voltammetry of the PPcy dyes vs.SCE.

Dye	HOMO (V vs. SCE)	LUMO (V vs. SCE)
TB144	1.10	-0.62
TB207	0.82	-0.80
TB179	0.84	-0.72
TB202	1.10	-0.56

4.3. Characterization of PPcy and thienyl-PPcy in solution

The absorption spectra of the PPcy dyes **TB144** and **TB207** and the thienyl-PPcy dyes **TB179** and **TB202** in solution are shown in Figure 57. All the dye solutions were prepared in a solvent mixture of chloroform and ethanol ($CHCl_3$/ethanol 1/9 v/v). These dyes exhibit the classical absorption fingerprint of PPcy derivatives, with a sharp, intense π-π transition. The spectra show a weaker vibronic band at a lower wavelength.

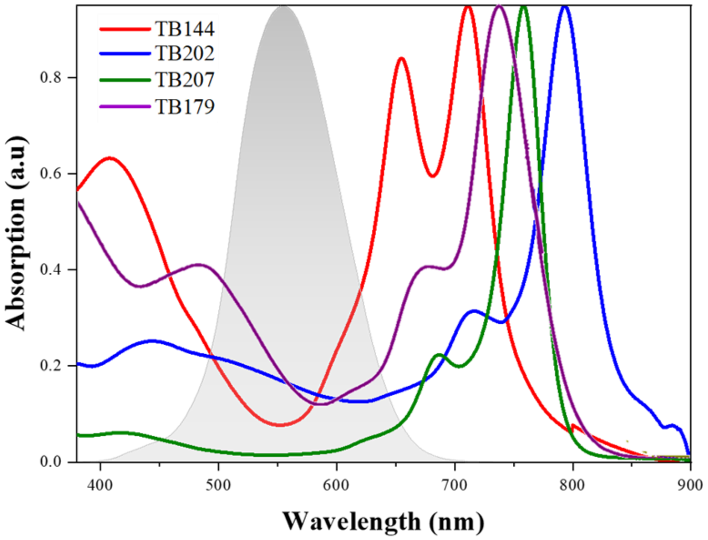

*Figure 57. Normalized UV-vis absorption spectra of the PPcy and thienyl-PPcy dyes **TB144** (red), **TB207** (green), **TB179** (purple), and **TB202** (blue) in $CHCl_3$/ethanol solvent mixture (1/9 ratio v/v). The shaded grey area represents the photopic response.*

The PPcy **TB144** and **TB207** dyes have an absorption maximum at 712 nm and 760 nm, respectively. Although the DFT calculation is not precise enough to determine an absolute good value, as aforementioned, the experimental red-shift by 48 nm falls in very good agreement with the calculations. The shift is attributed to the reduced electron density on the boron induced by fluorine, which stabilizes the HOMO level energy for **TB144**. As expected, a bathochromic shift of about 30nm is observed for **TB179** and **TB202** compared to **TB144** and **TB207**. **TB179** is red-shifted to its analogous **TB144** with maximum absorption at 748 nm, while **TB202** exhibits the most red-shifted absorption to 796 nm. The broad absorption between 400 and 700 nm observed for **TB179** and **TB202** dyes is potentially related to the addition of thienyl groups in the structure and directly influences the color of the final compounds. As a result, the dyes **TB144** and **TB207** present a green coloration in solution, whereas **TB179** and **TB202** are rather brownish. The sought shift of the absorption into the NIR region objective is thus verified by substituting phenyls with thienyls. However, a decrease in the molar absorption coefficient (ε) is observed for **TB202** and **TB179** compared to **TB207** and **TB144 (**Table 15**)**. It is noteworthy to highlight that the presented dyes show a bathochromic shift compared to PPcy dyes reported in the literature, which are without anchoring groups.[197] This shift stems from the electron-withdrawing character of the carboxylic acid moieties that tend to stabilize the LUMO levels. A promising feature of **TB207** is the negligible absorption in the visible range (400-650 nm). For **TB144**, **TB179**, and **TB202**, we still observe residual absorption in the range of the photopic response, thus potentially penalizing the aesthetic of the final device.

The effect of the structural changes on the photoluminescence properties of the presented PPcy dyes has been herein investigated by using steady-state fluorescence spectroscopy and time-resolved correlated single photon counting (TCSPC). The 2D excitation/emission plots of the fluorescence of **TB144**, **TB207**, **TB179**, and **TB202** are reported in Figure 58. All of the dyes exhibit an intense emission in the NIR region, which corresponds to the radiative deactivation of the S_0-S_1 transition. This PL is about one order of magnitude more intense for **TB202** and **TB207** dyes, in which the boron atom holds the phenyl group, than the fluorine-derivatives **TB144** and **TB179**. We attribute this to the quenching caused by the formation of aggregates. These results stand as evidence of the role of the phenyl group on the boron atom in de-aggregating the dye molecules. Another feature observed from the excitation/emission maps is the additional bands in the visible region (400-700 nm) for **TB179** and **TB202** dyes. These results also confirm that the substitution of phenyl by thienyl units on the PPcy ring modifies the excitation/emission properties significantly (Figure 57). All the experimental optical properties are summarized in Table 15.

Table 15. Spectroscopic parameters of the PPcy and thienyl-PPcy dyes

	λ_{abs}^{max} (nm)	$\lambda_{abs}^{shoulder}$	ε (M^{-1} cm^{-1})	λ_{em}^{max} (nm)
TB144	712	655	-	730
TB207	758	685	$1.38\ 10^5$	782
TB179	740	665	-	772
TB202	793	715	$4.27\ 10^4$	815

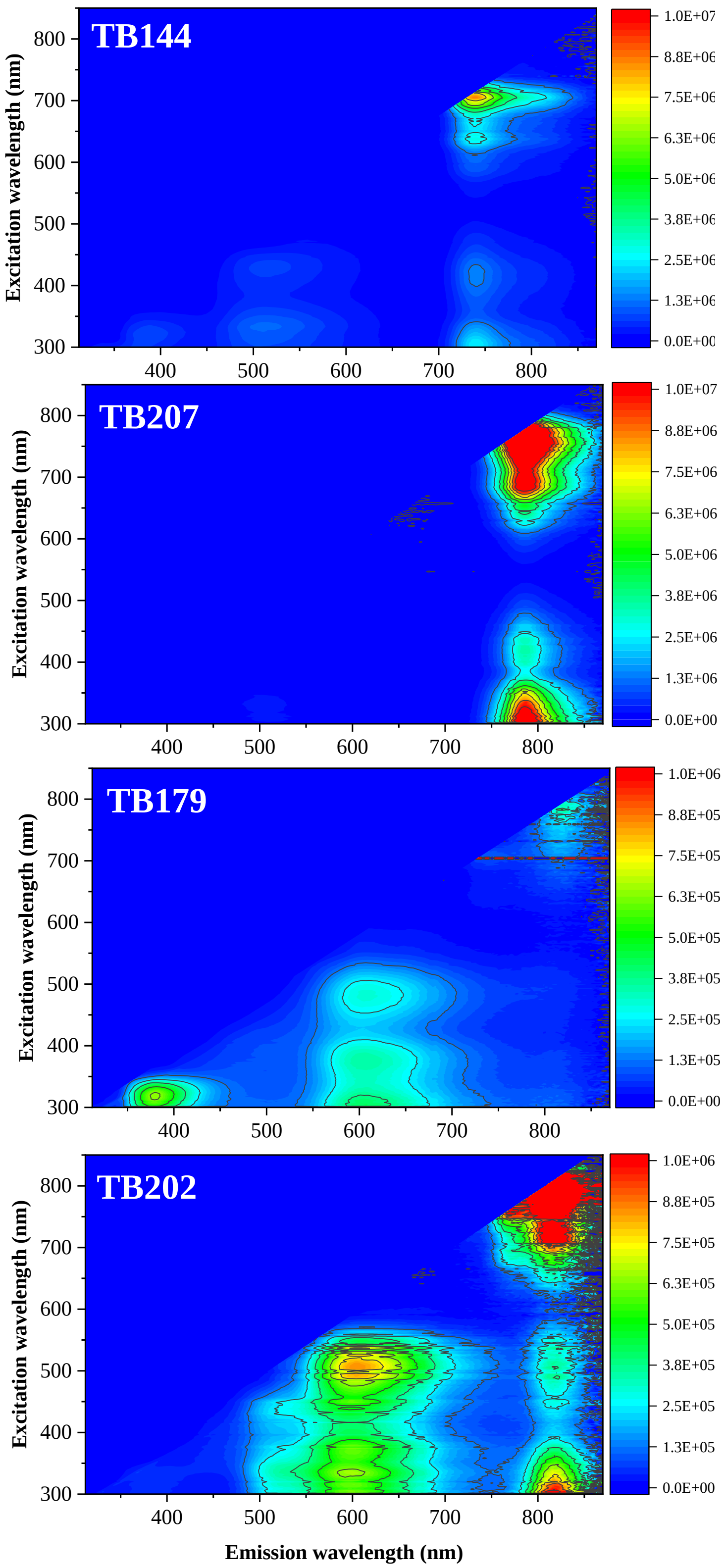

*Figure 58. 2D contour plot of the excitation/emission maps of **TB144**, **TB207**, **TB179**, and **TB202** in $CHCl_3$/ethanol (1/9 v/v) solution.*

The time-resolved PL decays of the PPcy dyes in a solvent mixture of $CHCl_3$/ethanol (1/9 *v*/*v*) are reported in Figure 59.a. The studied dye solutions are free of any de-aggregating agent such as CDCA, with an OD lower than 0.8 at the excitation wavelength (640 nm). The new dyes series of DPP derivatives possess two timescales of the excited-state lifetime depending on the structure: the PPcys dyes **TB144** and **TB207** show a remarkable long-lived excited state with a lifetime of 3.74 and 3.11 ns, whereas the thienyl-PPcy **TB179** and **TB202** dyes show a shorter-lived excited state within 0.74 and 0.88 ns, respectively. These results show that the substitution of the phenyls on the PPcy ring with thienyl units shortens the excited state lifetime in solution, which can contribute to lower injection efficiency for the thienyl-PPcy dyes. Our reference NIR dye for the moment, **VG20-C$_{16}$**, shows a short lifetime of the excited state of 0.39 ns in solution, and its PL decay is compared to that of **TB207** in Figure 59.b.

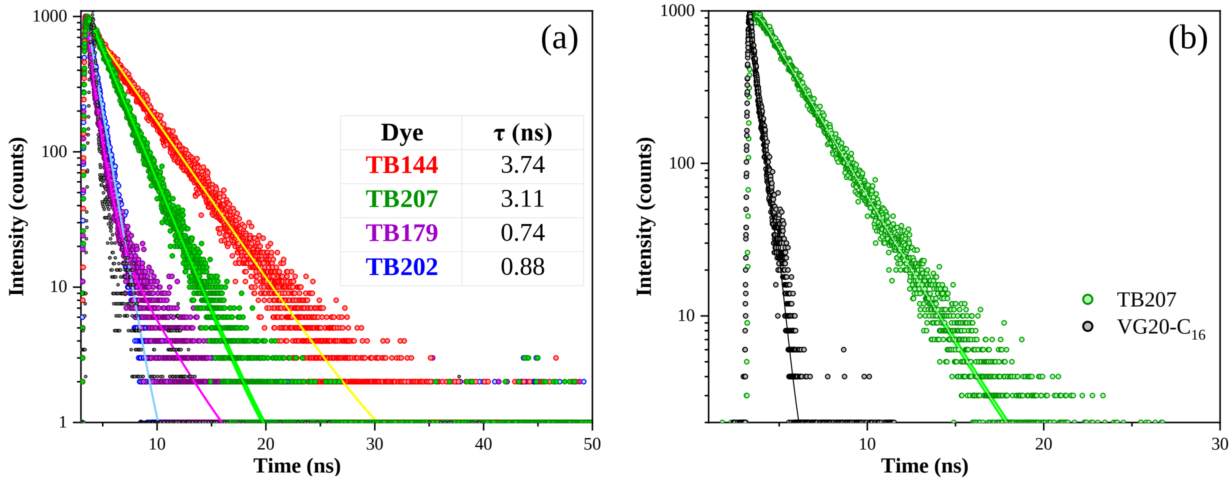

Figure 59. Comparison of PL decays measured by TCSPC for (a) PPcy and thienyl-PPcy dyes in $CHCl_3$/ethanol (1/9 v/v) solvent mixture. The black scatter represents the IRF. (b) ***VG20-C$_{16}$*** *cyanine dye (in black) and* ***TB207*** *PPcy dye (in green).*

4.4. Optimization of the photovoltaic performance of PPcy and thienyl-PPcy based NIR-DSSC

The acquired knowledge from **VG20-C$_{16}$** cyanine dye clarifies that hampering aggregation is our starting point for optimizing this new family of dyes. For that, we use the conventional chenodeoxycholic acid (CDCA) as a de-aggregating agent added to the dye solution. The dye concentration is fixed at 0.1 mmol/L for all dyes in a solvent mixture of $CHCl_3$/ethanol (1/9 ratio v/v). Taking into consideration the studied sensitizers' potentials, we kept the electrolyte composition as the one optimized for the cyanine **VG20-C16** dye (1 mol/L DMII, 1 mol/L LiTFSI, and 30 mmol/L I_2 in a solvent mixture of 85/15 of acetonitrile/valeronitrile).

The PPcy dye **TB144** and the thienyl-PPcy dyes **TB179** and **TB202** measure very low PCE with CDCA free sensitization (Figure 60). On the other hand, the PPcy dye **TB207** achieved a remarkable 3.1% PCE without introducing CDCA in the dyeing solution. This high performance stems from the noteworthy high short-circuit current density (J_{sc}) with a value of 15.7 mA/cm². All the photovoltaic parameters and PCE measured for de-aggregating agent-free sensitization conditions are gathered in Table 16.

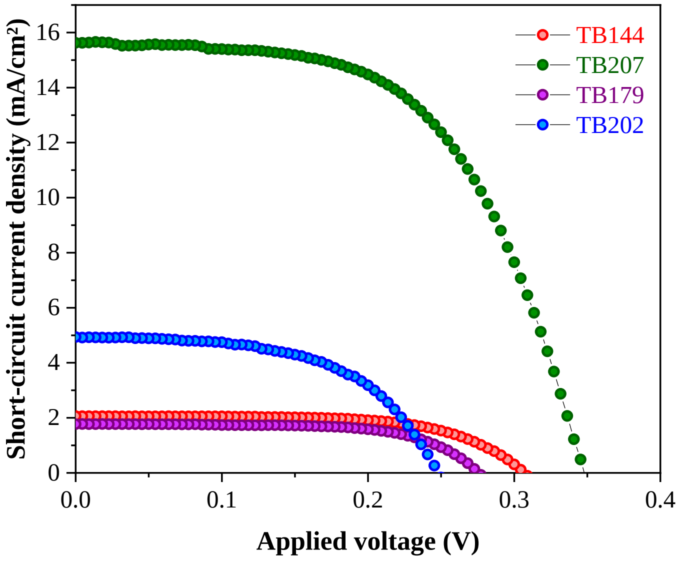

Figure 60. Evolution of J-V curves as a function of the dyes with no de-aggregating agent in the sensitizing solution.

*Table 16. Photovoltaic parameters of the different PPcy (**TB144** and **TB207**) and thienyl-PPcy (**TB179** and **TB202**) dyes with no de-aggregating agent in the sensitizing solution.*

Dye	J_{sc}(mA/cm^2)	V_{oc} (mV)	FF	PCE (%)
TB144	2.1	307	0.63	0.4
TB207	15.6	348	0.57	3.1
TB179	1.8	276	0.65	0.3
TB202	4.9	248	0.55	0.7

Adding 1 mmol/L of CDCA in the **TB207** dye solution allows enhancing the V_{oc} to 367 mV while measuring a slight drop in J_{sc} (14.9 mA/cm²), resulting in 3.2% PCE. The increment of CDCA concentration to 5 mmol/L allows achieving a PCE maximum of 3.8%, owing to an increase in J_{SC} from 15.6 to 16.5 mA/cm², and a ca.50 mV increase in the open-circuit voltage (V_{oc}) from 348 mV to 394 mV. As presented in the J-V curve evolution as a function of CDCA concentration in Figure 61, a further increase in the CDCA concentration to 10 mmol/L (corresponding to 1/100 ratio) leads to a slight drop in J_{sc} to 14.9 mA/cm². This results in a drop in PCE to 3.2 %. All the values are presented in Table 17. The J_{sc} drop with 10 mmol/L CDCA can be attributed to the competition between the dye and CDCA molecules to adsorb on the TiO_2 surface. As such, the optimized condition for **TB207** is 1/50 ratio by concentration between the dye and CDCA.

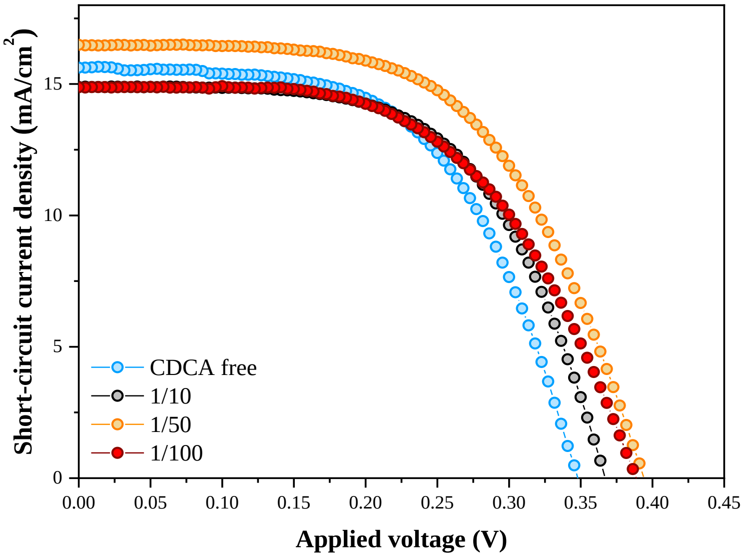

Figure 61. J-V curve evolution for TB207-based DSSC as a function of CDCA concentration

Table 17. Photovoltaic parameters of TB207-based DSSC with different CDCA concentration.

[CDCA] (mmol/L)	J_{SC} (mA/cm^2)	V_{OC} (mV)	FF	PCE (%)
0	15.6	348	0.57	3.1
1	14.9	367	0.59	3.2
5	16.5	394	0.58	3.8
10	14.9	388	0.56	3.2

By contrast to this latter, **TB144**, **TB179,** and **TB202** dyes require a 1/500 ratio of dye/CDCA in order to achieve the best performances, namely 1.2%, 0.6%, and 1.5% PCE, thus indicating that these structures are prone to form more harmful aggregation in the self-assembled monolayer. One principle limitation of these dyes is the low short-circuit current density lying between 4 to 7 mA/cm². The evolution of the (J-V) curves and the different photovoltaic parameters of the different dyes in their optimized CDCA conditions are presented in Figure 62 and Table 18.

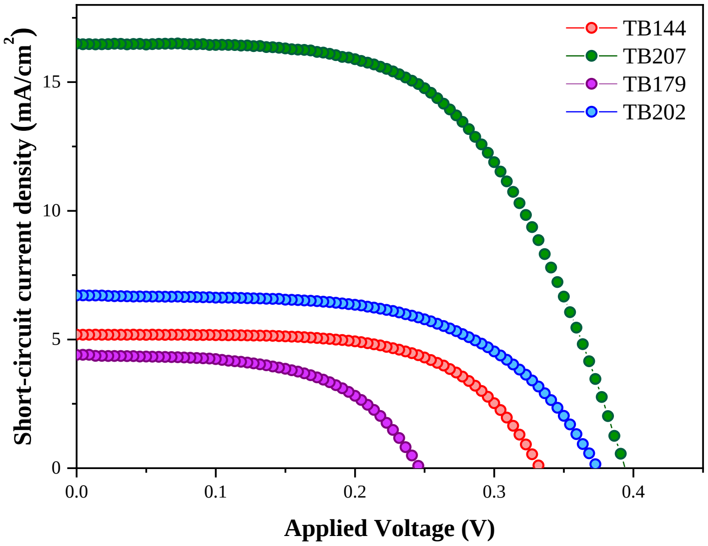

Figure 62. Evolution of J-V curves at the optimized CDCA concentration of the different PPcy and thienyl-PPcy dyes: ***TB144*** *(red),* ***TB207*** *(green),* ***TB179*** *(purple), and* ***TB202*** *(blue).*

*Table 18. Photovoltaic parameters of the different PPcy (**TB144** and **TB207**) and thienyl-PPcy (**TB179** and **TB202**) dyes with optimized CDCA concentration conditions.*

Dye	CDCA (mmol/L)	J_{sc} (mA/cm^2)	V_{oc} (mV)	FF	PCE (%)
TB144	50	5.2	333	0.62	1.2
TB207	5	16.5	394	0.58	3.8
TB179	50	4.4	246	0.56	0.6
TB202	50	6.8	367	0.58	1.5

For a more detailed understanding of the structural modification effect on the photovoltaic performances, intensity-modulated photovoltage/photocurrent spectroscopy (IMVS/PS) and dark charge extraction experiments were performed for the PPcy and thienyl-PPcy dyes in their optimized conditions.

The IMVS results presented in Figure 63.a highlight two main outcomes of the dye structural modifications. First, they show that the PPcy dyes **TB144** and **TB207** exhibit a longer electron lifetime than the thienyl-PPcy **TB179** and **TB202**. The second outcome is that the substitution of fluorine (**TB144** and **TB179**) by phenyl (**TB207** and **TB202**) on the boron atom results in a longer electron lifetime. This is attributed to the role played by the bulkier phenyl groups as a barrier between the triiodide in the electrolyte and the injected electron in TiO_2, thus reducing the non-geminate recombination.

The transport time is also affected by the dye structural modification to a lesser extent except for **TB202,** which shows a one-order of magnitude faster transport time (Figure 63.b). These data allow us to evaluate charge collection efficiencies of 59% for **TB179,** 97% for **TB202**, 87% for **TB144**, and 81% for **TB207**.

The trap energies are affected by the structural modifications as observed from the dark charge experiments shown in Figure 63.c. This is attributed to the different dipole moments of the dye on the surface of TiO_2, which gives indirect proof to argue that the dye geometry in the SAM is different depending on the substitution (e.g., the introduction of a bulkier phenyl group to hamper aggregation). The results suggest a trend of a downshift in the surface states upon the substitution of fluorine (**TB144** and **TB179**) with phenyl (**TB202** and **TB207**).

These results are in agreement with the open-circuit photovoltage recorded for these dyes, explaining the V_{oc} measured. For instance, the low V_{oc} value of 246 mV measured in **TB179** devices is a result of the high non-geminate recombination rate, and a downshift in the trap states.

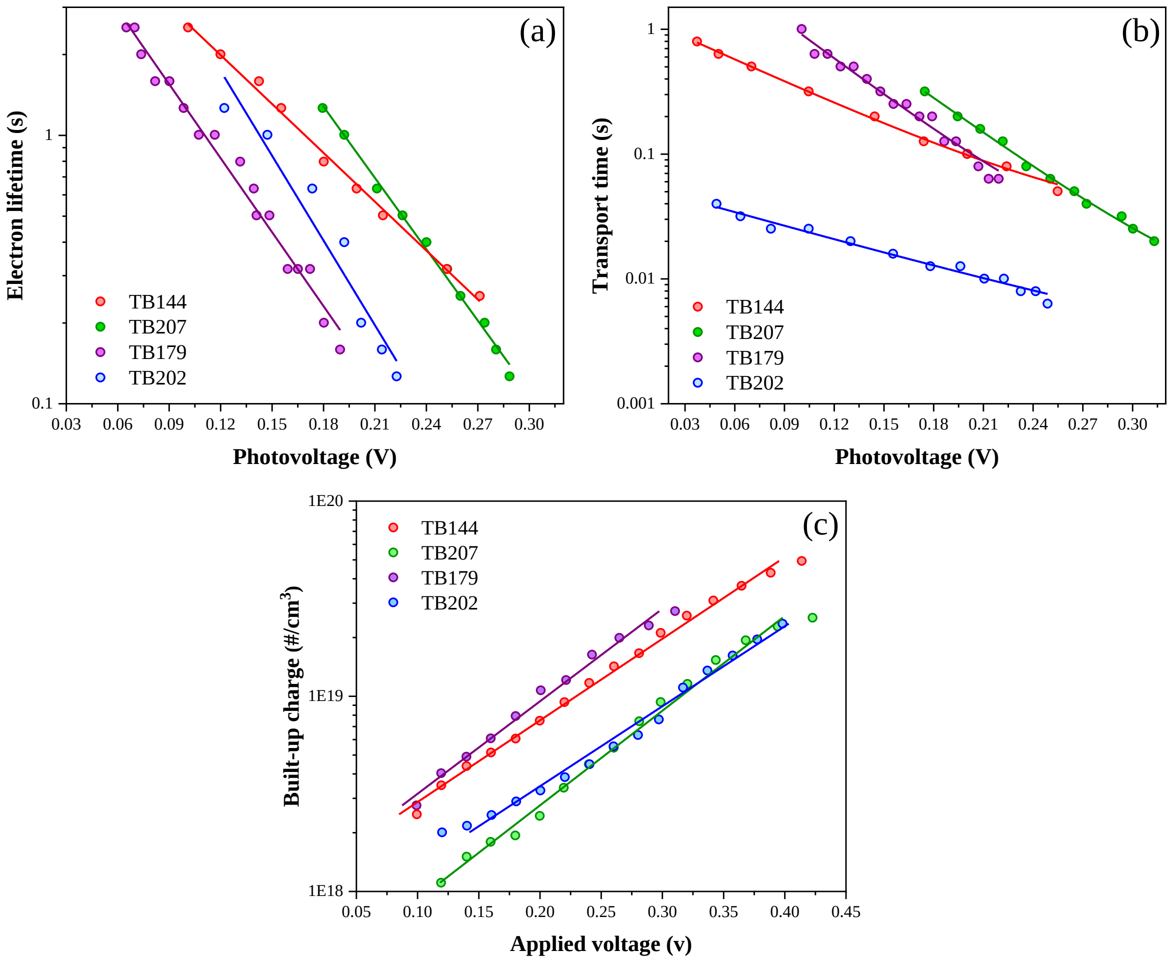

*Figure 63. (**a**) Evolution of (a) electron lifetime deduced from IMVS, (**b**) transport time deduced from IMPS, and (**c**) dark charge extraction measurements on NIR-DSSC based on the PPcy and thienyl-PPcy dyes **TB144** (red), **TB207** (green), **TB179** (purple) and **TB202** (blue).*

4.4.1. Electrochemical approach to enhance the open-circuit photovoltage

Deciphering the limitations of reaching higher PCE values, the open-circuit voltage (V_{oc}) appears to be a primary contributor to our system. The difference between the quasi-Fermi level of TiO_2 photoanode under illumination and the electrolyte's redox potential level is considered the theoretical maximum value of V_{oc}. Moreover, the non-geminate recombination of the electrons in the TiO_2 to the oxidized species in the electrolyte (e.g., I_3^-) is also considered a source of the drop in $V_{oc,}$ resulting systematically in lower PCE. An interhalogen-based binary-redox couple was proposed by the group of Jae-Joon Lee, denoted by (I_3^-, I_2Br^-)/(I^-, Br^-), introducing a novel redox couple with more positive potential than the classical I_3^-/ I^- to boost up the V_{oc} of DSSC.[199]

The electrolyte with interhalogen-based binary redox couples, denoted **B1**, was prepared by mixing 0.04 mol/L of Br_2 solution in acetonitrile with 0.4 mol/L of LiI. When LiI was added into the Br_2 solution, iodine (I_2) and Br^- were formed spontaneously according to equation 1:

$$Br_2 + 2I^- \rightarrow I_2 + 2Br^- \qquad \textit{Eq (1)}$$

Then, I_2 can successively react with both I^- and Br^- to form I_3^- and I_2Br^-, according to the equilibriums represented by equations (2) and (3), respectively.

$$I^- + I_2 \rightleftharpoons I_3^- \qquad \textit{Eq (2)}$$

$$Br^- + I_2 \rightleftharpoons I_2Br^- \qquad \textit{Eq (3)}$$

The reaction of Br^- with I_2 can generate interhalogen anions, such as I_2Br^- and IBr_2^-, of which the concentrations are dependent on the concentration of Br^- in the solution. Generally, IBr_2^- dominates over I_2Br^- only when $[Br^-] > 2$ mmol/L.[199] However, the formation of the I_2Br^- was favored in the present composition since the excess amount of I^- in the solution suppressed the formation of IBr_2^- according to the following equation:

$$I_2Br^- + Br^- \rightleftharpoons IBr_2^- + I^- \qquad \textit{Eq (4)}$$

The above equilibrium relations indicated that I^-, I_3^-, Br^-, and I_2Br^- are major anionic components of **B1**, and the formation of I_2Br^- will induce the net decrease of I_3^-; therefore, the overall equilibrium will shift to the left side of Eq. (2).

Both redox pairs, I_3^-/I^- and $I_2Br^-/(I^-, Br^-)$, coexist in **B1** to form a binary redox system with the standard electrochemical potential for the latter being more positive up to ca. 0.1 V than the former. The Fermi energy level of **B1** was essentially determined from the weighted-average of both redox reactions, denoted by $(I_3^-, I_2Br^-)/(I^-, Br^-)$, and it was very close to the energy level of I_3^-/I^- as described in Scheme 6 since I_3^-/I^- is still a major component of this electrolyte.

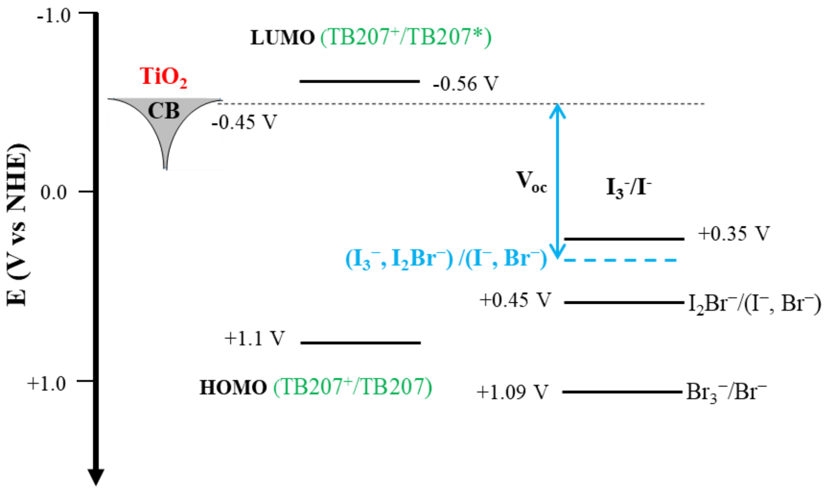

Scheme 6. Energy diagram for the weighted average of the equilibrium of both redox reactions of ***B1*** *electrolyte with binary redox couples (I_3^-, I_2Br^-)/(I^-, Br^-). The HOMO and LUMO levels of* ***TB207*** *and the CB level of TiO_2 are also reported.*

The absorption of the **B1** electrolyte is compared to that of the **EI** one in Figure 64. The binary electrolyte has the same absorption fingerprint as the conventional triiodide/iodide one. The expected absorption peaks for I_2Br^- at 350 and 280 nm were not present clearly because I_3^- dominates over I_2Br^- in this electrolyte composition in agreement with literature.[199] However, we observe for **B1** electrolyte a slight decrease in the 360 nm band corresponding to the absorption of I_3^-. This supports the formation of I_2Br^-.

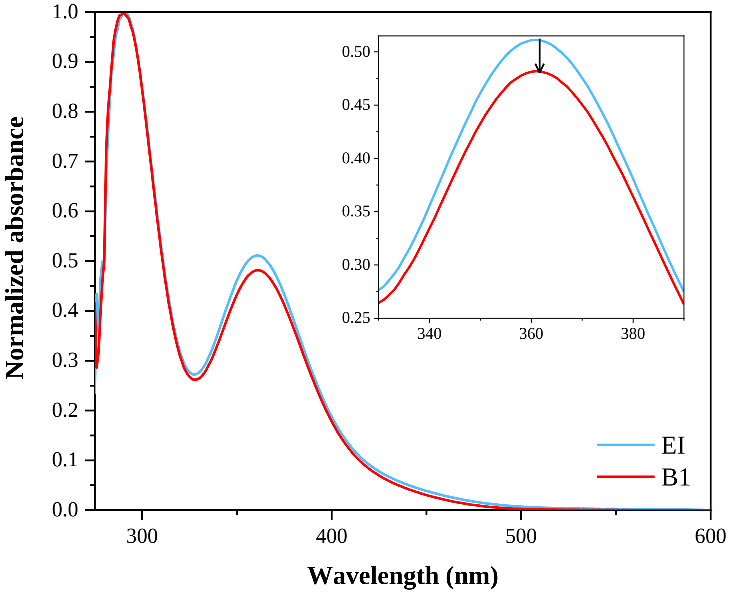

Figure 64. UV-vis absorption spectra of ***EI*** *and* ***B1*** *electrolytes in acetonitrile. The inset shows a magnified view of the spectra highlighting the band attributed to I_3^-absorption.*

Integrating this interhalogen binary-electrolyte with our NIR PPcy dye **TB207**, we achieved an increase of >30 mV in the V_{oc}, reaching 430 mV (Figure 65.a). A decrease in J_{sc} from 16.5 mA/cm² to 15.6 mAcm² is attributed to the lower concentration of Li^+ used in the B1 electrolyte (0.4 mol/L) compared to the EI one (1 mol/L). However, adding a 1 mol/L LiI to 0.04 mol/l Br_2 leads to maintaining the short-circuit current density at 16.4 mA/cm² on the expense of losing the gain expected in the photovoltage (398 mV), with a final PCE of 3.85% similar to EI electrolyte. The slight decrease in J_{sc} can also be associated with the decrease of the electrolyte's ionic conductivity when the concentration of I_2Br^- is increased. For the B1 electrolyte, despite the slight drop in the J_{sc}, and with a 59% FF, a 5% increase in the PCE is achieved, leading to a 4% efficiency of **TB207** based devices, a never reached value for NIR-selective DSSC.

IMVS experiments (Figure 65.b) show that the interhalogen binary electrolyte affects mainly the electron lifetime, as devices with I_3^-/I^- (**EI**) possess a shortened electron lifetime when compared to $(I_3^-, I_2Br^-)/(I^-, Br^-)$ electrolyte (**B1**). This implies that the interhalogen species in the binary electrolyte reduce the non-geminate recombination helping increase V_{oc}, in agreement with the previous studies in the literature.[199,200] The transport time was affected to a less extent, as shown in Figure 65.c, which leads to charge extraction efficiencies of 92 and 81 % for **B1** and **EI** -based devices, respectively. The additional dark charge extraction experiment (Figure 65.d) suggests that the trap energies are not drastically affected by the different electrolytes, which implies almost no change in the surface states below the conduction band of TiO_2 nanoparticles upon the variation of the redox species in the electrolyte, which is in agreement to literature.[199]

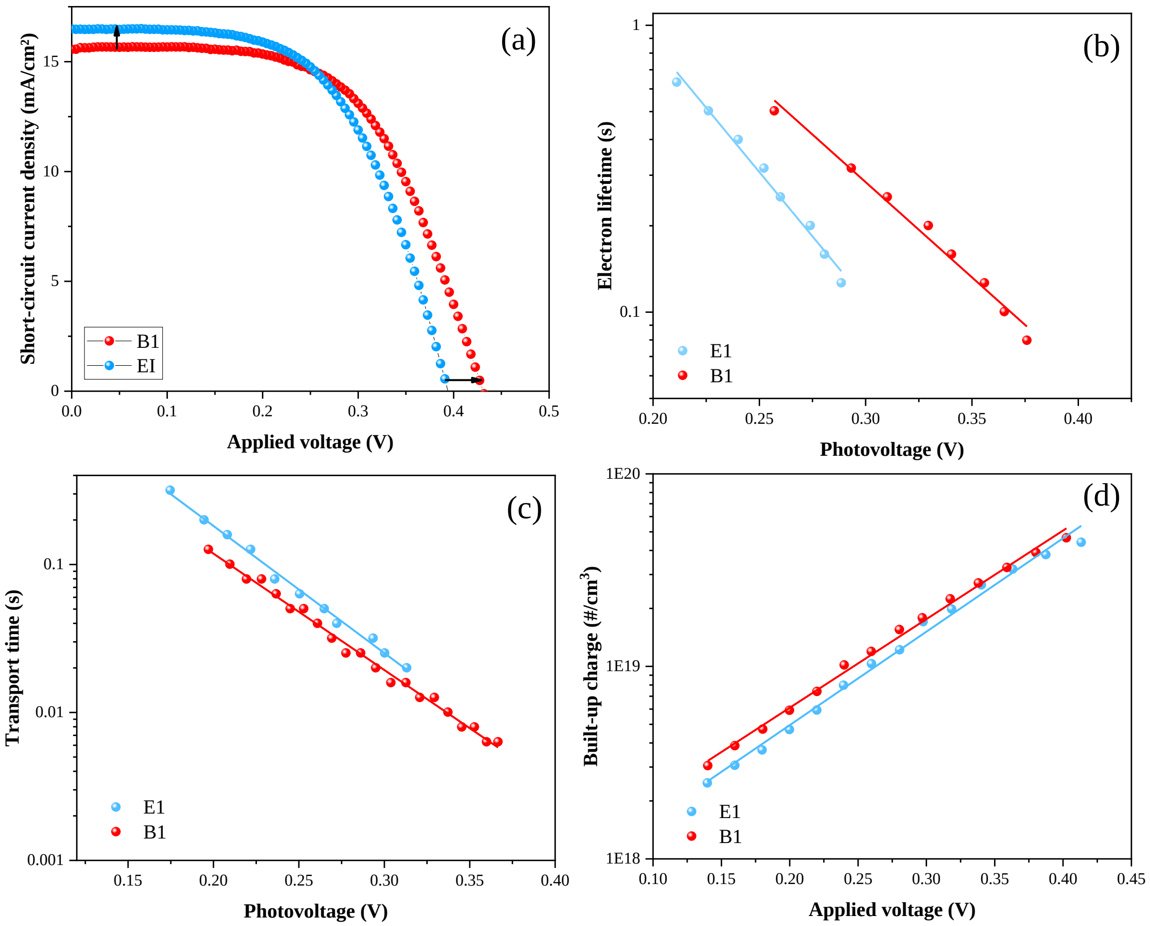

*Figure 65. (**a**) J-V curves of **TB207** PPcy DSSC with the conventional iodine electrolyte **EI** (blue) and the interhalogen binary electrolyte **B1** (red) (**b**) electron lifetime evolution measured by IMVS, (**c**) electron transport time measured by IMPS, and (**d**) dark charge extraction measurements on **TB207**-DSSC with **E1** and **B1** electrolytes.*

As a member of the cyanine family, one drawback of these dyes is their stability. Figure 66 shows the shelf-life stability of **TB207** dye with **EI** and **B1** electrolyte, compared to our reference **VG20-C$_{16}$** cyanine dye in the same conditions. Even though **TB207** is still not stable under aging conditions, it shows the enhanced performance when compared to **VG20-C$_{16}$**, as the steepness of the stability curve is less intense.

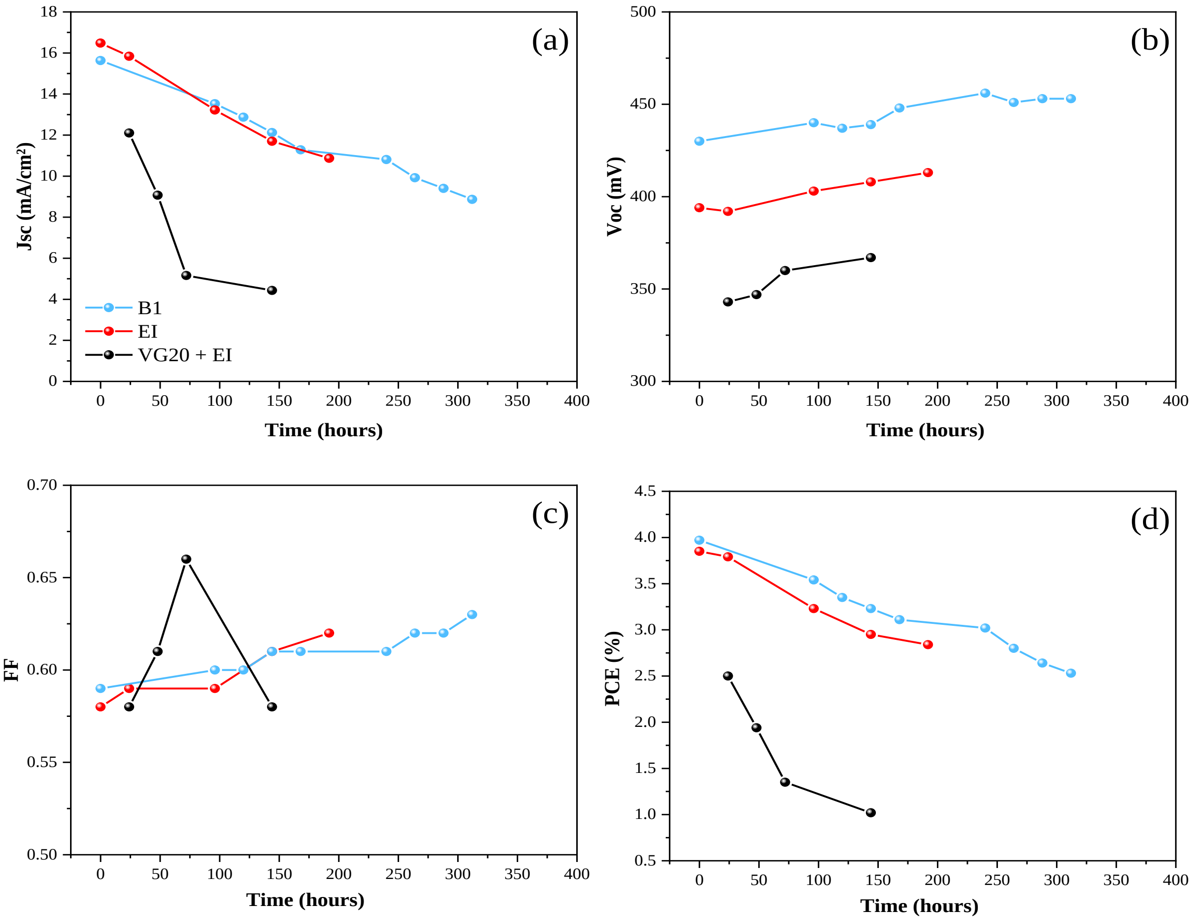

*Figure 66. Evolution of (a) J_{sc}, (b) V_{oc}, (c) FF, and (d) PCE under shelf-life aging conditions for **TB207** DSSC (room temperature sensitization) either using **EI** (in red) or **B1** (in blue) electrolytes. **VG20-C$_{16}$** stability is added in black for comparison.*

4.5. Ultrafast spectroscopy of carrier injection, dye regeneration, geminate recombination, and concurrent processes of TB207-NIR-DSSC

The performances of **TB207** with a relatively low concentration of CDCA to achieve the maximum PCE (5 mmol/L compared to 50 mmol/L for **VG20-C$_{16}$** dye) comprises our first evidence that the structural dye engineering was successful in avoiding the harmful dye aggregations. However, as pointed out in Figure 67, which presents the absorption spectrum of **TB207** on TiO_2 compared to absorption in solution, this dye still exhibits the fingerprint of aggregates formation. This can be deduced from the broadening of the main S_0-S_1 transition band and the increase of the shoulder at 720 nm.

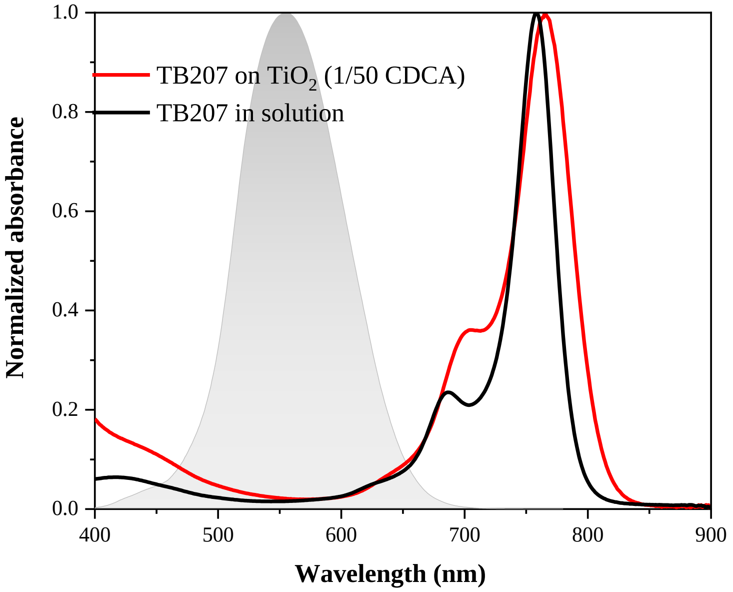

*Figure 67. Normalized absorption spectra of **TB207** on 3µm thick TiO_2 film with 5 mmol/L of CDCA (red) along with that in solution (black). The shaded grey area represents the human photopic response.*

Monomer-to-aggregate energy transfer is identified to be one important loss channel reducing the charge injection yield in the case of **VG20-C**$_{\mathbf{16}}$ dye. Femtosecond up-conversion fluorescence and transient absorption spectroscopy measurements were combined to evaluate the ultrafast dynamic of **TB207**-based NIR-DSSC. This work was carried out in collaboration with Ilias Nikolinakos and Prof. Stefan Haack at IPCMS within the frame of the VISION-NIR ANR project.

Femtosecond transient absorption spectroscopy measurements in solution reveal the transient products subsequently to light excitation (Figure 68.a). The positive signal between 440-720 nm and 900-1030 nm detected a few picoseconds (0.75 ps) after excitation corresponds to the excited state absorption (ESA) of **TB207**. The negative signal at around 750 nm is in agreement with the steady-state absorption spectrum and is ascribed to the ground state bleaching (GSB). The GSB superimposes with the stimulated emission (SE) in the range of 720-900 nm. The dye returns to ground state between 2 and 5 ns, which is good agreement with the previously obtained lifetime value of 3.2 ns determined by TCSPC.

The following experiments were performed on **TB207** grafted on TiO_2 and Al_2O_3 as a non-injecting semiconductor. Due to the higher bandgap, Al_2O_3 serves as the reference non-injecting DSSC, and the energy transfer (ET) is the only excited state quenching process. We compare in the following a complete TiO_2 DSSC with 5mmol/L CDCA and a 0mM CDCA Al_2O_3 device since their absorption spectra indicate about the same monomer-to-aggregate ratio. Upon excitation (0.75 ps), the transient absorption spectrum of **TB207** on Al_2O_3 without CDCA shows the same positive signals as in solution, at 450-690 nm and 830-1030 nm, corresponding to the absorption of the singlet excited state (Figure 68.b). Moreover, we also find the superposition of the GSB/SE, but this time, it deactivates much faster than in solution. Indeed, 50% of the ground state is depopulated after 50 ps on Al_2O_3 against 1000 ps in solution. In parallel, the absorption of the excited state (at more than 920 nm) decreases in favor of a new positive absorption band around 830-920 nm. The ESA at 680 nm undergoes a hypsochromic shift of 40 nm from 50 ps, and then its intensity decreases until it returns to the ground state. These changes reveal the energy transfer (ET) from the monomer to the aggregates, which de-excites to form a neutral species again in less than a nanosecond.

In the transient absorption spectrum of **TB207** on TiO_2 with 5mM CDCA (Figure 68.c), the spectral characteristics of GSB/SE are identical to those observed on Al_2O_3, with a decrease of about 50% at 40-50ps. In addition, the highest intensity positive peak is shifted by 50 nm relative to Al_2O_3, i.e., 620 nm compared to 670 nm previously. The intensity of the ESA does not decrease with time and indicates that the ground state has not completely reformed. Therefore, this attests to the injection of electrons into the conduction band of TiO_2. This process occurs very quickly since the intensity maximum is almost obtained after 10 ps. Moreover, no absorption of the excited aggregates is observed at 880 nm and the ESA around 900-1030 nm is very low. All these parameters indicate an ultrafast injection process in the order of picoseconds predominating over the charge transfers between the monomer and the aggregates.

Femtosecond TAS confirms that, due to structural inhomogeneities, both electron injection and ET occur on time scales of roughly 1-100 ps.

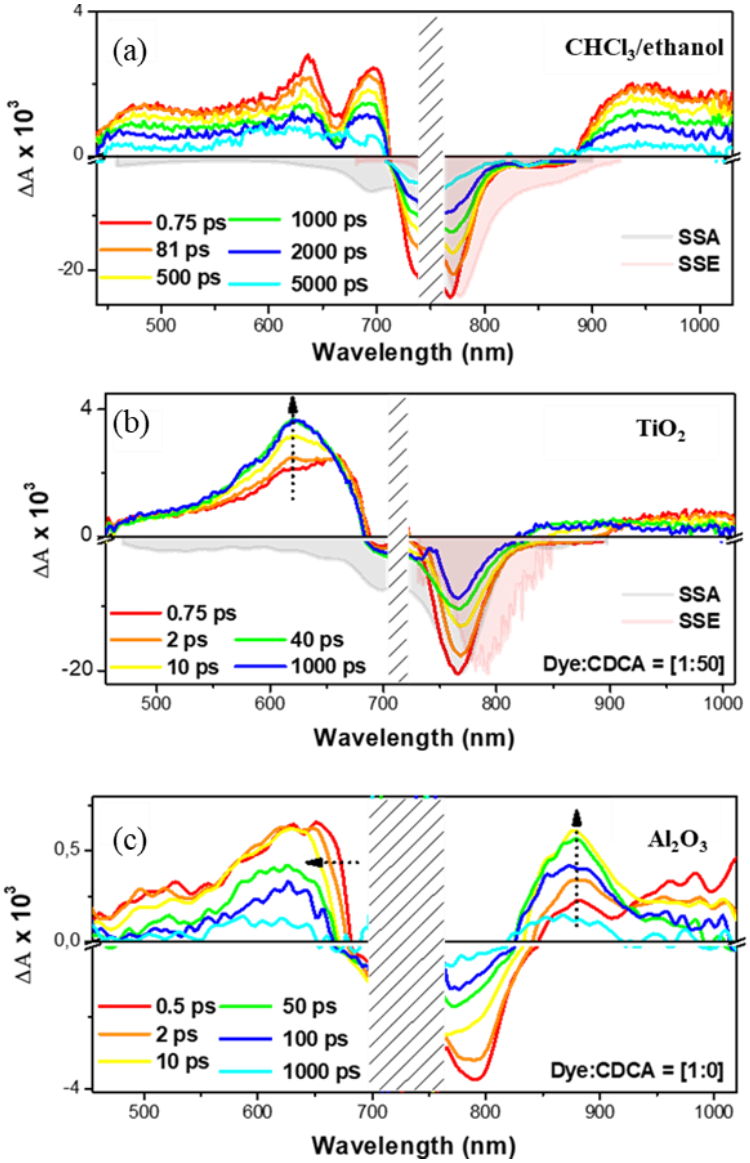

Figure 68. Transient absorption spectra of ***TB207*** *PPcy dye in (**a**) solution of $CHCl_3$/ethanol (1/9), (**b**) in DSSC based on TiO_2 photoanode with 5 mmol/L CDCA, and (**c**) in non-injection Al_2O_3 DSSC. Excitation at 730 nm. Excitation energy is 20µJ/cm².*

Figure 69 displays the wavelength-averaged and normalized fluorescence kinetic traces of complete DSSC devices with EI electrolyte with **TB207** grafted on TiO_2 (blue), and Al_2O_3 (green), and of **TB207** in an $CHCl_3$/ethanol (1/9) solution (red) recorded with 0.2 ps time resolution. The lifetime of **TB207** in solution is found to be 3.11 ns as measured by TCSPC. Both the TiO_2 and Al_2O_3 DSSC kinetics are strongly quenched compared to solution and fully decay in the 1 ns time window. The fluorescence of **TB207** anchored on the semiconductor is dominated by monomer emission, with the excited state quenching being due to monomer-to-aggregate ET for the Al_2O_3

DSSC. On the other hand, the TiO_2 DSSC kinetics decay even faster because of the additional mechanism of charge injection. A three-exponential fit is required to capture the main decay times. Their values, as well as the relative amplitudes, are given in Table 19.

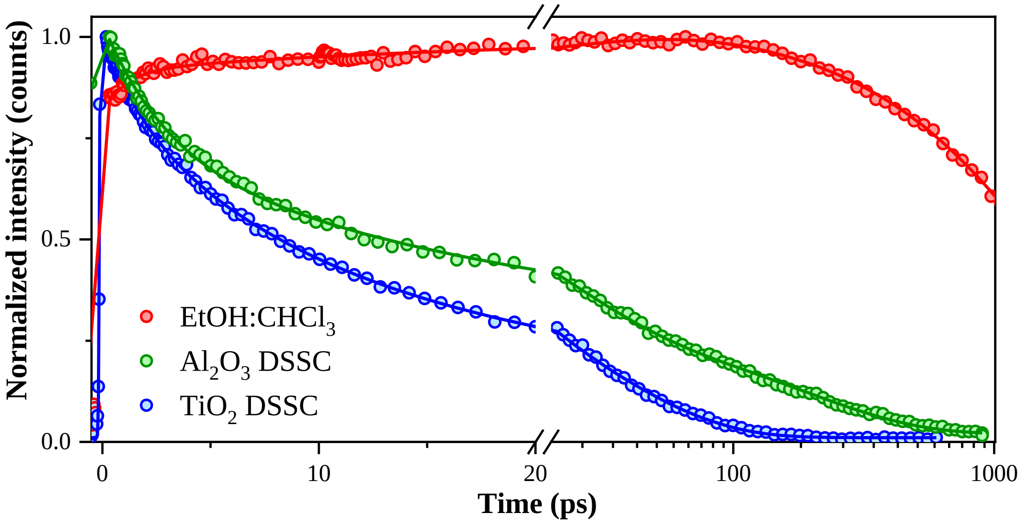

Figure 69. Normalized fluorescence up-conversion kinetic traces, with the respective fitting curves as solid lines, averaged over the fluorescence spectrum of ***TB207*** *in $CHCl_3$/ethanol (1/9) (red), 0 mM CDCA Al_2O_3 DSSC (green), and 5 mM CDCA TiO_2 DSSC (blue). The samples were excited at 730 nm with 20 $\mu J/cm^2$ fluence. Note the break in the time axis. Log. scale after 20 ps.*

Table 19. Time constants obtained by fitting the kinetic traces of Figure.69 with a sum of 3 exponentials convoluted with a 150-fs Gaussian (temporal resolution). τ and k refer to the average lifetime and the corresponding average rate.

Sample	A_1%	τ_1/ps	A_2%	τ_2/ps	A_3%	τ_3/ps	τ/ps	k/ps^{-1}
Al_2O_3 DSSC	35	2.0	39	17	26	180	54.1	0.0185
TiO_2 DSSC	16	1.5	43	8	41	35	18.0	0.055

A simple method of evaluating the carrier injection efficiency Φ_{inj} is based on the average rates of carrier injection $<k_{inj}>$, energy transfer $<k_{ET}>$, and monomer excited state decay $<k_{mono}>$:

$$\Phi_{inj} = <k_{inj}> / (<k_{inj}> + <k_{ET}> + <k_{mono}>)$$

Since the former rates k_{inj} and k_{ET} largely dominate, the carrier injection efficiency is thus evaluated as follows:

$$\Phi_{inj} \approx \langle k_{inj} \rangle / (\langle k_{inj} \rangle + \langle k_{ET} \rangle)$$

With $\langle k(Al_2O_3) \rangle = \langle k_{ET} \rangle$ and $\langle k(TiO_2) \rangle = \langle k_{ET} \rangle + \langle k_{inj} \rangle$. The measured kinetics reveals a $\langle k_{ET} \rangle = 0.0185\ ps^{-1}$ and $\langle k_{inj} \rangle = 0.037\ ps^{-1}$, which means an injection efficiency $\Phi_{inj} \approx 67\ \%$. This injection quantum yield is much higher than the one evaluated for **VG20-C16** dye ($\Phi_{inj} \approx 30\ \%$), which comprises an advantage of the PPcy dye structure over the cyanine one.

The excited-state reactions in the **TB207**/TiO_2 DSSC are cast in Scheme 7, highlighting the roughly 2/3-to-1/3 excited state branching between electron injection and ET. Excited aggregates (Agg*) decay on a slower time scale, back to the ground state (S_0), but some contribution to carrier injection and thus to J_{sc} cannot be excluded.[201]

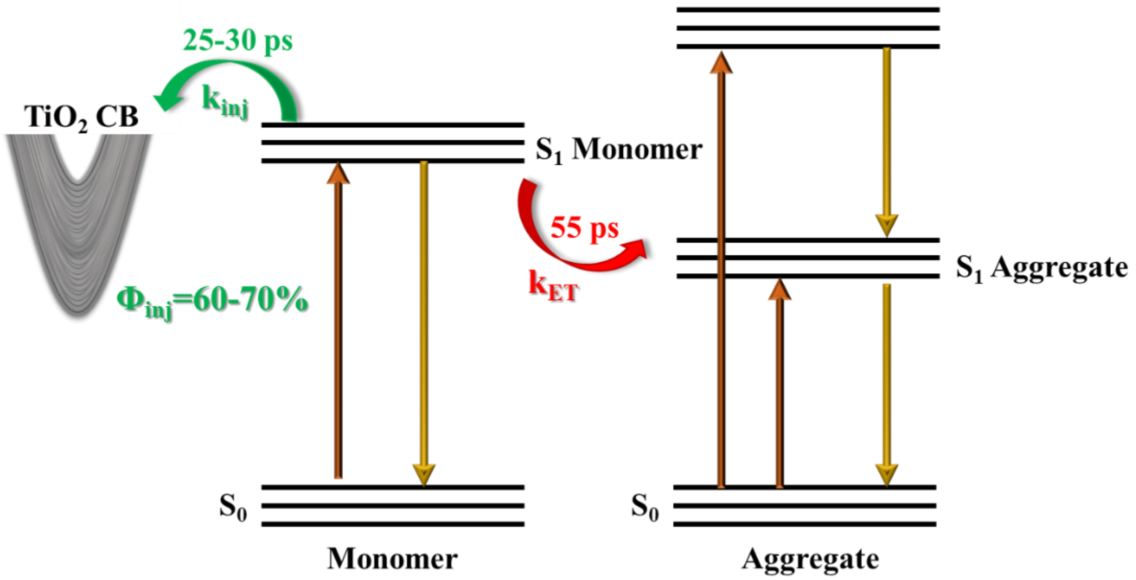

*Scheme 7. Main electronic processes deduced from fluorescence up-conversion involved in **TB207**-based DSSC.*

TB207 dye radical cation regeneration and geminate recombination kinetics have been evaluated using a ps pump-probe transient absorption spectroscopy associated with a streak camera for spectral and temporal resolution (at LRCS). The **TB207** radical cation absorbs in the visible region between 530 to 680 nm (Figure 70). The related transient decay corresponds to the dye radical cation depopulation upon a 30 ps pump pulse at 785 nm is studied for the two optimized electrolytes, **EI** and **B1**, and inert electrolyte.

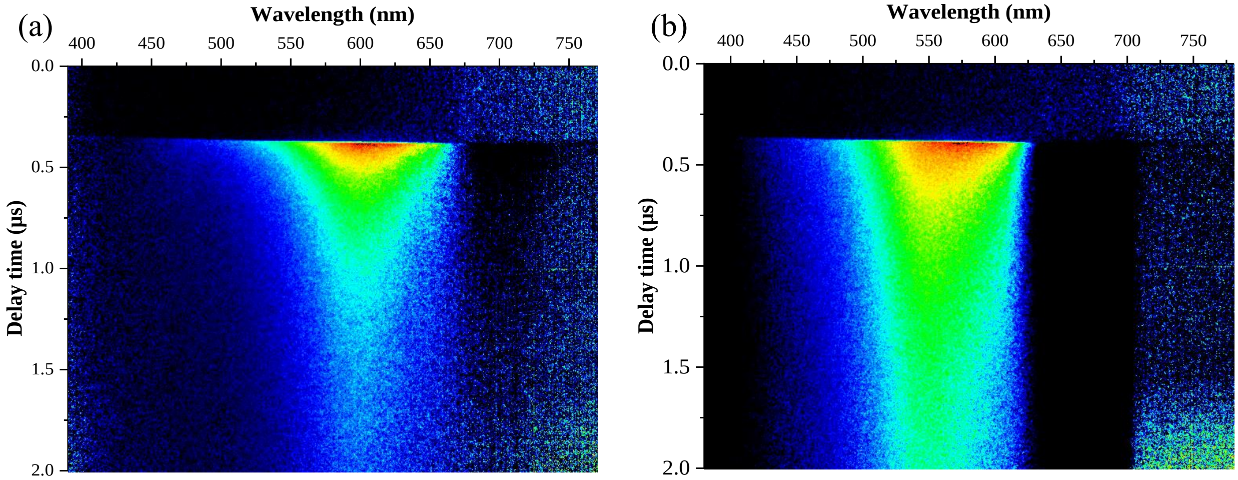

*Figure 70. Time-resolved transient absorption spectral streak image of the **TB207** based DSSC in 2 µs time-window for (**a**) the I_3^-/I^-redox couple, and (**b**) the binary (I_3^-, I_2Br^-)/(I^-, Br^-) redox couple.*

For the triiodide/iodide redox couple, the regeneration takes place within τ_1= 0.38 µs (±0.018 µs) (f_1 = 72 %) and τ_2= 2.52 µs (±0.16 µs) (f_2 = 28 %) (Figure 71.a). These values are almost one order of magnitude faster than **VG20-C16** dye, and those reported for conventional dyes such as D-π-A dyes or ruthenium complexes.[177–179] The exponential decay required two components. As confirmed by the fs-TAS and up-conversion studies, aggregates contribute to the carrier injection. As such, it is convenient to account the faster component to the regeneration of the dye monomer while the slower one is attributed to the dye aggregate regeneration.

The regeneration kinetics were found to be slightly different for devices based on the binary electrolyte **B1**. Figure 71.a shows the depopulation of the **TB207** dye radical cation probed at 650 nm in the presence of either **EI** (black) or **B1** electrolyte (red), in a 10 µs time window. The kinetics with **EI** electrolyte decay completely in this timescale while a longer kinetic is observed for B1 electrolyte. In order to record the full decay of **TB207** with **B1** binary electrolyte, the kinetics were followed in the 50 µs time window. The fitting reveals two lifetimes: τ_1= 2.5 µs (±0.41 µs) (f_1 = 59%) and τ_2= 13.2 µs (±2.5 µs) (f_2 = 41 %). We attribute the longer regeneration lifetime in the case of **B1** electrolyte to the fact that the binary redox couple (I^-, Br^-)/ (I_3^-, I_2Br^-) exhibits a more positive potential compared to I^-/I_3^- couple, and thus the driving force for the hole transfer is reduced, i.e., $- \Delta G°_{reg} (I^-/I_3) < - \Delta G°_{reg} (I^-, Br^-)/(I_3^-, I_2Br^-)$.

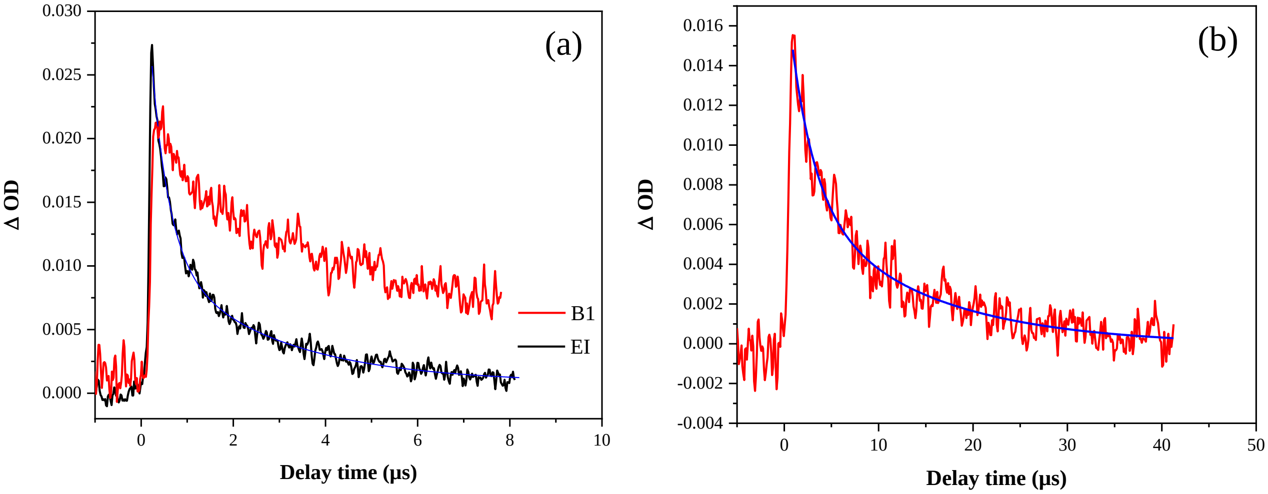

*Figure 71. Transient absorption kinetics of the **TB207** based DSSC at 650 nm in the presence (**a**) the I_3^-/I^-redox couple (**EI**), and the binary (I_3^-, I_2Br^-)/(I^-, Br^-)redox couple (**B1**) in a 10 µs timescale window and (**b**) **B1** electrolyte in a 50 µs timescale window.*

These values have to be compared to the geminate recombination process. For this, an inert electrolyte is used. In this case, the lifetime of **TB207** radical cation with a redox-free inert electrolyte shows long-lived species within τ_1= 0.08 ms (±0.008 ms) as the dominant species with f_1 = 65 %, and τ_2= 0.87 ms (±0.05 ms) (f_2 = 35 %) (Figure 72). A simple method of evaluating the dye regeneration efficiency Φ_{reg} is based on the average rates of dye radical cation regeneration $\langle k_{reg} \rangle$, and geminate recombination decay $\langle k_{rec} \rangle$:

$$\Phi_{reg} = \langle k_{reg} \rangle / (\langle k_{reg} \rangle + \langle k_{rec} \rangle)$$

The measured kinetics reveals a $\langle k_{reg} \rangle = 1.031\ \mu s^{-1}$ and $\langle k_{rec} \rangle = 2.78\ 10^{-3}\ \mu s^{-1}$, which means a dye regeneration efficiency Φ_{reg} = 99.7 %. Even though the geminate recombination kinetics of **TB207** are faster than those measured for **VG20-C16** cyanine dye (0.94 ms ±0.02 ms), it remains fast enough compared to the two orders of magnitude faster regeneration, thus allowing devices to reach quantitative regeneration yields with this new family of dyes for both electrolyte compositions.

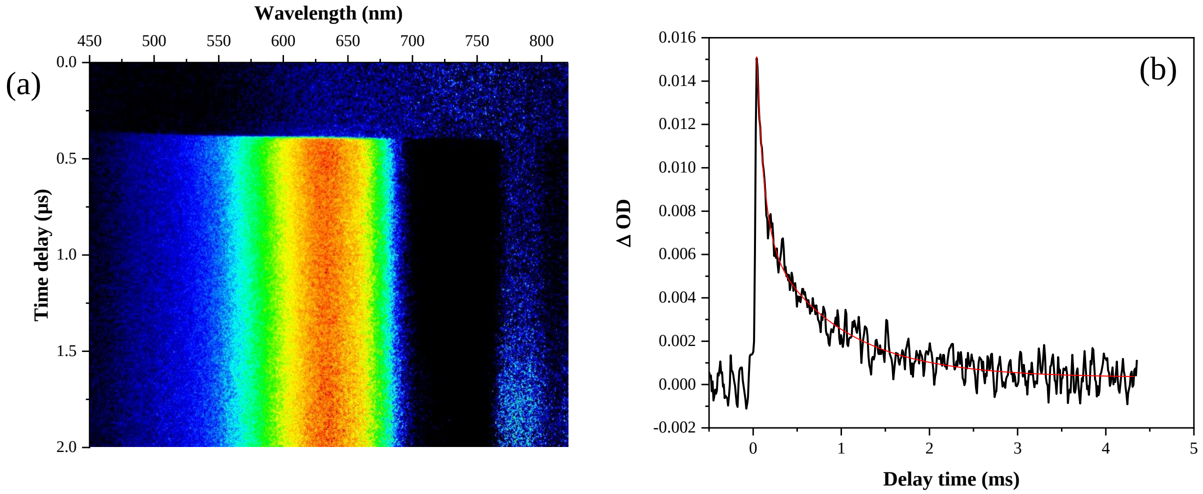

*Figure 72. (**a**) Time-resolved transient absorption (a) spectral streak image of the **TB207** based DSSC in 2 μs time-window for inert electrolyte to show the long-lived species, and (**b**) kinetics of the **TB207** based DSSC at 650 nm in inert electrolyte. The full decay is measured in the 5 ms time-window.*

4.6. Conclusions

In this chapter, DPP derivatives were developed for selective NIR light conversion. This led to the synthesis of a new series of pyrrolopyrrole cyanine dyes based either on PPcy or thienyl-PPcy skeleton. The TD-DFT calculations revealed that the main electronic density is concentrated on the PPcy core for both HOMO and LUMO levels, with a short-range delocalization. Moreover, the electronic density on unoccupied molecular orbitals appears to be sufficiently intense on the carboxylic acid anchoring group, ensuring correct directionality in the charge transfer processes at the excited states and thus an efficient charge injection.

The thienyl-PPcy dyes denoted as **TB179** and **TB202** exhibit a red-shifted absorption compared to the PPcy dyes coded **TB144** and **TB207**. However, **TB207** was the most promising for future transparent and colorless DSSC application with negligible absorption in the visible region. The optimization of these dyes yielded a new record for NIR-DSSC with **TB207** dye achieving a 3.8 % PCE with I^-/I_3 redox couple, whereas the highest performances achieved for **TB144**, **TB179**, and **TB202** were < 1.5%. We also highlighted the importance of the phenyl group instead of the fluorine on the boron atom, which serves as a barrier against the non-geminate recombination process and helps in forming a less-aggregated self-assembled monolayer. The outcome of the different characterization methods applied in this study on the different PPcy structures is summarized in the following and in Figure 73 : the substitution of phenyl (highlighted in pink) by thienyl (highlighted in blue) groups on the cyanine core results in i) redshifted absorption maximum (ca. 30 nm), ii) shortened PL lifetime in solution from ca. 3 ns to ca. 1 ns, iii) shortened electron lifetime which is attributed to more non-geminate recombination, and iv) affected SAM due to different aggregation level and thus different molecular packing on the TiO_2. On the other hand, the substitution of fluorine (highlighted in red) by phenyl group (highlighted in green) on the boron position results in i) redshifted absorption maximum (ca. 45 nm), ii) enhanced electron lifetime as a result of less non-geminate recombination, iii) downshifted surface trap states of TiO_2 due to different SAM layer, and iv) less aggregated molecules both in solution and on TiO_2. The combination of the phenyl group on both the cyanine core and on the boron position yields to the optimized structure of the presented PPcy dyes, which corresponds to **TB207** dye.

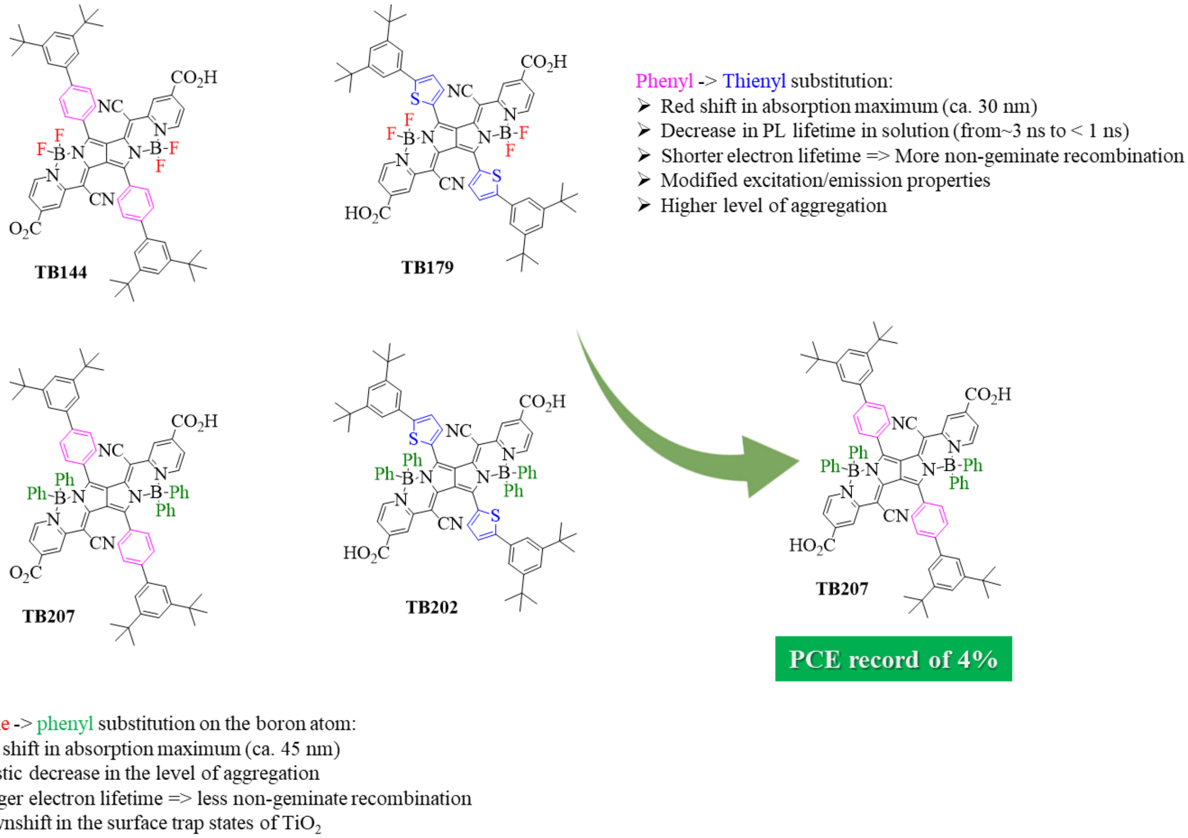

Phenyl -> Thienyl substitution:
- Red shift in absorption maximum (ca. 30 nm)
- Decrease in PL lifetime in solution (from~3 ns to < 1 ns)
- Shorter electron lifetime => More non-geminate recombination
- Modified excitation/emission properties
- Higher level of aggregation

PCE record of 4%

Fluorine -> phenyl substitution on the boron atom:
- Red shift in absorption maximum (ca. 45 nm)
- Drastic decrease in the level of aggregation
- Longer electron lifetime => less non-geminate recombination
- Downshift in the surface trap states of TiO_2

*Figure 73. Representation of the different molecular structure modifications on the PPcy dyes resulting in **TB144**, **TB207**, **TB179**, and **TB202**, with their main outcome.*

The kinetic study carried on **TB207** by femtosecond fluorescence and transient absorption spectroscopy confirmed the enhancement of the injection efficiency to 60-70 % compared to 30%

to the cyanine dye **VG20-C$_{16}$**. The results suggest that even the monomer-to-aggregate energy transfer is happening in 55 ps while injection from monomer is in the 25-30 ps timescale, electron injection wins the kinetic competition over ET into residual aggregates. Moreover, aggregates are believed to contribute to carrier injection and thus to J_{sc}. This characteristic of **TB207** PPcy dye is an advantage over the former **VG20** cyanine dye limited with the non-productive monomer-to-aggregates energy transfer. Moreover, the PPcy **TB207** dye showed fast dye regeneration kinetics with the triiodide/iodide redox couple, with τ_1= 0.38 μs (±0.018 μs) and τ_2= 2.52 μs (±0.16 μs). These values are faster than those reported for conventional dyes such as D-π-A dyes or ruthenium complexes and what we reported for **VG20-C$_{16}$** cyanine dye. As such, quantitative regeneration yields are achieved within the **TB207**-based DSSC.

Chapter 5

Chapter 5. Aesthetic optimization with colorless electrolyte and second generation of PPcy dyes for higher PCE

In the previous chapter, we introduced a new series of dyes based on pyrrolopyrrole cyanine. The PPcy dye **TB207** showed good performances with the conventional tri-iodide/iodide redox couple (3.8 % PCE) and can reach a value of 4.0 % in association with a binary interhalogen-based redox couple.

This chapter will cover the two last approaches followed in my work. The first is the exploration of a colorless redox mediator, starting with cobalt-based electrolytes. Then, the aesthetic evaluation with the I_3^-/I^- redox couple and cobalt complexes will be presented for **TB207-**DSSC. In the aim of optimizing aesthetics, we introduced a transparent hybrid sulfur/iodide-based redox couple in order to reach a color-neutral wavelength-selective NIR-DSSC. The work presented will provide the photovoltaic performances with the hybrid electrolyte as well as an optimization of the electrolyte composition. Moreover, the comparison of AVT and different color metrics of **TB207-**devices in the presence of the I_3^-/I^- or the hybrid sulfur/iodide redox mediators will be given, highlighting the outcome of the new colorless electrolyte. This evaluation is within an in-depth optimization of the photoanode's thickness to find the best balance between performances and transparency, using the light utilization efficiency (LUE) metric.

The second part of this chapter is dedicated to the extension of the PPcy dyes with the push-pull approach to increase the dyes' performances. Preliminary results of the PV performances and aesthetics evaluation are presented.

5.1. Cobalt-based electrolyte with TB207-DSSC towards color-neutrality

Among the alternative redox couples that have been investigated so far to replace the orange-colored I_3^-/I^- redox mediator, a few can fit into the requirements of the NIR dyes. The suitability of an efficient redox couple in a NIR-DSSC depends on several properties, but most importantly, on its ability to regenerate the oxidized dye efficiently. Moreover, the redox couple should exhibit a low molar extinction coefficient in the visible range and low internal reorganization energy subsequently to the hole transfer process.

Historically, cobalt complexes represent a successful way to replace tri-iodide/iodide redox couple.[156] One advantage of introducing Co complexes for NIR-DSSC stems from the low absorption coefficient of both the reduced and oxidized form.[202] The reduced form has a weak absorption feature in the visible region compared to the typical I_3^-/I^- redox couple. As a first attempt, $[Co(phen)_3]^{3+/2+}$ (E = +0.62 V vs NHE) redox mediator was selected and studied with **TB207**-DSSC. A first composition, coded **ECo**, is composed of 0.25 mol/L $Co(phen)_3^{2+}$, 0.05 mol/L $Co(phen)_3^{3+}$and 0.5 mol/L LiTFSI in the acetonitrile/valeronitrile solvent mixture (85/15 v/v). The measured J-V curve is reported in Figure 74. With this electrolyte, a drastic drop in J_{sc} is observed (J_{sc} = 2.4 mA/cm²) despite a comparatively good value of photovoltage due to the higher oxidizing potential of the redox mediator. It led to a very modest PCE of 0.6 %.

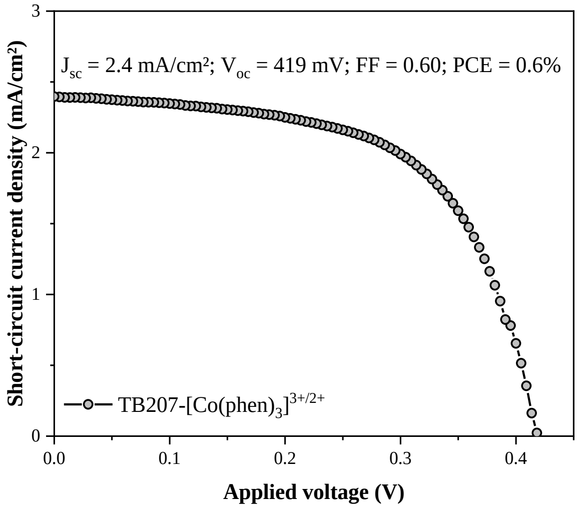

*Figure 74. J-V curve of **TB207**-based NIR-DSSC with $[Co(phen)_3]^{3+/2+}$-based electrolyte under A.M. 1.5G conditions.*

Although the PCE is not totally promising, we evaluated the aesthetic gain with the cobalt-based electrolyte. As reported in Figure 75.a, the transmittance spectra of **TB207**-based DSSC including a Co-based electrolyte shows a slightly different fingerprint than the **EI**-counterpart. The singlet absorption maximum of the dye is red-shifted by 7 nm to reach λ_{max} = 774 nm. The shoulder at around 700 nm is more pronounced with Co-electrolyte than with **EI**, which overlaps with the red tail of the photopic response. This suggests that the cobalt complexes strongly interact with the dye and may even impact the molecular aggregation. Even though an apparent gain in transmittance in the blue/UV region (< 450 nm) is obtained for **ECo** electrolyte as expected, a slight transmittance loss is measured in the 450-600 nm range, which corresponds to the region where the photopic response is at its maximum. This led to a decrease in the AVT value from 70% to 68%, whereas the CRI increased from 89.7 to 93.2. The calculated chromaticity coordinates positioned on the CIE1931 color space in Figure 75.b show the different hues perceived by **TB207**-DSSC incorporating either **EI** or **ECo**. The dominant wavelength of **TB207**-DSSC with **EI** is 570 nm, with a color saturation of 28%. On the other hand, a 3 nm shift in the dominant wavelength is obtained with **ECo** (567 nm) while decreasing the color saturation to 16%, revealing a more color-neutral device.

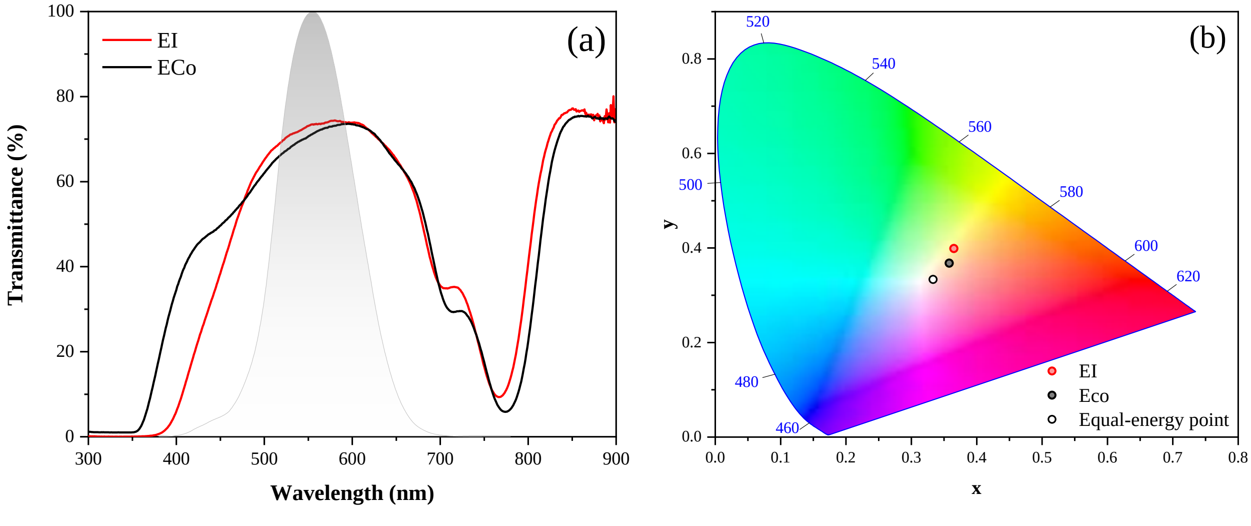

*Figure 75. (**a**) Comparison of the transmittance spectrum of **TB207**-based NIR-DSSC with a 4 µm-thick* TiO_2 *photo-anode with either **EI** (red) or **ECo** (black) electrolyte. The shaded grey area represents the photopic response. (**b**) the chromaticity diagram of these devices in the CIE1931 color space. The white point is the equal-energy point.*

5.2. Optimization of TB207-DSSC with transparent and colorless electrolyte: an approach with hybrid sulfur/iodide electrolyte

Scrutinizing the different colorless and transparent redox mediators that can replace the conventional electrolytes, the most simple and efficient way is to suppress the triiodide formation in the electrolyte directly. Cong et al. introduced back in 2012 a highly efficient and colorless sulfur/iodide-based hybrid electrolyte that enhanced the performance of the benchmark Ru complex dye N719.[203] We herein adopt the concept of a hybrid electrolyte between S_n^{2-}/S^{2-} and I^- with the NIR-dyes in order to reach a non-intrusive color-neutral wavelength-selective DSSC.

5.2.1. Synthesis and characterization of S_n^{2-}/S^{2-} with tetramethylammonium cation

The first step is to synthesize the tetramethylammonium sulfide (TMAS) salt. For this, 44 mmol of tetramethyl ammonium is added to 22 mmol of ammonium sulfide. Both are aqueous solutions, and the mixture is stirred until the solution turns from yellow to colorless. Next, the water solvent is removed by rotary evaporation, and the resulting white salt is dried at 50°C under vacuum for four hours.

The redox couple, consisting of S_n^{2-}/S^{2-} with the organic tetramethylammonium cation, was synthesized by mixing equivalent amounts (1.25 mmol) of sulfur and the tetramethylammonium sulfide in acetonitrile and then heated at 70°C for 3 hours. The obtained solution is dark green. It turns transparent and colorless after overnight stirring at room-temperature (Figure 76).

Figure 76. Pictures taken during the different steps of the synthesis of the S_n^{2-}/S^{2-} with the organic tetramethylammonium cation.

Mass spectrometry (MS) analysis has been carried out to confirm the nature of the species in the solution. The MS results confirmed the presence of the TMA^+ cation and polysulfide chain that is composed by n = 2, 3, and 4 in S_n^{2-} (m/z = 339 for $S_4(TMA^+)_2C_2H_2NNa$ and m/z = 74 for the cation TMA^+ (Figure 77).

The peak at m/z = 275 is attributed to $S_2(TMA^+)_2$ C_2H_2NNa. A difference of 32u for two times is measured, which corresponds to the atomic weight of S. These differences are highlighted by the black stars in Figure 77, and they correspond to $S_3(TMA^+)_2$ C_2H_2NNa and $S_4(TMA^+)_2$ C_2H_2NNa. The same trend is followed at higher m/z ratios (highlighted with green stars). We attribute the m/z = 446 to the dimer where also a difference of 32u is recorded (m/z = 478 and 510).

Polysulfides systems are well-known for having different coloration depending on the chain length. A clear correlation between polysulfide species and absorbance can be found in the literature.[204–206] For NIR-DSSC application, keeping the number of polysulfide chains as small as possible is crucial to avoid parasitic light absorption in the visible range. The solvent can control the chain length through its dielectric constant (ε), donor number (DN), and the Lewis acidity of the cation.[207–209] Selecting a low ε and DN solvent stabilizes the short chains $(n \leq 4)$.[210] Acetonitrile is the solvent of choice for our electrolyte. It is characterized by an intermediate ε value (35.9) and a low DN (14.1). However, TMA^+ is a weak solvating cation in acetonitrile.[209] As such, it explained why the polysulfide (S_n^{2-}/S^{2-}) solution is mainly composed of n = 2, 3 and 4, which is in very good agreement with the MS results.

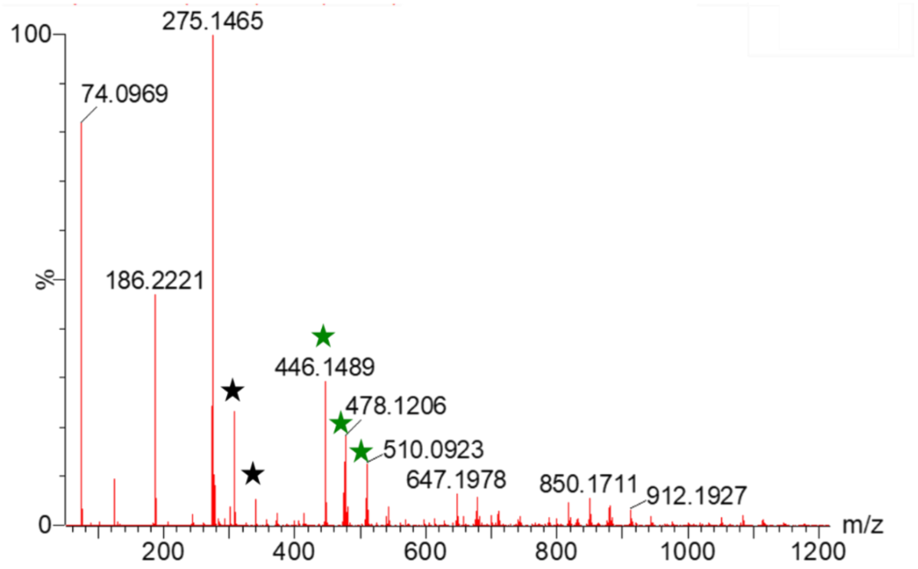

Figure 77. Mass spectrometry in positive ion mode of S_n^{2-}/S^{2-} electrolyte. The black and green symbols are referred to the difference of 32u, indicating the polysulfide chains present in the electrolyte.

The type of species present in the solution is also highly influencing the redox potential of the mediator. The electrochemical properties of the hybrid electrolyte were studied by cyclic voltammetry. The corresponding CV curve, presented in Figure 78, shows two successive and irreversible oxidation peaks at 0.64 V and 0.84 V vs. Ag^+/Ag, which correspond to +0.60 V vs. SCE and 0.80 V vs. SCE, and are ascribed to the oxidation of S^{2-}. These results suggest that the polysulfide redox couple is non-suitable for the efficient regeneration of the **TB207** dye (HOMO at +0.82 V vs. SCE).

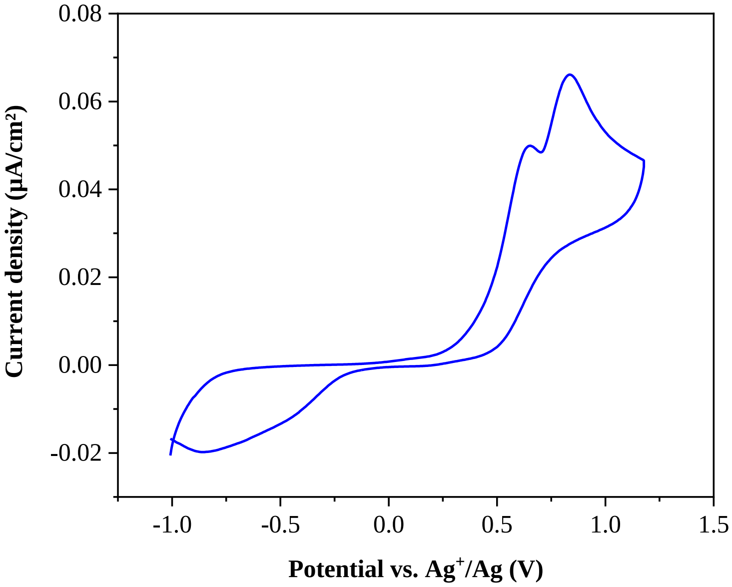

Figure 78. Cyclic voltamperogram at 100 mV/s scan rate of the S_n^{2-}/S^{2-} *with* I^- *hybrid redox couples in acetonitrile. The working electrode was a glassy carbon, Pt wire counter-electrode, and* Ag^+*/Ag quasi-reference electrode. The electrolyte contains 0.01 M of tetrabutylammonium hexafluorophosphate (*$TBAPF_6$*) as supporting salt.*

Upon optimization of the ratio between the sulfide and iodide in our electrolyte (further discussion below), the hybrid S_n^{2-}/S^{2-} and I^- electrolyte was formed by mixing the 0.02 mol/L of polysulfide (S_n^{2-}/S^{2-}) with the organic tetramethylammonium cation, 1 mol/L of 1,3-dimethylimidazolium iodide (DMII) and 0.5 mol/L of lithium iodide (LiI). It yields to a colorless and transparent electrolyte (coded **ESI**) (Figure 79.a). The absorption fingerprint of the conventional I_3^- /I^- electrolyte (**EI**) exhibits a main absorption band at 362 nm in the UV with a tail in the blue region (<500 nm), where the humans' cones are less sensitive. The absorption spectrum of the hybrid electrolyte shows negligible absorption in the whole UV and visible region. The advantage of the color neutrality of **ESI** on the optical transparency of the NIR-DSSC was validated by the total transmittance measurements of reference devices of the following structure: FTO glass / 2 µm

TiO_2 / electrolyte / FTO glass (coded Ref **EI** or Ref **ESI**) (Figure 79.b). The higher transmittance obtained in the 350-500 nm range with **ESI** electrolyte translates into a gain of ca. 2% in AVT for a final device without sensitizer, i.e., 73.5 % for Ref **EI** and 75.3 % for Ref **ESI** cells. However, more importantly, the utilization of **ESI** electrolyte affords a noticeable shift towards the white point in color coordinates from (x = 0.3646, y = 0.3877) (x = 0.3455, y = 0.3585) (Figure 79.c). This gain in AVT and the shift in the x,y color coordinates are translated into an increase in CRI value from 94 with **EI** to 98 with **ESI** electrolyte, thus highlighting the added value of the hybrid sulfur/iodide electrolyte in achieving higher optical transparency and better final aesthetics for selective NIR-DSSC.

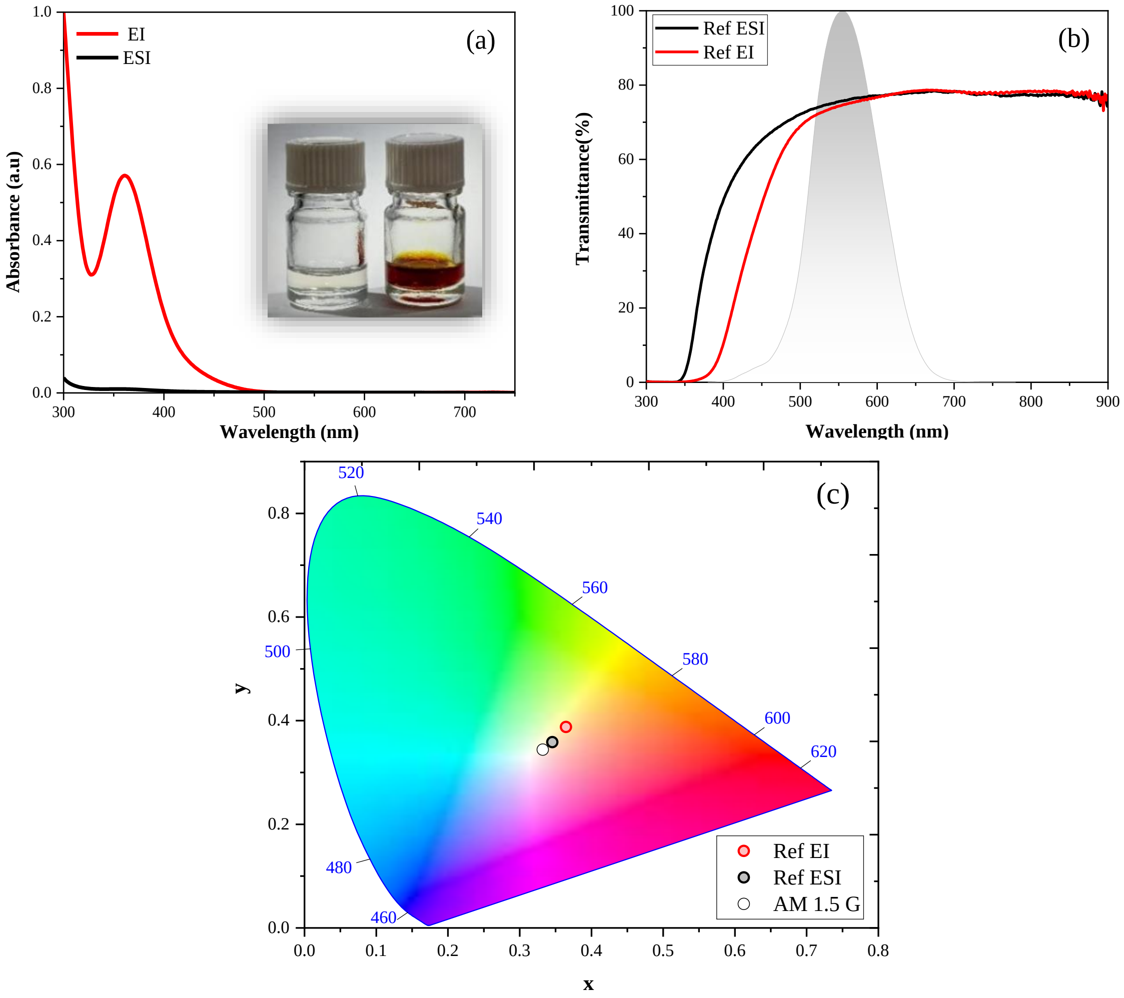

*Figure 79. Comparison between **EI** and the hybrid **ESI** electrolyte from (**a**) Steady-state absorption spectrum (in the inset is showed a picture of the two electrolytes) (**b**) Total transmission curve of the following device structure: FTO glass / 2 µm TiO_2 / electrolyte/ FTO glass (TiO_2 is not sensitized), (**c**) CIE 1931 chromaticity diagram positioning the actual color of the reference devices.*

We determined the dominant wavelength of each of the reference cells to be 572 nm with **EI** electrolyte and 570 nm for the **ESI** electrolyte device. The most important outcome of the replacement of **EI** by **ESI** is the decrease of the color saturation from 27 % to 11 %. This result emphasizes the capability of reaching higher transparency and more colorless NIR-DSSC by incorporating the hybrid S_n^{2-}/S^2 and I^- electrolyte.

5.2.2. Optimization of the hybrid electrolyte with TB207 PPcy dye

In order to optimize the hybrid electrolyte with **TB207** dye, we investigated 4 different compositions varying the ratio of the components (Figure 80). In these electrolytes, the source of I^- is LiI and DMII. Our reference **EI** electrolyte allows achieving 3.8 % PCE with a J_{sc} of 16.5 mA/cm^2, V_{oc} of 394 mV, and a FF of 0.55. All the photovoltaic parameters measured with the different **ESI** electrolytes are summarized in Table 20. Considering the optimized tri-iodide/iodide electrolyte **EI**, we start with a 1 mol/L DMII and 1 mol/L LiI, mixed with 0.02 mol/L of the S_n^{2-}/S^{2-} electrolyte, forming our first hybrid electrolyte, **ESI1**. The integration of **ESI1** into **TB207** devices yields a 3.1% PCE, with a short-circuit current density of 15.7 mA/cm^2 and a FF of 0.52. This J_{sc} value is slightly lower than the one measured with **EI**. Also, the V_{oc} undergoes a 28 mV drop compared to **EI** (V_{oc} = 366 mV). Increasing the S_n^{2-}/S^{2-} concentration to 0.03 mol/L (**ESI2** electrolyte) results in a drop in J_{sc} to 13.6 mA/cm^2, while the FF is enhanced to 0.57 and the V_{oc} equals 380 mV, leading to a PCE of 2.9%. On the other hand, decreasing S_n^{2-}/S^{2-} concentration to 0.01 mol/L (**ESI3**), an even larger drop in the J_{sc} is observed with a value of 12.5 mA/cm^2. However, the V_{oc} increases to 397 mV, and with a FF of 0.58, the devices reach a PCE of 2.9%.

In the following, we selected the concentration of 0.02 mol/L of S_n^{2-}/S^{2-} as the optimal condition. We investigated the effect of LiI added with a concentration of 0.5 mol/L (**ESI4**). Compared to **ESI1** (1 mol/L of LiI), the short-circuit current density is not noticeably affected (J_{sc} = 15.4 mA/cm^2), whereas the open-circuit photovoltage is increased by 18 mV (V_{oc} = 384 mV). The fill factor is also enhanced from 0.52 for **ESI1** to 0.55 for **ESI4**. This electrolyte achieved the highest efficiency within the **ESI** series, leading to a PCE value of 3.3 %.

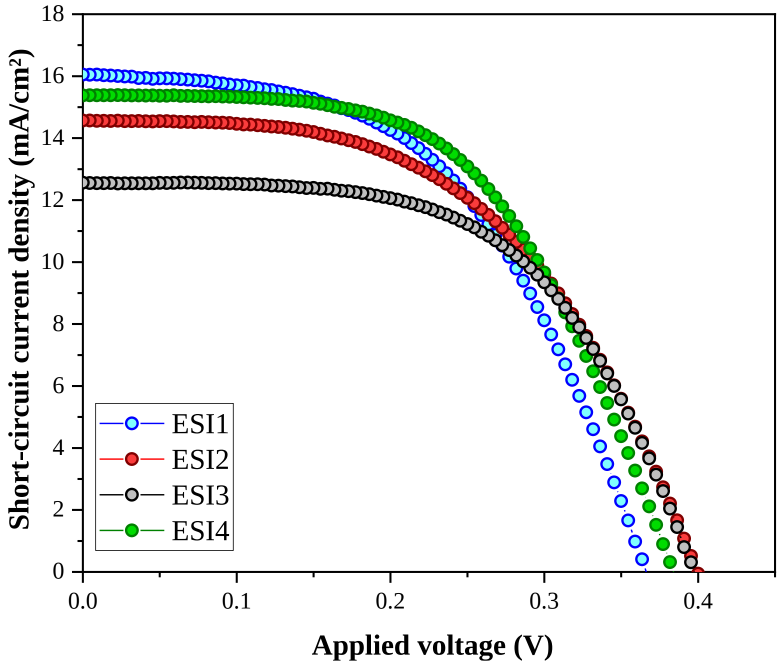

*Figure 80. Evolution of the (J-V) curves for **TB207**-based NIR-DSSC with different compositions of the hybrid* S_n^{2-}/S^{2} *and* I^- *electrolyte.*

*Table 20. summary of the different compositions of the studied hybrid electrolytes and the photovoltaic parameters of **TB207**-DSSC in the presence of each of them.*

Electrolyte	DMII (mol/L)	LiI (mol/L)	S/TMAS (mol/L)	J_{SC} (mA/cm^2)	V_{OC} (mV)	FF	PCE (%)
ESI1	1	1	0.02	16.1	366	0.52	3.1
ESI2	1	1	0.03	13.6	380	0.57	2.9
ESI3	1	1	0.01	12.5	397	0.58	2.9
ESI4	1	0.5	0.02	15.4	384	0.55	3.3

As a part of understanding the behavior of this new type of electrolyte for the application, we compared the IMVS, IMPS, and dark charge extraction experiments between the standard **EI** electrolyte and the best performing **ESI4** electrolytes (Figure 81). A longer electron lifetime is measured with **ESI4** electrolyte (Figure 81.a). We attribute this to the reduction of I_3^- species in the electrolyte by the S^{2-}, and thus decreasing the amount of the oxidized species in the electrolyte that can undergo recombination with the injected electrons. Moreover, the presence of the TMA^+ cation in the electrolyte can play a role in hindering the non-geminate recombination between the

I_3^- and S_n^{2-} species in the electrolyte and the injected electrons in TiO_2. The electron transport time, measured by IMPS, is only slightly affected (Figure 81.b).[171,172] As a result, the charge collection efficiency is enhanced from 81% with **EI** to 93% with **ESI4** electrolyte.

The dark charge extraction experiments show only a slight change in the shallow traps-energy with a ca. 30 mV upshift and distribution (Figure 81.c). Therefore, the new redox couple has no influence on the dye monolayer geometry and on the interfacial dipole moment.

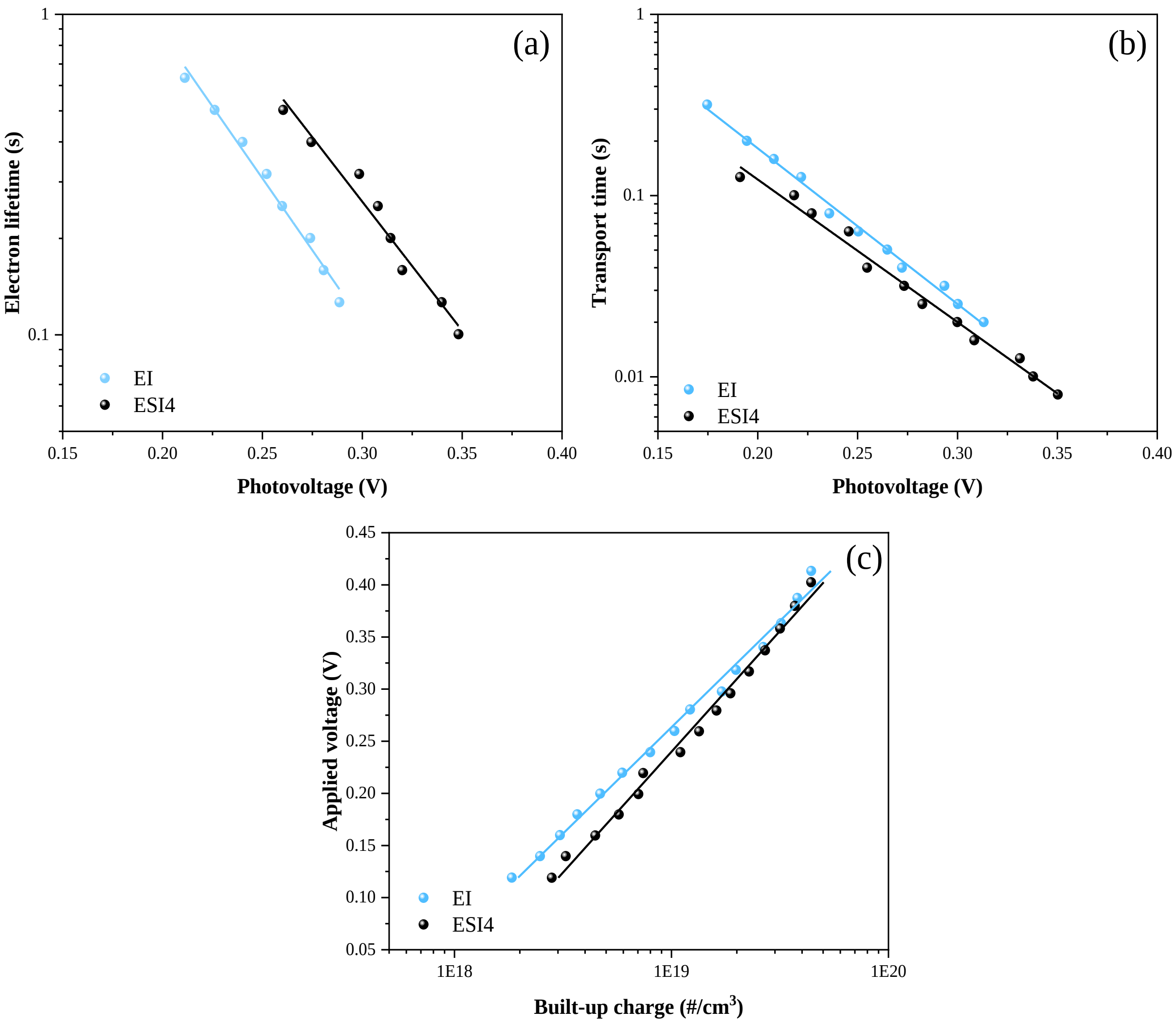

*Figure 81. Comparison between **EI** (blue) and **ESI4** (black) electrolyte on (**a**) the electron lifetime, (**b**) transport time, and (**c**) surface states distribution and energetics in* TiO_2.

5.3. Aesthetic optimization of TB207-based NIR-DSSC with EI and ESI electrolytes

The relationship between photo-anode thickness (2, 4, and 6 µm) and the device's optical properties with a conventional I_3^-/I^- based electrolyte (**EI**) is reported in Figure 82. A concentration of 5 mmol/L CDCA is kept constant, which corresponds to the optimized conditions. As one could expect, the AVT value is affected by the film's thickness. With **EI** electrolyte, an increase of 10 % in AVT value is observed, from 63 % for 6 µm, 70 % for 4 µm, and to 73 % for 2 µm thick TiO_2 film (Figure 82.a). In these comparative experiments, an anti-reflective coating (ARC) based on a thin layer of SiO_2 nanoparticles was deposited by spin-coating on the external sides of the devices to minimize glass reflections. The ARC deposition allows achieving ca. 4 % gain in AVT by minimizing light reflection at the interface between glass and air. In other words, a 77 % AVT is reached for the 2 µm thick TiO_2, whereas 75 % and 68 % are obtained for 4 µm and 6 µm thick photo-anode, respectively. The calculated absorbance spectra from the total transmission measurements show that while increasing the thickness of TiO_2 films, we certainly increase the film's optical density, but without favoring the formation of more aggregates. This can be concluded from the direct comparison between the ratio of the main absorption band at 770 nm and the shoulder at ca. 700 nm (Figure 82.b).

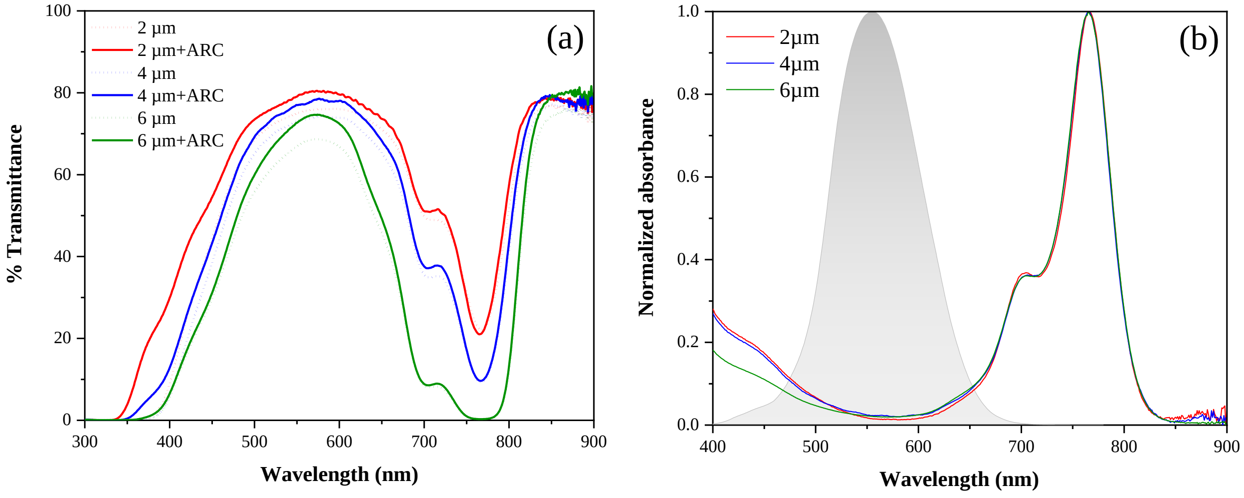

*Figure 82. (**a**) Total transmittance spectra of full devices employing different TiO_2 thicknesses sensitized with **TB207** dye including **EI** electrolyte (dotted lines) and with SiO_2 ARC deposited on both external sides of the devices (lines). (**b**) Normalized absorbance spectra of full devices employing different TiO_2 thicknesses with **EI** electrolyte The shaded area in grey represents the human eyes' photopic response.*

However, it is crucial while optimizing the photoanode’s thickness for aesthetics to evaluate the photovoltaic performance, as the TiO_2 thickness controls the number of dye molecules grafted and thus has a direct effect on the power conversion efficiencies. The different thicknesses of TiO_2 used in the AVT study were also investigated for their effect on the PCE values. The J-V curves corresponding to these devices are reported in Figure 83.a. While the V_{oc} is almost not affected, the J_{sc} drops from 12.5 mA/cm² for a 6 µm thick TiO_2, to 11.8 mA/cm² and 8.3 mA/cm² for the 4 and 2 µm TiO_2, respectively. This leads to a loss, even though moderate, of the PCE from 2.7 % to 2.5 % and 1.9 %.

Here the importance of the light utilization efficiency (LUE) is highlighted to determine the best condition balancing both AVT and PCE values. As reported in Figure 83.b, the LUE increases from 1.46 % for a 2 µm-based DSSC to 1.87 % with the 4 µm thick photo-anode and then stabilizes (LUE = 1.84 % for 6 µm thickness). In other words, the 2 µm-based device achieves the highest level of transparency, whereas the thicker one affords to achieve the best PCE. However, as moving from 4µm to 6 µm TiO_2 leads to a loss of 7% in AVT, and as the PCE is not drastically affected (2.5% and 2.7%), the best condition would be the 4 µm TiO_2.

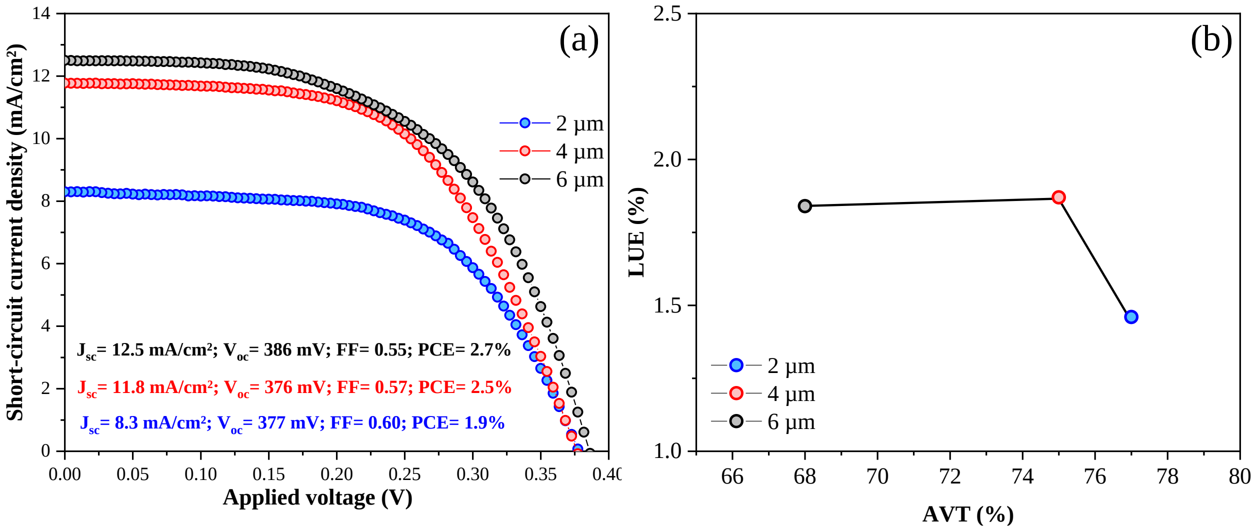

*Figure 83. (**a**) Comparison of (J-V) curves of **TB207**-based NIR-DSSC using different TiO_2 thicknesses, 2 µm in blue, 4 µm in red, and 6 µm in black. (**b**) LUE evolution as a function of AVT for different TiO_2 thicknesses.*

For a quantitative color perception, we calculated the CIE 1931 x,y chromaticity coordinates, CRI, CCT values and determined the dominant wavelength and the color purity of the full device incorporating both **EI** and **ESI4** electrolytes and different TiO_2 thicknesses. As for AVT, the TiO_2

thickness affects the color rendering properties of the final device. Figure 84 shows that the CIE x,y coordinates of devices with **EI** electrolyte shift towards the white point as the TiO_2 thickness decreases, with increasing CRI values of 82.1, 89.7, and 92.9 for 6 µm, 4 µm, and 2 µm-thick photoanode, respectively.

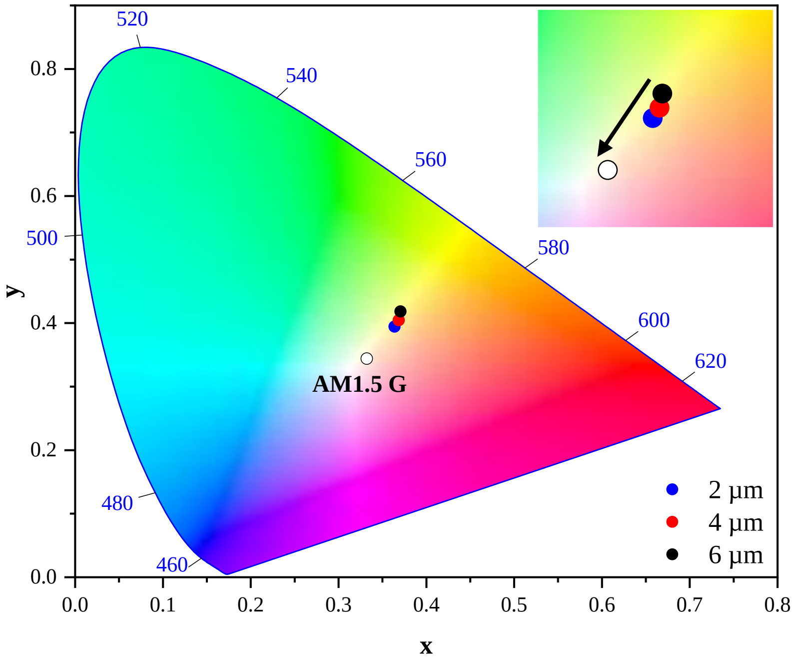

Figure 84. 1931 CIE chromaticity diagram showing the shift towards the white point (AM 1.5G in this case) when decreasing the thickness of TiO_2 film in the ***TB207****-based DSSC with* ***EI*** *electrolyte.*

The CCT values are around 4500 K, which indicates that the perceived colors of the transmitted light are considered natural white. However, both dominant wavelength and color purity are intuitive quantities that will give a better understanding of the color perceived.[128] The dominant wavelength with **EI** electrolyte is determined to be 570 nm for 2 µm and 4 µm thick TiO_2 and 568 nm for the 6 µm thick film. The 570 nm represents an orange-yellow, while the 568 represents a slight shift to green. We calculated a color saturation value of 28 % and 32 % of the 570 nm-dominated color for 2 µm and 4 µm thick TiO_2, respectively. For the 6 µm thick TiO_2, the color saturation was 35 %. These values imply two main conclusions: the TiO_2 thickness plays a role in controlling the coloration of the DSSCs, and higher dye loading of **TB207** with thicker TiO_2 leads to the greenish-yellow appearance when combined with **EI** electrolyte. This is due to the increased absorbance of the NIR light by the dye molecules. All the calculated aesthetical values for all the reported devices are summarized in Table 21.

*Table 21. Transparency and color metrics calculated for **TB207**-based NIR-DSSC with **EI** electrolyte and for different TiO_2 thicknesses*

TiO_2 thickness (µm)	AVT (%)	AVT (%) + ARC	CRI	CCT (K)	x,y CIE 1931	Dominant wavelength (nm)	Color saturation (%)
2	73	77	92.9	4786.0	x = 0.3543 y = 0.3798	570	28
4	70	75	89.7	4554.1	x = 0.3650 y = 0.3988	570	32
6	63	68	82.1	4475.5	x = 0.3719 y = 0.4206	568	35

As confirmed with **EI** electrolyte, the aesthetics are correlated to the film's thickness. As such, we carried out the same set of experiments with the hybrid sulfur/iodide electrolyte **ESI4** to identify the influence of the transparent redox mediator in the final values of AVT and color metrics. Note that all metrics are for devices with SiO_2 ARC layers. Figure 85.a shows the evolution of the transmittance spectra of **TB207**-based NIR-DSSC in the presence of **ESI4** electrolyte and as a function of different TiO_2 thicknesses (2, 4, and 6 µm). Increasing the latter induces an AVT decrease from 78 % for 2 µm to 75% with 4 µm and 68 % with 6 µm thick photo-anode. The AVT values calculated with the colorless hybrid electrolyte (**ESI4**) are not different from those evaluated with the tri-iodide/iodide redox couple (**EI**). However, the color parameters are significantly affected.

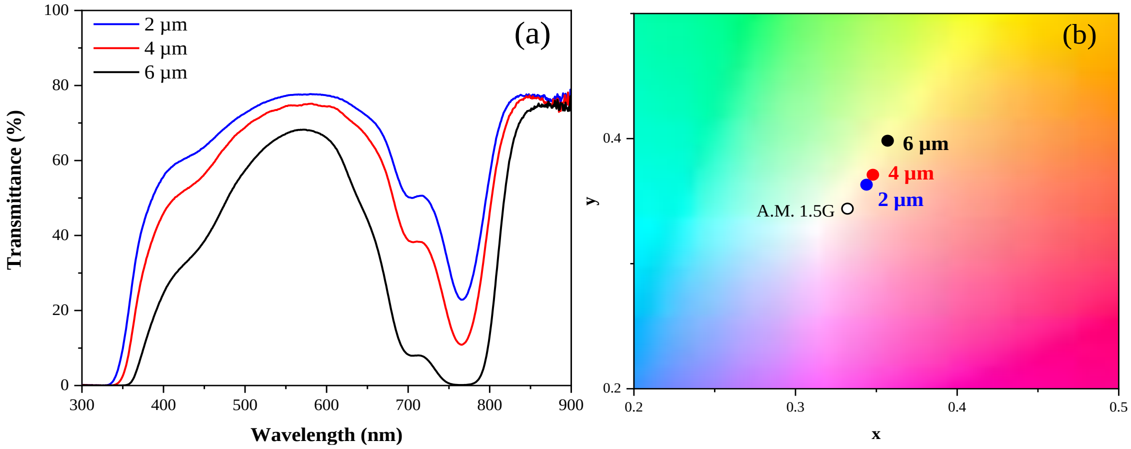

*Figure 85. (**a**) Evolution of the transmittance spectra of **TB207**-based NIR-DSSC incorporating different TiO_2 thicknesses, 2 µm (blue), 4 µm (red), and 6 µm (black) with **ESI4** electrolyte. (**b**) 1931 CIE chromaticity diagram showing the shift towards the white point (AM 1.5G in this case) when decreasing the thickness of TiO_2 film in the **TB207**-based DSSC with **ESI4** electrolyte.*

Indeed, a significant increase in CRI is observed, reaching an excellent value of 95 for the 2 µm-TiO_2-device. Such a high value is maintained even for higher photo-anode thicknesses; the CRI reaches 93.4 for 4 µm thick photo-anode and 84.6 for 6 µm thick photo-anode. Moreover, the x,y chromaticity coordinates are shifting closer to the white point, indicating improved color neutrality with **ESI4** electrolyte. The same trend of the dominant wavelength with **EI** electrolyte is observed for **ESI4** as the 2 and 4 µm-thick TiO_2 exhibit a 570 nm value, while 568 nm is determined for the 6 µm device. The advantage of the colorless **ESI4** electrolyte is confirmed with the decrease of the color saturation down to 12 % for a 2 µm device compared to 28 % with **EI** electrolyte. The color saturation increases with the increasing TiO_2 thickness to a value of 16 % for 4 µm thick device and 28 % for the 6 µm one. This is an important result that highlights the position of the device point near the white reference, thus revealing the important advantage to have introduced this **ESI4** electrolyte for rendering the NIR-DSSC free of any discernable coloration (Table 22).

*Table 22. Transparency and color metrics calculated for **TB207**-based DSSC with **ESI4** electrolyte incorporating different TiO_2 thicknesses*

TiO_2 thickness (µm)	AVT (%)	AVT(%) + ARC	CRI	CCT (K)	x,y CIE 1931	Dominant wavelength (nm)	Color saturation (%)
2	76	78	95.0	5075.9	x = 0.3440 y = 0.3631	570	12
4	73	75	93.4	4962.8	x = 0.3479 y = 0.3711	570	16
6	63	68	84.6	4776.9	x = 0.3570 y = 0.3983	568	28

As the 4 µm TiO_2 was chosen for best LUE values, we built up a transparent **TB207**-based NIR-DSSC with **ESI4** electrolyte. The obtained results are presented in Figure 86. The removal of the scattering layer results in a drop in the J_{sc} from 15.4 mA/cm² to 10.9 mA/cm², while the V_{oc} increases to 408 mV. It leads to a PCE of 2.5 %. This result underlines that the replacement of **EI** electrolyte by **ESI4** yields a similar level of performance while significantly improving the final aesthetics.

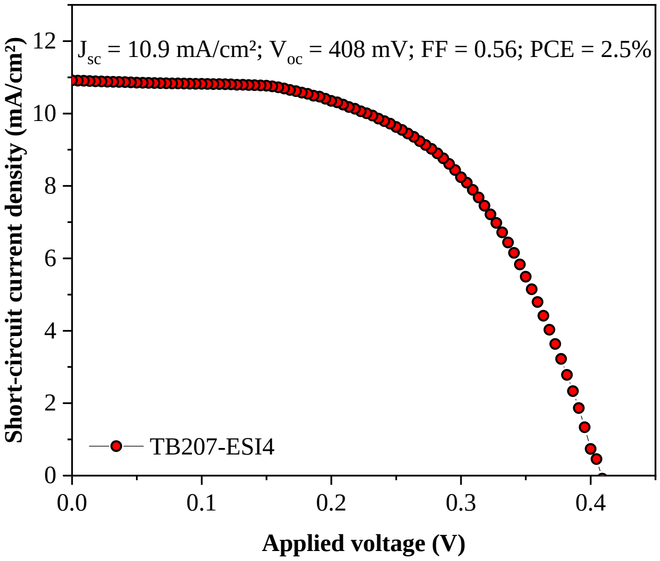

*Figure 86. (J-V) curve of a fully transparent 4 µm NIR-DSSC based on **TB207** dye and **ESI4** electrolyte under A.M.1.5G conditions*

In order to better perceive the impact of these numbers, the picture presented in Figure 87 shows a **TB207**-based NIR-DSSC with a 4 µm TiO_2 incorporating **EI** electrolyte (left picture) or **ESI4** electrolyte (right picture). The difference in color saturation, namely 28 % with **EI** and 12 % with **ESI4**, is revealed by the fading of the color seen in the picture. Moreover, the calculated shift in the chromaticity coordinates towards the white point is also confirmed by the visual appearance of the devices, where the **ESI4**-based device tends to have more color neutrality compared to the **EI**-based one. Based on all these results, we argue that the electrolyte is the main contributor to the final aesthetics of the devices after the dye. Even though the transparency level is not highly affected, the color saturation is totally dependent on the nature of the absorbing redox species in the electrolyte. Therefore, the S_n^{2-}/S^2 and I^- hybrid redox mediator constitutes the most promising candidate so far for the development of NIR-selective DSSC.

*Figure 87. Picture of full **TB207**-DSSC with a 4 µm TiO$_2$ incorporating **EI** electrolyte (left) and **ESI4** electrolyte (right).*

5.4. Dye regeneration study of TB207-based NIR-DSSC with the hybrid electrolyte

One excellent feature of **TB207** dye, as discussed in the previous chapter, is the sub-microsecond regeneration in contact with I_3^-/I^- redox couple (τ_1= 0.38 µs and τ_2= 2.52 µs). This fast half-time is in part related to the driving force for the hole transfer, in other words, on the redox potential of the mediator. Similar experiments were performed with the optimal **ESI4** electrolyte following rigorously the same conditions.

The streak images, in the 2 µs timescale, show a very comparable transient fingerprint corresponding to the **TB207** dye radical cation (Figure 88.a,b). The fit of the exponential decay obtained at 650 nm when **ESI4** electrolyte is used shows two components: τ_1= 0.20 µs (±0.03 µs) and τ_2= 1.92 µs (±0.15 µs) (Figure 88.c). These lifetimes are similar or slightly faster than the reference electrolyte based on I_3^-/I^-, which therefore suggests that S_n^{2-}/S^{2-} does not affect the dye regeneration kinetic. We propose the following mechanism of reactions of different species in the hybrid electrolyte as inspired by the original work of Sun et al.:[203]

$$2I^- + h^+ \rightarrow I_2^{-\cdot}$$

$$S^{2-} + I_2^{-\cdot} \rightarrow {}^{1}/_{2}\, S_2^{2-} + 2I^-$$

$$xS_2^{2-} \rightarrow (x-1)S^{2-} + S_{x+1}^{2-}$$

$$S_{x+1}^{2-} + 2e^- \rightarrow S_x^{2-} + S^{2-}$$

This mechanism shows that the hole transfer is still happening **TB207** radical cation to the I^- species in the electrolyte. In this reaction scheme, S^{2-} can efficiently reduce radical iodine $I_2^{-\cdot}$ to I^- before the latter disproportionate into I_3^- species, thus explaining that the electrolyte remains colorless under operation. At the counter-electrode/electrolyte interface, the polysulfides (i.e., S_n^{2-}, with n= 2, 3, and 4) play the role of the electron acceptor, thus closing the total regenerative loop of the device.

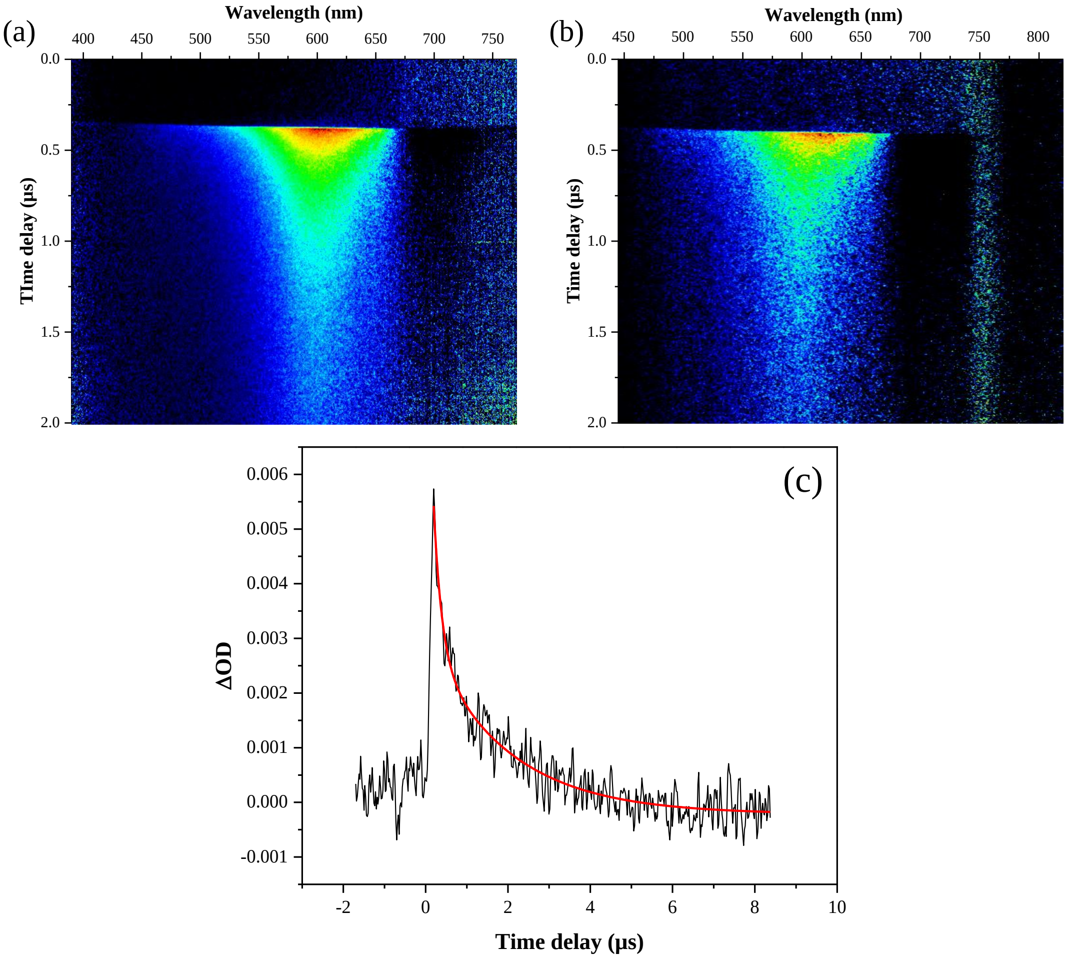

*Figure 88. Time-resolved transient absorption Streak image of the **TB207**-based NIR-DSSC in 2 µs time window for (**a**) the I_3^-/I^-redox couple (**EI** electrolyte), and (**b**) the hybrid S_n^{2-}/S^{2-} and I^- (**ESI4**) electrolyte. (c) Transient absorption kinetic measured at a probed 650 nm wavelength for **ESI4** electrolyte.*

5.5. Structural optimization of the PPcy dyes: New attempt with an asymmetrical push-pull dye

A glance into the literature was enough to highlight that the donor-π-bridge-acceptor (D- π -A) design has resulted in exceptional performances because of the use of a bulky, surface-protecting donor group referred to as the "Hagfeldt donor." For instance, developing the **SGT-137** dye, which possesses the Hagfeldt donor unit, allowed to achieve DSSCs with PCE of 12% in a conventional device, then 14.64% from a tandem cell fabricated with the zinc porphyrin **SGT-021**.[211] Furthermore, the co-sensitization of the dyes **ADEKA-1** and **LEG-4** on TiO_2 leads to solar devices converting solar energy at 14.2% and 14.7% under reduced light intensity (50%).[212]

5.5.1. Presentation of TB336 dye by computational study and synthesis procedure

Following this motivation, the general structure of the targeted molecule is presented in Figure 89, along with the structure of the synthesized dye, coded **TB336**. This dye molecule is still based on the same PPcy unit (highlighted in red) substituted by di-tert-butyl phenyls in order to provide solubility and limit the aggregation phenomenon (highlighted in yellow). The dye is non-symmetric and contains only one anchoring function of the carboxylic acid type, and is substituted at the para of the nitrogen atom (highlighted in grey). Through such structure, the objective is to direct the charge transfer on the PPcys, from the triphenylamine (TPA) electron donor unit, "push," to the electro-deficient unit or anchoring function, "pull." This is why it was chosen to place these substituents on either side of the cyanine system. In addition, and in accordance with the studies on different PPcy and thienyl-PPcy structures in chapter 4, phenyls are placed on the boron atom rather than fluorine to make the dye more reductive in the excited state and limit aggregation (highlighted in blue). Finally, the TPA unit is substituted on the para position with respect to the nitrogen atom.

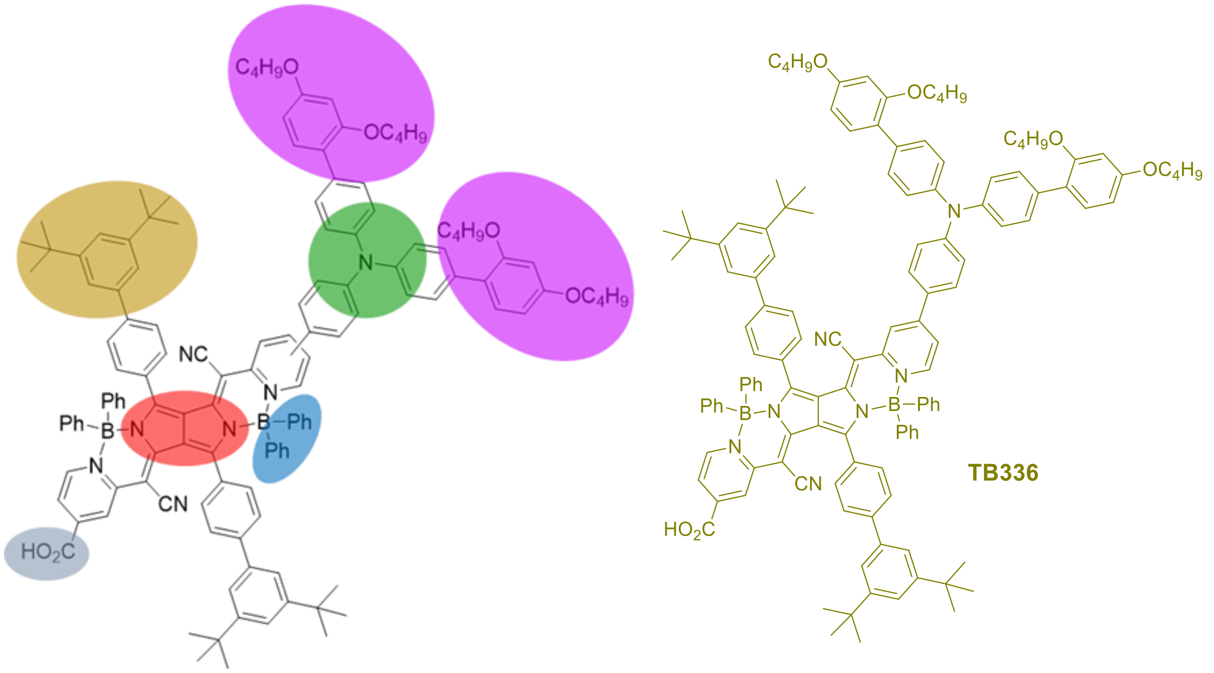

*Figure 89. The general structure of the push-pull pyrrolopyrrole cyanine dyes (PPcy) with the main features highlighted. On the right is the structure of the synthesized **TB336** dye.*

The DFT calculations show that the electronic density of the **TB336** dye on the HOMO orbitals is very sparsely distributed on the arylamine units, as shown in Figure 90. As for the PPcy **TB207** and **TB144** described previously, the electronic density repartition of the HOMO and LUMO levels are mainly distributed on the center of the molecule, i.e., on the pyrrolopyrrole cyanine core. A hypsochromic shift in the absorption band is expected for **TB336**.

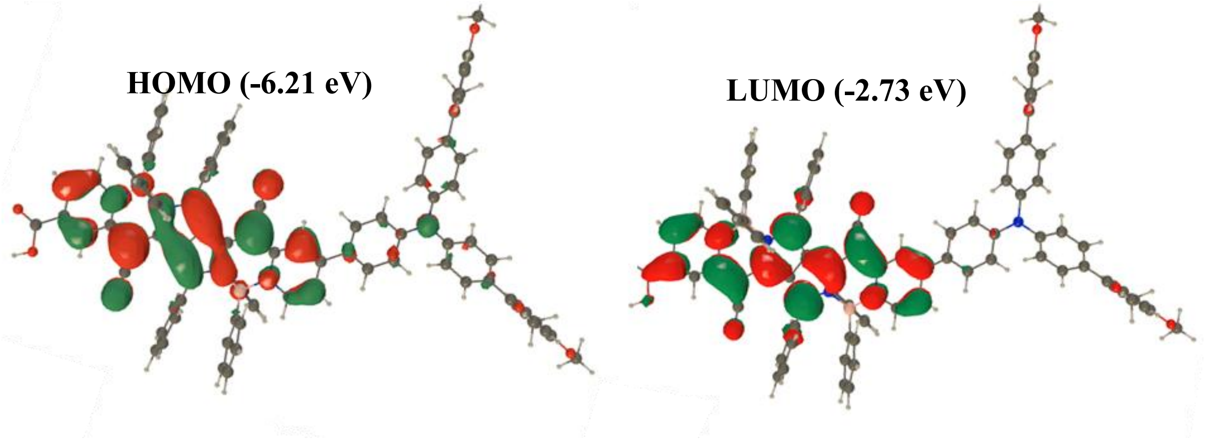

*Figure 90. Electronic repartition on the HOMO and LUMO levels of **TB336** dye obtained by DFT and TD-DFT calculations. The calculated values of HOMO and LUMO are also reported.*

The synthetic procedure is summarized in Scheme 8. The starting molecule is obtained during the synthesis of **TB144** and **TB207** dyes, as presented in chapter 4. The tri-arylamine intermediate was prepared in the lab at CEISAM with a yield of 90%.

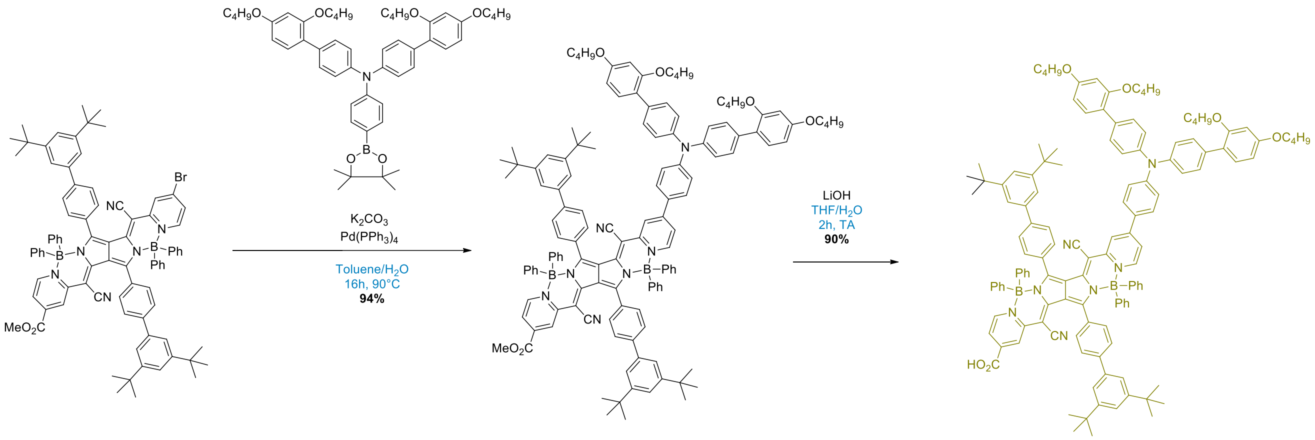

*Scheme 8. Synthetic procedure of the push-pull PPcy dye **TB336***

5.5.2. Characterization of TB336 dye in solution

The normalized absorption spectrum of **TB336** dye in chloroform/ethanol (1/9 v/v) solvent mixture is reported in Figure 91.a, along with the absorption of **TB207** dye for comparison. **TB336** exhibits the same optical fingerprint as **TB207,** with an absorption maximum being 3 nm red-shifted (λ_{max} = 761 nm). The shoulder is shifted to 688 nm. It contains a contribution from vibronic states slightly less pronounced in **TB336** than **TB207**. However, we can notice that the S_0-S_n transition, at around 400 nm, is more intense for **TB336**, which renders the dye solution brownish-yellow rather than greenish like **TB207**.

The absorption spectrum of **TB336** also possesses the fingerprint of the triphenylamine (TPA) group at ca. 340 nm. However, this absorption lies out of the photopic response range, and we expect no harmful effect on the AVT values. The molar extinction coefficient ($\varepsilon = 1.28 \times 10^5$ $M^{-1}cm^{-1}$) is in the same order of magnitude than **TB207** ($\varepsilon = 1.38 \times 10^5$ $M^{-1}cm^{-1}$). The excited-state lifetime of **TB336** in solution is 2.8 ns, thus also comparable to **TB207** (τ = 3.2 ns) (Figure 91.b).

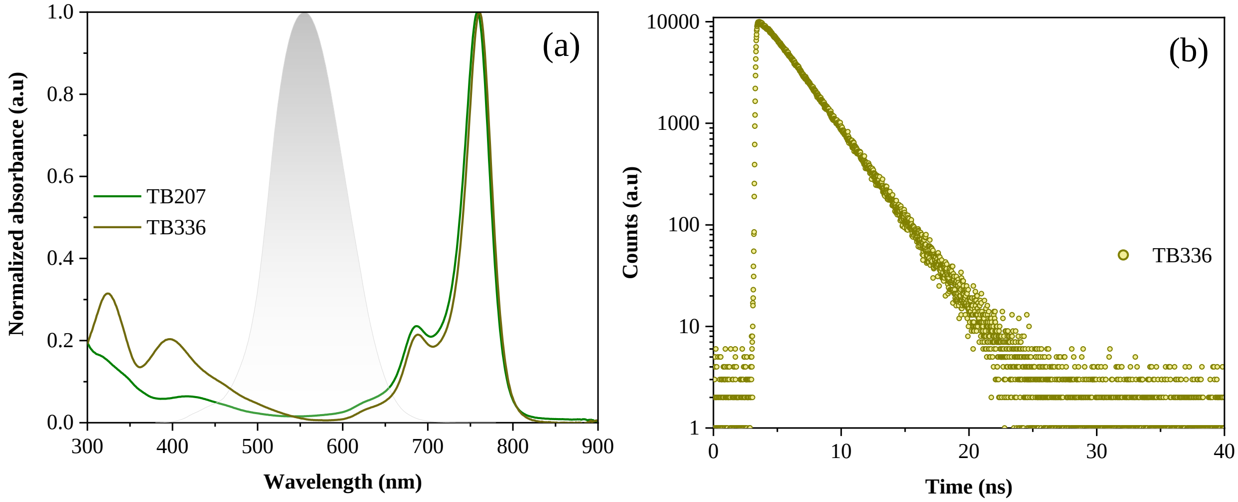

*Figure 91. (**a**) Normalized absorption spectra of **TB336** and **TB207** dyes in chloroform/ethanol (1/9) solvent mixture. The shaded grey area represents the human's eye photopic response (**b**) PL decay of **TB336** dye in solution with an excitation wavelength of 640 nm and emission wavelength of 780 nm.*

The PL properties of **TB336** were followed by steady-state excitation/emission mapping presented in Figure 92. The 2D-contour plot shows an intense emission in the NIR region at ca.800 nm with excitation wavelength at the 300-400 nm and at the 700-800 nm range. The PL cartography is similar to the one recorded for the PPcy **TB207**.

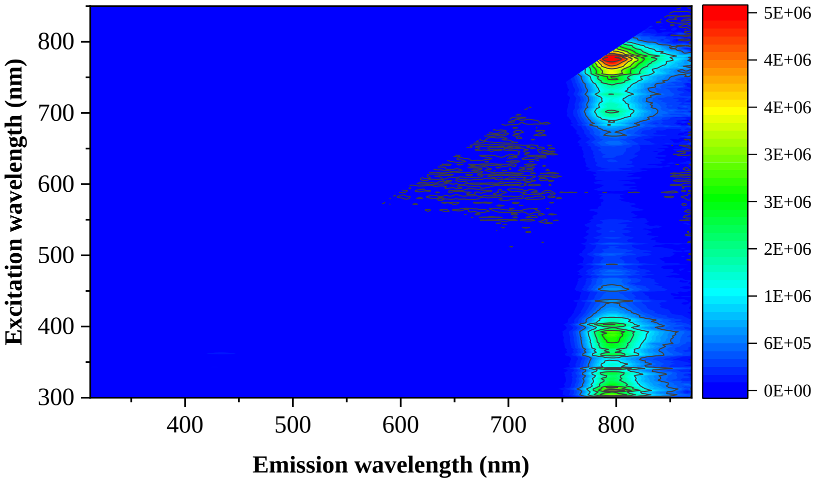

*Figure 92. 2D contour plot of the excitation/emission map of **TB336 dye** in CHCl$_3$/ethanol (1/9 v/v) solution.*

5.5.3. Photovoltaic performance and aesthetic evaluation of the push-pull PPcy dye TB336

We started the optimization of **TB336** dye with the conventional tri-iodide/iodide redox couple. For this, we used the same electrolyte **EI** optimized for **TB207** dye, i.e., 1 mol/L DMII, 1 mol/L

LiTFSI, and 0.03 mol/L I_2 in acetonitrile/valeronitrile (85/15 v/v) solvent mixture. Interestingly, the **TB336** dye achieves a very good 3.6 % PCE without any CDCA. It produces a relatively high J_{sc} value of 18.3 mA/cm². The V_{oc} measured in the CDCA-free condition is 388 mV which is 40 mV higher than what is measured in the same conditions for the **TB207** dye. Increasing the CDCA concentration to 1 mmol/L (corresponding to 1/10 dye/CDCA ratio) leads to a slight decrease in the J_{sc} value to 17.7 mA/cm². However, a 26 mV gain in V_{oc} is achieved, and an increased fill factor value to 0.54 affords to reach 4.1% PCE. A same trend is observed upon increasing the CDCA concentration to 2 mmol/L (1/20 ratio) leading to 4.2 % PCE (J_{sc} = 17.3 mA/cm², V_{oc} = 430 mV, ff = 0.56). The J-V evolution of **TB336**-based DSSC and the photovoltaic parameters are presented in Figure 93 and Table 17, respectively.

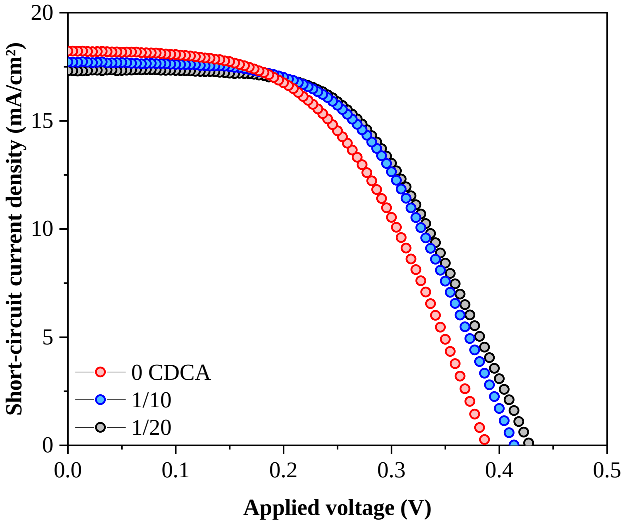

*Figure 93. Evolution of the (J-V) curve for **TB336**-based DSSC as a function of CDCA concentration under A.M. 1.5G conditions.*

*Table 23. Photovoltaic parameters of **TB336**-based DSSC with different CDCA concentration.*

[CDCA] (mmol/L)	J_{SC} (mA/cm^2)	V_{OC} (mV)	FF	PCE (%)
0	18.3	388	0.51	3.6
1	17.7	414	0.54	4.1
2	17.3	430	0.56	4.2

All of the above devices were achieved with a 6 µm-thick mesoporous TiO_2 sheltered by a 5 µm-thick scattering one. For a fully transparent **TB336**-DSSC, we adopted the LUE optimized conditions for **TB207** dye. For this, we built up devices with only a 4 µm transparent mesoporous TiO_2 layer, and the results with **EI** and **ESI4** electrolytes are shown in Figure 94. The J-V curves reported in Figure 94.a show that removing the scattering layer leads to a drop in J_{sc} from 17.3 mA/cm² to 13.8 mA/cm² with the **EI** electrolyte. A slight drop of 20 mV in V_{oc} to 410 mV is noticed while the FF value is not affected. As a result, the PCE of the transparent DSSC achieves 3.2%. Replacing **EI** with the colorless **ESI4** electrolyte, we experienced a slightly better PCE reaching a record of 3.4 % (J_{sc} = 13.1 mA/cm², V_{oc} = 423 mV and FF = 0.61).

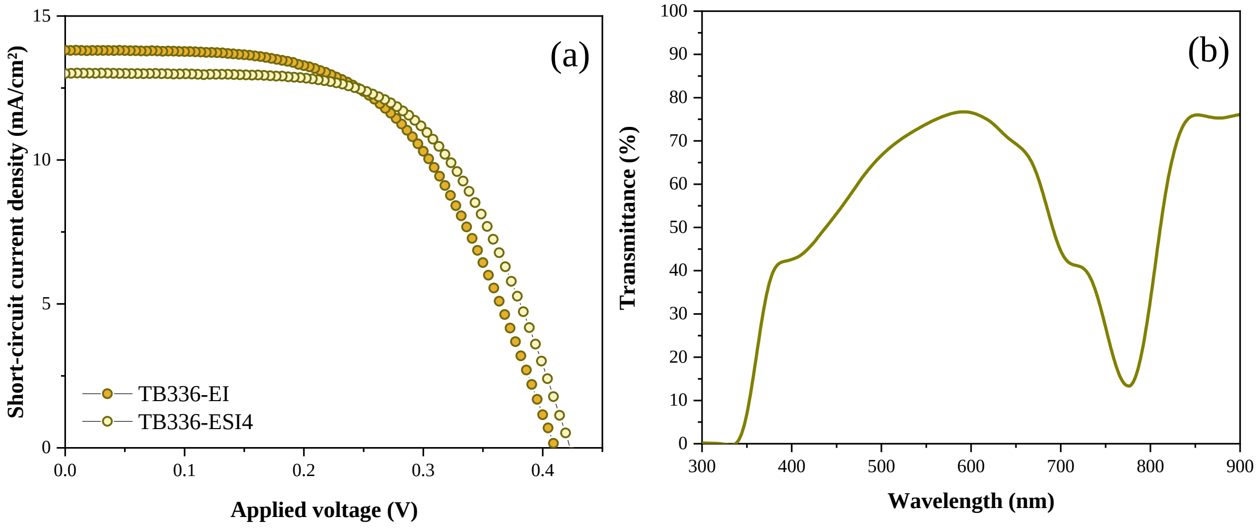

*Figure 94. (**a**) Comparison of the (J-V) curve of **TB336**-based DSSC with either **EI** (orange) or **ESI4** (yellow) electrolytes. (**b**) Transmittance spectrum of **TB336**-DSSC with a 4 µm-TiO_2 and **ESI4** electrolyte. SiO_2 ARC is deposited on both external sides of the device.*

The transmittance of a device built with the same conditions, i.e., 4 µm TiO_2, **TB336** dye with 1/20 ratio of CDCA, and **ESI4** electrolyte, is reported in Figure 94.b. This device exhibits an AVT of 73 %, leading to a LUE of 2.5 %. The chromaticity coordinates are calculated to be x = 0.3554 and y = 0.3753, with a CCT value of 4735 K (ie. 200 K lower than **TB207**) (Figure 95). The **TB336-ESI4**-DSSC achieved an excellent CRI value of 94. We highlight here that the AVT and CRI values are similar to **TB207**. This is revealed by the different hues perceived through the two different devices, as the dominant wavelength for the **TB336**-DSSC is 571 nm compared to 568 nm for **TB207**. The color saturation of the **TB336** device is 19 %, compared to 16 % for **TB207**.

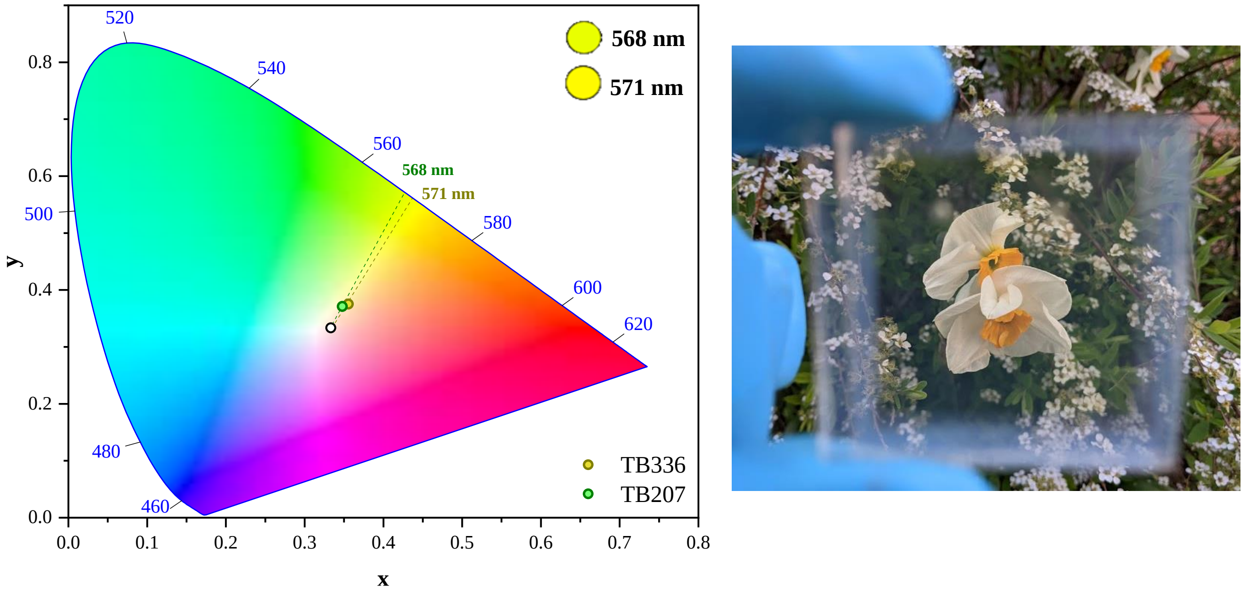

*Figure 95. CIE1931 x,y chromaticity diagram with the position of **TB207**-based DSSC (green point) and **TB336**-based DSSC (dark yellow point) with **ESI4** electrolyte. The white point is the equal energy point. In the inset is the color perceived from the dominant wavelength calculated for each device. The picture on the right is for the **TB336**-DSSC used in this evaluation (4 µm TiO_2 and **ESI4** electrolyte).*

Another very interesting characteristic of **TB336** dye is its enhanced stability in devices in comparison to the PPcy dye **TB207**. Figure 96 shows the evolution of photovoltaic parameters of both **TB336** and **TB207** DSSC with **EI** electrolyte under shelf-life aging conditions. While **TB207**-DSSC tends to lose >50% of its initial PCE after 300 hours, the PCE of **TB336**-DSSC retains >90% of its initial value up to 950 hours. We consider this as a very promising feature of **TB336** as a NIR-dye, and which, upon optimization, can achieve good performances under accelerated stability testing.

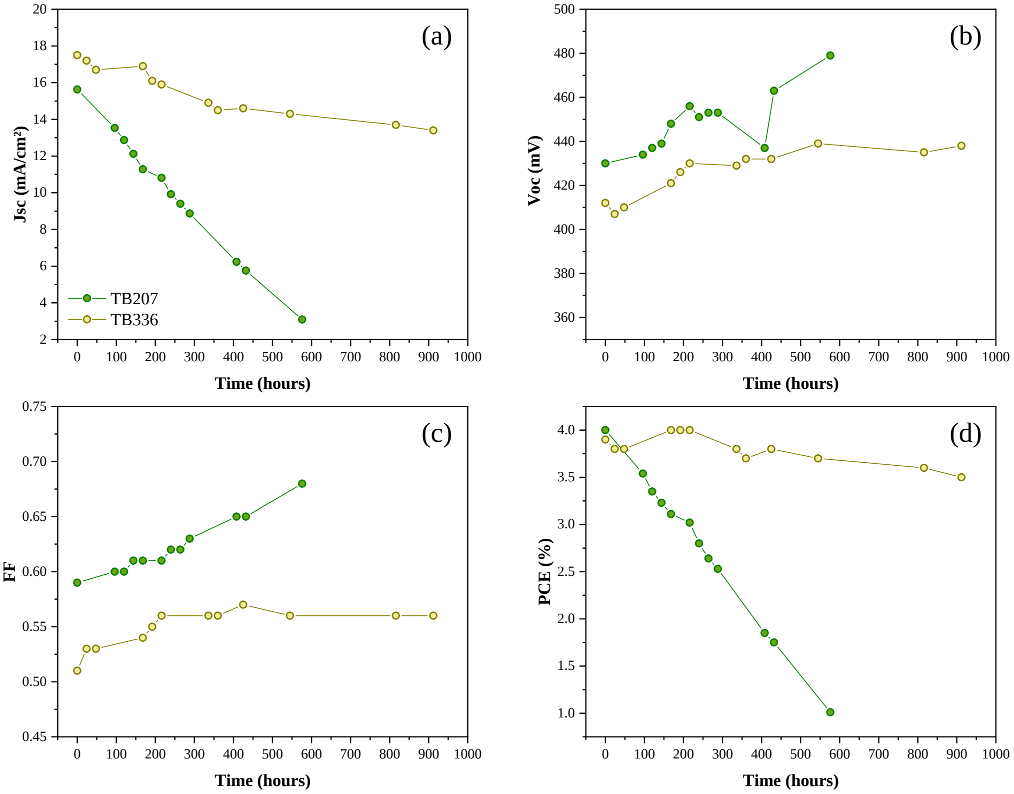

Figure 96. Evolution of (a) J_{sc}, (b) V_{oc}, (c) FF, and (d) PCE of ***TB207*** *(green) and* ***TB336*** *(yellow) -DSSC with* ***EI*** *electrolyte under shelf-life ageing conditions.*

5.6. Conclusions

In this chapter, we showed two approaches to the optimization of NIR-DSSC. Starting by comparing the color metrics between **TB207**-DSSC with the I_3^-/I^- (**EI**) and $[Co(phen)_3]^{3+/2+}$ (**ECo**) electrolytes, the results showed the dependence of AVT, CRI, and color metrics on the redox mediator. Even though AVT showed a slight drop from 70% to 68% while replacing **EI** with **ECo**, the CRI increased from 89.7 to 93.4, and the color saturation decreased from 28 % to 16 %. Therefore, the electrolyte was identified as the main-role player in the final visual appearance of the DSSC. However, this very good aesthetic level is mitigated by the low photovoltaic performances of the **TB207** associated with **ECo**. As such, encouraged by this first step towards a transparent electrolyte, we introduced a new electrolyte based on a hybrid sulfide/iodide redox mediator (coded **ESI**) to improve both the aesthetics and the performance. In particular, combining **TB207** dye and the hybrid electrolyte affords to achieve the highest aesthetic level so far reported for transparent DSSC (AVT 78%, CRI 95 and CIE *x,y* chromaticity coordinates very close to the white point (x = 0.3440; y = 0.3631). The color purity can be reduced from 32 % to 16 %. Upon optimization of the electrolyte composition, a 3.3% PCE is reached with the **ESI4** electrolyte incorporating a scattering layer and 2.5 % for a fully transparent device. We also presented the effect of the photoanode's thickness on both PCE and aesthetics, where 4 µm was found to be the best thickness to balance the performances (PCE = 2.5%) and the transparency (AVT = 75%).

The second approach consisted of dye engineering, where the concept of PPcy dyes was extended to a push-pull through the incorporation of a triphenylamine group, well-known as the "Hagfeldt donor." This dye, coded as **TB336**, achieved a remarkable performance, crossing 4% PCE with a relatively low concentration of CDCA. One very important outcome of this approach is that this new dye overcomes, even more, the formation of harmful aggregation, with a PCE of 3.6% with CDCA free conditions and up to 4.2% with 1/20 (**TB336**/CDCA). A fully transparent DSSC with a 4 µm TiO_2 sensitized with TB336 achieved 3.2% with the conventional **EI** electrolyte and a 3.4% with the colorless **ESI4** one. With an excellent CRI value of 94, an AVT of 74%, a low color saturation of 19%, and an enhanced shelf-life stability, **TB336**-based DSSC represents so far the best solution to reach highly transparent, colorless, and efficient selective-NIR DSSC.

Conclusions and perspectives

Conclusions and perspectives

The main objective of this thesis work was to develop an efficient NIR-selective-DSSC, which exhibits high transparency and color neutrality. This technology falls into the domain of wavelength-selective TPV, which witnessed rapid progress in the past decade. The added value of UV/NIR-wavelength-selective TPV technologies is to avoid the significant inherent trade-off between performance (PCE) and transparency (AVT) occurring in broadband absorbing non-wavelength selective PV materials. Even when practical limitations are considered (including resistive losses, charge recombination, diode non-idealities, parasitic electrode absorption), it is estimated that single-junction and three-junction TPV solar cells fabricated with UV/NIR selective materials can achieve 13% PCE and 20% PCE, respectively (assuming 10% loss in SQ photocurrent, 10% losses in the SQ fill factor and 20% loss in SQ photovoltage), approaching conventional PV technologies commercially available today, with almost none of the visible absorption. Moreover, TPV characterization is more than PCE, as aesthetics are equally important. As such, we provide in chapter 2 a detailed explanation of colorimetry for photovoltaics that can help understand how to report the aesthetics of a PV device. Most importantly, we pave the way to a standard procedure to homogenize the comparison of different technologies.

Chapter 3 covers our first attempt towards NIR-DSSC development. Whereas the cyanine dye **VG20-C$_x$** provided the original impetus for the proof-of-concept a few years ago, the optimization of the dye structure, electrolyte composition, and sensitizing conditions, **VG20-C$_{16}$** led to a PCE of 3.1% with the conventional I_3^-/I^- redox couple (**EI** electrolyte). The in-depth kinetics study highlighted the limitation of the performances by the harmful dye aggregation, which was proved to hinder the charge injection (injection efficiency< 30%) due to the fast, non-productive monomer-to-aggregate charge transfer. Moreover, these aggregates are also responsible for the intense coloration of the DSSC, and avoiding the formation of the aggregates renders the device more color neutral. With the optimized conditions, our first attempt towards transparent NIR-DSSC achieved an AVT of 76% and a remarkable CRI value of 93.4. However, the hue perceived through our device is dominated by a 573 nm wavelength, which renders a yellowish-orange coloration with a 31% color saturation. This hue is attributed to the I_3^-/I^- electrolyte.

The second step was to tackle the dye engineering to avoid the detrimental aggregation issue limiting the performances of the NIR dyes. This resulted in developing a new series of dyes from the pyrrolopyrrole cyanine family discussed in chapter 4. One of these dyes, coded **TB207**, achieved the sought goal by recording remarkable performances, with a 3.1% PCE with no de-aggregating agent and up to 4% when optimized with the proper CDCA concentration and electrolyte composition. The kinetic study carried on **TB207** by femtosecond fluorescence and transient absorption spectroscopy confirmed the success of increasing the injection efficiency to 60-70 % compared to 30% to the cyanine dye **VG20**. The results suggest that even the monomer-to-aggregate energy transfer is happening in a 55 ps timescale, aggregates are believed to contribute to carrier injection and thus to J_{sc}.

Moreover, the PPcy **TB207** dye showed fast dye regeneration kinetics with the triiodide/iodide redox couple, with τ_1= 0.38 µs (±0.018 µs) and τ_2= 2.52 µs (±0.16 µs). These values are faster than those reported for conventional dyes and **VG20-C$_{16}$** cyanine dye. As such, quantitative regeneration yields are achieved within the **TB207**-based DSSC.

The last chapter dealt with two approaches dedicated to achieving color neutrality through colorless electrolytes and reaching higher performances. In the search for colorless electrolytes, cobalt complexes seemed the first obvious choice, as it has been widely studied in the literature. However, even it enhanced the final aesthetics of **TB207**-based DSSC, the performances were poor (PCE = 0.6%). As such, we introduced a new transparent electrolyte based on a hybrid sulfide/iodide redox mediator (coded **ESI**) to improve the aesthetics of wavelength-selective NIR-DSSC. The objective of the hybrid redox mediators is to achieve the reduction of the colored I_3^- species by the S^{2-}, and thus obtain a transparent and color-neutral electrolyte. Combining **TB207** dye and the hybrid electrolyte affords to achieve the highest aesthetic level so far reported for transparent DSSC (AVT 78%, CRI 95 and CIE *x,y* chromaticity coordinates very close to the white point (x = 0.3440; y = 0.3631). The color purity can be reduced from 32% with **EI** to 16% with the hybrid **ESI** electrolyte. Upon optimizing the electrolyte composition, a 3.3% PCE is reached with the **ESI4** electrolyte incorporating a scattering layer, whereas 2.5 % is achieved for a fully transparent device. We also presented the effect of the photoanode's thickness on both PCE and aesthetics, where 4 µm was found to be the best condition balancing the performance (PCE = 2.5%) and transparency (AVT = 75%), with an LUE of 1.87%.

The second approach consisted of dye engineering, where the concept of PPcy dyes was extended to a push-pull concept by incorporating a triphenylamine group, well-known as the “Hagfeldt donor.” This dye, denoted as **TB336**, achieved remarkable performance crossing 4% PCE, with a relatively low concentration of CDCA. One significant outcome of this approach is that the designed dye overcomes, even more, the formation of harmful aggregation, with a PCE of 3.6% with CDCA free conditions and up to 4.2% with 1/20 (**TB336**/CDCA). A fully transparent DSSC with a 4 µm TiO_2 sensitized with **TB336** achieves 3.2% with the conventional **EI** electrolyte and a 3.4% with the colorless **ESI4** one. With an excellent CRI value of 94, an AVT of 74%, a low color saturation of 19%, and enhanced shelf-life stability, **TB336**-based DSSC paves the way for highly transparent and colorless efficient **DSSC**, based on the NIR-selective light conversion. Such achievement credibly places the NIR-DSSC based on the PPcy dyes **TB207** and **TB336** as one of the best TPV technologies.

As the field of TPV matures, we expect more promising results from NIR-DSSC. Based on this thesis, a co-sensitization approach between the PPcy dye **TB207** (or eventually **TB336**) with the cyanine dye **VG20-C$_{16}$** represents an apparent approach to boost the PCE. As shown in Figure 97, the absorption of the PPcy-dyes **TB207** is blue-shifted compared to the cyanine **VG20-C$_{16}$**. A co-sensitization between these dyes will allow harvesting a larger portion of the NIR-light in the range of 700-900 nm. As both dyes were proved to exhibit the requirements for color-neutral DSSC, we expect that their combination will result in a fully transparent and color-neutral DSSC with a PCE > 5% with the hybrid sulfur/iodide electrolyte.

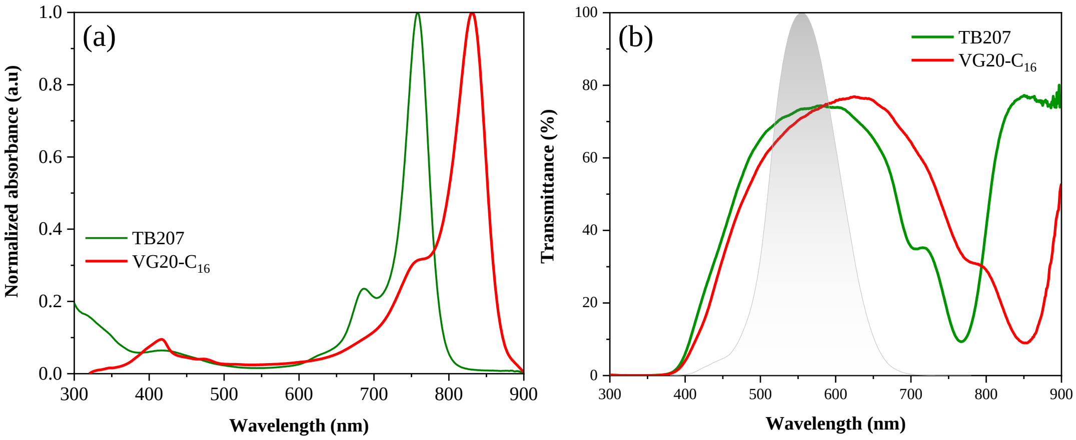

*Figure 97. (**a**) normalized absorption spectra of **TB207** and **VG20-C$_{16}$** in solution. (**b**) total transmittance spectra of full NIR-DSSC with **EI** electrolyte incorporating a 4 µm thick TiO_2 based on **TB207** (green) or **VG20-C$_{16}$** (red).*

On the other hand, based on the total sun photon flux between 350 to 400 nm and 700 to 950 nm, and considering the high currents produced by the PPcy dyes (> 15 mA/cm²), we can estimate that a fully optimized selective NIR-DSSC can reach a maximum PCE value of ca. 6%. This would be the result of a maximum photocurrent density achievable ca. 20 mA/cm², a cell photovoltage of ca. 0.45 V considering the redox potential of the hybrid sulfur/iodide electrolyte and a fill factor value of 0.65.

Moreover, the certified value of the best research-cell efficiency for DSSC technology remains 13% for the moment. The development of the NIR-DSSC with PCE > 4% opens the door to achieving higher PCE values. We propose either a co-sensitization approach or a tandem-DSSC one between our champion dye **TB336** and a panchromatic dye like the porphyrin **SGT137**. The suggested dye (**SGT137**) exhibits a broad IPCE spectrum in the range of 300-700 nm, with a maximum of 76% at 550 nm. As such, with our novel NIR-dyes, the IPCE spectrum can be extended up to 900 nm. However, the stability of the NIR-DSSC based on the cyanine and PPcy developed dyes remains the Achilles' heel, and the next steps in the field should pursue further studies on increasing the photochemical stability.

Every significant advance over the previous decade in the development of DSSCs has been made by the introduction of new principles, techniques, and materials. Herein, we presented for the first time selective NIR-light-harvesting in DSSC achieving PCE > 4%. Upon careful aesthetics optimization, the developed NIR-DSSC finds its position in the domain of TPV. We present in Figure 98 the literature on wavelength-selective TPV technologies, highlighting our work as the red star. For AVT values > 60%, our NIR-DSSC based on the PPcy dye **TB336** comprises one of the best outcomes in terms of LUE compared to other technologies. This work opens up new scientific and technological directions for the field of transparent PV, filling the gap between OPV having high performances with relatively lower AVT in the range of 50 % and LSC reaching above 80 % AVT but with relatively low performances.

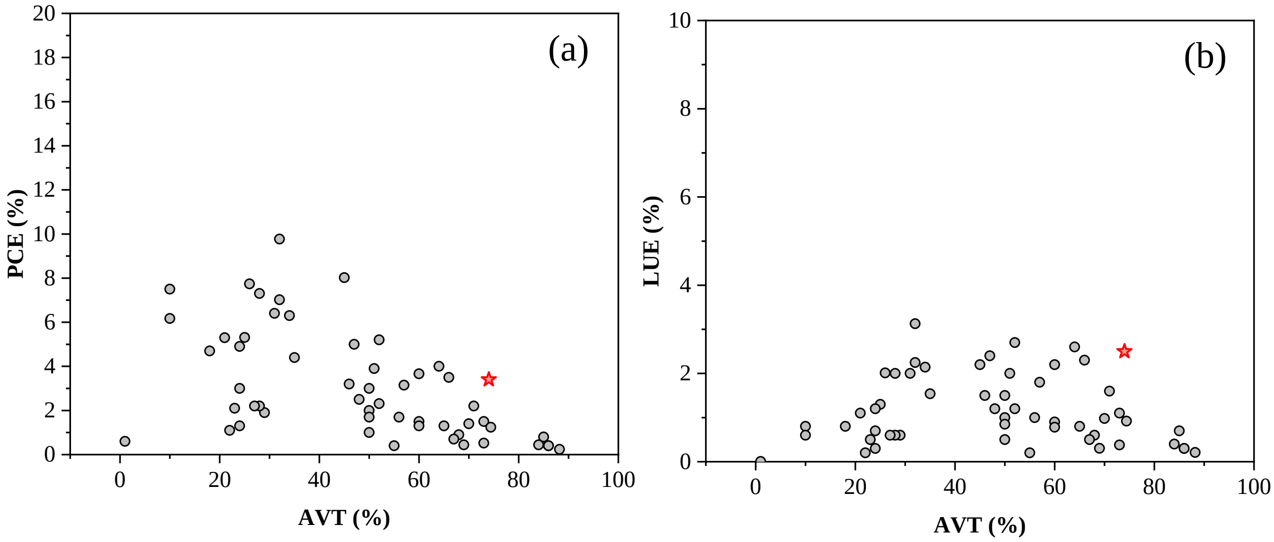

*Figure 98. (**a**) PCE vs. AVT and (**b**) LUE vs. AVT for wavelength-selective TPV technologies reported in the literature. The red star corresponds to the best outcome of my thesis work with NIR-DSSC based on **TB336** PPcy dye and hybrid sulfur/iodide electrolyte.*

New technologies emerge from R&D investment as low-volume, intrinsically expensive products. They rely on economies of scale to reduce production costs, shifting from operator-cost driven to bulk-material and process-cost driven. A critical stage in commercializing a new PV technology is to enter into a niche market by offering innovative service or unique product characteristics that are unattainable by the best alternative (e.g., silicon photovoltaics). Production scale is then expected to increase progressively, thereby lowering specific costs. Thus, to introduce NIR-DSSC technology, we must identify and target niches to create a market pull to advance the onset of the technology. Herein, we refer to the integration requirement chart presented in Figure 99. Envisaging the targeted application, the optimization of the photovoltaic performance and aesthetic quality can be clarified. We urge the developers to reflect on the end-user needs as the requirements are discussed. While BIPV and tinted architectural glass require a minimum of 50% AVT, electronic displays necessitate AVT > 80%. Electronic smart windows and low-power displays can be powered by 2-5% PCE, while they require high AVT values (> 50%). As aforementioned, the LUE metric is referenced across the different TPV technologies. LUE > 2.5% is required to achieve a competitive Levelized cost of electricity in BIPV application with PCE values of at least 5-10%. The achievement of my thesis work with a fully transparent and color-neutral NIR-DSSC is represented in Figure 99 as a red star. This technology achieving a 3.4% PCE and an AVT of 74%, thus an LUE value of 2.5%, positions itself in the domain of electronic smart windows. However, our expectations of such development increase the opportunities towards low-power displays for higher AVT values or window-integrated PV PCE values > 6%.

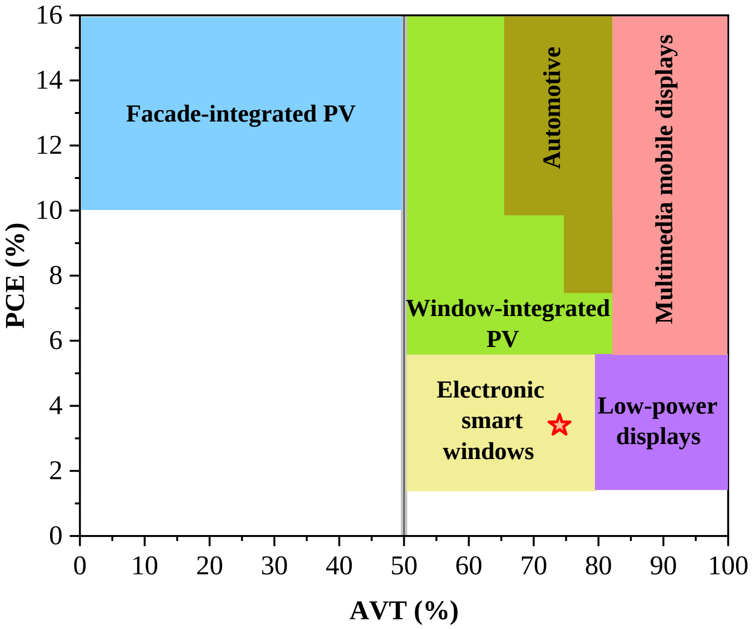

Figure 99. PV integration requirement as a function of PCE and AVT. The red star corresponds to the best outcome of my thesis work with NIR-DSSC based on ***TB336*** *PPcy dye and hybrid sulfur/iodide electrolyte.Reproduced from reference [24].*

On the other hand, my vision regarding the development of new technologies dedicated to harvesting renewable energy is to consider the sustainability and recyclability of the materials. Even though the DSSC has not yet reached the mass market, with various fields of application, vast quantities of DSSCs could be produced in the future and eventually end up in recycling processes. Applying the circular economy concept, there is now an opportunity to design DSSCs so that they can be easily recycled at the end of their useful life. In the case of the NIR-DSSC developed within the frame of my thesis work, the dyes are organic metal-free molecules. Even though Pt was used as a counter electrode, the research in our group is focusing on polymer-based transparent materials to optimize the technology.

References

[1] REN21. Renewables 2020 global status report. Paris. 2020.

[2] M. Ram, M. Child, A. Aghahosseini, D. Bogdanov, A. Lohrmann, C. Breyer, *J. Clean. Prod.* **2018**, *199*, 687.

[3] [IEA] - International Energy Agency. World energy outlook. 2020. p. 2020. Paris.

[4] IEA, https://www.iea.org/reports/the-critical-role-of-buildings.

[5] B. Energy, BP Energy Outlook: 2019 Edition, BP p.l.c., London 2019.

[6] BIPV Technologies and Markets: 2017-2026 (n-tech Research, 2017); https://www.ntechresearch.com/market-reports/buildingintegrated- photovoltaics-reports-2017-2024/.

[7] J. Yan, Y. Yang, P. Elia Campana, J. He, *Nat. Energy* **2019**, *4*, 709.

[8] E. Rey, *Lucerne, Quart Publ.* **2014**, *coll. Nota*.

[9] D. E. Attoye, K. A. T. Aoul, A. Hassan, *Sustain.* **2017**, *9*.

[10] E. Biyik, M. Araz, A. Hepbasli, M. Shahrestani, R. Yao, L. Shao, E. Essah, A. C. Oliveira, T. Del Cano, E. Rico, *Eng. Sci. Technol. an Int. J.* **2017**, *20*, 833.

[11] H. C. Curtius, *Renew. Energy* **2018**, *126*, 783.

[12] H. Q. Chen, T. Honda, M. C. Yang, *J. Mech. Des. Trans. ASME* **2013**, *135*.

[13] A. Faiers, C. Neame, *Energy Policy* **2006**, *34*, 1797.

[14] Http://www.statista.com/statistics/, 567212/reason-for-solar-panel-disinterest-in-the-us-among-utilitycustomers/.

[15] (n-tech Research), **2017**, https://www.ntechresearch.com/market.

[16] https://www.marketwatch.com/press-release/building-integrated-photovoltaics-bipv-market-size-2021-analysis-by-business-share-strategies-investment-opportunities-revenue-expectation-future-trends-prominent-players-covid-19-impact-analysis-and-forecast-till.

[17] M. Pagliaro, R. Ciriminna, G. Palmisano, *Prog. Photovoltaics Res. Appl.* **2010**, *18*, 61.

[18] P. Heinstein, C. Ballif, L. E. Perret-Aebi, *Green* **2013**, *3*, 125.

[19] C. Ballif, L. E. Perret-Aebi, S. Lufkin, E. Rey, *Nat. Energy* **2018**, *3*, 438.

[20] BIPV Product Overview for Solar Facades and Roofs (SUPSISEAC, 2015).

[21] A. Hagfeldt, G. Boschloo, L. Sun, L. Kloo, H. Pettersson, *Chem. Rev.* **2010**, *110*, 6595.

[22] H. J. Snaith, *Adv. Funct. Mater.* **2010**, *20*, 13.

[23] F. Sauvage, F. Di Fonzo, A. Li Bassi, C. S. Casari, V. Russo, G. Divitini, C. Ducati, C. E. Bottani, P. Comte, M. Graetzel, *Nano Lett.* **2010**, *10*, 2562.

[24] C. J. Traverse, R. Pandey, M. C. Barr, R. R. Lunt, *Emergence of highly transparent photovoltaics for distributed applications*, Vol. 2, Nature Publishing Group, **2017**, pp. 849–860.

[25] P. Boyce, N. Eklund, S. Mangum, C. Saalfield, L. Tang, *Int. J. Light. Res. Technol.* **1995**, *27*, 145.

[26] M. Biancardo, K. Taira, N. Kogo, H. Kikuchi, N. Kumagai, N. Kuratani, I. Inagawa, S. Imoto, J. Nakata, *Sol. Energy* **2007**, *81*, 711.

[27] G. E. Eperon, V. M. Burlakov, A. Goriely, H. J. Snaith, *ACS Nano* **2014**, *8*, 591.

[28] S. Mattiello, A. Sanzone, F. Bruni, M. Gandini, V. Pinchetti, A. Monguzzi, I. Facchinetti, R. Ruffo, F. Meinardi, G. Mattioli, M. Sassi, S. Brovelli, L. Beverina, *Joule* **2020**, *4*, 1988.

[29] C. Chen, L. Dou, R. Zhu, C. Chung, T. Song, Y. B. Zheng, C. E. T. Al, *ACS Nano* **2012**, 120712084458005.

[30] J. Yoon, A. J. Baca, S. Il Park, P. Elvikis, J. B. Geddes, L. Li, R. H. Kim, J. Xiao, S. Wang, T. H. Kim, M. J. Motala, B. Y. Ahn, E. B. Duoss, J. A. Lewis, R. G. Nuzzo, P. M. Ferreira, Y. Huang, A. Rockett, J. A. Rogers, *Nat. Mater.* **2008**, *7*, 907.

[31] G. E. Eperon, D. Bryant, J. Troughton, S. D. Stranks, M. B. Johnston, T. Watson, D. A. Worsley, H. J. Snaith, *J. Phys. Chem. Lett.* **2015**, *6*, 129.

[32] X. Zhang, G. E. Eperon, J. Liu, E. M. J. Johansson, *Nano Energy* **2016**, *22*, 70.

[33] M. Saifullah, S. Ahn, J. Gwak, S. Ahn, K. Kim, J. Cho, J. H. Park, Y. J. Eo, A. Cho, J. S. Yoo, J. H. Yun, *J. Mater. Chem. A* **2016**, *4*, 10542.

[34] R. Karsthof, P. Räcke, H. Von Wenckstern, M. Grundmann, *Phys. Status Solidi Appl. Mater. Sci.* **2016**, *213*, 30.

[35] E. Della Gaspera, Y. Peng, Q. Hou, L. Spiccia, U. Bach, J. J. Jasieniak, Y. B. Cheng, *Nano Energy* **2015**, *13*, 249.

[36] A. Polman, M. Knight, E. C. Garnett, B. Ehrler, W. C. Sinke, *Science (80-.).* **2016**, *352*.

[37] R. Brendel, *Thin-film crystalline silicon solar cells: physics and technology*, John Wiley & Sons, **2011**.

[38] S. Wang, B. D. Weil, Y. Li, K. X. Wang, E. Garnett, S. Fan, Y. Cui, *Nano Lett.* **2013**, *13*, 4393.

[39] C. Y. Tsai, C. Y. Tsai, *Renew. Energy* **2020**, *145*, 2637.

[40] E. Franklin, V. Everett, A. Blakers, K. Weber, *Adv. Optoelectron.* **2007**, *2007*.

[41] K. Lee, N. Kim, K. Kim, H. D. Um, W. Jin, D. Choi, J. Park, K. J. Park, S. Lee, K. Seo, *Joule* **2020**, *4*, 235.

[42] National Renewable Energy Laboratory, “Best research-cell efficiency chart” (2021). https://www.nrel.gov/pv/cell-efficiency.html (accessed 10,December, 2021).

[43] J. Wu, J. Chen, Y. Zhang, Z. Xu, L. Zhao, T. Liu, D. Luo, W. Yang, K. Chen, Q. Hu, F. Ye, P. Wu, R. Zhu, Q. Gong, **2017**.

[44] Z. Li, M. Yang, J. Park, S. Wei, J. J. Berry, K. Zhu, **2016**, *2*.

[45] S. S. Shin, W. S. Yang, J. H. Noh, J. H. Suk, N. J. Jeon, J. H. Park, J. S. Kim, W. M. Seong, S. Il Seok, *Nat. Commun.* **2015**, *6*, 1.

[46] G. Wang, D. Li, H. C. Cheng, Y. Li, C. Y. Chen, A. Yin, Z. Zhao, Z. Lin, H. Wu, Q. He, M. Ding, Y. Liu, Y. Huang, X. Duan, *Sci. Adv.* **2015**, *1*, 1.

[47] J. Harwell, J. Burch, A. Fikouras, M. C. Gather, A. Di Falco, I. D. W. Samuel, *ACS Nano* **2019**, *13*, 3823.

[48] C. H. Lin, B. Cheng, T. Y. Li, J. R. D. Retamal, T. C. Wei, H. C. Fu, X. Fang, J. H. He, *ACS Nano* **2019**, *13*, 1168.

[49] H. Wang, R. Haroldson, B. Balachandran, A. Zakhidov, S. Sohal, J. Y. Chan, A. Zakhidov, W. Hu, *ACS Nano* **2016**, *10*, 10921.

[50] L. Zhang, M. T. Hörantner, W. Zhang, Q. Yan, H. J. Snaith, *Sol. Energy Mater. Sol. Cells* **2017**, *160*, 193.

[51] D. H. Cao, C. C. Stoumpos, C. D. Malliakas, M. J. Katz, O. K. Farha, J. T. Hupp, M. G. Kanatzidis, *Apl Mater.* **2014**, *2*, 91101.

[52] D. Liu, C. Yang, P. Chen, M. Bates, S. Han, P. Askeland, R. R. Lunt, *ACS Appl. Energy Mater.* **2019**, *2*, 3972.

[53] R. R. Lunt, *Appl. Phys. Lett.* **2012**, *101*.

[54] A. J. Lopez-garcia, A. Bauer, R. F. Rubio, D. Payno, Z. J. Li-kao, S. Kazim, D. Hariskos,

V. Izquierdo-roca, E. Saucedo, A. Pérez-rodríguez, **2020**, *2000470*, 1.

[55] D. Liu, C. Yang, R. R. Lunt, *Joule* **2018**, *2*, 1827.

[56] ASTM G173-03(2020), Standard Tables for Reference Solar Spectral Irradiances: Direct Normal and Hemispherical on 37° Tilted Surface, **2020**.

[57] S. Y. Chang, P. Cheng, G. Li, Y. Yang, *Joule* **2018**, *2*, 1039.

[58] K.-S. Chen, J.-F. Salinas, H.-L. Yip, L. Huo, J. Hou, A. K.-Y. Jen, *Energy Environ. Sci.* **2012**, *5*, 9551.

[59] K. H. Hendriks, W. Li, M. M. Wienk, R. A. J. Janssen, *J. Am. Chem. Soc.* **2014**, *136*, 12130.

[60] Z. Liu, P. You, S. Liu, F. Yan, *ACS Nano* **2015**, *9*, 12026.

[61] Z. M. Beiley, M. G. Christoforo, P. Gratia, A. R. Bowring, P. Eberspacher, G. Y. Margulis, C. Cabanetos, P. M. Beaujuge, A. Salleo, M. D. McGehee, *Adv. Mater.* **2013**, *25*, 7020.

[62] C.-C. Chueh, S.-C. Chien, H.-L. Yip, J. F. Salinas, C.-Z. Li, K.-S. Chen, F.-C. Chen, W.-C. Chen, A. K.-Y. Jen, *Adv. Energy Mater.* **2013**, *3*, 417.

[63] X. Hu, L. Chen, L. Tan, Y. Zhang, L. Hu, B. Xie, Y. Chen, *Sci. Rep.* **2015**, *5*, 12161.

[64] C.-Y. Chang, L. Zuo, H.-L. Yip, Y. Li, C.-Z. Li, C.-S. Hsu, Y.-J. Cheng, H. Chen, A. K.-Y. Jen, *Adv. Funct. Mater.* **2013**, *23*, 5084.

[65] Q. Liu, L. G. Gerling, F. Bernal-Texca, J. Toudert, T. Li, X. Zhan, J. Martorell, *Adv. Energy Mater.* **2020**, *10*, 1904196.

[66] J. Zhang, G. Xu, F. Tao, G. Zeng, M. Zhang, Y. (Michael) Yang, Y. Li, Y. Li, *Adv. Mater.* **2019**, *31*, 1.

[67] M. G. Debije, P. P. C. Verbunt, B. C. Rowan, B. S. Richards, T. L. Hoeks, *Appl. Opt.*

2008, *47*, 6763.

[68] X. Luo, T. Ding, X. Liu, Y. Liu, K. Wu, *Nano Lett.* **2019**, *19*, 338.

[69] Y. Zhao, G. A. Meek, B. G. Levine, R. R. Lunt, *Adv. Opt. Mater.* **2014**, *2*, 606.

[70] C. Yang, M. Moemeni, M. Bates, W. Sheng, B. Borhan, R. R. Lunt, *Adv. Opt. Mater.* **2020**, *8*, 1.

[71] B. O'Regan, M. Gratzel, *Nature* **1991**, *353*, 737.

[72] K. Kakiage, Y. Aoyama, T. Yano, K. Oya, J. I. Fujisawa, M. Hanaya, *Chem. Commun.* **2015**, *51*, 15894.

[73] K. Zhang, C. Qin, X. Yang, A. Islam, S. Zhang, H. Chen, L. Han, *Adv. Energy Mater.* **2014**, *4*, 1.

[74] Q. Huaulmé, V. M. Mwalukuku, D. Joly, J. Liotier, Y. Kervella, P. Maldivi, S. Narbey, F. Oswald, A. J. Riquelme, J. A. Anta, R. Demadrille, *Nat. Energy* **2020**, *5*, 468.

[75] A. Roy, A. Ghosh, S. Bhandari, P. Selvaraj, S. Sundaram, T. K. Mallick, *J. Phys. Chem. C* **2019**, *123*, 23834.

[76] A. Ghosh, P. Selvaraj, S. Sundaram, T. K. Mallick, *Sol. Energy* **2018**, *163*, 537.

[77] K. Kim, S. K. Nam, J. H. Moon, *ACS Appl. Energy Mater.* **2020**, *3*, 5277.

[78] A. Fakharuddin, R. Jose, T. M. Brown, F. Fabregat-Santiago, J. Bisquert, *Energy Environ. Sci.* **2014**, *7*, 3952.

[79] D. Joly, L. Pellejà, S. Narbey, F. Oswald, T. Meyer, Y. Kervella, P. Maldivi, J. N. Clifford, E. Palomares, R. Demadrille, *Energy Environ. Sci.* **2015**, *8*, 2010.

[80] M. Godfroy, J. Liotier, V. M. Mwalukuku, D. Joly, Q. Huaulmé, L. Cabau, C. Aumaitre, Y. Kervella, S. Narbey, F. Oswald, E. Palomares, C. A. González Flores, G. Oskam, R. Demadrille, *Sustain. Energy Fuels* **2021**, *5*, 144.

[81] M. Godfroy, J. Liotier, V. M. Mwalukuku, D. Joly, Q. Huaulmé, L. Cabau, C. Aumaitre, Y. Kervella, S. Narbey, F. Oswald, E. Palomares, C. A. González Flores, G. Oskam, R. Demadrille, *Sustain. Energy Fuels* **2021**, *5*, 144.

[82] M. K. Nazeeruddin, P. Péchy, T. Renouard, S. M. Zakeeruddin, R. Humphry-Baker, P. Cointe, P. Liska, L. Cevey, E. Costa, V. Shklover, L. Spiccia, G. B. Deacon, C. A. Bignozzi, M. Grätzel, *J. Am. Chem. Soc.* **2001**, *123*, 1613.

[83] A. Abbotto, F. Sauvage, C. Barolo, F. De Angelis, S. Fantacci, M. Graetzel, N. Manfredi, C. Marinzi, M. K. Nazeeruddin, *Dalt. Trans.* **2011**, *40*, 234.

[84] S. Altobello, R. Argazzi, S. Caramori, C. Contado, S. Da Fré, P. Rubino, C. Choné, G. Larramona, C. A. Bignozzi, *J. Am. Chem. Soc.* **2005**, *127*, 15342.

[85] A. Baumann, C. Curiac, J. H. Delcamp, *ChemSusChem* **2020**, *13*, 2503.

[86] J. Park, G. Viscardi, C. Barolo, N. Barbero, *Chimia (Aarau).* **2013**, *67*, 129.

[87] T. Higashino, Y. Kurumisawa, S. Nimura, H. Iiyama, H. Imahori, *European J. Org. Chem.* **2018**, *2018*, 2537.

[88] W. M. Campbell, A. K. Burrell, D. L. Officer, K. W. Jolley, *Coord. Chem. Rev.* **2004**, *248*, 1363.

[89] Y. Fu, T. Lu, Y. Xu, M. Li, Z. Wei, H. Liu, W. Lu, *Dye. Pigment.* **2018**, *155*, 292.

[90] Ö. Birel, S. Nadeem, H. Duman, *J. Fluoresc.* **2017**, *27*, 1075.

[91] D. Saccone, S. Galliano, N. Barbero, P. Quagliotto, G. Viscardi, C. Barolo, *European J. Org. Chem.* **2016**, *2016*, 2244.

[92] M. K. Nazeeruddin, R. Humphry-Baker, M. Grätzel, D. Wöhrle, G. Schnurpfeil, G. Schneider, A. Hirth, N. Trombach, *J. Porphyr. Phthalocyanines* **1999**, *3*, 230.

[93] J.-J. Cid, J.-H. Yum, S.-R. Jang, M. K. Nazeeruddin, E. Martínez-Ferrero, E. Palomares, J.

Ko, M. Grätzel, T. Torres, *Angew. Chemie* **2007**, *119*, 8510.

[94] P. Y. Reddy, L. Giribabu, C. Lyness, H. J. Snaith, C. Vijaykumar, M. Chandrasekharam, M. Lakshmikantam, J. H. Yum, K. Kalyanasundaram, M. Grätzel, M. K. Nazeeruddin, *Angew. Chemie - Int. Ed.* **2007**, *46*, 373.

[95] S. Mori, M. Nagata, Y. Nakahata, K. Yasuta, R. Goto, M. Kimura, M. Taya, *J. Am. Chem. Soc.* **2010**, *132*, 4054.

[96] T. Ikeuchi, H. Nomoto, N. Masaki, M. J. Griffith, S. Mori, M. Kimura, *Chem. Commun.* **2014**, *50*, 1941.

[97] M. E. Ragoussi, J. J. Cid, J. H. Yum, G. De La Torre, D. Di Censo, M. Grätzel, M. K. Nazeeruddin, T. Torres, *Angew. Chemie - Int. Ed.* **2012**, *51*, 4375.

[98] M. E. Ragoussi, J. H. Yum, A. K. Chandiran, M. Ince, G. De La Torre, M. Grätzel, M. K. Nazeeruddin, T. Torres, *ChemPhysChem* **2014**, *15*, 1033.

[99] S. Mathew, A. Yella, P. Gao, R. Humphry-Baker, B. F. E. Curchod, N. Ashari-Astani, I. Tavernelli, U. Rothlisberger, M. K. Nazeeruddin, M. Grätzel, *Nat. Chem.* **2014**, *6*, 242.

[100] M. Pengshung, J. Li, F. Mukadum, S. A. Lopez, E. M. Sletten, *Org. Lett.* **2020**, *22*, 6150.

[101] E. D. Cosco, A. L. Spearman, S. Ramakrishnan, J. G. P. Lingg, M. Saccomano, M. Pengshung, B. A. Arús, K. C. Y. Wong, S. Glasl, V. Ntziachristos, *Nat. Chem.* **2020**, *12*, 1123.

[102] Z. Li, Z. hui Jin, K. Kasatani, H. Okamoto, *Phys. B Condens. Matter* **2006**, *382*, 229.

[103] C. Encinas, E. Otazo, L. Rivera, S. Miltsov, J. Alonso, *Tetrahedron Lett.* **2002**, *43*, 8391.

[104] H. Tian, F. Meng, In *Organic Photovoltaics*, CRC Press, **2017**, pp. 313–330.

[105] L. Zhang, J. M. Cole, *J. Mater. Chem. A* **2017**, *5*, 19541.

[106] Z. Yan, S. Guang, X. Su, H. Xu, *J. Phys. Chem. C* **2012**, *116*, 8894.

[107] C. H. Chang, Y. C. Chen, C. Y. Hsu, H. H. Chou, J. T. Lin, *Org. Lett.* **2012**, *14*, 4726.

[108] J. H. Yum, P. Walter, S. Huber, D. Rentsch, T. Geiger, F. Nüesch, F. De Angelis, M. Grätzel, M. K. Nazeeruddin, *J. Am. Chem. Soc.* **2007**, *129*, 10320.

[109] J. Park, C. Barolo, F. Sauvage, N. Barbero, C. Benzi, P. Quagliotto, S. Coluccia, D. Di Censo, M. Grätzel, M. K. Nazeeruddin, G. Viscardi, *Chem. Commun.* **2012**, *48,* 2782.

[110] T. Geiger, S. Kuster, J.-H. Yum, S.-J. Moon, M. K. Nazeeruddin, M. Grätzel, F. Nüesch, *Adv. Funct. Mater.* **2009**, *19*.

[111] S. Kuster, F. Sauvage, M. K. Nazeeruddin, M. Grätzel, F. A. Nüesch, T. Geiger, *Dye. Pigment.* **2010**, *87*, 30.

[112] T. Maeda, Y. Hamamura, K. Miyanaga, N. Shima, S. Yagi, H. Nakazumi, *Org. Lett.* **2011**, *13*, 5994.

[113] T. Geiger, S. Kuster, J. H. Yum, S. J. Moon, M. K. Nazeeruddin, M. Grätzel, F. Nüesch, *Adv. Funct. Mater.* **2009**, *19*, 2720.

[114] C. Magistris, S. Martiniani, N. Barbero, J. Park, C. Benzi, A. Anderson, C. H. Law, C. Barolo, B. O'Regan, *Renew. Energy* **2013**, *60*, 672.

[115] T. Maeda, S. Mineta, H. Fujiwara, H. Nakao, S. Yagi, H. Nakazumi, *J. Mater. Chem. A* **2013**, *1,* 1303.

[116] J. Park, N. Barbero, J. Yoon, E. Dell'Orto, S. Galliano, R. Borrelli, J. H. Yum, D. Di Censo, M. Grätzel, M. K. Nazeeruddin, C. Barolo, G. Viscardi, *Phys. Chem. Chem. Phys.* **2014**, *16*, 24173.

[117] C. Qin, Y. Numata, S. Zhang, X. Yang, A. Islam, K. Zhang, H. Chen, L. Han, *Adv. Funct. Mater.* **2014**, *24*, 3059.

[118] S. Galliano, V. Novelli, N. Barbero, A. Smarra, G. Viscardi, R. Borrelli, F. Sauvage, C. Barolo, *Energies* **2016**, *9*.

[119] A. Ehret, L. Stuhl, M. T. Spitler, *J. Phys. Chem. B* **2001**, *105*, 9960.

[120] W. Wu, F. Meng, J. Li, X. Teng, J. Hua, *Synth. Met.* **2009**, *159*, 1028.

[121] G. Pepe, J. M. Cole, P. G. Waddell, S. McKechnie, *Mol. Syst. Des. Eng.* **2016**, *1*, 86.

[122] T. Ono, T. Yamaguchi, H. Arakawa, *Sol. Energy Mater. Sol. Cells* **2009**, *93*, 831.

[123] K. Sayama, S. Tsukagoshi, T. Mori, K. Hara, Y. Ohga, A. Shinpou, Y. Abe, S. Suga, H. Arakawa, *Sol. Energy Mater. Sol. Cells* **2003**, *80*, 47.

[124] K. Funabiki, H. Mase, A. Hibino, N. Tanaka, N. Mizuhata, Y. Sakuragi, A. Nakashima, T. Yoshida, Y. Kubota, M. Matsui, *Energy Environ. Sci.* **2011**, *4*, 2186.

[125] T. Geiger, I. Schoger, D. Rentsch, A. C. Véron, F. Oswald, T. Meyer, F. Nüesch, *Int. J. Photoenergy* **2014**, *2014*, 1.

[126] K. Pydzińska, M. Ziółek, *Dye. Pigment.* **2015**, *122*, 272.

[127] M. Jacobson, *Q. J. Exp. Physiol. Cogn. Med. Sci. Transl. Integr.* **1964**, *49*, 384.

[128] E. F. Schubert, *Light-Emitting Diodes*, Cambridge University Press, Cambridge, **2006**.

[129] E. U. Finlayson, D. K. Arasteh, C. Huizenga, M. D. Rubin, M. S. Reilly, *WINDOW 4.0: Documentation of calculation procedures*, Lawrence Berkeley Lab., CA (United States), **1993**.

[130] P. Fisette, *Windows: Understanding Energy Efficient Performance (University of Massachusetts)*, **2003**.

[131] M. R. Hunt, R.W.G.; Pointer, *Measuring Colour*, John Wiley & Sons Inc.: Chichester, UK, **2011**.

[132] M. K. Gunde, U. O. Krašovec, W. J. Platzer, *J. Opt. Soc. Am. A* **2005**, *22*, 416.

[133] B. S. En, *Br. Stand.* **1998**, 1.

[134] International Commission on Illumination., *Colorimetry*, Commission Internationale de l'Eclairage, **2004**.

[135] A. Ghosh, B. Norton, *Sol. Energy Mater. Sol. Cells* **2017**, *163*, 218.

[136] D. L. MacAdam, *Josa* **1943**, *33*, 18.

[137] G. Wyszecki, W. S. Stiles, *London Sydney John Wiley* **1982**.

[138] D. L'Eclairage, *Comm. Int. L'Eclairage Vienna, Austria,* **1995**.

[139] O. N, R. A, *Colorimetry: fundamentals and applications.*, **2006**.

[140] M. Li, L. Zeng, Y. Chen, L. Zhuang, X. Wang, H. Shen, *Int. J. Photoenergy* **2013**, *2013*.

[141] G. Y. Yoo, J. Jeong, S. Lee, Y. Lee, H. C. Yoon, V. Ben Chu, G. S. Park, Y. J. Hwang, W. Kim, B. K. Min, *ACS Appl. Mater. Interfaces* **2017**, *9*, 14817.

[142] E. Klampaftis, D. Ross, B. S. Richards, In *2014 IEEE 40th Photovoltaic Specialist Conference (PVSC)*, IEEE, **2014**, pp. 25–29.

[143] J. Halme, P. Mäkinen, *Energy Environ. Sci.* **2019**, *12*, 1274.

[144] D. B. Judd, D. L. MacAdam, G. Wyszecki, H. W. Budde, H. R. Condit, S. T. Henderson, J. L. Simonds, *Josa* **1964**, *54*, 1031.

[145] CIE (1967) Recommendations on standard illuminants for colorimetry, in: Proceedings of the CIE Washington Session, Vol. A, CIE Publ. 14, pp. 95–97.

[146] CIE (1964) Official recommendations, Committee E-1.3.1—Colorimetry, in: Proceedings of the 15th Session, Vienna, 1963, Vol. A, CIE Publication 11 A, p. 35.

[147] E. F. Schubert, *Light-emitting diodes*, Cambridge University Press, **2006**.

[148] V. Novelli, N. Barbero, C. Barolo, G. Viscardi, M. Sliwa, F. Sauvage, *Phys. Chem. Chem. Phys.* **2017**, *19*, 27670.

[149] N. Barbero, C. Magistris, J. Park, D. Saccone, P. Quagliotto, R. Buscaino, C. Medana, C. Barolo, G. Viscardi, *Org. Lett.* **2015**, *17*, 3306.

[150] H. Mustroph, *Phys. Sci. Rev.* **2020**, *5*, 1.

[151] B. Ciubini, S. Visentin, L. Serpe, R. Canaparo, A. Fin, N. Barbero, *Dye. Pigment.* **2019**, *160*, 806.

[152] F. Würthner, G. Archetti, R. Schmidt, H.-G. Kuball, *Angew. Chemie* **2008**, *120*, 4605.

[153] S. Pascal, A. Haefele, C. Monnereau, A. Charaf-Eddin, D. Jacquemin, B. Le Guennic, O. Maury, C. Andraud, *Opt. Photonics Counterterrorism, Crime Fight. Def. X; Opt. Mater. Biomater. Secur. Def. Syst. Technol. XI* **2014**, *9253*, 92531A.

[154] D. P. Hagberg, J. H. Yum, H. J. Lee, F. De Angelis, T. Marinado, K. M. Karlsson, R. Humphry-Baker, L. Sun, A. Hagfeldt, M. Grätzel, M. K. Nazeeruddin, *J. Am. Chem. Soc.* **2008**, *130*, 6259.

[155] A. B. Muñoz-García, I. Benesperi, G. Boschloo, J. J. Concepcion, J. H. Delcamp, E. A. Gibson, G. J. Meyer, M. Pavone, H. Pettersson, A. Hagfeldt, M. Freitag, *Chem. Soc. Rev.* **2021**, *50*, 12450.

[156] F. Grifoni, M. Bonomo, W. Naim, N. Barbero, T. Alnasser, I. Dzeba, M. Giordano, A. Tsaturyan, M. Urbani, T. Torres, C. Barolo, F. Sauvage, *Adv. Energy Mater.* **2021**, *2101598*.

[157] M. Grätzel, *Nature* **2001**, *414*, 338−344.

[158] M. K. Nazeeruddin, S. M. Zakeeruddin, R. Humphry-Baker, M. Jirousek, P. Liska, N. Vlachopoulos, V. Shklover, C. H. Fischer, M. Grätzel, *Inorg. Chem.* **1999**, *38*, 6298.

[159] A. Hagfeldt, M. Gratzel, *Acc. Chem. Res.* **2000**, *33*, 269.

[160] G. M. Paternò, N. Barbero, S. Galliano, C. Barolo, G. Lanzani, F. Scotognella, R. Borrelli, *J. Mater. Chem. C* **2018**, *6*, 2778.

[161] J. McCree-Grey, J. M. Cole, P. J. Evans, *ACS Appl. Mater. Interfaces* **2015**, *7*, 16404.

[162] N. Robertson, *Angew. Chemie Int. Ed.* **2006**, *45*, 2338.

[163] L. Zhang, X. Liu, W. Rao, J. Li, *Sci. Rep.* **2016**, *6*, 1.

[164] M. Kasha, H. R. Rawls, M. A. El-Bayoumi, *Pure Appl. Chem.* **1965**, *11*, 371.

[165] P. Salvatori, G. Marotta, A. Cinti, C. Anselmi, E. Mosconi, F. De Angelis, *J. Phys. Chem. C* **2013**, *117*, 3874.

[166] A. K. Chandiran, S. M. Zakeeruddin, R. Humphry-Baker, M. K. Nazeeruddin, M. Grätzel, F. Sauvage, *ChemPhysChem* **2017**, *18*, 2724.

[167] K. Ryuzi, K. Motohiro, S. Kodate, A. Furube, N. Fuke, N. Koide, *J. Phys. Chem. C* **2009**, *113*, 20738.

[168] S. E. Koops, B. C. O'Regan, P. R. F. Barnes, J. R. Durrant, *J. Am. Chem. Soc.* **2009**, *131*, 4808.

[169] G. Boschloo, L. Häggman, A. Hagfeldt, *J. Phys. Chem. B* **2006**, *110*, 13144.

[170] R. Katoh, N. Fuke, A. Furube, N. Koide, *Chem. Phys. Lett.* **2010**, *489*, 202.

[171] C. A. Kelly, F. Farzad, D. W. Thompson, J. M. Stipkala, G. J. Meyer, *Langmuir* **1999**, *15*, 7047.

[172] N. Park, S. Chang, J. V. D. L. K. Kim, A. J. Frank, **2000**, *21*, 985.

[173] J. E. Kroeze, N. Hirata, S. Koops, M. K. Nazeeruddin, L. Schmidt-Mende, M. Grätzel, J. R. Durrant, *J. Am. Chem. Soc.* **2006**, *128*, 16376.

[174] F. Sauvage, J. D. Decoppet, M. Zhang, S. M. Zakeeruddin, P. Comte, M. Nazeeruddin, P. Wang, M. Grätzel, *J. Am. Chem. Soc.* **2011**, *133*, 9304.

[175] P. Buskens, M. Burghoorn, M. C. D. Mourad, Z. Vroon, *Langmuir* **2016**, *32*, 6781.

[176] M. P. A. Williams, M. Ethirajan, K. Ohkubo, P. Chen, P. Pera, J. Morgan, W. H. White, M. Shibata, S. Fukuzumi, K. M. Kadish, R. K. Pandey, *Bioconjug. Chem.* **2011**, *22*, 2283.

[177] F. Sauvage, S. Chhor, A. Marchioro, J. E. Moser, M. Graetzel, *J. Am. Chem. Soc.* **2011**, *133*, 13103.

[178] A. Y. Anderson, P. R. F. Barnes, J. R. Durrant, B. C. O'regan, *J. Phys. Chem. C* **2011**, *115*, 2439.

[179] M. Flasque, A. N. Van Nhien, D. Moia, P. R. F. Barnes, F. Sauvage, *J. Phys. Chem. C* **2016**, *120*, 18991.

[180] S. S. Pandey, T. Inoue, N. Fujikawa, Y. Yamaguchi, S. Hayase, *J. Photochem. Photobiol. A Chem.* **2010**, *214*, 269.

[181] W. W. Bao, R. Li, Z. C. Dai, J. Tang, X. Shi, J. T. Geng, Z. F. Deng, J. Hua, *Front. Chem.* **2020**, *8*, 679.

[182] Y. Li, P. Sonar, L. Murphy, W. Hong, *Energy Environ. Sci.* **2013**, *6*, 1684.

[183] M. Grzybowski, D. T. Gryko, *Adv. Opt. Mater.* **2015**, *3*, 280.

[184] D. Chandran, K.-S. Lee, *Macromol. Res.* **2013**, *21*, 272.

[185] J.-H. Kim, M. Lee, H. Yang, D.-H. Hwang, *J. Mater. Chem. A* **2014**, *2*, 6348.

[186] S. Huang, C. Yang, J. Huang, X. Wang, M. Wang, *Dye. Pigment.* **2018**, *154*, 269.

[187] M. Bai, S. Achilefu, **2010**, *16*, 213.

[188] S. Wiktorowski, E. Daltrozzo, A. Zumbusch, *RSC Adv.* **2015**, *5*, 29420.

[189] R. Sen A. Weiss, C. Uhrich, G. Fischer, E. Daltrozzo, A. Zumbusch, J. Tanabe, J. H. Hwang, I. Bruder, P. Erk, *Organic Electronic Device with Active Layer*, **2015**.

[190] F. Guo, X. Liu, Y. Ding, F. Kong, W. Chen, L. Zhou, S. Dai, *RSC Adv.* **2016**, *6*, 13433.

[191] J. Tang, S. Qu, J. Hu, W. Wu, J. Hua, *Sol. energy* **2012**, *86*, 2306.

[192] T. W. Holcombe, J.-H. Yum, Y. Kim, K. Rakstys, M. Grätzel, *J. Mater. Chem. A* **2013**, *1*, 13978.

[193] J. Warnan, L. Favereau, Y. Pellegrin, E. Blart, D. Jacquemin, F. Odobel, *J. Photochem. Photobiol. A Chem.* **2011**, *226*, 9.

[194] Y. Farre, L. Zhang, Y. Pellegrin, A. Planchat, E. Blart, M. Boujtita, L. Hammarstrom, D. Jacquemin, F. Odobel, *J. Phys. Chem. C* **2016**, *120*, 7923.

[195] Y. Farré, M. Raissi, A. Fihey, Y. Pellegrin, E. Blart, D. Jacquemin, F. Odobel, *ChemSusChem* **2017**, *10*, 2618.

[196] G. M. Fischer, M. K. Klein, E. Daltrozzo, A. Zumbusch, *European J. Org. Chem.* **2011**, *2011*, 3421.

[197] G. M. Fischer, M. Isomäki-Krondahl, I. Göttker-Schnetmann, E. Daltrozzo, A. Zumbusch, *Chem. – A Eur. J.* **2009**, *15*, 4857.

[198] A. B. Pun, L. M. Campos, D. N. Congreve, *J. Am. Chem. Soc.* **2019**, *141*, 3777.

[199] N. C. D. Nath, H. J. Lee, W. Y. Choi, J. J. Lee, *Electrochim. Acta* **2013**, *109*, 39.

[200] N. C. D. Nath, J. J. Lee, *J. Ind. Eng. Chem.* **2019**, *78*, 53.

[201] M. Kawasaki, S. Aoyama, *Chem. Commun.* **2004**, 988.

[202] T. W. Hamann, *Dalt. Trans.* **2012**, *41*, 3111.

[203] J. Cong, X. Yang, Y. Hao, L. Kloo, L. Sun, *RSC Adv.* **2012**, *2*, 3625.

[204] M. U. M. Patel, R. Demir-Cakan, M. Morcrette, J. M. Tarascon, M. Gaberscek, R. Dominko, *ChemSusChem* **2013**, *6*, 1177.

[205] C. Barchasz, F. Molton, C. Duboc, J. C. Leprêtre, S. Patoux, F. Alloin, *Anal. Chem.* **2012**,

84, 3973.

[206] N. A. Cañas, D. N. Fronczek, N. Wagner, A. Latz, K. A. Friedrich, *J. Phys. Chem. C* **2014**, *118*, 12106.

[207] Y. C. Lu, Q. He, H. A. Gasteiger, *J. Phys. Chem. C* **2014**, *118*, 5733.

[208] G. Zhang, H. Peng, C. Zhao, X. Chen, L. Zhao, P. Li, J. Huang, Q. Zhang, *Angew. Chemie* **2018**, *130*, 16974.

[209] Q. Zou, Z. Liang, G. Y. Du, C. Y. Liu, E. Y. Li, Y. C. Lu, *J. Am. Chem. Soc.* **2018**, *140*, 10740.

[210] Q. He, Y. Gorlin, M. U. M. Patel, H. A. Gasteiger, Y.-C. Lu, *J. Electrochem. Soc.* **2018**, *165*, A4027.

[211] Y. K. Eom, S. H. Kang, I. T. Choi, Y. Yoo, J. Kim, H. K. Kim, *J. Mater. Chem. A* **2017**, *5*, 2297.

[212] K. Kakiage, Y. Aoyama, T. Yano, K. Oya, J. Fujisawa, M. Hanaya, *Chem. Commun.* **2015**, *51*, 15894.

Annex

Functions needed for the calculation of CRI for a PV device:

$$X_r = \sum_{380}^{780} P(\lambda)\,\bar{x}(\lambda)\,\Delta(\lambda) \tag*{Eq.(1)}$$

$$Y_r = \sum_{380}^{780} P(\lambda)\bar{y}(\lambda)\,\Delta(\lambda) \tag*{Eq.(2)}$$

$$Z_r = \sum_{380}^{780} P(\lambda)\bar{z}(\lambda)\,\Delta(\lambda) \tag*{Eq.(3)}$$

$$X_{r,i} = \sum_{380}^{780} P(\lambda)\beta i\ (\lambda)\,\bar{x}(\lambda)\,\Delta(\lambda) \tag*{Eq.(4)}$$

$$Y_{r,i} = \sum_{380}^{780} P(\lambda)\beta i\ (\lambda)\bar{y}(\lambda)\,\Delta(\lambda) \tag*{Eq.(5)}$$

$$Z_{r,i} = \sum_{380}^{780} P(\lambda)\beta i\ (\lambda)\bar{z}(\lambda)\,\Delta(\lambda) \tag*{Eq.(6)}$$

$$u_r = \frac{4X_r}{X_r+15Y_r+3Z_r} \tag*{Eq.(7)}$$

$$v_r = \frac{6X_r}{X_r+15Y_r+3Z_r} \tag*{Eq.(8)}$$

$$u_{r,i} = \frac{4X_{r,i}}{X_{r,i}+15Y_{r,i}+3Z_{r,i}} \tag*{Eq.(9)}$$

$$v_{r,i} = \frac{6X_{r,i}}{X_{r,i}+15Y_{r,i}+3Z_{r,i}} \tag*{Eq.(10)}$$

$$W^{*}{}_{r,i} = 25\left(\frac{100Y_{r,i}}{Y_r}\right)^{\frac{1}{3}} - 17 \tag*{Eq.(11)}$$

$$U^{*}_{r,i} = 13W^{*}_{r,i}\left(u_{r,i} - u_r\right) \tag*{Eq.(12)}$$

$$V_{r,i}^{*} = 13W_{r,i}^{*}\left(v_{r,i} - v_r\right) \qquad Eq.(13)$$

$$X_t = \sum_{380}^{780} P(\lambda)\tau(\lambda)\,\overline{x}(\lambda)\,\Delta(\lambda) \qquad Eq.(14)$$

$$Y_t = \sum_{380}^{780} P(\lambda)\tau(\lambda)\bar{y}(\lambda)\,\Delta(\lambda) \qquad Eq.(15)$$

$$Z_t = \sum_{380}^{780} P(\lambda)\tau(\lambda)\bar{z}(\lambda)\,\Delta(\lambda) \qquad Eq.(16)$$

$$X_{t,i} = \sum_{380}^{780} P(\lambda)\tau(\lambda)\beta i\ (\lambda)\,\overline{x}(\lambda)\,\Delta(\lambda) \qquad Eq.(17)$$

$$Y_{t,i} = \sum_{380}^{780} P(\lambda)\tau(\lambda)\beta i\ (\lambda)\bar{y}(\lambda)\,\Delta(\lambda) \qquad Eq.(18)$$

$$Z_{t,i} = \sum_{380}^{780} P(\lambda)\tau(\lambda)\beta i\ (\lambda)\bar{z}(\lambda)\,\Delta(\lambda) \qquad Eq.(19)$$

$$u_t = \frac{4X_t}{X_t+15Y_t+3Z_t} \qquad Eq.(20)$$

$$v_t = \frac{6X_t}{X_t+15Y_t+3Z_t} \qquad Eq.(21)$$

$$u_{t,i} = \frac{4X_{t,i}}{X_{t,i}+15Y_{t,i}+3Z_{t,i}} \qquad Eq.(22)$$

$$v_{t,i} = \frac{6X_{t,i}}{X_{t,i}+15Y_{t,i}+3Z_{t,i}} \qquad Eq.(23)$$

$$c_t = \frac{4-u_t-10v_t}{v_t} \qquad Eq.(24)$$

$$d_t = \frac{1.708v_t+0.404-1.481u_t}{v_t} \qquad Eq.(25)$$

$$c_{t,i} = \frac{4-u_{t,i}-10v_{t,i}}{v_{t,i}} \qquad Eq.(26)$$

$$d_{t,i} = \frac{1.708v_{t,i}+0.404-1.481u_{t,i}}{v_{t,i}} \qquad Eq.(27)$$

$$c_r = \frac{4-u_r-10v_r}{v_r} \qquad Eq.(28)$$

$$d_r = \frac{1.708v_r+0.404-1.481u_r}{v_r} \qquad Eq.(29)$$

$$u_{t,i}^{*} = \frac{10.872+0.404\frac{c_r}{c_t}c_{t,i}-4\frac{d_r}{d_t}d_{t,i}}{16.518+1.481\frac{c_r}{c_t}c_{t,i}-\frac{d_r}{d_t}d_{t,i}} \qquad Eq.(30)$$

$$v_{t,i}^{*} = \frac{5.520}{16.518+1.481\frac{c_r}{c_t}c_{t,i}-\frac{d_r}{d_t}d_{t,i}} \qquad Eq.(31)$$

$$W^{*}{}_{t,i} = 25\left(\frac{100Y_{t,i}}{Y_t}\right)^{\frac{1}{3}} - 17 \qquad Eq.(32)$$

$$U_{t,i}^{*} = 13W_{t,i}^{*}\left(u_{t,i}^{*} - u_r\right) \qquad Eq.(33)$$

$$V_{t,i}^{*} = 13W_{t,i}^{*}\left(v_{t,i}^{*} - v_r\right) \qquad Eq.(34)$$

$$\Delta E_i = \sqrt{(U^{*}{}_{t,i} - U^{*}{}_{r,i})^2 + (V^{*}{}_{t,i} - V^{*}{}_{r,i})^2 + (L^{*}{}_{t,i} - L^{*}{}_{r,i})^2} \qquad Eq.(35)$$

$$Ri = 100 - 4.6\Delta Ei \qquad Eq.(36)$$

$$CRI = \frac{1}{8}\sum_{i=1}^{8} Ri \qquad Eq.(37)$$

<u>Preliminary Computational study on PPcy molecules</u>:

In order to develop a new family of NIR absorbers based on the pyrrolopyrrole cyanines PPcys, eleven preliminary molecular targets were devised that vary only in the nature of the anchoring function and the type of π-conjugated connector (Figure A.1). In order to adsorb properly on TiO_2, PPcys dyes must have an appropriate anchoring function. This study was carried out by Professor Denis Jacquemin (CEISAM Laboratory, University of Nantes) using density functional theory (DFT) for the ground state properties and time-dependent density theory (TD-DFT) for the excited state properties.

The studied molecules are unsymmetrical, substituted on one side by a bromine atom, and have only one anchoring function. The presence of bromine serves as an input for further functionalization of the PPcy, for example, by an electron donor. As presented in Figure A.1, it appears that the spin densities of the HOMO orbitals are mainly concentrated at the pyrrolopyrrole cyanine ring and slightly at the boron atoms. The spin densities of the LUMO level are also located along with the cyanine system with higher intensity on the nitrogen atom of the pyridine ring. The anchor function causes a slight variation in the HOMO and LUMO orbitals. However, the theoretical wavelength values are significantly impacted (Table A.1).

<u>Influence of the nature and position of the anchor function</u>

In Figure A.1, the molecules 1-6 possess an anchor function directly connected to the cyanine system. The impact of the nature of the anchor function is studied: carboxylic acid in molecules **1** and **2**, cyanoacrylic acid in molecules **3** and **4**, phosphonic acid in molecule **5**, and acrylic acid in molecule **6**. The influence of the position (meta or para) of the anchor function in relation to the nitrogen atom of the pyridine ring was also studied. The dyes **3**, **4**, and **6** show a bathochromic shift compared to **1**, **2,** and **5**. This difference can be attributed to the more electron-withdrawing character of the acrylic units compared to the carboxylic and phosphonic acids, which the LUMO orbital. The electron densities of the LUMO orbitals are more intense on the anchor functions when they are positioned para to the pyridine nitrogen, as shown in the example of molecules **1** and **2** or **3** and **4**.

Impact of a π-conjugated connector

The addition of a π-conjugated connector is studied. The aim is to follow if this addition may extend the electronic conjugation. Thus, these additions are studied: a phenyl spacer in molecule **7**, furan in molecule **8**, thienyl in molecule **9**, alkyne in molecule **10**, and benzothiadiazole in molecule **11**. The HOMO and LUMO energy levels vary very little, with values around -0.24 eV and -0.11 eV. The introduction of furan, thienyl, and/or benzothiadiazole rings shifts the wavelength towards the red compared to a classical carboxylic acid function but in relatively small amplitudes. Also, the spin densities of the LUMO orbitals of all these compounds are very poorly concentrated on the anchor function. However, to favor the electron injection process, it makes more sense to have a high electron density on the anchor function to mix these dye orbitals with the conduction band wave function of TiO_2.

These quantum calculations make it possible to select the most promising targets to be synthesized as a priority. It is indeed observed that the spin densities of the HOMO and LUMO levels are mainly concentrated on the core of the molecule. It is also observed that there is very little delocalization of spin densities towards the end of the molecule on the LUMO, even when a π-conjugated connector is introduced. In order to favor the injection process, it, therefore, appears more sensible to place the anchor function directly on the pyridine ring without incorporating a spacer. In addition, it is noted that the spin density of the LUMO orbital on the anchor function is more significant when the latter is placed in the para position of the nitrogen atom rather than in the meta position.

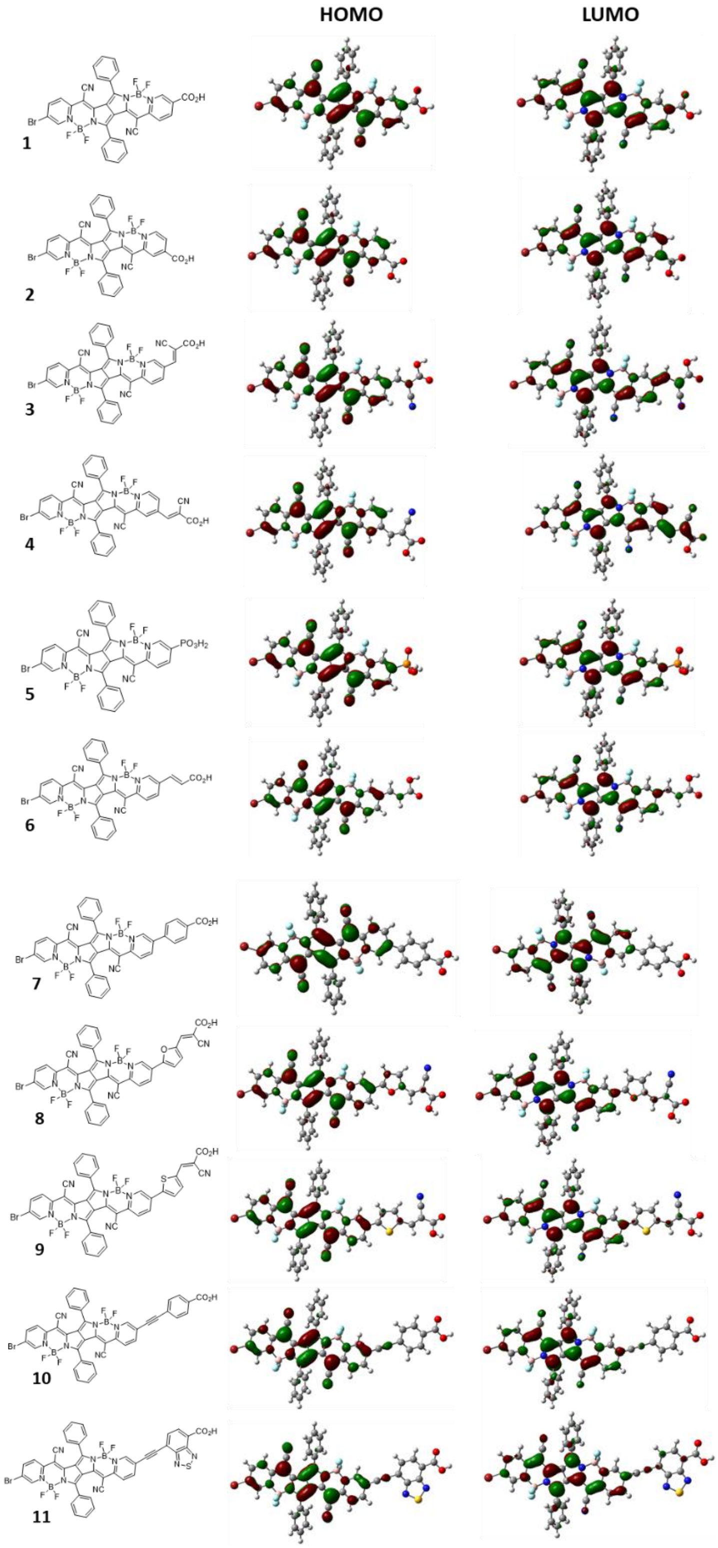

Figure A.1. Representation of the spin densities of the frontier orbitals determined by quantum calculations of the PPcy molecules 1, 2, 3, 4, 5, 6, 7, 8, 9, 10, and 11.

Table A.1. Summary table of DFT and TD-DFT calculations to investigate the impact of the type of anchor function on the pyrrolopyrrole cyanine dyes 1, 2, 3, 4, 5, 6, 7, 8, 9, 10, and 11.

Molecule	**Transition**	**λ_{max} [nm]**	**HOMO (eV)**	**LUMO (eV)**
1	HOMO → LUMO	629	-0,24	-0,11
2	HOMO → LUMO	629	-0,24	-0,11
3	HOMO → LUMO	652	-0,24	-0,12
4	HOMO → LUMO	650	-0,24	-0,11
5	HOMO → LUMO	627	-0,24	-0,11
6	HOMO → LUMO	641	-0,24	-0,12
7	HOMO → LUMO	632	-0,24	-0,11
8	HOMO → LUMO	645	-0,24	-0,11
9	HOMO → LUMO	629	-0,24	-0,11
10	HOMO → LUMO	641	-0,24	-0,11
11	HOMO → LUMO	645	-0,24	-0,11

Fabrication of Solar Cells

The fluorine-doped SnO_2 (FTO) conducting glass (NSG-10, Nippon Sheet Glass) was thoroughly cleaned with a detergent solution, acetone, and ethanol solvents. Then the substrates were treated with 40 mM $TiCl_4$ aqueous solution at 70 °C for 45 min in order to make a thin and compact TiO_2 underlayer. The colloidal TiO_2 paste of Dyenamo DNEP03 was used, and the electrodes were prepared by the screen-printing method yielding different thicknesses depending on the number of printed layers. For the device's performance, it was sheltered with a 5 μm thick 400 nm-based TiO_2 scattering layer. The TiO_2 film was sintered at 500 °C under dry airflow and cooled down to room temperature to obtain a mesoporous, electronic conductive film. The mesoporous TiO_2 film was treated in $TiCl_4$ (40 mmol/L) and kept at 70 °C in an oven for 30 min. After sintering at 500 °C in air and cooled down to 80 °C, the mesoporous TiO_2 electrodes were stained by immersing them into the dye solution at room temperature or 4 °C for 12 h and 7 days for experiments at −20 °C. The dye-coated TiO_2 film working electrode and thermally low-concentrated platinized conducting glass counter electrode were assembled using a 25 μm thick Surlyn hot-melt ring (DuPont, USA) heated at 125 °C. The internal space was filled with electrolyte using a vacuum pump through a predrilled hole on the counter electrode. The hole was sealed with a Surlyn sheet and a thin glass cover by heating.

Optical and Electrical Characterization of Solar Cells

During the photovoltaic performance measurements, a black metal mask with an aperture area of 0.158 cm^2 covered the solar cells. The solar cells were measured under radiation at 100 mW/cm^2 provided by a 450 W xenon lamp of the Oriel solar simulator (USA). The spectral output of the lamp passed a Schott K113 Tempax sunlight filter (Prazisions¨Glas & Optik GmbH, Germany), reducing the mismatch between the simulated and true solar spectra to less than 2%. The light intensity was determined using a calibrated Si reference diode equipped with an infrared cutoff filter (KG-3, Schott). The J−V curves were recorded by a Keithley 2400 source meter. The voltage scan rate was set to 20 mV/s. IPCE spectra were measured with a lock-in amplifier (Stanford Research System SR830 DSP) under chopped monochromatic light (2 Hz) generated by a white light source from a 300W xenon lamp passing through a Gemini-180 double monochromator (Jobin Yvon Ltd.). The optical properties of the dye in solution and in the device were measured using an Agilent Cary 5000 spectrophotometer. A quartz cuvette with 1 cm light path was used for solution in dual beam transmission mode. For devices, all measurements were carried out in total transmittance mode using a 150 mm integration sphere. Background and zero were corrected, however, without subtracting any external contributions such as glass absorption and reflection. All AVT measurements, therefore, correspond to a complete device assessment.

Picosecond Pump−Probe Transient Absorption Spectroscopy (TAS) Measurements

The picosecond setup for the TAS measurements was used to investigate regeneration and recombination kinetics of the dye radical cation. The setup is composed of (1) a Nd:YAG laser (EKSPLA, PL2550, 10 Hz repetition rate, 30 ps pulse duration, 532 or 355 nm excitation) in combination with an optical parametric generator (EKSPLA, PG400 with broad excitation range 420−2300 nm) which is pumped by the third harmonic of Nd:YAG; (2) three different probe systems (Hamamatsu Photonics): Xe breakdown cell for the shortest 0.5−20 ns time scale; Xe Flash lamp for the 50 ns to 2 μs time scale; and continuous 150 W Xe lamp for the 5 μs to 10 ms time scale; (3) detector part: spectrograph (Princeton Instruments, SP2300), high dynamic range streak camera (Hamamatsu Photonics, C13410) with digital readout camera (Hamamatsu Photonics, ORCA Flash4, C11440); (4) delay generator (Stanford Research Systems, DG645), delay unit, and shutters control unit (Hamamatsu Photonics) to synchronize all the setup parts controlled by computer through the HPD-TA software (Hamamatsu Phonics); and (5) white light input optics, excitation optics, pump and probe shutters, moving sample holder, and motorized 12-position optical density filter wheel for attenuation of laser excitation pulse energy. For the TAS measurements of the DSSC, the probe light was focused perpendicular to the sample, and the pump light was focused 45° to the sample. The probe light was attenuated with different optical density filters (Newport or Thorlabs) and transmitted through the sample. The resulting light was introduced into the spectrograph and analyzed by the streak camera. The energy of the pump pulse in the excitation wavelength range 810−830 nm was set to ca. 0.2 mJ. A 750 nm short pass cutoff filter (Thorlabs) was placed before the spectrograph to cut scattering light from the pump. Transient absorption is calculated from four streak images according to the equation:

$$\Delta A = -\log\left(\frac{data - emission}{monitor - dark}\right)$$

Where data is the intensity of the image obtained where both pump and probe are on, emission where only pump is on, monitor where only probe is on, and dark when both pump and probe are off in order to subtract the contribution of stray light. Each of these four images consisted of N integrated camera images. Measurements are performed in the sequence, data, emission, monitor, dark, and this sequence is repeated M times. In order to obtain a satisfactory signal-to-noise ratio, N was 500 and M = 5−10.

Femtosecond Pump−Probe Transient Absorption Spectroscopy (TAS) Measurements

To record the TA spectra, a home-built setup fs-TA spectrometer was utilized based on a Ti:sapphire regenerative amplifier laser system (Pulsar, Amplitude Technology) delivering 40 fs-long pulses, at 5 kHz, centered at 800 nm. One portion of the 800 nm beam is used directly as the pump beam, and the second for the white light generation (460−1030 nm) utilizing a 3 mm sapphire crystal. The residual fundamental at 800 nm was filtered by a conveniently concentrated solution of the IR125 dye (Lambda Physik) in EtOH in a 1 mm quartz cell. The relative linear polarization between the pump and probe beams is set at the magic angle (54.7°), and the fwhm of the instrument response function (IRF) is 35 fs. To ensure sufficient reduction of the noise level, for every time point, 200 spectra are averaged, and the final data result from averaging 8 different scans in solution and 6−8 in the DSSC samples, changing the 2 mm long excitation line every 3−4 scans to avoid degradation. Every individual scan lasts 7 min and over 4−5 scans no change of the kinetics is observed due to possible degradation. For solution samples, in order to avoid re-exciting the same molecules in the 0.5 mm quartz cuvette, we sufficiently circulate the sample using a peristaltic pump. The pump pulse intensity was set so as to ensure a linear dependence of the ground state bleach signals in all experiments reported here. A 90 μJ/cm² pump energy fluence was used both on the solution samples, as well as on the complete DSSC samples. The DSSC samples for the TA measurements were prepared under similar conditions as described above, restricted on single-TiO_2 or ZrO_2 or Al_2O_3 layers, and sensitization was carried out overnight (14 h) using the same composition of the dye solution. Data are processed to correct the effects of group velocity dispersion (chirp) in the white light continuum and to subtract the nonlinear signal from the solvent and the presence of any delay-independent background. After chirp correction, the zero time delay is defined with an error bar of 30 fs over the entire observation spectral window. Single wavelength fits are made with ORIGIN (eq 1), and global analysis, with the GLOTARAN software

$$\Delta A(\lambda, t) = \sum_i A_i(\lambda) e^{-\frac{t}{\tau_i}} \otimes \mathrm{IRF}$$

<u>Time-Correlated Single Photon Counting Measurements</u>

Excited state lifetimes were monitored using a time-correlated single photon counting (TCSPC) technique using an Edinburgh Instrument FLS980 spectrometer. The same spectrometer was used for steady state measurements using a continuous Xe light source and double excitation/emission monochromator. TCSPC experiments were carried out using a 70 ps width laser diode as an excitation source (20 MHz repetition rate, 5 pJ/cm² average energy, instrument response in the range of 90−100 ps fwhm) and a microchannel plate photomultiplier tube (MCP-PMT) Hamamatsu detector set after the first emission monochromator. A 780 nm long-pass filter was used in emission to reject light scattering from the glass of the device. The emission was monitored at 840 nm for VG20-C_x dye and at 780 nm for PPcy dyes with a slit opening of 10 nm in the emission monochromator. The numerical analysis of the excited-state lifetime has been determined after reconvolution of the photoluminescence decay considering the instrumental response function (IRF).

Intensity Modulated Photovoltage/Photocurrent Spectroscopy (IMVS/PS) experiments

IMVS/PS has been deemed an efficient way to obtain kinetic information about the electron transport in the photoanode and the non-geminate recombination of the injected electron in TiO_2 and the oxidized species in the electrolyte (I_3^-). These experiments are based on frequency-domain techniques, where small amplitude perturbations are superimposed on a large bias driving force, which is in the form of continuous irradiation. For measurements of IMPS and IMVS, a sinusoidal light perturbation with a small amplitude is applied over a frequency range. Similar to electron impedance spectroscopy (EIS), the instrument is generally operated with the main potentiostat (PS1) containing a built-in module as a frequency response analyzer. It requires another potentiostatic loop (PS2 and PS3) to control the intensity and modulation of the intensity and modulation of the LED source. For more precise determination, active feedback control of the intensity with PS2 from a photo-detector is added during the measurement. The LED light-weakly absorbed by the dye molecules- is driven by PS3 with the modulated light intensity much smaller than the continuous wave (cw) bias light intensity (Figure A.2).

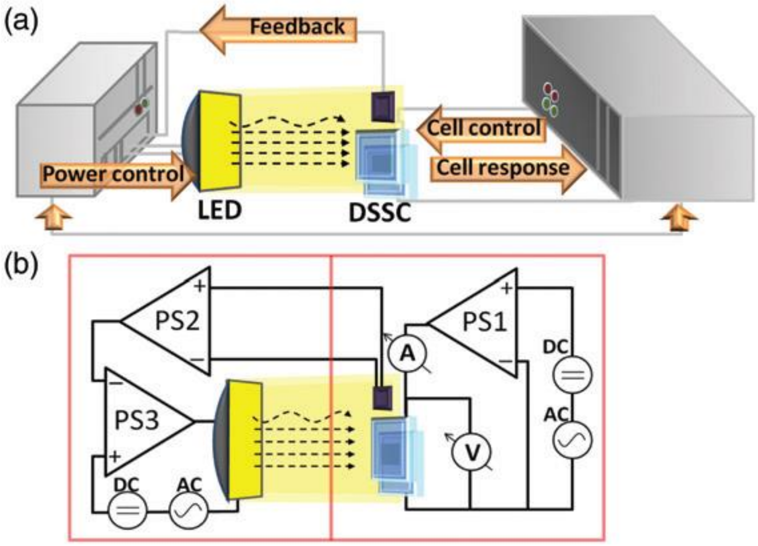

Figure A.2. Experiment for IMPS/IMVS methods: (a) schematic representation of the instrument and (b) general circuit diagram of the apparatus. PS represents a potentiostat with a built-in frequency response analyzer. The box on the right side is the master unit, and the slave unit on the left side performs small-amplitude modulation of the light intensity for IMPS/IMVS.

As shown in Figure A. 3, the kinetic information for the charge transport and non-geminate recombination processes are obtainable under two extreme conditions: short circuit and open circuit, respectively. For a homogeneous light absorption system, the quasi-Fermi level through the TiO_2 film is constant at the open-circuit condition, but at the short-circuit condition, a curve presented in Figure A. 3 is used to present the gradient of the Fermi level across the film, and the electrons diffuse directly into the TCO substrate. Under the short-circuit condition, the transport (diffusion) kinetics of the injected electrons in the CB of TiO_2 are monitored through IMPS. Under the open-circuit condition, the kinetics of the non-geminate charge recombination is probed via IMVS.

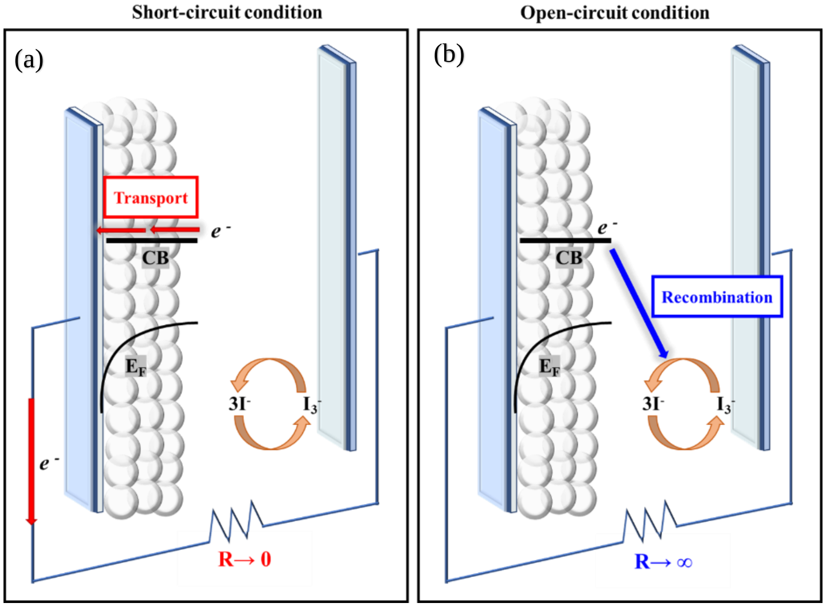

*Figure A. 3. Schematic representations of kinetic processes of a DSSC that are investigated via (**a**) intensity-modulated photocurrent spectroscopy (IMPS) under short-circuit condition and (**b**) intensity-modulated photovoltage spectroscopy (IMVS) under open-circuit condition. The solid arrows represent the most probable directions for electron transport (red) and charge recombination (blue) at the two extreme conditions.*

Keywords
Transparent photovoltaic, near-infrared, wavelength - selective, colorless, aesthetics, Dye-sensitized solar cells

Abstract

By combining visible transparency and solar energy conversion, transparent photovoltaics (TPV) prompted the interest to fill the gap of applications in which the conventional opaque solar cells are not feasible. In pioneering TPV adoption in practical application, aesthetics is equally important as photovoltaic performances. In this context, average visible transmittance (AVT), color rendering index (CRI), correlated color temperature (CCT), and chromaticity coordinates, along with other colorimetric evaluations, gain a crucial role in the TPV domain. Dye Sensitized Solar Cells (DSSC) have been deemed an interesting technology to achieve efficient energy conversion and the required visual comfort by being wavelength selective to the NIR. The peculiarity of being highly transparent and color-neutral can be achieved by consolidating the capability of harvesting selectively the NIR part of the solar spectrum with a fully colorless electrolyte. The results of this thesis work are divided into three main sections. In the first section, we report the first attempt towards NIR-DSSC through symmetrical cyanine dye coded **VG20**. This cyanine **VG20** dye achieved a power conversion efficiency (PCE) of 3.1% while rendering highly transparent devices with an AVT value of 76%, a 93.6 CRI, and a CCT of 4297 K. The main limitation of higher performances was identified to be the energy transfer from monomer to aggregates. In the second section, the identified limitations were tackled by dye engineering, resulting in novel pyrrolopyrrole cyanine dyes (PPcy). The PPcy dyes showed remarkable performances with PCE > 4% and AVT values > 75%. Finally, the third section investigates different colorless and transparent electrolytes, leading to achieving color-neutral NIR-DSSC with a high CRI of 96 and AVT value of 78%. This thesis work provides future directions to enhance the performances of this non-intrusive NIR-DSSC technology, which positions itself as one of the best TPV systems.

Mots-clés
Photovoltaïque transparent, proche-infrarouge, sélectif en longueur d'onde, incolore, esthétique, cellules solaires à colorant

Résumé en français

En combinant transparence et conversion de l'énergie solaire, le photovoltaïque transparent (TPV) rend possible des applications nouvelles qui ne sont pas réalisables avec des cellules solaires opaques conventionnelles. Pour l’intégration du TPV dans des applications pratiques, l'esthétique est aussi importante que les performances photovoltaïques. Dans ce contexte, la transmittance visible moyenne (AVT), l'indice de rendu de couleur (CRI), la température de couleur corrélée (CCT) et les coordonnées chromatiques, ainsi que d'autres évaluations colorimétriques, jouent un rôle crucial dans le domaine des TPV. Les cellules solaires à colorant (DSSC) ont été considérées comme une technologie intéressante pour obtenir à la fois une conversion énergétique efficace et le confort visuel requis, en étant sélectives en longueur d'onde dans le proche infrarouge (NIR). Les particularités de ces cellules d'être hautement transparente et incolore sont obtenues en consolidant la capacité à convertir sélectivement la partie NIR du spectre solaire avec un électrolyte totalement incolore. Les résultats de ce travail de thèse sont divisés en trois sections principales. Dans la première section, nous rapportons la première tentative vers le NIR-DSSC à travers le colorant cyanine symétrique codé VG20. Ce colorant a atteint un rendement de photoconversion (PCE) de 3,1% tout en étant hautement transparent avec une valeur AVT de 76%, un CRI de 93,6 et un CCT de 4297 K. La principale limitation dans l’amélioration des performances a été identifiée comme étant le transfert d'énergie du monomère aux agrégats. Dans la deuxième section, les limitations identifiées ont été surmontées par ingénierie moléculaire, ce qui a permis de découvrir de nouveaux colorants pyrrolopyrrole cyanine (PPcy). Les colorants PPcy ont montré des performances remarquables avec un PCE > 4% et des valeurs AVT > 75%. Enfin, dans la troisième section différents électrolytes incolores et transparents sont étudiés, permettant d'obtenir un NIR-DSSC de couleur neutre avec un CRI élevé de 96 et une AVT de 78 %. Ce travail de thèse fournit des perspectives futures pour améliorer les performances de cette technologie des NIR-DSSC, qui se positionne comme l'un des meilleurs systèmes TPV.